JUSTUS-LIEBIG-
UNIVERSITÄT
GIESSEN

Dissertation

Quarks and Gluons in the Phase Diagram of Quantum Chromodynamics

Christian Andreas Welzbacher

July 2016

Justus-Liebig-Universität Giessen

Fachbereich 07

Institut für theoretische Physik

Dekan:	**Prof. Dr. Bernhard Mühlherr**
Erstgutachter:	**Prof. Dr. Christian S. Fischer**
Zweitgutachter:	**Prof. Dr. Lorenz von Smekal**
Vorsitzende der Prüfungskommission:	**Prof. Dr. Claudia Höhne**
Tag der Einreichung:	**13.05.2016**
Tag der mündlichen Prüfung:	**14.07.2016**

So much universe, and so little time.

(Sir Terry Pratchett)

Quarks und Gluonen im Phasendiagramm der Quantenchromodynamik

Zusammenfassung

In der vorliegenden Dissertation wird das Phasendiagramm von stark wechselwirkender Materie untersucht. Dazu wird im Rahmen der Quantenchromodynamik der Quarkpropagator über seine quantenfeldtheoretischen Bewegungsgleichungen bestimmt. Diese sind bekannt als Dyson-Schwinger Gleichungen und konstituieren einen funktionalen Zugang, welcher mithilfe des Matsubara-Formalismus bei endlicher Temperatur und endlichem chemischen Potential angewendet wird. Theoretische Hintergründe der Quantenchromodynamik werden erläutert, wobei insbesondere auf die Dyson-Schwinger Gleichungen eingegangen wird. Chirale Symmetrie sowie Confinement und zugehörige Ordnungsparameter werden diskutiert, welche eine Unterteilung des Phasendiagrammes in verschiedene Phasen ermöglichen. Zudem wird der sogenannte Columbia Plot erläutert, der die Abhängigkeit verschiedener Phasenübergänge von der Quarkmasse skizziert.

Zunächst werden Ergebnisse für ein System mit zwei entarteten leichten Quarks und einem Strange-Quark mit vorangegangenen Untersuchungen verglichen. Eine Trunkierung, welche notwendig ist um das System aus unendlich vielen gekoppelten Gleichungen auf eine endliche Anzahl an Gleichungen zu reduzieren, wird eingeführt. Die Ergebnisse für die Propagatoren und das Phasendiagramm stimmen gut mit vorherigen Arbeiten überein. Einige zusätzliche Ergebnisse werden präsentiert, wobei insbesondere auf die Abhängigkeit des Phasendiagrammes von der Quarkmasse eingegangen wird.

Im Anschluss wird eine systematische Verbesserung der Trunkierung durch die Einführung eines dynamisch betrachteten Charm-Quarks durchgeführt. In dieser Untersuchung ist es insbesondere wichtig, die Skalen richtig zu justieren. Dazu werden die Eigenschaften von pseudoskalaren Mesonen im Vakuum, separat für $N_f = 2 + 1$ und $N_f = 2 + 1 + 1$, reproduziert. Der Vergleich der sich ergebenden Phasendiagramme zeigt, dass das Charm-Quark keinen Einfluss auf die Phasenstruktur hat.

Eine wichtige Frage für das Phasendiagramm von stark wechselwirkender Materie betrifft den Einfluss von hadronischen Freiheitsgraden. In einer explorativen Untersuchung für zwei Quarkarten wird der Einfluss des Nukleons in der Quark-Diquark

Näherung studiert. Dazu werden unbekannte Abhängigkeiten von Temperatur und chemischem Potential durch Vakuumeigenschaften ersetzt und eine Variation selbiger untersucht. Die Studie zeigt, dass baryonische Freiheitsgrade nur sehr geringen Einfluss auf Phasenübergänge im betrachteten Phasendiagramm haben.

Daraufhin wird die reduzierte Dyson-Schwinger Gleichung für den Quark-Gluon-Vertex bei endlicher Temperatur untersucht. Dieser erste Schritt in einer systematischen Studie zeigt wie sich Quarkart sowie Temperaturabhängigkeit auf den Vertex niederschlagen. Es wird offensichtlich, dass eine Rückkopplung der Gleichung für das Gluon notwendig ist.

Im letzten Kapitel untersuchen wir analytische Eigenschaften des Quarkpropagators im Vakuum und bei endlicher Temperatur. Dazu wird die Schwinger Funktion, als Fourier-Transformierte des euklidischen Propagators bezüglich (imaginärer) Zeit untersucht. Zudem wird die Spektralfunktion, welche alle Informationen über die analytische Struktur enthält, eingeführt. Die Bestimmung der Spektralfunktion erfordert die Lösung eines inversen Problems, wozu eine Bayes'sche Rekonstruktion genutzt wird. Ergebnisse für die Spektralfunktion von Testdaten, die mithilfe des Rothkopf-Burnier Algorithmus bestimmt wurden, werden präsentiert und notwendige nächste Schritte diskutiert.

Quarks and Gluons in the Phase Diagram of Quantum Chromodynamics

Abstract

In this dissertation we study the phase diagram of strongly interacting matter by approaching the theory of quantum chromodynamics in the functional approach of Dyson-Schwinger equations. With these quantum (field) equations of motions we calculate the non-perturbative quark propagator within the Matsubara formalism. We built up on previous works and extend the so-called truncation scheme, which is necessary to render the infinite tower of Dyson-Schwinger equations finite and study phase transitions of chiral symmetry and the confinement/deconfinement transition. In the first part of this thesis we discuss general aspects of quantum chromodynamics and introduce the Dyson-Schwinger equations in general and present the quark Dyson-Schwinger equation together with its counterpart for the gluon. The Bethe-Salpeter equation is introduced which is necessary to perform two-body bound state calculations. A view on the phase diagram of quantum chromodynamics is given, including the discussion of order parameter for chiral symmetry and confinement. Here we also discuss the dependence of the phase structure on the masses of the quarks.

In the following we present the truncation and our results for an unquenched $N_f = 2 + 1$ calculation and compare it to previous studies. We highlight some complementary details for the quark and gluon propagator and discus the resulting phase diagram, which is in agreement with previous work. Results for an equivalent of the Columbia plot and the critical surface are discussed.

A systematically improved truncation, where the charm quark as a dynamical quark flavour is added, will be presented in Ch. 4. An important aspect in this investigation is the proper adjustment of the scales. This is done by matching vacuum properties of the relevant pseudoscalar mesons separately for $N_f = 2 + 1$ and $N_f = 2 + 1 + 1$ via a solution of the Bethe-Salpeter equation. A comparison of the resulting $N_f = 2 + 1$ and $N_f = 2 + 1 + 1$ phase diagram indicates that a dynamical charm quark has no influence on the phase structure.

An open question about the phase diagram of quantum chromodynamics is the importance of hadronic degrees of freedom. These are subject to an exploratory study

in Ch. 5, where we perform a two flavour calculation and include the nucleon as a degree of freedom in the well-known quark-diquark approximation. Due to the lack of explicit knowledge of in-medium properties of the nucleon, we refer to vacuum results and test their influence by variation. The results show that in this truncation baryons have only very little influence on the phase diagram.

This is followed by an approach for a systematic investigation of the quark-gluon vertex Dyson-Schwinger equation at finite temperature. The presented work features an internal model vertex. Calculations taking an unquenched gluon as input are presented, where we compare the quark mass function to results from lattice calculations. We give details about the regularised condensate and study the impact of the different quark flavours and the dependence of the calculation on the chosen internal properties.

In the last chapter we perform an investigation of the analytical properties of the quark. The Schwinger function, as the Fourier transform of the Euclidean quark propagator with respect to (imaginary) time, is studied in the vacuum as well as the medium. The spectral function, obtained from correlator data by solving an ill-defined inverse problem, is introduced together with the Rothkopf-Burnier Bayesian reconstruction algorithm, which returns the Bayesian answer to the given inverse problem. The status of the reconstruction for test data is presented and an outline given.

Contents

1. Introduction **1**

2. Theoretical framework **7**
2.1. Aspects of quantum chromodynamics 8
2.1.1. Generating functional and symmetries 8
2.1.2. Imaginary time and Matsubara formalism 12
2.2. Dyson-Schwinger equations 14
2.2.1. Schematic derivation 14
2.2.2. Quark Dyson-Schwinger equation 15
2.2.3. Gluon Dyson-Schwinger equation 19
2.3. Bethe-Salpeter equation 21
2.3.1. Bound-state equation for mesons 21
2.3.2. Baryons in the quark-diquark picture 23
2.4. Phase transitions 24
2.4.1. The phase diagram of strongly interacting matter 24
2.4.2. Order parameter for chiral symmetry and confinement 25
2.4.3. Impact of dynamical quarks and their masses: Columbia plot . 28

3. QCD for $2+1$ quark flavours **31**
3.1. Truncation of the coupled set of Dyson-Schwinger equations 32
3.1.1. The quark-gluon vertex 32
3.1.2. The quenched gluon propagator - input from lattice QCD . . 34
3.1.3. The unquenched gluon propagator - calculating the quark-loop 35
3.2. Results for the quark and gluon propagators at finite T, μ 39
3.2.1. Quark propagator 39
3.2.2. Gluon propagator, quark-loop and thermal mass 43
3.3. Phase transitions of $N_f = 2+1$ QCD 45

4. The dynamical charm quark **53**
4.1. Introducing the charm quark and choosing the scale 54
4.2. Results in the vacuum and the medium for different N_f 57

5. Hadronic contributions and their effect on the phase structure of QCD **67**
5.1. Extension of the standard truncation with baryons 68
5.2. Results in the vacuum and at finite T with $\mu = 0$ 76

5.3. The phase diagram including baryonic degrees of freedom 79

6. Investigation of the quark-gluon vertex at finite temperature 87
6.1. Truncation of the quark-gluon vertex DSE 88
6.2. Results for an $N_f = 2 + 1$ flavour gluon as input 93

7. Analytic structure of the quark propagator 99
7.1. The Schwinger function 101
7.1.1. Definition and results in vacuum 101
7.1.2. Finite temperature and vanishing chemical potential 106
7.2. Solving an inverse problem - method of the Bayesian reconstruction . 112
7.3. Quark spectral functions at finite temperature 114
7.4. Bayesian reconstruction of test data 118

8. Conclusion and outlook 125

9. Acknowledgement 129

Appendices 131

A. Conventions 133

B. Numerical details 135

C. Quark-loop: Fit for $N_f = 2 + 1$ 141

Bibliography 145

1. Introduction

In the beginning there was nothing,
which exploded.

(Sir Terry Pratchett)

In the early years of the 20th century physicists believed their discipline to be mostly understood. This was emphasized by Max Planck, quoting his mentor Philipp von Jolly who had described the status of physics to him: "Possibly in one or another nook there would perhaps be a dust particle or a small bubble to be examined and classified, but the system as a whole stood there fairly secured, and theoretical physics approached visibly that degree of perfection which, for example, geometry has had already for centuries". This view was annulled by the following century of great discoveries, not least of which being quantum mechanics. As one of the major findings in recent history, the Higgs boson provided the final piece in the Standard Model of particle physics. Already predicted in the 1960s, the Higgs boson was hunted for as the means to provide the mass of particles. However, its contribution is only a small fraction of the mass we observe in nature with the far bigger part being attributed to the strong interaction. The very nature of the latter mass generation is of particular interest, for it displays an exceptional dependence on temperature and a connection to underlying symmetries. Among others, these effects can be combined in sketching a phase diagram, illustrating which state of matter occurs depending on temperature and density. The world we directly experience is restricted to the origin of such a diagram, with (close to) zero temperature and density, which is called vacuum. There the so-called hadrons exist, the most famous of which are the proton and the neutron, forming the nuclei of atoms. Such a sketch is shown in Fig. 1.1, where some possible phases of strongly interacting matter are shown depending on temperature and baryon chemical potential, which is related to baryon/quark density. Baryons are a subclass of hadrons and can thought of to be assembled by three quarks. For high temperatures the phase diagram features a quark-gluon plasma (QGP) phase, separated from the hadronic phase by different transition regions. For small densities the transition is found to be a crossover indicating a continuous change between the hadronic and the QGP phase, whereas for larger densities a sharp (first order) phase transition is expected. With decreasing density the first order transition ends in a critical endpoint (CEP). In the QGP quarks and gluons, as fundamental particles, are assumed to be no longer confined within hadrons and to have lost most of their

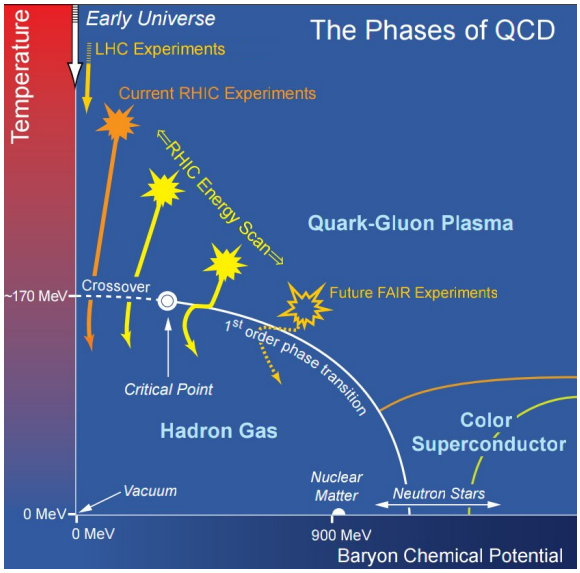

Figure 1.1. Sketch of the phase diagram for the strong interaction (adapted from [1]).

dynamically generated mass. The sketch in Fig. 1.1 indicates where the density of nuclear matter (nuclei of atoms) is located. It also shows the appearance of the so-called colour superconducting phase(s), which are sometimes assumed to appear for example in (neutron) stars. These phases come in a great varieties due to the different kinds of quarks, the quark flavours. An important phenomenon appears for very high densities of strange quark matter, where the two light quarks, up and down, as well as the strange quark are present. This is the so-called colour-flavour locking (*CFL*). In this phase quarks form Cooper pairs only in certain combinations of colour, the charge of the strong interaction, and flavour. Fig. 1.1 also shows, that our universe is believed to have undergone a transition from the QGP phase to the hadronic phase a short time after the Big Bang.

The true manifestation of this phase diagram is subject to many experimental and theoretical endeavours, for an overview see e.g. [2, 3]. There are four main experimental facilities which aim to shed light on the structure contained within the phase diagram, with their (future) investigations also being partly highlighted in Fig. 1.1. The already operating experiments are located at the Brookhaven National Lab (*BNL*), where the Relativistic Heavy Ion Collider (*RHIC*) is operating and the Large Ion Collider Experiment (*ALICE*) at the Large Hadron Collider (*LHC*). The two future facilities are at the Nuclotron-based ion Collider facility (*NICA*) as part of the Joint Institute for Nuclear Research (*JINR*) with the planned experiments Baryonic Matter at Nuclotron (*BMN*) and the Multi-Purpose Detector (*MPD*) as well as at the future Facility for Antiproton and Ion Research (*FAIR*) with the Compressed Baryonic Matter (*CBM*) experiment. An overview of the latter experiment, its program and aims, is given in [4]. The common principle of these experiments is

that they accelerate heavy ions to large fractions of the speed of light before colliding them, thus creating a zone of hot and dense matter. This zone, if certain conditions are met, is in the quark-gluon plasma phase, but quickly expanding and therefore cooling down to end in a phase with ordinary hadrons. A first indication for the QGP was found by the PHENIX experiment at RHIC in 2001 [5]. Since then the QGP was found to be "the most perfect fluid" found in experiments by observations of its properties [6–9]. The most recent experimental program is the RHIC beam energy scan where the centre of mass energy is changed to map out different paths in the phase diagram of the strong interaction (see [10]). Despite all efforts there are experimentally not-clarified theoretical predictions in this sketch, e.g. the appearance of a critical endpoint.

On the theoretical side one needs a theory to describe the observed natural phenomena. Over the last 50 years theoreticians developed quantum chromodynamics (*QCD*), a theory elucidating experimental results due to the strong interaction, where a colour charge, additional to the electric charge, is introduced. The existence of a transition from hadrons to a different phase was theoretically predicted in the 1960s and 1970s. The starting point was Hagedorn's statistical bootstrap model which, as a predecessor of QCD, featured an ultimate temperature T_H [11]. It was in good agreement with experiments of this time, but in conflict with observations due to the cosmic microwave background [12]. The riddle was resolved when Collins and Perry observed that asymptotic freedom of QCD implied weakly interacting quarks at short distances and hence free quarks and gluons in dense matter [13]. Their argument was given mainly for cold QCD, but in the same year Cabibbo and Parisi introduced the notion of understanding the Hagedorn temperature T_H as a transition temperature [14], separating the hadron gas from a plasma of quarks and gluons. Since then scientists followed different paths to investigate the theory of quarks and gluons at finite temperature and density.

One approach to describe the phenomena connected to the phase diagram of QCD is to investigate a dynamical theoretical system. Two main pillars dominate this field, the first of which being the transport approach. In this approach the evolution of the system is given by the transport theory of relativistic quantum many-body systems. The most famous descriptions are the Boltzmann-Uehling-Uhlenbeck equation and the more advanced Kadanoff-Baym equations. Those equations provide the means to sample stochastic processes in a Monte-Carlo simulation to investigate multiple potential outcomes. There are many transport approaches available, for example the ultrarelativistic quantum molecular dynamics model (*UrQMD*) [15], which is a microscopic model used to describe the hadronic processes in heavy ion collisions. Another example is the Parton-Hadron-String Dynamics (*PHSD*) approach. This ansatz covers the full (hadrons and partons) evolution of heavy ion collisions and connects them to the underlying theory of QCD [16–18]. The second pillar of the dynamical models is an approach to describe the QGP phase. Since there was experimental evidence for the QGP being a nearly perfect fluid, an approach assuming

local equilibrium was followed, where the equation of state is used as input (for a review see e.g. [19]). Given initial conditions for the colliding nuclei, the ideal hydrodynamical model was believed to predict processes in the QGP phase. It was found that ideal hydrodynamics is not appropriate to describe heavy ion collisions and was improved by including non-zero transport coefficients. Nowadays hydrodynamical calculations are mainly used in hybrid approaches, where part of the evolution is given by transport equations. Examples are the viscous Israel-Stewart hydrodynamics and UrQMD (*VISHNU*) code [20], the monotonic upstream centred scheme for ion collisions (*MUSIC*) [21] and the hybrid approach presented in [22]. While the aforementioned investigations are performed to describe the dynamical behaviour displayed in heavy ion collisions, in the following we describe attempts to make predictions for static observables in those experiments.

Among the most important static approaches to the full theory of quantum chromodynamics is lattice QCD. In this *ab initio* approach one discretises the theory on a (finite) space-time grid and performs numerous calculations based on Monte-Carlo simulations. Information is extracted by the consideration of expectation values of operators, which are weighted with an exponentially damped function. One problem in lattice QCD is the finite size of the respective space-time grid, which introduces finite volume effects and can be increased only with high cost with respect to computation time. For QCD this approach is hampered by a sign problem arising at finite density where the exponential function features an oscillatory contribution ruling out a probabilistic interpretation. Nonetheless, well-established results for zero density can be obtained, for recent reviews see e.g. [23–25]. There is much effort to solve the restrictions of finite chemical potential. Among those attempts an approach using the complex Langevin equation is much discussed [26], for reviews see e.g. [27–29].

Due to the notorious sign problem in lattice QCD, a widely used approach to learn about features of finite temperature QCD is to use effective field theories. These are based on QCD and can also be applied to get a view on the phase diagram of the strong interaction. One which has existed for a long time is the Nambu-Jona-Lasinio (*NJL*) model, where gluons are localized in coordinate space resulting in an effective four-fermion interaction. This yields an effective theory which is easier to solve than QCD, but shows some of the same symmetries, see [30] for a review and [31] for current results. An approach similar to the NJL model, where also mesons as degrees of freedom are accounted for, is the quark-meson (*QM*) model, see e.g. [32]. Since the non-existence of explicit gluonic degrees of freedom limits those models, they are extended by including Polyakov-loop variables. The resulting approaches are the Polyakov-loop extended NJL (*PNJL*) model, see [33–37], and the Polyakov-loop extended QM (*PQM*) model [38–40]. The latter are also interesting in a two-colour version of QCD [41, 42] and the determination of mesonic spectral functions [43]. All these effective models have in common that their solution is much easier to realize compared to full QCD.

As a final class of approaches we mention the so-called functional methods. In this

non-perturbative framework one derives equations from the generating functional which inherits any desired information about QCD (or any other theory of interest). However, in functional approaches calculations are subject to truncations, necessary to render the system of equations finite. Two main schools follow this approach. First of all there is the functional renormalisation group (*FRG*), where one is concerned with the solution of differential equations for Green's functions, with respect to an auxiliary infrared (*IR*) scale. Those functions contain information about observables within the given theory. Investigations of the phase diagram and QCD at finite temperature are given in [44, 45]. Phase transitions in the FRG approach are studied in [46–48]. Additionally, in [49] gluon and ghost propagators have been studied in quenched QCD, while the computation of real time correlators is presented in [50]. In the FRG framework thus far effective field theories with the (most) relevant degrees of freedom are employed.
Secondly, there are the Dyson-Schwinger equations (*DSEs*), which we make use of in this work. The DSEs represent the equations of motion for the same Green's functions as in the FRG or lattice QCD. They are represented by an infinite tower of coupled integral equations and give, once solved exactly, the correct results within the given theory and therefore could be called *ab initio*. Within this approach, many studies of the QCD phase diagram have been performed. In the review [51] (and references therein), the authors give a broad overview of approaching QCD at finite temperature and density in the Dyson-Schwinger framework. The colour superconducting phase was studied within the DSE approach in a series of PhD theses [52, 53] and publications [54–58], for a general overview see [59]. In [60, 61] studies of the Yang-Mills sector, a system without quarks, at finite temperature were presented. Quenched QCD, where no back coupling from the quarks to the gluonic part takes place, was investigated concerning phase transitions in [62–64]. In [65] back coupling effects from bare quarks to the Yang-Mills system have been introduced. Upon this unquenching effects of dynamical quarks for two and two plus one quark flavours ($N_f = 2 + 1$) were built in [66]. This is as well presented in [67], which also summarizes the work from [68] where the Polyakov loop potential is investigated. One further facet of earlier studies in the context of the phase diagram of QCD are spectral functions of quarks and gluons. While in the FRG approach the authors of [69, 70] used the maximum entropy method (*MEM*) to obtain gluonic spectral functions, in [71–75] the authors shed light on quark spectral functions, partly by using MEM as well and partly be assuming a certain shape for the spectral function and applying a fitting algorithm. The latter approach was also used for results from lattice QCD in [76–78]. Spectral functions are interesting for linking calculations in a (flat) Euclidean space to the real world Minkowski space. They are also important to give fundamental input to the hydrodynamical and transport approaches.

In this work we focus on the transitions from hadrons to the QGP but are not concerned with the superconducting phases. We follow three main paths throughout this thesis. After discussing selected general concepts of QCD in Ch. 2, we start by

reviewing the status of the DSE approach as presented in [66]. There a truncation using input from lattice QCD for the (quenched) gluon propagator together with an ansatz for the quark-gluon interaction guided by phenomenology was applied. This setup also features the back coupling from the light and strange quark matter to the Yang-Mills sector (gluons) incorporating important behaviour at finite temperature. In Ch. 3 we compare to previous works and give some complementary results. Upon this truncation we extend the system by taking into account the charm quark in Ch. 4, where we discuss a means to couple the charm quark to the complete system. Progress in the calculation of bound states in [79] enabled us to adjust the scales properly to perform a sensible comparison to gauge the impact of the charm. Results and implications in the light of finite temperature predictions within the phase diagram are presented, partly based on the published work in [80]. A second extension of the truncation of [66] is, to take baryonic contributions at finite temperature and density into account. In Ch. 5 we present an exploratory study, where this was done by utilizing results in the continuum and extending them to finite temperature. In order to make baryons explicit, the Dyson-Schwinger equation for the quark-gluon vertex are considered and relevant terms identified. This investigation, partly published in [81], is performed for two quark flavours and properties of the considered baryons extended from vacuum to finite temperature and chemical potential.

The second road we follow is concerned with a setup different from the truncation in [66]. In this study, performed together with Richard Williams, we aim to gain knowledge about the quark-gluon vertex itself by solving its truncated Dyson-Schwinger equation at finite temperature. A first step towards a systematic investigation of this important quantity, highlighting its inherent flavour and temperature dependence, is presented.

Eventually we follow the third route, where we consider the analytic properties of the quark, presented in Ch. 7. We extract information in the continuum and at finite temperature from the Schwinger function, a quantity closely related to the spectral function. The latter is then investigated, using a Bayesian reconstruction different from MEM, as introduced in [82], which was done together with Alexander Rothkopf. The current status is discussed and an outline for further steps given. We close with a conclusion and an outlook in Ch. 8.

2. Theoretical framework

> It's still magic even if you know how it's done.
>
> *(Sir Terry Pratchett)*

In general, physicists aim to understand the very nature of processes by observation and interpretation of what is seen. The ever running cycle of setting up a theory and testing it against experiments, in order to falsify the theory or extend its applicability, is part of what both theoreticians and experimentalists participate in. This cycle helps step by step to understand the rules our surrounding nature inherits from fundamental principles. Where the experimental physicist uses machinery in form of experiments including various kinds of detectors to obtain observations, the theoretical physicist needs to set up a theoretical framework, which reveals its implications after performing numerous mathematical operations, written on a piece of paper or, in a discretised version on high performance computers. In the current chapter we introduce the theoretical machinery used throughout this thesis to obtain predictions which eventually are to be tested against the real world in form of experiments.

The structure of this chapter is given in the following way: we begin by introducing basic aspects of quantum chromodynamics, which describes interactions arising due to the strong force, including the presentation of one possible way to perform calculations of its implications at finite temperature and quark chemical potential. In the second section our functional approach in form of the Dyson-Schwinger equations is introduced, which is the theoretical equivalent of an experimental setup and detector system, referring to a way to obtain information within the theory. We discuss this framework in the vacuum and the case of finite temperature and quark chemical potential for various quantities of interest. In the third section we discuss equations used to obtain bound-state properties in the vacuum, which will be relevant in some investigations presented in this work. Finally we discuss the phase diagram and the character of phase transitions in our framework and introduce order parameters as possible observables measured in theoretical calculations.

2.1. Aspects of quantum chromodynamics

In this section we briefly discuss the theoretical background used to describe quantum chromodynamics, as the non-Abelian theory explaining phenomena of the strong interaction. In particular we are interested in features at finite temperature.

2.1.1. Generating functional and symmetries

At the base of a theory one can define a functional, containing all informations to derive predictions for the included particles or fields, which is the Lagrangian or Lagrangian density $\mathcal{L}$. For the non-Abelian SU(3) theory of QCD this object can be derived from the fundamental principles of Poincaré invariance, locality, parity and time-reversal as well as gauge symmetry and renormalisability. In a highly compressed notation the Lagrangian we use for QCD in Euclidean space-time can be written as

$$\mathcal{L}_{QCD}[\Psi, \overline{\Psi}, A] = \sum_{\text{flavour}} \overline{\Psi} \left(i\not{D} - M \right) \Psi - \frac{1}{4} \text{Tr}_c(F^{\mu\nu} F^{\mu\nu}) \,, \tag{2.1}$$

with the quark fields Ψ and $\overline{\Psi}$ in the matter part of the Lagrangian $\mathcal{L}_M$, the field strength tensor $F_{\mu\nu} = [D_\mu, D_\nu]$ and the Feynman slash-notation $\not{D} = \gamma_\mu D_\mu$. We use the Dirac γ-matrices (for our conventions see App. A) and the covariant derivative $D_\mu = \partial_\mu + i g_s A_\mu$, where g_s is the unrenormalised strong coupling constant. The mass matrix M represents the diagonal matrix $\text{diag}(m_u, m_d, m_s, ...)$ with the current quark masses generated by the Higgs mechanism. The spinors of the quark field transform under a gauge transformation as elements of the fundamental representation of SU(3) while the gauge fields A^a_μ are given in the adjoint representation $A_\mu = t^a A^a_\mu$ with the generators of the group t^a, fulfilling $\left[t^a, t^b\right] = i f^{abc} t^c$.

Generating functional

In the vacuum, e.g. at temperature $T = 0$ and quark chemical potential $\mu_q = 0$, it is easy to write down the so-called generating functional from Eq. (2.1), which is defined as

$$\mathcal{Z}[J, \overline{\eta}, \eta] = \int \mathcal{D}\Psi \, \mathcal{D}\overline{\Psi} \, \mathcal{D}A \; exp \left(-\mathcal{S}[\Psi, \overline{\Psi}, A_\mu] + \int d^4x \; \left(A^a_\mu J^a_\mu + \overline{\eta}\Psi + \overline{\Psi}\eta \right) \right) \tag{2.2}$$

with the Euclidean action

$$\mathcal{S}[\Psi, \overline{\Psi}, A] \;\; = \;\; \int d^4x \; \mathcal{L}_{QCD} \,, \tag{2.3}$$

and the Grassmann variables $\eta, \overline{\eta}$ as sources for the quark/antiquark and the source J^a_μ for the gauge fields.

Gauge Symmetry

The Lagrangian Eq. (2.1) was constructed along several guiding principles. One of these is the invariance under (local) gauge transformations $\mathrm{U}(x)$, where the transformation is described by

$$\begin{aligned} A_\mu &\to \mathrm{U}(x) A_\mu \mathrm{U}^\dagger(x) - (\partial_\mu \mathrm{U}(x))\, \mathrm{U}^\dagger(x) \,, \\ \Psi &\to \mathrm{U}(x)\Psi \,. \end{aligned} \tag{2.4}$$

The integration over fields in the generating functional Z covers all possible configurations of A_μ. A subset of the gauge fields is connected by the gauge transformation via Eq. (2.4) and has the same physical content. This leads to over-counting in Eq. (2.2), making it for us inevitable to use a prescription to pick only one representation from each of the aforementioned subsets. This procedure is called gauge fixing. A common procedure is to follow the lines of Faddeev and Popov [83], resulting in a covariant gauge with parameter ξ and the additional gauge-fixed part

$$\mathcal{L}_{g.f.}[\Psi, \overline{\Psi}, A] = \frac{1}{2\xi} \mathrm{Tr}_c(\partial_\mu A_\mu \partial_\nu A_\nu) + i\overline{c}\partial_\mu D_\mu c \,,$$

with the Faddeev-Popov ghost fields $c, \overline{c}$.
The particular choice of ξ defines the used gauge. In our work we use

$$\xi \to 0 \,, \tag{2.5}$$

which implies the Landau gauge. It was shown by Gribov in [84], that the procedure described by Faddeev and Popov results in non-unique gauge fields even in a gauge fixed scenario, where so-called Gribov copies appear. This was investigated in lattice QCD [85–87] but also in the DSE approach [88, 89]. However, the over-counting due to Gribov copies is thought to mostly concern the infrared behaviour of Green's functions [90–92], which is below the temperature scales we are interested in. Therefore we can safely neglect the effects related to this problem.

Renormalisation

After the gauge fixing procedure we also need to introduce a renormalisation scheme to deal with arising infinities in the calculations. As in earlier works [67, 93, 94], we use the framework of multiplicative renormalisation and introduce several renormalisation constants for the quark wave function (Z_2), the quark mass (Z_m), the strong coupling constant (Z_g), the gluon propagator (Z_3), the ghost propagator ($\tilde{Z}_3$) and the gauge fixing term (Z_ξ). Those constants are defined by

$$\Psi \to Z_2^{1/2}\Psi, \;\; M \to Z_m M, \;\; g \to Z_g g, \;\; A_\mu \to Z_3^{1/2} A_\mu, \;\; c \to \tilde{Z}_3^{1/2} \overline{c} c, \;\; \xi \to Z_\xi \xi. \tag{2.6}$$

Note that due to Eq. (2.5), Z_ξ is not needed in Landau gauge. Additionally, five (vertex-) renormalisation constants can be related to those in Eq. (2.6) by Slavnov-Taylor identities (*STIs*) (see e.g. [95]),

$$Z_1 = Z_g Z_3^{3/2}, \quad \tilde{Z}_1 = Z_g \tilde{Z}_3 Z_3^{1/2}, \quad Z_{1F} = Z_g Z_2 Z_3^{1/2}, \quad Z_4 = Z_g^2 Z_3^2, \quad \tilde{Z}_4 = Z_g^2 \tilde{Z}_3^2 \, .$$

All renormalisation constants depend on the cutoff of our theory Λ and the renormalisation point ζ and are introduced to interchange the cutoff dependence of the fundamentally divergent diagrams for a dependence on ζ.

Chiral symmetry

There are various symmetries related to the phase diagram of QCD. The behaviour of strongly interacting matter is thereby classified due to its state with respect to those symmetries, whereof chiral symmetry is one of the most important ones. Thereby chirality is the property of a particle, which determines whether the particle transforms under a left or right handed representation of the Poincaré group. Dirac spinors, as superposition of both representations, are usually split into their projections onto the left respectively right handed Weyl spinors

$$\Psi_R = \frac{1}{2}(1+\gamma_5)\Psi, \quad \Psi_L = \frac{1}{2}(1-\gamma_5)\Psi \tag{2.7}$$

as chirality eigenstates. Eq. (2.1) can then be rewritten with

$$\overline{\Psi}\left(i\not{D} - M\right)\Psi = \overline{\Psi}_L\left(-i\not{D}\right)\Psi_L + \overline{\Psi}_R\left(-i\not{D}\right)\Psi_R + \overline{\Psi}_L M \Psi_R + \overline{\Psi}_R M \Psi_L, \tag{2.8}$$

where M once again is the diagonal mass matrix, including entries according to the number N_f of quark flavours under consideration. For N_f massless quarks, i.e. $M = 0$, it is apparent from Eq. (2.8) that the right and left handed quarks decouple and the Lagrangian is invariant under global $U_L(N_f) \times U_R(N_f)$ transformations,

$$\Psi_L \to U_L(N_f)\Psi_L, \quad \Psi_R \to U_r(N_f)\Psi_R \, .$$

This case is referred to as the chiral limit.

One can reorganize this representation by defining axial- and vector-transformations leading to the underlying symmetry group of

$$SU_A(N_f) \times SU_V(N_f) \times U_A(1) \times U_V(1)$$

(see [67,94]). Here V and A represent vector and axial-vector symmetries respectively. $SU_V(N_f)$ manifests itself in isospin symmetry and is for N_f quarks with equal mass always conserved, also on a quantum level. Of particular interest is the $SU_A(N_f)$ group, which is spontaneously broken by dynamical mass generation and one of the key features of QCD, which changes its behaviour in the phase diagram. Additionally, $U_V(1)$ is connected to baryon number conservation, being an unbroken symmetry also on the quantum level. In general, we are concerned with the two main cases

- **Explicit chiral symmetry breaking:** The quark masses, as generated by the Higgs mechanism, break chiral symmetry explicitly. In the case of $M = m \cdot \mathbb{1}$, $U_V(1)$ and $SU_V(N_f)$ are preserved, while $U_A(1)$ and $SU_A(N_f)$ are broken explicitly by the finite quark masses additional to their anomalous breaking by quantum effects.

- **Spontaneous chiral symmetry breaking:** Even for $M = 0$ the strong interaction generates quark masses dynamically, which is a purely non-perturbative phenomenon.

While the explicit breaking of chiral symmetry is independent of temperature and/or chemical potential, the spontaneous breaking of chiral symmetry is restored in certain conditions. Spontaneous chiral symmetry breaking and the $U_A(1)$ anomaly are dominant even away from the chiral limit and important for physical masses.

Confinement

An intriguing facet of QCD is the yet not completely understood phenomenon of confinement. One has to distinguish between colour and quark confinement with different scenarios explaining their appearance. Colour confinement is concerned with the complete absence of (free) coloured particles from the physical state space. A possible explanation of this effect is the Kugo-Ojima scenario [96, 97] where in Landau gauge two conditions have to be met [98]:

- Transverse gluon correlations contain no massless particle poles

- There are unbroken global colour charges

For quark confinement one usually considers the potential

$$V(r) = \frac{\alpha}{r} + \sigma r \ ,$$

with the linear component σr and the string tension σ. Due to this component the latter part is referred to as a linear rising potential. If such a potential is found between two (heavy) quarks one would need an infinite amount of energy to separate them. This can be interpreted as the two quarks are confined. In QCD with physical quark masses the energy stored due to the separation of the quarks is eventually enough to create a quark-antiquark pair, referred to as string breaking. For the linear rising potential this implies a plateau after some distance r_B of the quarks and confinement in the sense of inseparable quarks is not given [99,100]. Nonetheless the created quark-antiquark pairs are as well colour-neutral and colour confinement still fulfilled. Connected to the linear rising potential is the so-called Polyakov loop. This quantity can be obtained by taking the colour trace of the Wilson loop in direction

of the so-called imaginary time τ, which will be introduced in the next section. The Polyakov loop of the field A is then given by

$$L[A] \coloneqq \frac{1}{N_c}\mathrm{Tr}\mathcal{P}e^{i\int d\tau A_4(\mathbf{x},\tau)} \ ,$$

where Tr represents the colour trace and $\mathcal{P}$ is the path ordering operator. The expectation value of the Polyakov loop $\langle L[A]\rangle$ is connected to the free energy of a static quark F_q (see e.g. [101]) by

$$\langle L[A]\rangle \propto e^{-F_q/T} \ ,$$

and therefore one finds

$$\langle L[A]\rangle = \begin{cases} 0 & \text{if } F_q = \infty \\ \text{finite} & \text{if } F_q < \infty \end{cases} \ ,$$

which mirrors the implications of the linear rising potential and gives, in this sense, a possible definition of confinement. The connection of the Polyakov loop to centre symmetry, as a particular symmetry with respect to the centre of a $\mathrm{SU(N}_c\mathrm{)}$ group, and the dressed Polyakov loop are discussed elsewhere [67]. For quark confinement one can as well apply the criterion of reflection positivity and positivity violations of spectral representations. If the correlator has negative norm contributions, the corresponding state can not be part of the physical state space. This will be topic of Ch. 7 and discussed there in more detail.

Both, spontaneous chiral symmetry breaking and quark confinement are possibly linked, indicated also by their similar behaviour in the phase diagram and investigated i.e. in [102].

2.1.2. Imaginary time and Matsubara formalism

In order to investigate QCD at finite temperature and finite chemical potential, one needs a framework to describe its features. There are in general two strategies to follow, the real time formalism and the imaginary time formalism (for both see e.g. [101, 103]). We follow the latter approach for equilibrium properties, where the key idea is to express expectation values of operators in one of the ensembles as an expectation value of a quantum field theory, which was rotated to an imaginary time. From statistical mechanics one knows three thermal ensembles, describing different types of systems.

- *Microcanonical ensemble:* isolated systems with fixed energy, particle number and volume
- *Canonical ensemble:* closed system which is in contact with a heat bath

- *Grand canonical ensemble:* system which is in contact with a heat bath and possible particle exchange

We are concerned with the latter one, since we aim to introduce chemical potential as the Lagrange multiplier for the particle number. We introduce imaginary time

$$\tau = -it \ ,$$

with t being the standard Minkowski time. τ is constrained to an interval $\tau \in [0, \beta]$, with the inverse temperature $\beta = 1/T$ and units with $k_B = 1$. Additionally, due to the statistical theorem, we have well defined boundary conditions: fermionic fields have to fulfil $\Psi(\mathbf{x}, \tau) = -\Psi(\mathbf{x}, \tau+\beta)$, while bosonic fields obey $\phi(\mathbf{x}, \tau) = +\phi(\mathbf{x}, \tau+\beta)$. The Euclidean action defined in Eq. (2.3) changes then to

$$\mathcal{S}[\Psi, \overline{\Psi}, A] = \int_{-\infty}^{\infty} dx_0 \int d^3x \ \mathcal{L}_{QCD} \rightarrow \int_0^{\beta} d\tau \int d^3x \ \mathcal{L}_{QCD} \ .$$

Following [67], we introduce the net quark density $n = \int_0^{\beta} d\tau \int d^3x \Psi^{\dagger}\Psi$, with $\Psi^{\dagger} = \overline{\Psi}\gamma_4$. This quantity gives the difference between quarks and antiquarks per unit volume. To keep the total particle number constraint, the chemical potential as a Lagrange multiplier is added, and the generating functional then reads

$$\mathcal{Z} = \int \mathcal{D}\Psi \ \mathcal{D}\overline{\Psi} \ \mathcal{D}A \ exp\left(-\mathcal{S} + \mu n + \int_0^{\beta} d\tau \int d^3x \ \left(AJ + \overline{\eta}\Psi + \overline{\Psi}\eta\right)\right) \ , \qquad (2.9)$$

where we can absorb the term proportional to n into the kinetic γ_4-part of the Lagrangian and find for the modified matter part of the action

$$\mathcal{S}_M = \int_0^{\beta} d\tau \int d^3x \ \left[\overline{\Psi}\left(-\boldsymbol{\gamma} \cdot \boldsymbol{\partial} - \gamma_4(\partial_4 - \mu) - m\right)\Psi\right] \ .$$

Matsubara formalism

At this point we introduce the Matsubara formalism, which is connected to the Fourier transform of a given function in imaginary time. Since the imaginary time variable obeys periodic or anti-periodic boundary conditions, its Fourier transform will be discrete and have either even or odd character. For a function f which is periodic in the imaginary-time direction, $f(\tau) = f(\tau + \beta)$, we define

$$f(\tau) = T \sum_{n=-\infty}^{\infty} e^{-i\omega_n^{Bos}\tau} f(i\omega_n^{Bos}) \ , \quad f(i\omega_n^{Bos}) = \int_0^{\beta} d\tau \ e^{i\omega_n^{Bos}\tau} f(\tau) \qquad (2.10)$$

where

$$\omega_n^{Bos} = 2n \ \pi \ T$$

is the bosonic Matsubara frequency.
In case of a fermionic function, obeying the anti-periodic boundary conditions $\Psi(\tau) = -\Psi(\tau + \beta)$, the Matsubara frequency is of the form

$$\omega_n = (2n + 1)\ \pi\ T\ ,$$

while the Fourier transformation is the same as in Eq. (2.10). For more details on the conventions see App. A.

2.2. Dyson-Schwinger equations

The Dyson-Schwinger equations are at the heart of our functional approach. The key idea of this approach was developed around 1950 by Dyson and Schwinger [104,105]. To judge the importance of the DSEs a comparison with classical mechanics is helpful, where the principle of least action implies that any variation of the classical action with respect to generalized coordinates vanishes, leading to the well known Euler-Lagrange equations. The principle of least action applied in a quantum field theory gives constraints for the expectation values of variations in the fields, resulting in the corresponding equations of motion, the DSEs. On a schematic level this will be shown in the next paragraph.

2.2.1. Schematic derivation

The exact derivation of the Dyson-Schwinger equations can be found elsewhere, here we schematically follow [67]. At this point we want to highlight only the most important steps one can follow in the vacuum. The derivation for finite temperature would be formally equivalent but is not shown here for brevity.

The starting point of the derivation is the generating functional of correlation functions denoted by $Z[J]$, where J is a place holder for all necessary source terms of the theory. By taking the logarithm, we obtain the generating functional of all connected correlators, which is often called the Schwinger functional

$$W[J] = \ln\left(Z[J]\right)\ .$$

The most important functional we need for the generation of the Dyson-Schwinger equations is given by the so-called effective action, which is merely the Legendre transform of the Schwinger functional with respect to all the sources

$$\Gamma[\Phi] = \sup_J\left(-W[J] + J\Phi\right)\ , \tag{2.11}$$

which now depends on the classical fields $\Phi = \langle\varphi\rangle_{\mathcal{Z}}$, where the expectation value $\langle . \rangle_{\mathcal{Z}}$ is calculated via the generating functional $\mathcal{Z}$. φ is yet again another place holder for all possible fields $\varphi \in \left\{\Psi, \bar{\Psi}, A_\mu, c, \bar{c}\right\}$. The effective action Eq. (2.11) can be

understood as a generating functional of one-particle irreducible (*1PI*) correlation functions, including the 2-point functions or propagators

$$\left[D^{-1}(x,y)\right]_{i,j} = \left.\frac{\partial^2\Gamma[\Phi]}{\partial\Phi_i(x)\partial\Phi_j(y)}\right|_{J=0} ,$$

where we set the sources to zero at the end. If a quantity carries an index J, it indicates that the sources are not yet set to zero. The central equation, the so-called master Dyson-Schwinger equation, is given by

$$\frac{\partial\Gamma[\Phi]}{\partial\Phi} = \left.\frac{\partial S}{\partial\varphi}\right|_{\varphi\to\Phi+D^J\frac{\partial}{\partial\Phi}} , \tag{2.12}$$

where $S = \int \mathrm{d}^4\mathrm{x}\mathcal{L}$ is the action of the corresponding theory and D^J is a correlator still containing source terms. This is derived using the fact, that if an additional functional derivative is added to the generating functional, the integral over the fields vanishes due to Gauss's law

$$\int \mathcal{D}\varphi \frac{\partial}{\partial\varphi} e^{-S+\int J\varphi} = 0 ,$$

see for example [106].

If one applies n more derivatives on Eq. (2.12) and eventually sets the sources J to zero, the result will be the DSE for an $n+1$-point function, depending on at least $n+2$-point functions. This already shows the tower-like character of the approach to the solution of a theory with DSEs. However, by describing any given quantum field theory in terms of its DSEs is a non-perturbative and exact way to solve for its properties, if one is capable of dealing with the infinite tower of equations.

2.2.2. Quark Dyson-Schwinger equation

At the foundation of the infinite tower of equations are the DSEs for the two-point functions, also called propagators or correlators. In our investigations we are mostly interested in quarks and gluons as the basic degrees of freedom of QCD. In this paragraph we introduce the equation which needs to be solved to obtain information about the matter sector and its implications at finite temperature. As seen in the previous paragraph, the DSEs can be obtained from the effective action by taking appropriate derivatives. A diagrammatic representation of the resulting equation for the (inverse) quark propagator is shown in Fig. 2.1. The appearing quantities are the bare quark propagator (solid line), the fully dressed quark propagator (solid line with large white circle), the fully dressed gluon correlator (curly line with large orange circle) as well as the fully dressed quark-gluon vertex (large black circle). The diagrammatic representation implies a lot about the structure the equation

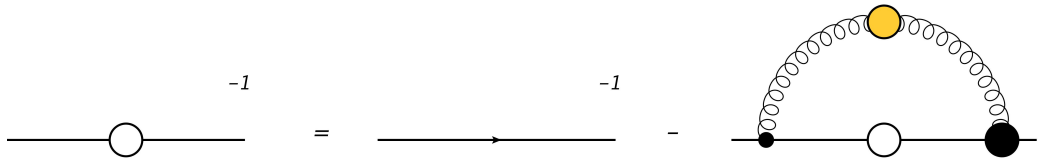

Figure 2.1. Diagrammatic representation of the quark Dyson-Schwinger equation. The large filled circles indicate the fully dressed quark propagator (white), the fully dressed quark-gluon vertex (black) and the fully dressed gluon propagator (orange).

inherits: the loop-diagram, which modifies the bare propagator and is called the quark self-energy contribution, is represented by an integral depending on, among others, the full quark propagator itself. The tower like structure becomes clear, once one acknowledges that the fully dressed gluon propagator has to obey its own DSE (presented in the next paragraph), which depends itself on higher n-point functions. The same is true for the quark-gluon vertex, which is yet an even more difficult quantity that we dedicate Ch. 6 to. We will now have a closer look at the quark propagator and the quark DSE in vacuum and in the medium, which can be treated as if the gluon propagator and the quark-gluon vertex are given as an ansatz or obtained by solving their corresponding DSEs.

Vacuum

In the vacuum, the bare inverse quark propagator has, as a fermionic degree of freedom, the following structure

$$S_0^{-1}(p) = i\not{p} + m_0 \mathbb{1} \ , \tag{2.13}$$

where $\not{p} = \gamma_\mu p^\mu$ with p being the Euclidean four momentum and m_0 the bare mass as it appears in the Lagrangian. The bare mass is related to the renormalised mass m_R by $m_0 = Z_m m_R$. The self-energy spinor can be expressed in a basis as the vector part and the scalar part, implying for the fully dressed propagator the form

$$S^{-1}(p) = i\not{p}A(p^2) + \mathbb{1}B(p^2) \ ,$$

with the unknown functions $A(p^2)$ and $B(p^2)$, called the quark dressing functions. Note that, due to translational invariance, they depend on p^2 only. While A carries no dimensions, the scalar dressing function has (energy) dimension one. The self-energy contribution can be written as

$$\Sigma(p^2) = Z_{1F} C_F (ig)^2 \int_l [\gamma_\mu S(l) \Gamma_\nu(p,l) D^{\mu\nu}(q)] \ , \tag{2.14}$$

where the abbreviation for the integral is defined as $\int_l = \int d^4l/(2\pi)^4$ and $D^{\mu\nu}(q)$ being the bosonic gluon-propagator with gluon momentum $q = p - l$. By writing

down Eq. (2.14) we already chose a particular momentum routing with the loop momentum going through the internal quark propagator and performed the trace in colour space, leading to the Casimir $C_F = \frac{N_c^2-1}{2N_c}$. Here Z_{1F} is the quark-gluon vertex renormalisation constant with $Z_{1F} = Z_2(\tilde{Z}_3)^{-1}$ (where we use $\tilde{Z}_1 = 1$, i.e the Taylor scheme in Landau gauge [107]) and each vertex supplying a factor of (ig) as dictated by the Feynman rules. Together with Z_2, the wave function renormalisation constant and Z_m, this ensures multiplicative renormalisability.

The quark DSE then reads

$$S^{-1}(p) = Z_2 S_0^{-1}(p) - \Sigma(p^2) \,,$$

which needs to be projected in order to identify the different contributions. Therefore one applies the projectors

$$\mathbb{P}_A(p) = \frac{\not{p}}{4ip^2} \,, \quad \mathbb{P}_B(p) = \frac{\mathbb{1}}{4} \,,$$

before performing the Dirac trace to obtain an equation for each dressing function. However, the exact form of the self-energy will depend on the structure of the gluon correlator and the quark-gluon vertex. The most general expression reads

$$\begin{aligned} A(p^2) &= Z_2 - \mathrm{Tr}_D \left[\mathbb{P}_A(p)\Sigma(p^2)\right] \\ B(p^2) &= Z_2 Z_m m_R - \mathrm{Tr}_D \left[\mathbb{P}_B(p)\Sigma(p^2)\right] \end{aligned}$$

From the two dressing functions A and B one can construct a renormalisation point independent Euclidean mass function $M(p^2) = B(p^2)/A(p^2)$. This function will mirror the impact of the renormalised mass as well as dynamically generated contribution due to spontaneous chiral symmetry breaking. In order to obtain the values for the renormalisation constants, one needs to set the renormalisation conditions, which are given, depending on the renormalisation point ζ by $A(\zeta^2) = 1$ and $B(\zeta^2) = m_R$. Note, this procedure is only valid for large renormalisation points ζ

Medium

The bare quark propagator for finite temperature and finite chemical potential is closely related to its vacuum counterpart in Eq. (2.13). Due to an explicit introduction of an assigned direction for the heat-bath, the Euclidean four momentum splits into a spatial part and its fourth (heat-bath) component, which we refer to as the Matsubara part. The propagators read

$$\begin{aligned} S_0^{-1}(p) &= i\,\mathbf{p}\cdot\boldsymbol{\gamma} + Z_m m_R \mathbb{1} + i\,\tilde{\omega}_n \gamma_4 \,, \\ S^{-1}(p) &= i\,\mathbf{p}\cdot\boldsymbol{\gamma}\, A(p) + B(p)\mathbb{1} + i\,\tilde{\omega}_n\gamma_4\, C(p) + i\,\tilde{\omega}_n\gamma_4\,\mathbf{p}\cdot\boldsymbol{\gamma}\, D(p) \,, \end{aligned} \tag{2.15}$$

where bold symbols indicate the spatial components and we used the shorthand notations

$$\tilde{\omega}_p = \omega_p + i\mu \ , \quad (p) = (\mathbf{p}^2, \omega_p; \mu) \ , \tag{2.16}$$

to keep track of the parameter dependence on quark chemical potential and temperature. We emphasize the appearance of a fourth component proportional to $\tilde{\omega}_n \gamma_4 \, \mathbf{p} \cdot \boldsymbol{\gamma}$, which has no perturbative counterpart in the bare propagator. This contribution can only be present at finite temperature, indicated by the vacuum limits

$$\lim_{\mu,T\to 0} [A(p) - C(p)] = 0 \ , \quad \lim_{\mu,T\to 0} [D(p)] = 0 \ . \tag{2.17}$$

From these limits we infer, that at scales much higher than the temperature, we expect $D(p)$ to vanish and $A(p)$ and $C(p)$ to become degenerate.

The expression for the self-energy does not look much different from what is shown in Eq. (2.14), but takes into account the presence of the heat bath and the chemical potential as a parameter, therefore includes a Matsubara sum

$$\Sigma(p) = Z_{1F} C_F (ig)^2 \sum\!\!\!\!\!\!\int_l [\gamma_\mu S(l) \Gamma_\nu(p,l) D^{\mu\nu}(p-l)] \ , \tag{2.18}$$

where we used the shorthand $\sum\!\!\!\!\!\!\int_l = T \sum_{\omega_l} \int d^3 l/(2\pi)^3$, and the argument of the quark and gluon propagator as well as the quark-gluon vertex have to be understood with Eq. (2.16) in mind. This implies, that also the gluon correlator has an implicit dependence on the quark chemical potential, which we will shed light on in the next paragraph.

Just as in the vacuum, we define projectors to find the appropriate parts of the self-energy for each dressing function,

$$\mathbb{P}_A(p) = \frac{\mathbf{p}\cdot\boldsymbol{\gamma}}{4i\mathbf{p}^2} \ , \quad \mathbb{P}_B(p) = \frac{\mathbb{1}}{4} \ , \quad \mathbb{P}_C(p) = \frac{\tilde{\omega}_p \gamma_4}{4i\tilde{\omega}_p^2} \ , \quad \mathbb{P}_D(p) = \frac{(\tilde{\omega}_p \gamma_4)\,(\mathbf{p}\cdot\boldsymbol{\gamma})}{4\tilde{\omega}_p^2 \mathbf{p}^2} \ .$$

The most general expressions are similar to the vacuum and read

$$\begin{aligned} A(p^2) &= Z_2 \qquad\quad - \mathrm{Tr}_D \left[\mathbb{P}_A(p)\Sigma(p^2)\right] \ , \\ B(p^2) &= Z_2 Z_m m_R - \mathrm{Tr}_D \left[\mathbb{P}_B(p)\Sigma(p^2)\right] \ , \\ C(p^2) &= Z_2 \qquad\quad - \mathrm{Tr}_D \left[\mathbb{P}_C(p)\Sigma(p^2)\right] \ , \\ D(p^2) &= \qquad\quad\ \ -\mathrm{Tr}_D \left[\mathbb{P}_D(p)\Sigma(p^2)\right] \ , \end{aligned} \tag{2.19}$$

with $\Sigma(p^2)$ defined in Eq. (2.18). The renormalisation constants can be taken from the vacuum calculation, since neither finite temperature nor finite chemical potential introduce any new divergences, see e.g. [101, 103].

By inspecting Eq. (2.19) closer, one notices the absence of a constant term implying

the D function will fall of like a power-law in the ultraviolet (UV) and is only generated when the kernel of the integral in Eq. (2.19) contains driving terms from the other dressing functions. This is not the case for certain truncations, such as the well-known Rainbow-Ladder truncation, where the quark-gluon vertex has only a γ_μ component and does not depend on the quark correlator. As noted in [67], a non-vanishing D function indicates chiral symmetry breaking. The vanishing commutator

$$\left[\left(\tilde{\omega}_p \gamma_4\right)\left(\mathbf{p}\cdot\boldsymbol{\gamma}\right), \gamma_5\right] = 0 \,, \tag{2.20}$$

highlights the relation to the (chiral) condensate as for the B function, where the commutator was given by $[\mathbb{1}, \gamma_5] = 0$.

2.2.3. Gluon Dyson-Schwinger equation

Up to now we only introduced the equation which gives information about the quark sector of QCD. We have seen that the quark DSE needs the fully calculated gauge boson, the gluon, as input. Since QCD is a non-Abelian theory, the gauge boson carries colour charge and is therefore able to interact as well with other gluons. Additionally, due to the path-integral formalism and the presence of gauge symmetry, we have to work in a gauge-fixed scheme leading to the appearance of Faddeev-Popov ghosts. While the non-Abelian character of the theory is mirrored in the first two lines of the diagrammatic equation in Fig. 2.2 (featuring the tadpole-, sunset-, squint- and gluon-loop diagram), the ghost-loop appears due to Landau gauge. The last diagram, the quark-loop, has an equivalent in quantum electrodynamics (QED) and connects the gauge sector to the matter sector. Note that in most diagrams at least one fully dressed internal gluon propagator appears. In order to solve the DSE shown in Fig. 2.2, one would not only need the dressed quark propagator and the quark-gluon vertex, but also higher n-point functions in the gauge sector, such as the three- and four-gluon vertex in addition to the ghost-gluon vertex and the fully dressed ghost propagator. In general, in the vacuum the gluon propagator in Landau gauge is transverse to its four momentum and has the structure

$$D^{\mu\nu}(q) = \frac{Z(q^2)}{q^2}\mathbb{T}^{\mu\nu}(q) \,,$$

with the transverse projector

$$\mathbb{T}^{\mu\nu}(q) = \delta^{\mu\nu} - \frac{q^\mu q^\nu}{q^2} \,, \tag{2.21}$$

and the gluon dressing function $Z(q^2)$. Note that a numerical calculation of the self-energy contributions obtained from Fig. 2.2 might contain spurious longitudinal contributions one has to deal with (see e.g. [93]). We will come back to this problem later. In the medium, the gluon propagator splits into two parts, one longitudinal (L)

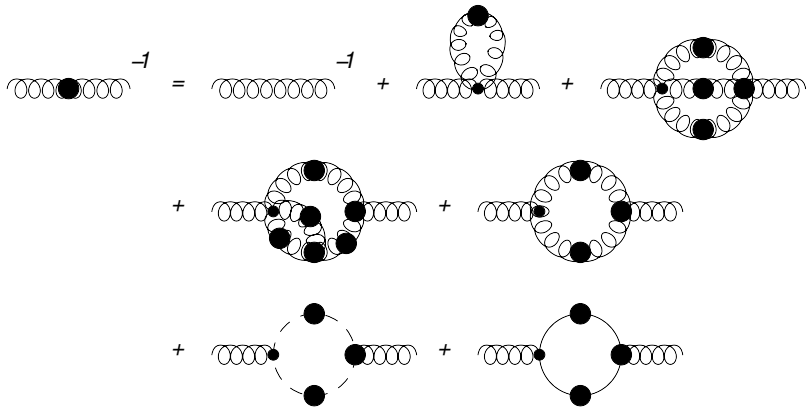

Figure 2.2. Diagrammatic representation of the full gluon DSE featuring gluon (curly lines), ghost (dashed lines) and quark (solid lines) propagators. Larger filled circles indicate fully dressed objects.

and one transverse (T) with respect to the heat bath. Both parts are still transverse with respect to the gluon four-momentum. The finite temperature gluon correlator reads

$$D^{\mu\nu}(q) = \frac{Z_L(q^2)}{q^2}\mathbb{P}_L^{\mu\nu}(q) + \frac{Z_T(q^2)}{q^2}\mathbb{P}_T^{\mu\nu}(q)\,,$$

where we used the two projectors

$$\mathbb{P}_T^{\mu\nu}(q) = (1-\delta_{\mu 4})(1-\delta_{\nu 4})\left(\delta_{\mu\nu} - \frac{q_\mu q_\nu}{\mathbf{q}^2}\right), \tag{2.22}$$

$$\mathbb{P}_L^{\mu\nu}(q) = \mathbb{T}^{\mu\nu}(q) - \mathbb{P}_T^{\mu\nu}(q)\,, \tag{2.23}$$

with $\mathbb{T}^{\mu\nu}$ as defined in Eq. (2.21). Note the appearance of only the spatial part of q in the denominator in Eq. (2.22). At finite temperature the four momentum is defined as $q = (\mathbf{q}, \omega_{n_q})$ with $\omega_{n_q} = 2n_q\pi T$. The vacuum limit, as in Eq. (2.17), shows that the gluon dressing functions reduce smoothly to their vacuum values

$$Z_T(q^2), Z_L(q^2) \xrightarrow[\mu,T\to 0]{} Z^{\mathrm{vac}}(q^2).$$

With given chromo-electric (Z_L) and chromo-magnetic (Z_T) dressing functions, the in-medium gluon is completely defined. The DSE for the gluon is highly non-trivial (see e.g. [60,61,108–110]), in particular due to its direct dependence on higher n-point functions. There is as well effort in the FRG approach to obtain gluon propagators at finite temperature, see e.g. [49]. Due to the complexity we abstain from attempting to solve the gluon DSE and therefore the whole Yang-Mills part of the theory and do not show the explicit form of the gluon DSE here. For the solution of the quark DSE we use input for the gluon propagator as well as a model ansatz for the quark-gluon vertex, which will be discussed in Ch. 3.

2.3. Bethe-Salpeter equation

In this section we introduce the Bethe-Salpeter equation (*BSE*), which is the two-body bound state equation in the functional Dyson-Schwinger approach. Its three constituent counterpart, the Faddeev equation, was not used for this work and is therefore not discussed. It is important to highlight in the beginning, that no bound state calculation at finite temperature or chemical potential is performed throughout this work. We solely consider the vacuum properties of bound states such as pseudoscalar mesons, as done in Ch. 4, or the nucleon in a quark-diquark picture, applied in Ch. 5, to use their properties as physical input. Nevertheless the BSE is an important functional ingredient for the aforementioned chapters. We follow in our description along the lines of [67].

2.3.1. Bound-state equation for mesons

Our starting point is the inhomogeneous BSE shown in Fig. 2.3. The diagrammatic form of the equation already shows, that the (in this case) quark-antiquark two-body propagator T is related to the two-particle irreducible scattering kernel K, with a bare propagator as an inhomogeneous term. Usually one uses the so-called pole-representation (shown in the second line of Fig. 2.3), where the propagator T is written as a sum of bound state poles in the total momentum P at the bound state masses M_{BS} and a regular part,

$$T = \sum_{\mathrm{BS}} \overline{\Gamma} \frac{\mathcal{N}_{\mathrm{BS}}}{P^2 + M_{\mathrm{BS}}^2} \Gamma + \mathrm{reg.} \tag{2.24}$$

Here Γ is the quark-meson vertex, which is often referred to as the Bethe-Salpeter amplitude (*BSA*), and $\mathcal{N}_{\mathrm{BS}}$ represents a normalisation constant, with $\mathcal{N}_{\mathrm{BS}} = 1$ for bosonic and $\mathcal{N}_{\mathrm{BS}} = 2M_{\mathrm{BS}}$ for fermionic bound states. If one applies Eq. (2.24) to the first line of the diagrammatic equation in Fig. 2.3 and projects on the (desired) bound state, the result is the homogeneous BSE as given in Fig. 2.4. The homogeneous BSE describes an on-shell meson, where the interaction of the bound state with the quarks is given in terms of the quark-antiquark scattering kernel K. In Fig. 2.4 we show the untruncated (left) version as well as its counterpart in ladder-approximation (right). A mathematical form of the homogeneous BSE is given by

$$\Gamma_{ab}(p, P) = \int \frac{d^4 l}{(2\pi)^4} K_{ab,cd}(p, P, l) \left[S(l_+) \Gamma(l, P) S(l_-) \right]_{cd} \ ,$$

where S represents the fully dressed quark propagator depending on the shifted momenta $l_\pm = P \pm l/2$ and the indices carrying information about colour, flavour and Dirac component. In order for the resulting bound state to follow certain symmetries, the kernel has to fulfil constraints. The most important one is the Goldstone boson

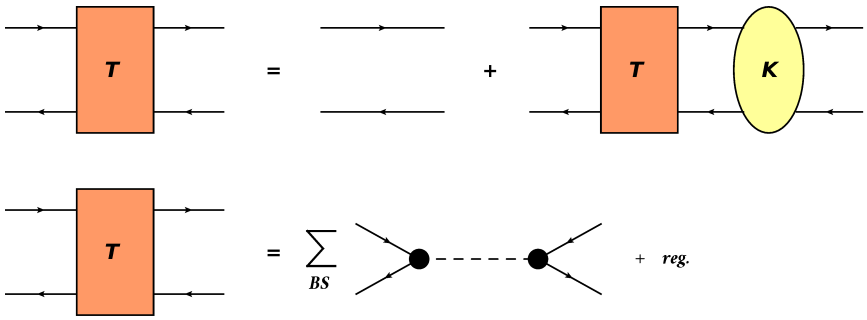

Figure 2.3. Diagrammatic representation of the Bethe-Salpeter equation (top), where T is the two-body propagator and K the 2PI kernel. The lower figure shows the so-called pole-representation, where the T matrix is represented as a sum over bound state poles and a regular part.

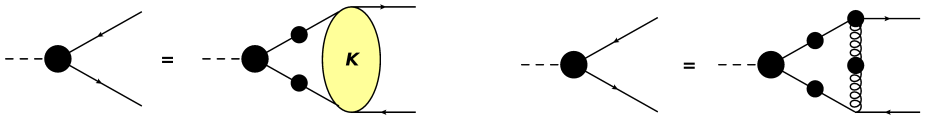

Figure 2.4. Representation of the BSE after introduction of the pole-representation and projecting on a particular bound state for the untruncated system (left) and in Rainbow-Ladder approximation (right).

nature of the pion. As discussed in a previous section, QCD exhibits spontaneous chiral symmetry breaking and therefore has several Goldstone bosons. However, since the finite quark masses explicitly break chiral symmetry, the Goldstone bosons will not be massless. For the BSE this constraint connects the interaction of quarks and mesons to the quark self-energies via the well-known axial-vector Ward-Takahashi identity ($AxWTI$) (see e.g. [111]). The BSA can in general be decomposed in terms of various dressing functions in a basis obeying the desired quantum numbers and needs normalisation, see [112–114]. With the normalised BSA one can calculate the residues for the coupling to axial-vector and pseudo-scalar currents, which can be combined with the AxWTI to obtain the generalized Gell-Mann-Oakes-Renner ($GMOR$) relation

$$f_\pi^2 M_\pi^2 = -2 m_R \langle \bar{\psi}\psi \rangle \ , \tag{2.25}$$

where f_π is the pion decay constant, M_π the pion mass, m_R the renormalised quark mass and $\langle \bar{\psi}\psi \rangle$ the quark condensate, which will be discussed in the next section. In the normalisation scheme applied in the calculations for this work, we have $f_\pi \approx 93$ MeV.

2.3.2. Baryons in the quark-diquark picture

In Ch. 5 we will consider effects due the introduction of baryonic degrees of freedom to a system of quarks in the medium. For this investigation we use the often employed quark-diquark approximation for baryons, in particular for the nucleon. Viewing the nucleon as being a bound state of mostly quark and diquark correlations is a well studied approach giving reasonable results (see e.g. [115], detailed references are given in Ch. 5). To analyse the baryon being generated by three different quarks, one has to refer to the Faddeev-equation. In this paragraph we briefly want to discuss the BSE, as the two-body bound state equation, in this case for a quark and a diquark where three-body forces are neglected. The reduction of the Faddeev-equation to a two-body Bethe-Salpeter equation is realised by introducing a separable ansatz for diquark correlations. This entails that the Faddeev components are separable in their relative momenta.

In Fig. 2.5 we show a diagrammatic representation of the resulting equation. The BSA for the diquark Γ is given by a separate solution of a BSE projected onto the diquark as a bound state. A solution of this homogeneous equation for the baryon in

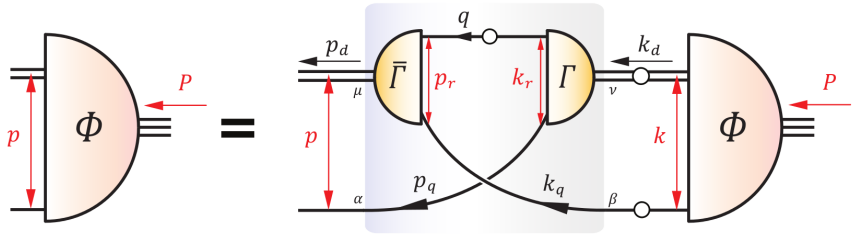

Figure 2.5. Diagrammatic representation of the quark-diquark approximation for the baryon amplitude ϕ using the diquark amplitude Γ as input (figure taken from [115]).

the quark-diquark picture yields the baryon BSA, which will be needed in particular in Ch. 5. An explicit form is given by

$$[\Phi_B]^a_{\alpha\beta}(p,P) = \int \left[K^{ab}(p,k,P)S(k_q)\Phi^c_B(k,P)\right]_{\alpha\beta} D^{bc}(k_d)\ , \tag{2.26}$$

where the kernel K is

$$K^{ab}_{\alpha\beta}(p,k,P) = \left\{\Gamma^b(k_r,k_d)S^T(q)\overline{\Gamma}^a(p_r,-p_d)\right\}\ ,$$

with the diquark propagator D^{bc} and S the fully dressed quark propagator. The Latin labels a,b represent the type of diquark, i.e. scalar or axial-vector, and the

momenta are given by

$$p_q = p + \frac{1}{2}P, \quad p_d = -p + \frac{1}{2}P, \quad k_q = k + \frac{1}{2}P, \quad k_d = -k + \frac{1}{2}P,$$
$$q = p_d - k_q, \quad p_r = \frac{1}{2}k_q - \frac{1}{2}q, \quad k_r = \frac{1}{2}p_q - \frac{1}{2}q\ .$$

The truncation used for solving the nucleon bound state equation then implicitly includes the diquark amplitudes.

2.4. Phase transitions

In this section we introduce the QCD phase diagram and appropriate order parameter for chiral symmetry and the confinement transition as investigated in our functional approach. We introduce the curvature as an important attribute of the transition lines in the phase diagram and discuss the impact of a change in the quark masses, which is schematically shown in the so-called Columbia plot at the end of the paragraph

2.4.1. The phase diagram of strongly interacting matter

Different phases of a certain kind of matter can be distinguished according to their physical properties, depending on thermodynamic quantities such as temperature and density. Within our functional approach to QCD we are concerned with phases of the strong interaction characterized by chiral symmetry and whether it is dynamically broken or not and the phenomenon of (colour/quark) confinement/deconfinement. A sketch showing features of the expected phase structure is given in Fig. 2.6. On the vertical axis we plot the temperature T, while the horizontal one represents the quark chemical potential μ_q. We find a rich structure and various effects. In this thesis we will investigate the crossover-region, where one finds a continuous change between phases, and the 2^{nd} order critical endpoint connecting to 1^{st} order transition line. These transitions occur between two phases:

- **The hadronic phase:** In this phase chiral symmetry is spontaneously broken due to the formation of a $\langle\bar{\psi}_{\text{L}}\psi_{\text{R}}\rangle$ quark condensate. Dynamically generated mass contributes a huge amount to the mass of hadrons. These hadrons are the physical degrees of freedom and colour confinement is realised.

- **The quark-gluon plasma:** In this phase chiral symmetry is (approximately) restored and no colour confinement is expected. Quarks and gluons are the relevant degrees of freedom.

Our investigations will be mostly performed for $N_f = 2+1$ quark flavours, indicating two degenerate light quarks and a strange quark. Details and references will be given

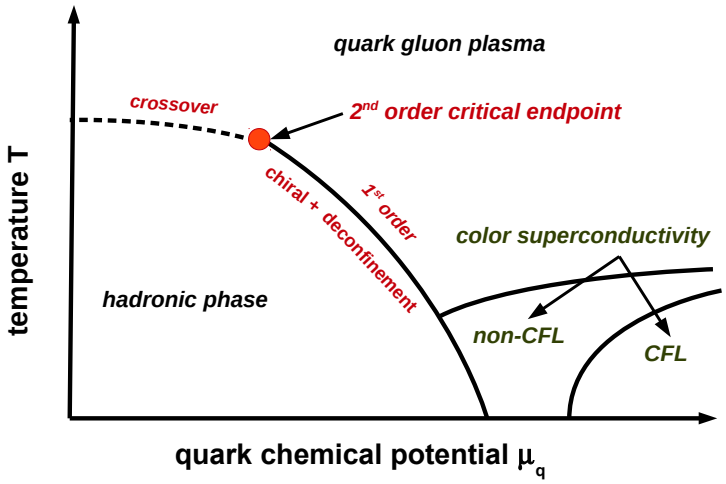

Figure 2.6. Sketch of the QCD phase diagram as investigated with functional methods showing different phases for chiral symmetry and confinement/deconfinement.

in Ch. 3.

For large chemical potential, small temperature and $N_f = 2 + 1$ one can also find a colour-flavour locked phase. This is the most symmetric realisation of a colour superconducting phase, where the three quark flavours symmetrically participate in forming Cooper pairs. In this phase chiral symmetry is broken. However, the breaking pattern is different to the formation of condensate by pairing left-handed and right-handed quarks as e.q. in the vacuum ($T = 0, \mu_q = 0$). In the CFL phase left-handed quarks are paired with each other with the same being true for the right-handed ones (for details see e.g. [59]). Important for this phase is, that the differences due to the quark masses can be neglected. This distinguishes it from the non-CFL phases. Among those the most important one is the two-flavour superconducting ($2SC$) phase, where the two light flavours form a Cooper pair and the strange with the residual colour-charge is left unpaired. These phenomena have been studied within the DSE approach in a series of PhD theses [52, 53] and publications [54–58].

2.4.2. Order parameter for chiral symmetry and confinement

An order parameter measures the realisation of a phase, e.g. by how much chiral symmetry is broken. Therefore the knowledge about the temperature behaviour of the order parameters gives insight about the phase structure of a theory.

Chiral symmetry: quark condensate and T_c in a crossover region

The quark condensate for a flavour f is given by

$$\langle\bar{\psi}\psi\rangle_f = Z_2 Z_m N_c T \sum_n \int \frac{d^3p}{(2\pi)^3} \mathrm{Tr}_D \left[S_f(p)\right], \tag{2.27}$$

where Z_2 is the quark wave function renormalisation constant, Z_m the quark mass renormalisation constant, N_c the number of colours and Tr_D indicates the Dirac trace. It is referred to as the chiral condensate if the renormalised mass is zero (chiral limit). Since we are mostly interested in a system calculated with non-zero quark mass, we instead wish to determine what may be called the *massive condensate*. We find this quantity to be quadratically divergent making a regularisation necessary. Since the divergent part is proportional to the bare quark mass at leading order one may regularise the condensate by

$$\Delta_f = \langle\bar{\psi}\psi\rangle_f - \frac{m_f}{m_h}\langle\bar{\psi}\psi\rangle_h \,, \tag{2.28}$$

where the index h indicates a (test) quark with $m_f << m_h$, which is not necessarily back coupled to the system. Eq. (2.28) is what we call in general a regularised (massive) condensate.

It is important to note that we consider two ways to define a (pseudo-) critical temperature, which are both connected to the quark condensate. The first one is the so called inflection point method, where one uses the point of change in curvature of the quark condensate with respect to temperature,

$$\left|\frac{\partial\langle\bar{\psi}\psi\rangle_f}{\partial T}\right|_{T=T_c^{infl.}} = \max_{\forall T}\left|\frac{\partial\langle\bar{\psi}\psi\rangle_f}{\partial T}\right| . \tag{2.29}$$

The second one returns the maximum of the chiral susceptibility

$$\left|\frac{\partial\langle\bar{\psi}\psi\rangle_f}{\partial m_f}\right|_{T=T_c^{\chi}} = \max_{\forall T}\left|\frac{\partial\langle\bar{\psi}\psi\rangle_f}{\partial m_f}\right| , \tag{2.30}$$

which shows the reaction of the system to a small change in the quark mass.

Both definitions are independent of the regularisation of the divergent part (finite masses). They give different results for T^c in a crossover region but return the same position for a critical endpoint and 1$^{\mathrm{st}}$ order transitions.

As shown in Eq. (2.20), a non-vanishing D function is connected to the (chiral) quark condensate as defined in Eq. (2.27). This makes it possible to define the quantity

$$\langle\bar{\psi}\psi\rangle_f^D = Z_2 Z_m N_c T \sum_n \int \frac{d^3p}{(2\pi)^3} \mathrm{Tr}_D \left[\left(\tilde{\omega}_p\gamma_4\right)\left(\mathbf{p}\cdot\boldsymbol{\gamma}\right) S_f(p)\right],$$

which is related to chiral symmetry (breaking), but is free of quadratic divergences.

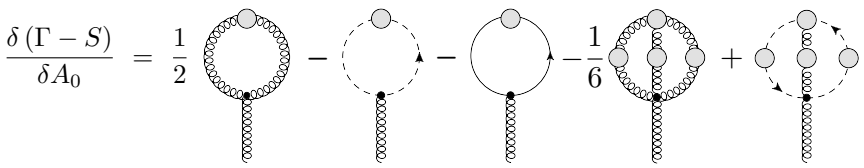

Figure 2.7. The DSE for a background field $\langle A_0 \rangle$. All curly propagators at the bottom represent the background field which couples to a gluon-, ghost- and quark-loop as well as to a pair of two-loop diagrams involving gluon and ghost propagators.

Deconfinement transition: the background field potential

Considering confinement to be connected to a linear rising potential, the Polyakov loop, as introduced earlier, is an often employed order parameter to study confinement/deconfinement phase transitions. These transitions have been investigated with functional methods via the dressed Polyakov loop [44,48,62,64–66], the Polyakov loop potential [68, 116, 117] and the analytic properties of the quark propagator [72–74]. In Ch. 4 we will show results for the Polyakov loop potential used to determine the deconfinement transition in the phase diagram. In [117] the DSE for a background field $\langle A_0 \rangle$ has been introduced, which yields upon integration the potential of the background field. This then can be connected to the Polyakov loop $L[A_0]$ by

$$
\begin{aligned}
L[\langle A_0 \rangle] \geq \langle L[A_0] \rangle \ , \quad L[\langle A_0 \rangle] = 0 \leftrightarrow \langle L[A_0] \rangle = 0 \ , \\
L[A_0] \coloneqq \frac{1}{N_c} \mathrm{Tr} \mathcal{P} e^{i \int d\tau A_0(\mathbf{x},\tau)} \ ,
\end{aligned}
$$

where the Tr represents the colour trace and $\mathcal{P}$ is the path ordering operator (see also [67]). Therefore, the Polyakov loop evaluated for the background field serves as an upper bound for the Polyakov loop expectation value, used as an order parameter for confinement. If we follow [67], the 2-loop diagrams in Fig. 2.7 can be dropped and one is able to obtain the potential solely from the QCD propagators. This has been used in [68] for the first time for unquenched QCD and at finite chemical potential. In the same work, it has also been shown that the deconfinement transition temperature agrees with that obtained from the dressed Polyakov loop. For more details see [67, 68, 117].

If the transitions between confined/deconfined as well as chirally broken/restored phases are taken into account one can distinguish several phases in the QCD phase diagram. It is noteworthy that there are attempts to link the chiral and deconfinement transitions, see e.g [102] and references therein, since their appearance seems to be correlated.

Curvature

There is one property of the transition lines in a phase diagram, which is of great interest, for lattice QCD in particular. Since the calculations on the lattice are hampered by the notorious sign problem, they seek to define quantities which give some information about the shape of the phase diagram at $\mu > 0$. One such quantity is the curvature, which is the first coefficient in a Taylor series expansion of the transition line in terms of μ/T. Since we work mostly with quark chemical potential, we define it according to this quantity. Note, however, that on the lattice it is often defined with respect to baryon chemical potential, where $\kappa(\mu_q) = 9\kappa(\mu_B)$. The curvature κ is given via the equation

$$\frac{T^c(\mu)}{T_0^c} = 1 - \kappa \left(\frac{\mu}{T_0^c}\right)^2 + O\left[\left(\frac{\mu}{T_0^c}\right)^4\right] , \tag{2.31}$$

where T_0^c is the transition temperature for $\mu = 0$. Therefore the curvature as well depends on the choice of definition of T^c in the crossover regime.

2.4.3. Impact of dynamical quarks and their masses: Columbia plot

At the end of this chapter we emphasize one aspect of phase transitions in QCD: their dependence on the quark masses, which is summarized in the Columbia plot for the case of $\mu = 0$, shown as a sketch in Fig. 2.8. On the horizontal axis the light quark mass is plotted, while the vertical axis labels the strange quark mass. The sketch displays possible phase transitions, as a 1^{st} order (discontinuity in the order parameter) or a 2^{nd} order transition (with different universality classes), as well as the case of a smooth continuous transition called a crossover. Some particularly interesting cases are contained within this sketch:

- **Pure Yang-Mills theory:** A theory where only ghosts and gluons are consider can be found in the upper right corner of the Columbia plot.
- **QCD for physical quark masses:** The physical point is highlighted in Fig. 2.8 with a red dot. From lattice QCD it is already established, that we expect a crossover for $\mu = 0$ in this scenario.
- **QCD in the (light quark) chiral limit:** This limit, indicated by the horizontal line through the physical point, is of particular interest in the light of the position of the tricritical strange quark mass and whether it is smaller or bigger than the physical one.

In addition the $N_f = 3$ line is indicated, where all three quark flavours are degenerate.

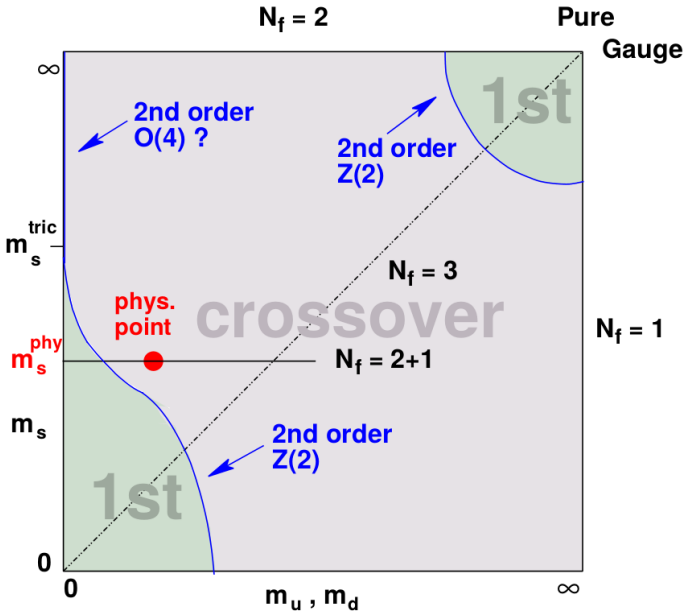

Figure 2.8. A sketch of the so-called Columbia plot showing the dependence of the order of the phase transition in QCD on the quark masses for $\mu = 0$, taken from [118].

The Columbia plot is of particular interest, since a correct representation of different parts of the underlying physics is required to cover all its features correctly. It is noteworthy that there are no units at the axis, therefore the relative size of the 1^{st} order regions is not pinned down.

Investigations of Fig. 2.8 are extended to finite chemical potential in order to get information about the very existence of a critical endpoint. In order for such a critical point to exist, the line of 2^{nd} order transitions must continue as a surface eventually bending towards the physical point or a second critical surface has to appear. There are several investigations of this aspect, in particular from lattice QCD for $N_f = 2$ [119, 120].

3. QCD for $2+1$ quark flavours

> The limits of your language are the limits of your world.
>
> *(Ludwig Wittgenstein)*

Recent calculations by lattice QCD at $\mu = 0$ show the importance of the number of flavours and the connections between the gauge and the matter sector for the phase diagram of QCD [23, 27, 121–123]. While quenched QCD, where there is no back coupling of quarks to the Yang-Mills sector, inherits a 1^{st} order phase-transition at a temperature of $T_c \approx 277$ MeV, the scenario dramatically changes upon the inclusion of quark effects onto the gauge part. Not only the scale of the transition is reduced upon the inclusion of light quark effects, but also its very nature changes to a crossover compared to a sharp transition. The implementation of a strange quark then reduces the scale of the transition furthermore by about 25 percent [66].

In this chapter we shed light on investigations of finite temperature and density QCD in the functional Dyson-Schwinger approach. The employed state of the art truncation was carefully developed and investigated during the last decade, see e.g. [62–66, 68]. While in [62, 63] the authors considered quenched QCD and derived order parameters to pin down the occurring phase transitions, the work in [64] was concerned with pure Yang-Mills correlation functions. A first step towards connecting the matter and gauge part via the inclusion of quark-loops was done in [65], where the quark-loop was calculated for bare quarks in a scheme comparable to hard-thermal-loop (*HTL*) calculations (for a review of the current status of the HTL approach see [124] and references therein). Upon this first approximation to unquench the gluon propagator, i.e. to include quark effects, the authors in [66] set up a truncation scheme featuring self-consistent back-feeding of information between the quark and gluon propagator. Eventually in [68] the Polyakov loop potential was used to define an order parameter for confinement. As a first step in developing a computer code to handle the solution of the coupled system of Dyson-Schwinger equations, a comparison with already investigated and published results is necessary. Therefore the results presented in this section partly overlap with those presented in the aforementioned references and also of [67, 94].

This chapter is organized in the following way: we begin by introducing the truncation scheme, which is used to render the infinite tower of equations to a finite set.

To this end we elaborate on the used ansatz for the quark-gluon vertex and on the input from lattice QCD for the quenched gluon propagator, before we shed light on the unquenching procedure. The following paragraph is dedicated to results for the quark and gluon propagators of our calculation, where we highlight some specific features of its outcome. Finally we turn to the phase transitions of $N_f = 2+1$ QCD, where we discuss the (regularised) quark condensate, the impact from a variation of a parameter in the vertex ansatz as well as the quark masses in the light of the Columbia plot for $\mu = 0$ and also $\mu > 0$. In this section we also present our state of the art Dyson-Schwinger prediction for the QCD phase diagram.

3.1. Truncation of the coupled set of Dyson-Schwinger equations

In order to render the infinite tower of coupled integral equations finite, a truncation has to be applied to the system. In this section we introduce the setup which is applied throughout this chapter and will be built upon later. The truncation involves an ansatz for the quark-gluon vertex, input for the quenched gluon propagator for $T \geq 0$ from lattice QCD as well as a way to take the back coupling of quarks to the gluon sector into account.

3.1.1. The quark-gluon vertex

In this section we explain the ansatz of a crucial component needed in order to provide a calculable quark DSE, the ansatz for the quark-gluon vertex. This vertex in general satisfies a Slavnov-Taylor identity [125] given by

$$i\, k_\mu\, \Gamma_\mu(q,k) = G(k^2) \times [S^{-1}(p) H(p,q) - \bar{H}(q,p)\, S^{-1}(q)], \tag{3.1}$$

where $G(k^2)$ represents the dressing function of the ghost propagator and $H(q,p)$ the ghost-quark scattering kernel with its conjugate $\bar{H}$. The quark momenta are given by p, q and $k = p - q$ is the corresponding gluon momentum. There is no exact solution to Eq. (3.1) available, since the non-perturbative form of $H(p,q)$ is still unknown but subject of investigations (see [126, 127] for recent work). The problem can be circumvented by using the Abelian counterpart of the STI, where $G = H = \bar{H} = 1$. By also taking into account regularity at zero gluon momentum, the corresponding Ward-Takahashi identity (*WTI*) has been solved by Ball and Chiu [128]. At zero temperature and chemical potential the solution is given by

$$\begin{aligned} \Gamma^{BC}_\mu(p,q,k) \;=\; & \frac{A(p^2)+A(q^2)}{2}\gamma_\mu + i\frac{B(p^2)-B(q^2)}{p^2-q^2}(p+q)_\mu \\ & + \frac{A(p^2)-A(q^2)}{2(p^2-q^2)}(\not{p}+\not{q})(p+q)_\mu \,, \end{aligned} \tag{3.2}$$

constraining parts of the vertex. It is not clear whether the exact solution of the STI leads to a similar structure. Hence taking into account the full vertex structure in Eq. (3.2) is not *a priori* a good approximation. Our ansatz for the quark-gluon vertex takes into account the leading γ_μ-part of Eq. (3.2) and is then generalized to finite temperature. It reads

$$\Gamma^f_\mu(p,q,k) = \gamma_\mu \cdot \Gamma(x) \cdot \left(\delta_{\mu,4} \frac{C^f(p) + C^f(q)}{2} + \delta_{\mu,i} \frac{A^f(p) + A^f(q)}{2} \right), \tag{3.3}$$

$$\Gamma(x) = \frac{d_1}{d_2 + x} + \frac{x}{\Lambda^2 + x} \left(\frac{\beta_0 \alpha_\mu \ln[x/\Lambda^2 + 1]}{4\pi} \right)^{2\delta}, \tag{3.4}$$

with the corresponding vacuum expression as implied by Eq. (2.17) and flavour dependence indicated by f. The squared momentum variable x in Eq. (3.4) is the squared gluon momentum k^2 in the quark DSE, but the sum of the two squared quark momenta $p^2 + q^2$ in the calculation of the quark-loop. The infrared part is contains $\Lambda = 1.4$ GeV and $d_2 = 0.5$ GeV^2 as well as the effective infrared strength of the vertex d_1. The perturbative quantities are

$$\alpha_\mu = 0.3\,, \quad \beta_0 = \frac{11N_c - 2N_f}{3}\,, \quad \delta = \frac{-9N_c}{44N_c - 8N_f}\,, \tag{3.5}$$

where α_μ is the running coupling at a chosen scale μ, β_0 the well-known beta-function and δ the anomalous dimension of the vertex. Further information, such as the origin of the effective infrared strength d_1, can be obtained from the difference of the STI and the WTI [129]. The FRG [49] and lattice QCD [130] supply information about the ghost dressing function $G(k^2)$ on the right-hand side of the STI [64] which displays almost no temperature dependence in the infrared regime. Additionally, in [126,127] an infrared enhancement at zero temperature of the ghost-quark scattering kernel was found.

Hence the final construction of our ansatz for the quark-gluon vertex then consists of a factorized non-Abelian part Γ and the leading tensor structure of the Abelian Ball-Chiu construction, where we understand the infrared effects of the remaining components of the vertex as subsumed in the parameter d_1. The dressing function Γ represents the generic momentum running of the leading dressing functions of the vertex as extracted from explicit results for the vertex DSE at zero temperature (see [131] and references therein): these functions run logarithmically at large momenta and become comparably large at typical (infrared) QCD scales. The vertex ansatz inherits some important aspects:

- It is correct in the perturbative momentum domain, where the leading γ_μ-part dominates and the dressing function Γ contains the correct running of one-loop resumed perturbation theory
- It maintains charge conjugation symmetry required of the full vertex

- It contains potential temperature and chemical potential dependence of the full vertex via the leading part of the Ball-Chiu construction

In a full computation, the γ_μ-part might not be sufficient for a correct pattern of dynamical chiral symmetry breaking. In this case the scalar part is present and becomes likely important. In particular the way the scalar part of the vertex vanishes will be crucial for a complete description of the phase transition.

In our standard truncation for $N_f = 2 + 1$ flavour QCD, the infrared strength d_1 in Eq. (3.4) is adjusted to match the scale of the regularised condensate from lattice QCD and a value of $d_1 = 8.05$ GeV^2 is obtained [67]. With this vertex ansatz at hand we are in position to perform unquenched calculations, once we have input for the quenched gluon propagator, e.g. from lattice QCD as presented in the next paragraph, and a procedure for the unquenching as introduced later. More details on the quark-gluon vertex including an investigation of its DSE are presented in Ch. 6.

3.1.2. The quenched gluon propagator - input from lattice QCD

The quenched gluon propagator, as originating from the solution of the pure Yang-Mills system, is taken as input in the manner of earlier works. As explained in [67] and references therein, it is given as a fit to data obtained from lattice QCD discussed in [64]. The fit function is of the form

$$Z_{T,L}(q^2) = \frac{\hat{q}^2}{\left(\hat{q}^2+1\right)^2}\left[\left(\frac{\hat{c}}{\hat{q}^2 + a_{T,L}(T)}\right)^{b_{T,L}(T)} + \hat{q}^2\left(\beta_0\frac{\alpha_\mu}{4\pi}ln(\hat{q}^2+1)\right)^\gamma\right] , \qquad (3.6)$$

where $\hat{q}^2 = \frac{q^2}{\Lambda^2}$ and $\hat{c} = \frac{c}{\Lambda^2}$ with $\Lambda = 1.4$ GeV and $c = 11.5$ GeV^2 being temperature independent. The correct perturbative behaviour is entailed in the UV-term with α_μ and β_0 as defined in Eq. (3.5) and the anomalous dimension of the gluon $\gamma = (-13N_c + 4N_f)/(22N_c - 4N_f)$. The anomalous dimension used for Eq. (3.6) is in agreement with 1-loop resumed perturbation theory for $N_f = 0$, which is therefore used in our work. The fit function in Eq. (3.6) is given depending on the squared four momentum q^2 only and implies the approximation of $\omega_q = 0$, which we call the 0^{th} Matsubara frequency approximation.

The parameter $a_{T,L}$ and $b_{T,L}$ are extracted from fits to the (finite temperature) lattice propagator for specific temperatures, including $T = 0$. In order to have input available for any temperature, the values for $a_{T,L}$ and $b_{T,L}$ have been additionally fitted in temperature direction [67]. With a transition temperature of $T_c = 277$ MeV

for the quenched SU(3) theory, the temperature-dependent parameters are given by

$$\begin{aligned}
a_L(t) &= \begin{cases} 0.595 - 0.9025 \cdot t + 0.4005 \cdot t^2 & \text{if } t < 1 \\ 3.6199 \cdot t - 3.4835 & \text{if } t > 1 \end{cases} , \\
a_T(t) &= \begin{cases} 0.595 + 1.1010 \cdot t^2 & \text{if } t < 1 \\ 0.8505 \cdot t - 0.2965 & \text{if } t > 1 \end{cases} , \\
b_L(t) &= \begin{cases} 1.355 - 0.5741 \cdot t + 0.3287 \cdot t^2 & \text{if } t < 1 \\ 0.1131 \cdot t + 0.9319 & \text{if } t > 1 \end{cases} , \\
b_T(t) &= \begin{cases} 1.355 + 0.5548 \cdot t^2 & \text{if } t < 1 \\ 0.4296 \cdot t + 0.7103 & \text{if } t > 1 \end{cases}
\end{aligned} \tag{3.7}$$

with $t := T/T_c$. Some more numerical details on the gluon propagator are given in App. B.

3.1.3. The unquenched gluon propagator - calculating the quark-loop

It has been shown that unquenching the gluon propagator, i.e. taking the quark-loop into account, is important to cover sizeable effects in the medium [66]. Therefore we use the given techniques involved in solving the unquenched system also for this work and summarize them in this paragraph. We consider the vacuum and the medium separately to highlight different matters of importance. Note that with the introduction of the quark-loop different quark flavours are coupled via the gluon propagator making an $N_f = 2 + 1$ flavour calculation meaningful.

Vacuum

In vacuum the quark-loop has been investigated in different works, e.g [93]. In general it is given as

$$\Pi^{\mu\nu}(q) = \frac{g^2}{2} \sum_f Z_{1F}^f \int_l \mathrm{Tr}_D \left[\gamma_\mu S^f(l+q) \Gamma_\nu^f(l,q) S^f(l) \right] . \tag{3.8}$$

The gluon self-energies may contain spurious longitudinal contributions, visible in

$$\Pi^{\mu\nu}(q) = \Pi_{\mathcal{T}}(q) \mathbb{T}^{\mu\nu}(q) + \Pi_{\mathcal{L}}(q) \mathbb{P}_{\mathcal{L}}^{\mu\nu}(q) , \tag{3.9}$$

with $\mathbb{P}_{\mathcal{L}}^{\mu\nu}(q) = \frac{q^\mu q^\nu}{q^2}$ longitudinal to the gluon four momentum and the transverse projector $\mathbb{T}^{\mu\nu}(q)$ defined in Eq. (2.21). However, in Landau gauge the gluon propagator must be purely transverse. Additionally, due to a finite cutoff, this quantity contains quadratic divergences. To take care of those unphysical contributions the application of an appropriate projector is needed, where we define for now a one-parameter

family of projectors

$$\mathbb{P}^{\mu\nu}_{\zeta}(q) = \frac{1}{N_\zeta}\left(\delta^{\mu\nu} - \zeta\frac{q^\mu q^\nu}{q^2}\right) , \tag{3.10}$$

with the normalisation factor $N_\zeta = \sqrt{(1-\zeta)^2+3}$ and the products

$$\begin{aligned}\mathbb{P}^{\mu\nu}_{\zeta}(q)\mathbb{T}^{\mu\nu}(q) &= \frac{3}{N_\zeta} , \\ \mathbb{P}^{\mu\nu}_{\zeta}(q)\mathbb{P}^{\mu\nu}_{\mathcal{L}}(q) &= \frac{1-\zeta}{N_\zeta} .\end{aligned} \tag{3.11}$$

With those projectors at hand, we can consider the equation which defines the unquenched gluon propagator

$$D^{-1}_{\mu\nu}(q) = \left[D^{que.}_{\mu\nu}(q)\right]^{-1} - \sum_f^{N_f}\Pi^f_{\mu\nu}(q) , \tag{3.12}$$

with the explicit flavour dependence indicated by the superscript f. All other contributions to the gluon DSE are approximated to be contained in $D^{que.}_{\mu\nu}(q)$, which neglects the second order effects of the quark-loop to the contained full propagator (compare Fig. 2.2). This approximation was checked in the vacuum and is precise on a five percent level [129]. The projectors Eq. (3.10) are then applied to Eq. (3.12), which leads to an expression for the dressing function

$$\left[Z^{unq.}(q^2)\right]^{-1} = \left[Z^{que.}(q^2)\right]^{-1} + \frac{1}{3q^2}\Pi^{reg.}(q^2) . \tag{3.13}$$

One can represent the regulated quark-loop by

$$\Pi^{reg.}(q^2) = 3\Pi_{\mathcal{T}}(q^2) + (1-\zeta)\Pi_{\mathcal{L}}(q^2) . \tag{3.14}$$

In [93] it was shown, that $\zeta = 4$ cancels all divergences arising from spurious longitudinal parts in the quark-loop and additionally removing artificial terms due to the regularisation. The projector $\mathbb{P}^{\mu\nu}_{\zeta=4}(k) = \mathbb{P}^{\mu\nu}_{BP}(k)$ is called Brown-Pennington projector [132]. Performing the actual projection and using the previously defined quark-gluon vertex Eq. (3.3), one finds the regularised expression for the quark-loop in vacuum with p, l being the quark momenta and $D_f(x) = A_f^2(x)x^2 + B_f^2(x)$

$$\begin{aligned}\Pi^{\text{reg.}}(q^2) = -g^2\sum_f Z^f_{1F}\int_l \frac{\Gamma(p^2+l^2)}{D_f(l)D_f(p)} \\ \times\left[2\left(\frac{A_f(l)+A_f(p)}{2}\right)A_f(l)A_f(p)\left(8\frac{(q\cdot l)(q\cdot p)}{q^2} - 2(lp)\right)\right] .\end{aligned} \tag{3.15}$$

Finite temperature and quark chemical potential

In the medium we follow the same strategy as in the vacuum. However, we have to be aware that the quadratic divergences are accompanied by the so-called thermal mass. In our investigations this quantity will only be present in the longitudinal part (with respect to the heat bath) of the gluon propagator. There it is referred to as the Debye mass which is related to screening of colour interactions at high temperature and its conjectured to be gauge independent (see [133] and references therein). However, a counterpart for the transverse contribution may also arise at small temperatures and large chemical potential, see e.g. [53, 134]. It is visible in the zero-momentum limit

$$\Pi_L(q^2 \to 0) = 2m^2_{\text{thermal}}(T,\mu) + c\Lambda^2 \,, \tag{3.16}$$

where the constant c in Eq. (3.16) is proportional to the renormalised quark mass and accompanies a quadratically divergent term. By applying the Brown-Pennington projector, we do not spoil m^2_{thermal}. The general form of the quark-loop at finite temperature and chemical potential is the same as in Eq. (3.8). Since the gluon propagator splits into two parts, longitudinal and transverse with respect to the heat bath, we first apply the Brown-Pennington projector $\mathbb{P}^{\mu\nu}_{BP}(q)$ and then $\mathbb{P}^{\mu,\nu}_{L,T}(q)$, as defined in Eqs. (2.22) and (2.23). In this case Eq. (3.13) translates into

$$\left[Z^{unq.}_{L,T}(q^2)\right]^{-1} = \left[Z^{que.}_{L,T}(q^2)\right]^{-1} + \Pi_{L,T}(q^2) \,. \tag{3.17}$$

where $\Pi_{L,T}(q)$ are free of quadratic divergences due to a finite cutoff or spurious longitudinal parts with respect to the four momentum (for more details see [67]). However, up to this point they still contain divergences due to the thermal mass.

Note the appearance of the four-momentum in Eq. (3.17) rather than the three-momentum. Since we work in the 0^{th} Matsubara frequency approximation (compare Eq. (B.10)) for the gluon, we apply that assumption to the quark-loop and use equivalently

$$\Pi_{L,T}(q^2) = \Pi_{L,T}(\mathbf{q}^2, \omega_q = 0) \,.$$

The longitudinal and transverse part of the quark-loop are given by

$$\Pi_T(q^2) = -\frac{2g^2}{q^2}\sum_f Z^f_{1F} \sum\!\!\!\!\!\!\int_l \sigma^f_A(l)\sigma^f_A(p)\Gamma^s_f \left(3\frac{(\mathbf{q}\cdot\mathbf{l}\,)(\mathbf{q}\cdot\mathbf{p}\,)}{\mathbf{q}^{\,2}} - (\mathbf{l}\cdot\mathbf{p}\,)\right) \,,$$

$$\begin{aligned}\Pi_L(q^2) = -\frac{2g^2}{q^2}\sum_f Z^f_{1F} \sum\!\!\!\!\!\!\int_l \Bigg\{ &\sigma^f_A(l)\sigma^f_A(p)\left[\Gamma^s_f\left(2\frac{(\mathbf{q}\cdot\mathbf{l}\,)(\mathbf{q}\cdot\mathbf{p}\,)}{\mathbf{q}^{\,2}} - (\mathbf{l}\cdot\mathbf{p}\,)\right)\right. \\ &\left. + \Gamma^4_f\,(\mathbf{l}\cdot\mathbf{p}\,)\right] + \sigma^f_B(l)\sigma^f_B(p)\left[\Gamma^4_f - \Gamma^s_f\right] - \tilde{\omega}_l\tilde{\omega}_q\sigma^f_C(l)\sigma^f_C(p)\left[\Gamma^4_f + \Gamma^s_f\right]\Bigg\} \,,\end{aligned}$$

where we assume only the 0^{th} Matsubara frequency externally. We abbreviate

$$\Gamma_f^s = \frac{A_f(p) + A_f(l)}{2}\Gamma(p^2 + l^2)$$
$$\Gamma_f^4 = \frac{C_f(p) + C_f(l)}{2}\Gamma(p^2 + l^2)$$

for the quark-gluon vertex with Γ defined in Eq. (3.4) and

$$\sigma_{\mathcal{D}}^f(x) = \frac{\mathcal{D}_f(x)}{A_f^2(x)\mathbf{x}^{\,2} + B_f^2(x) + \tilde{\omega}_x^2 C_f^2(x)}$$

with $\mathcal{D}_f \in \{A_f, B_f, C_f\}$. The dependence on the chemical potential is given via $\tilde{\omega}_n = \omega_n + i\mu$ and implicitly for the dressing functions. Finally we need to take care of the thermal masses and take the limit of $\mathbf{q} \to 0$ explicitly, where we obtain

$$\lim_{\mathbf{q}\to 0} \Pi_T(\mathbf{q}^2, \omega_q = 0) = 0 \,, \tag{3.18}$$
$$\lim_{\mathbf{q}\to 0} \Pi_L(\mathbf{q}^2, \omega_q = 0) = -2\, g^2 \sum_f Z_{1F}^f \sum\!\!\!\!\!\!\int_l \Gamma(l^2 + l^2) \Bigg\{ \mathbf{l}^{\,2} \left(\sigma_A^f(l)\right)^2 \left[C_f(l) - \frac{1}{3}A_f(l)\right]$$
$$+ \left(\sigma_B^f(l)\right)^2 \left[C_f(l) - A_f(l)\right] - \tilde{\omega}_l{}^2 \left(\sigma_C^f(l)\right)^2 \left[C_f(l) + A_f(l)\right] \Bigg\} \,.$$

With these quantities at hand, we can split the quark-loop into non-divergent parts and the thermal mass

$$\Pi_{L,T}(\mathbf{q}^2, 0) = \lim_{\mathbf{q}\to 0} \Pi_{L,T}(\mathbf{q}^2, 0)\, \frac{1}{q^2} + \Pi_{L,T}^{regular}(\mathbf{q}^2, 0) \tag{3.19}$$

We define the thermal mass of the gluon to be the quark-loop contribution to the Debye mass

$$m_{\text{thermal}}^2(T, \mu) = \frac{1}{2} \lim_{\mathbf{q}\to 0} \Pi_L(\mathbf{q}^2, \omega_q = 0) \,, \tag{3.20}$$

where the contributions from the Yang-Mills sector are encoded in the quenched propagator and the factor $\frac{1}{2}$ introduced to match the definition with HTL calculations. Finally we want to comment on the usage of the Brown-Pennington projector: we checked also a setup where we projected the gluon with a transverse projector ($\zeta = 1$) rather than the Brown-Pennington one. This influences the results only in a minor way, in particular the effects can be absorbed into the infrared vertex strength d_1, i.e. d_1 has a ζ dependence. More details on the numerics are given in App. B.

3.2. Results for the quark and gluon propagators at finite T, μ

In this section we present results for the quark and gluon propagators obtained by solving the Dyson-Schwinger equations according to the truncation detailed in the previous paragraph and discuss some of their properties at finite temperature T and finite (quark) chemical potential μ.

3.2.1. Quark propagator

The essential quantity calculated by solving the quark DSE is the quark propagator, which is decomposed into dressing functions as detailed in Eq. (2.15). The numerical details of the solution of the quark DSE are relegated to App. B.1. Here we only mention the renormalised quark masses to be $m_l = 0.8$ MeV for the light and $m_s = 21.6$ MeV for the strange quark at a renormalisation scale of 80 GeV as well as the vertex infrared strength $d_1 = 8.05$ GeV^2. The light quark mass has been fixed by the GMOR relation Eq. (2.25) while d_1 was chosen to reproduce the scale of the regularised condensate given by lattice QCD. The strange quark mass was then obtained with the established relation of $m_s = 27 \cdot m_l$ [67].

First we consider the (real) dressing functions obtained at $\mu = 0$ for the light quark. In Fig. 3.1a the vector dressing function A for the 0^{th} Matsubara frequency is plotted against the four momentum $p^2 = \mathbf{p}^2 + \omega_n^2$ for the vacuum (solid black line) and various temperatures. The starting point of the curves varies due to the different temperatures and the usage of p rather than $\mathbf{p}$. For small temperatures (solid blue, red and green line) we observe the tendency towards the vacuum solution for decreasing T. From $T = 110$ MeV on we see a change of the behaviour in the IR region. In the smaller panel of Fig. 3.1a the change of the behaviour in the mid momentum region is displayed in a zoomed version, where we observe a decreasing infrared value. Similar plots are shown in Fig. 3.1b and Fig. 3.1c for the scalar and Matsubara dressing function. For the B function we observe a degeneracy with the vacuum solution up to $T \approx 110$ MeV, from whereon the effect of chiral restoration starts to take place. For the C function we find the correct vacuum limit behaviour and again a change in the behaviour at $T = 110$ MeV. All dressing functions display no temperature effects at momenta bigger than $p \approx 50$ GeV.

While at $\mu = 0$ the dressing functions are real functions, the introduction of chemical potential leads to a non-vanishing imaginary part (compare Eq. (B.1)). Fig. 3.1d shows the result for the 0^{th} Matsubara frequency for the imaginary part of the C function at $\mu = 100$ MeV and various temperatures. Note that in this graph we plot again the spatial momentum squared. There are several remarkable features to highlight in this figure. First of all, the absolute scale of the imaginary part is at least one order of magnitude smaller than the real part in Fig. 3.1c. The value

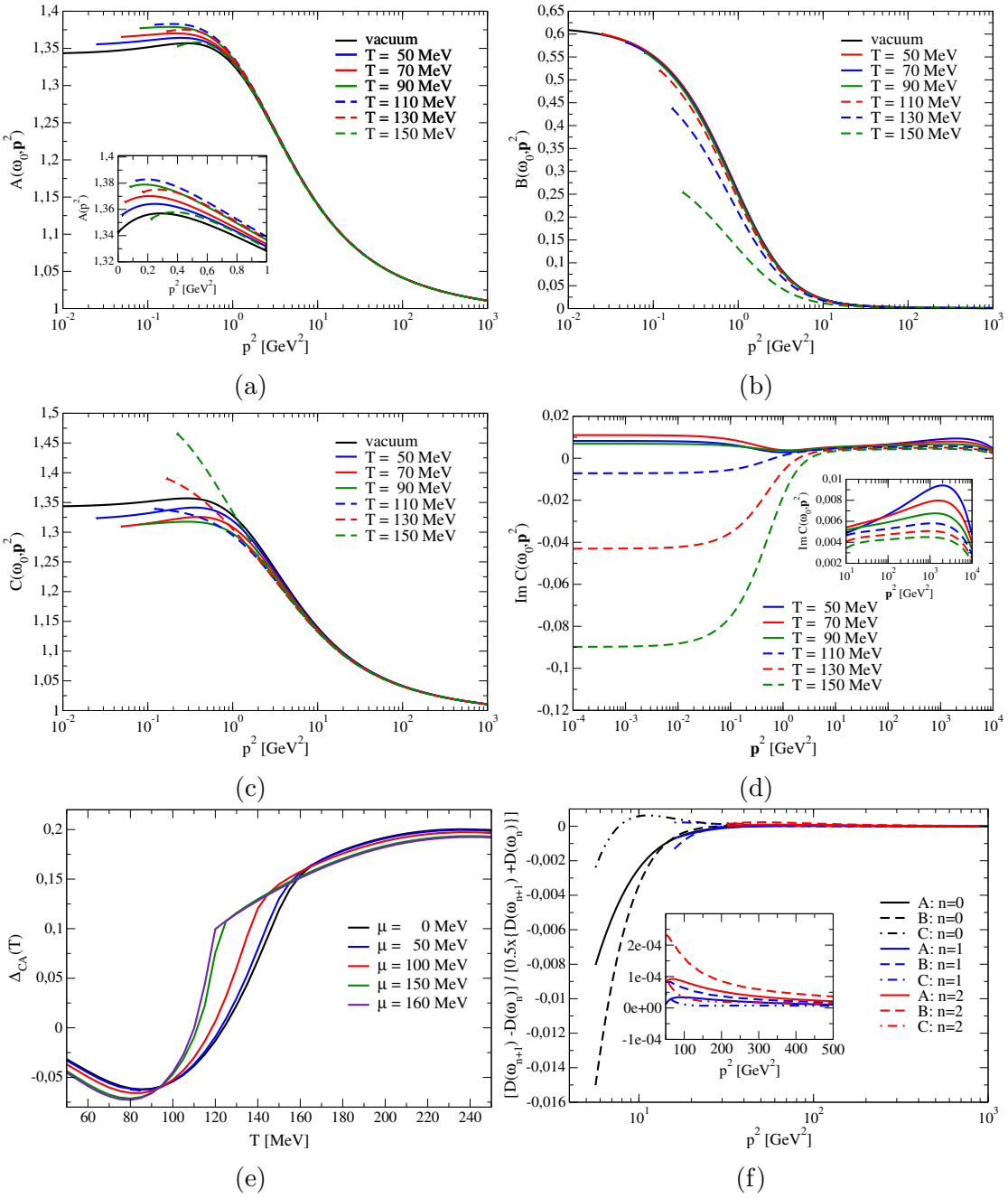

Figure 3.1. Collection of results for the quark propagator: in (a)-(c) we display the results for the A, B and C functions for the 0^{th} Matsubara frequency plotted against p^2 depending on temperature for $\mu = 0$, (d) shows the imaginary part of $C(\mathbf{p}, \omega_0)$ plotted against $\mathbf{p}^2$ for various temperatures and $\mu = 100$ MeV, in (e) we present the difference Δ_{CA} of the infrared values of the A and C dressing function for the 0^{th} Matsubara frequency for different μ depending on T, while in (f) the dressing functions are plotted for the first ($n = 0$), second ($n = 1$) and third ($n = 2$) Matsubara frequency against p^2, showing the precision of the isotropic extrapolation.

in the infrared changes its sign at $T = 110$ MeV, where we already noticed for the real parts the impact of chiral restoration. For temperatures bigger than 90 MeV we also find a zero crossing in the intermediate momentum regime. Additionally we observe a bump for large momenta. Both were found to be numerical artefact and the bump scales with the chemical potential μ. The reduction of the numerical errors is particularly important since they hamper calculation of the quark number susceptibility (QNS) as an important quantity to make connections to experiments (for details see [135–140]). Different approaches to resolve the errors were used, in particular we checked the following:

- Variation of the O(4) cutoff
- Usage of a Pauli-Villars scale in the gluon momentum
- In-medium renormalisation
- Fit to the UV behaviour of the dressing functions rather then a constant extrapolation
- Change from O(4) to an O(3) cutoff $\mathbf{\Lambda}$ and a separate cutoff for the Matsubara sum Λ_ω

While the first test revealed the nature as a numerical error due to the bump changing with the cutoff, the second approach only damped the noise but changed the results for all the other parts of the dressing functions on a non-negligible scale. The in-medium renormalisation did not change much, since the conditions for the A and B function only constrain the real part of those functions. The UV behaviour of the dressing functions did not change the results much, but did not cure the problematic behaviour of $Im(C)$ either. Only the last attempt cured the behaviour for large momenta. However, this approach only replaces one (numerical) evil with another, since it breaks O(4) invariance explicitly and puts a question mark on multiplicative renormalisability. One possible solution for the latter problem could be, to take the A and B function from the vacuum and transfer information about the values at the renormalisation point, which needs to be investigated in future work.

Note however, that the impact of the numerical artefacts in the UV regime of the imaginary part of the C function do not influence results for the phase diagram. The scale of the imaginary part is one order below the real part and suppressed due to the appearance in the UV regime.

Since we do not show results for negative Matsubara frequencies, we want to highlight at this point that the dressing functions obey certain symmetries with respect to the Matsubara frequencies, given by

$$\mathcal{D}(\mathbf{p}, \omega_n) = \mathcal{D}^*(\mathbf{p}, \omega_{-(n+1)}) \ ,$$

which is a natural outcome of the solution of the quark DSE.

In Fig. 3.1e we show the temperature dependence of the difference of the infrared values of the A and C function, $\Delta_{CA} = C(\omega_0, \mathbf{0}) - A(\omega_0, \mathbf{0})$. This is of particular interest, since the order of A and C changes in form of a jump at the critical endpoint, which will be close to $T = 115$ MeV for a light quark chemical potential of $\mu \approx 160$ MeV according to Fig. 3.1e. Eventually in Fig. 3.1f the relative difference of the dressing functions for the nth and (n+1)th Matsubara frequency is plotted against the four-momentum. This shows in particular that the isotropic extrapolation, as given in Eq. (B.9) in the appendix, is well justified.

For Ch. 7, where we will attempt to reconstruct the quark spectral function from our Euclidean data, we will need yet another piece of information on the quark propagator: its values for frequencies which differ from the Matsubara frequencies. There are two possible approaches to the task:

1. Interpolate between the Matsubara frequencies to obtain the desired data

2. Solve additionally the DSE for non-Matsubara frequencies

Since the first suggestion gives results having additionally an unnecessary numerical error, we refer to the second approach and solve the system separately also for values in-between Matsubara frequencies. To this end we define $\omega = \omega_n + \delta$, where its obvious from the explicit form of the equations for the dressing functions as given in the appendix in Eq. (B.1), that each dressing function $\mathcal{D}(\mathbf{p}, \omega_n, \delta)$ depends on itself as well as the other dressing functions for all Matsubara frequencies for the shift δ. We emphasize the importance of applying the shift also applied to the limits of the integral for the implicit Matsubara frequencies (compare Eq. (B.13)). Without appropriate boundary conditions, values in between the Matsubara poles are not well defined, see e.g. [101, 103]). We assume that by solving the DSE with the given perturbative behaviour at large momenta as boundary conditions, the solution for non-Matsubara frequencies is unique.

In Fig. 3.2 we present the relative difference for frequencies between ω_0 and ω_1 for the A and B function and $T = 250$ MeV, $\mu = 0$. We defined $\omega_j = \omega_0 + j \cdot \delta$, with $\delta = \frac{2\pi T}{5}$, therefore $\omega_{j=5} = \omega_1$. The relative difference is defined as

$$\Delta_{\mathcal{D}}(j) = \frac{\mathcal{D}(\omega_{j+1}, \mathbf{p}) - \mathcal{D}(\omega_j, \mathbf{p})}{\frac{1}{2}\left[\mathcal{D}(\omega_{j+1}, \mathbf{p}) + \mathcal{D}(\omega_j, \mathbf{p})\right]} \,, \tag{3.21}$$

where $\mathcal{D}$ represents either A or B. Note, that we rescale the results for B by 1/100. The plot shows, that a naive linear interpolation between ω_0 and ω_1 would give false results, in particular since the ordering of the ratios $\Delta_{\mathcal{D}}(j)$ is not monotonic (compare $j = 2, 3, 4$ for A). Therefore direct calculation is superior to mere (linear) interpolation, especially since it would necessarily be done as a more demanding two dimensional interpolator in frequency-momentum space. We observe, that the

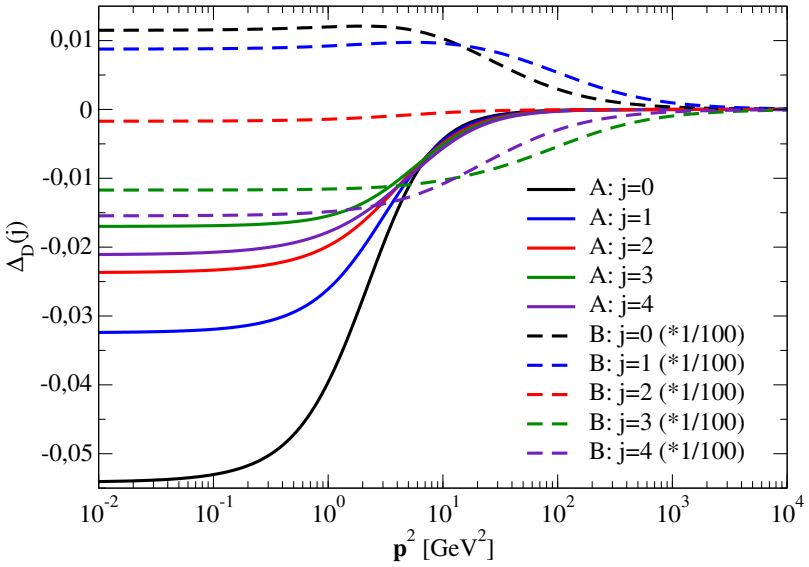

Figure 3.2. Relative change in the A and B dressing functions for non-Matsubara frequencies between $\omega_{j=0}$ and $\omega_{j=4}$ with $\omega_j = \omega_0 + j \cdot \delta$ and the shift $\delta = \frac{2\pi T}{5}$.

change in A is on a few percent level, while the results for B seem tremendously huge in the light of its rescaling. Additionally we observe that the ratio changes its sign. The B function seems to display a smooth behaviour, if evaluated for Matsubara frequencies, however is quite sensitive once one does not use the poles in frequency space exactly. As expected, A, B and C (not shown) have the same UV behaviour and therefore $\Delta_{\mathcal{D}}(j) \to 0$ for large spatial momenta.

Imaginary chemical quark potential, which is connected to our investigation, is subject to several investigations in lattice QCD since its introduction does not lead to a complex fermion determinant (see e.g. [141,142]) and extrapolations to real quark chemical potential are possible. QCD for imaginary chemical potential displays an additional symmetry visible in a periodicity of the grand canonical partition function

$$Z(\mu) = Z\left(\mu + \frac{2\pi i k}{N_c}\right) \ , k \in \mathbb{N} \ , \tag{3.22}$$

and is called Roberge-Weiss symmetry [143]. Its rich phase structure was not subject to our studies but subject to other work, see e.g. [144].

3.2.2. Gluon propagator, quark-loop and thermal mass

This section is dedicated to the results of the unquenched gluon propagator and one of the main impacts of the back coupling from the matter sector at finite temperature/chemical potential, the thermal mass. In Fig. 3.3 we present the results for the

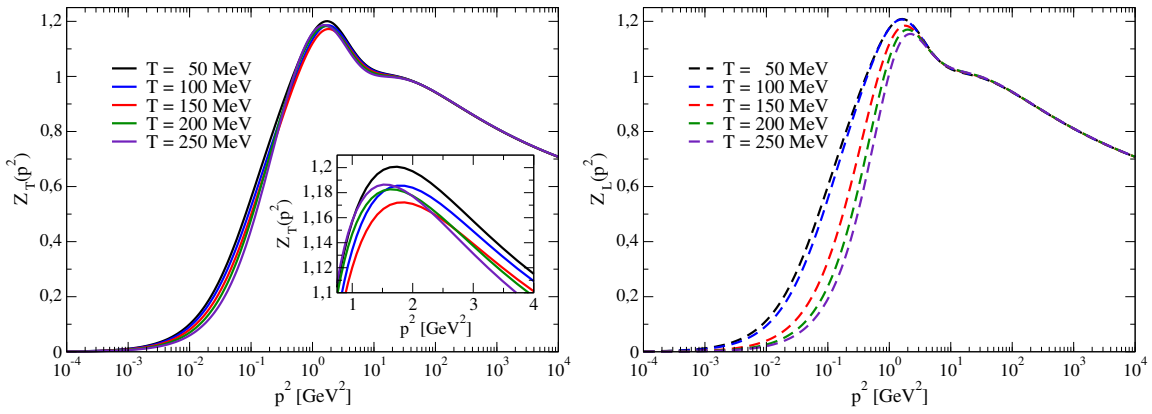

(a) (b)

Figure 3.3. Unquenched gluon dressing functions for $N_f = 2+1$ at $\mu = 0$ for various temperatures. In the left figure we present the transverse part while the longitudinal part is shown in the right picture.

transverse as well as the longitudinal gluon dressing functions at $\mu = 0$ for various temperatures. The dressing functions are quite similar in the qualitative behaviour but show some difference in the quantitative features. While Z_T is almost independent of the temperature, the electric dressing function shows a rather visible change in its maximum and the scale where it rises. This behaviour is mostly triggered by the thermal mass introduced by the quark-loop. To get an idea of the difference between the longitudinal and the transverse part, we show the quantity

$$\Delta_{\Pi_T,\Pi_L}(p^2) = \frac{\Pi_T^{regular}(p^2) - \Pi_L^{regular}(p^2)}{\frac{1}{2}\left[\Pi_T^{regular}(p^2) + \Pi_L^{regular}(p^2)\right]}\,, \tag{3.23}$$

in Fig. 3.4a, where $\Pi_{T,L}^{regular}$ are defined in Eq. (3.19). As expected, $\Delta_{\Pi_T,\Pi_L}(p^2)$ tends to 0 for small temperatures, since Z_T and Z_L have to become degenerate in the vacuum. The ratio seems to be almost independent for temperatures above 200 MeV, where only the scale of the decrease from $\Delta_{\Pi_T,\Pi_L}(p^2)$ changes slightly. This quantity is not influenced by the (squared) thermal mass in the longitudinal part, whose temperature dependence is displayed in Fig. 3.4b for various chemical potentials. Its behaviour is connected to the shape of the quark condensate, which gets ever steeper the closer one gets to the critical value of the chemical potential for the CEP. A decreasing condensate is initiated by the reduction of the scalar dressing function B. For the thermal mass this reduction of B leads to an increase, since from Eq. (3.18) we expect that $m^2_{thermal} \propto \int \frac{1}{p^2+B^2}$. For $\mu = 160$ MeV we observe a kink at $T = 115$ MeV, which is close to the CEP (see next section). The behaviour of the thermal mass for high temperatures seems to approach a straight line with an μ-independent slope but different offsets. HTL calculations predict $m^2_{thermal} \propto T^2$

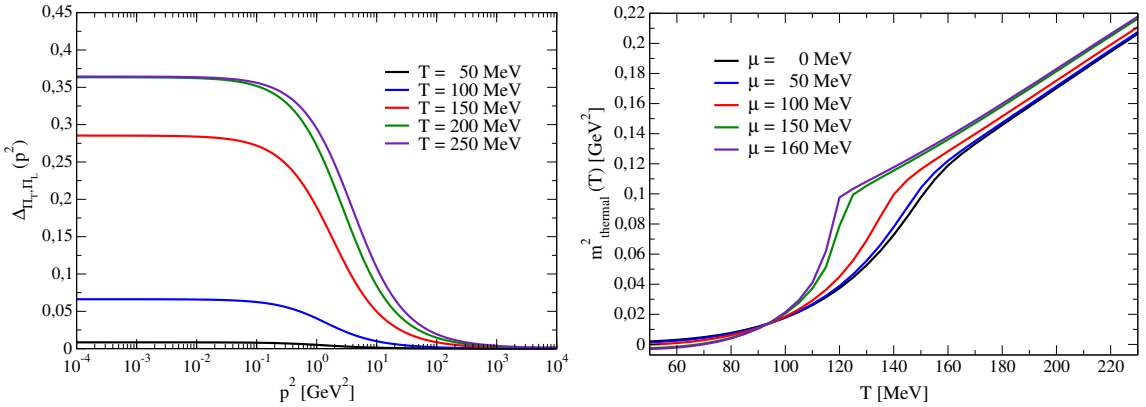

(a) (b)

Figure 3.4. Results for the quark-loop in an $N_f = 2 + 1$ flavour calculation. Left: ratio of the regular part of the transverse and longitudinal contribution. Right: temperature dependence of the quark-loop contribution to the Debye mass.

for high temperatures, whereas we observe in the given range that $m^2_{thermal} \propto T$. However, the applicability of HTL (to one loop order) results is given only for higher temperatures. In App. C we summarize the results for a fit to the quark-loop, as we obtain it after convergence of the coupled system of equations, which can be used to solve an unquenched system. Note that the here discussed thermal mass is only the quark-loop contribution to the Debye mass.

3.3. Phase transitions of $N_f = 2 + 1$ QCD

In this section we report on the results of the phase structure for $\mu = 0$ as well as for the phase diagram. We put particular emphasis on the influence of the vertex strength parameter d_1 and discuss the impact of the quark masses in light of the Columbia plot Fig. 2.8 and its version for finite (light) quark chemical potential.

Transitions and the regularised condensate for $\mu = 0$

Before discussing results for light quark chemical potential $\mu_l = 0$ for the regularised condensate, we mention an investigation with strange quark chemical potential $\mu_s > 0$. In a heavy ion collision conservation laws, e.g for charge, strangeness and baryon number, are fulfilled giving restrictions to relate the strange quark to the light quark chemical potential. In theoretical works these relations are usually given in Taylor series expansions, e.g. for $\mu_s(\mu_l)$, which are applicable for small μ_l. For our investigation we used the coefficients $s_{1,3}(T)$ (with even coefficients vanishing)

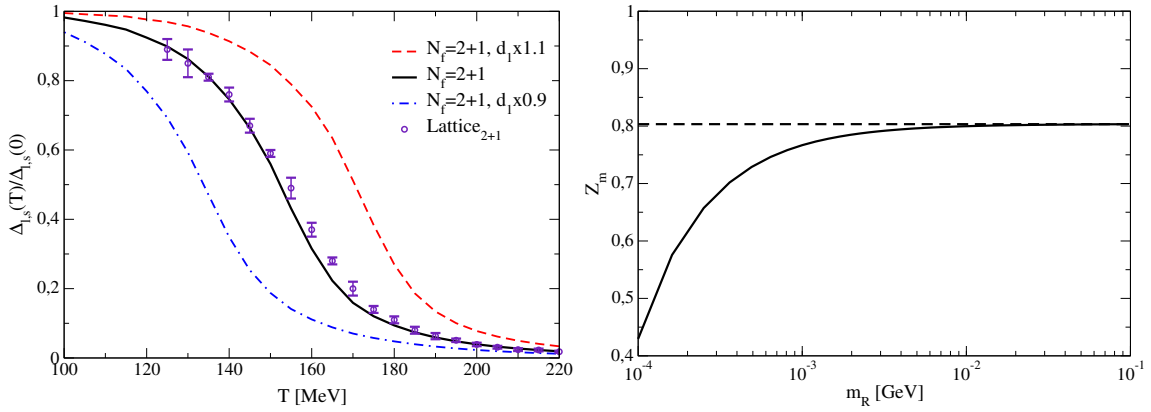

(a) (b)

Figure 3.5. Left: Regularised condensate for $N_f = 2 + 1$ including a variation of the vertex strength parameter d_1 and a comparison to results from lattice QCD [121]. Right: Behaviour of Z_m depending on the renormalised quark mass.

of the results given in [145], provided by Claudia Ratti. We found that the resulting $\mu_s(\mu_l)$ does not change the outcome. Indeed, even a calculation with $\mu_s = \mu_l$ only influences the finite temperature/chemical potential behaviour very little. Therefore we consider only cases with $\mu_s = 0$ throughout our work.

We turn now to the case of $\mu_s = 0$ and refer to the light quark chemical potential from now on as μ. In order to cancel the quadratic divergences appearing in the light quark condensate we subtract from it the condensate of the strange sector, scaled with a factor $\frac{m_l}{m_s}$ and normalize it to its low temperature value. In Fig. 3.5a we show the result (solid black line) and compare it to the results from lattice QCD [121] (symbols). Additionally we added curves for the used $d_1 = 8.05$ GeV^2 lowered by 10 percent (blue dash-dotted line) and increased by 10 percent (red dashed line). From Fig. 3.5a it is apparent, that we find a crossover behaviour for the $N_f = 2 + 1$ case and that a change of d_1 by 10 percent shifts the curve by about 20 MeV to smaller/bigger temperatures, but leaves the slope of the condensate unaltered to the eye. The critical temperature, as defined from the inflection point method Eq. (2.29), agrees with lattice predictions [121] and is

$$T_c^{infl.} \approx 155 \text{ MeV} , \tag{3.24}$$

as expected due to the adjustment of the scale to the corresponding lattice calculations. The corresponding results for the critical temperature defined via the maximum of the chiral susceptibility is given by

$$T_c^{\chi} \approx 160 \text{ MeV} . \tag{3.25}$$

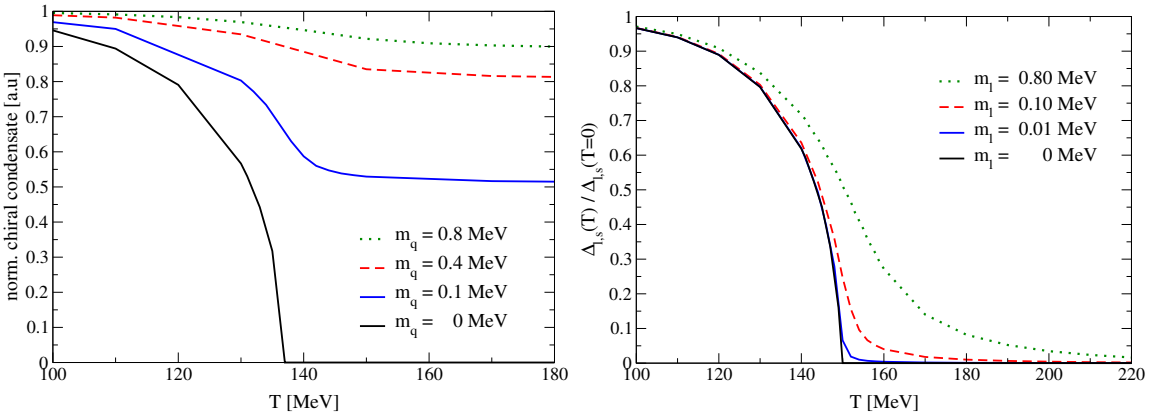

(a) (b)

Figure 3.6. Left: Three (degenerate) flavour quark condensate depending on the quark mass. Right: Comparison of the regularised quark condensate for different light quark masses and a strange quark mass of $m_s = 21.6$ MeV.

This result is somewhat larger than the lattice result in [121] and in particular bigger than the one in Eq. (3.24), whereas the corresponding value in [121] is smaller than the value obtained from the inflection point method. However, it agrees with previous results [66,67]. At $\mu = 0$ we are as well interested in the dependence on the quark masses with fixed vertex strength d_1, which is our view on the Columbia plot Fig. 2.8. In order to perform the limit $m_{\text{quark}} \to 0$ caution with the renormalisation procedure is necessary. Certain terms of the Operator-Product expansion (*OPE*) are neglected and we get a wrong result for Z_m if we simply reduce the renormalised mass m_R. This is highlighted in Fig. 3.5b, where we show how the mass renormalisation constant Z_m changes with decreasing m_R. For the calculation of the Columbia plot we therefore used the asymptotic value of Z_m, as indicated in Fig. 3.5b.

To get an idea of the appearance of the Columbia plot in our approach we investigated the two cases $N_f = 2 + 1$, with two degenerate light quarks, and $N_f = 3$ with three degenerate quark flavours. This might give details about the position of the tricritical strange quark mass and the 1^{st} order region in the lower left corner. In Fig. 3.6a we display the quark condensate for $N_f = 3$ normalised to its low temperature value plotted against the temperature for four different quark masses. In the chiral limit (solid black line) we observe a second order phase transition, while for masses of 0.1, 0.4 and 0.8 MeV we already find a crossover behaviour. This implies that the region in the left corner of an equivalent plot to Fig. 2.8 in our approach is very small if it exists at all. If we interpret the findings in Fig. 3.6a as a 2^{nd} order transition in the chiral limit, there is no 1^{st} order region. Since physics in the chiral limit in our approach is possibly not captured accurate, e.g. pions as the lightest Goldstone bosons are no explicit degrees of freedom, predictions are to be treated with restraint. Note that we do not regularise the condensate, therefore the large

temperature behaviour is different.

If we now turn to the $N_f = 2+1$ flavour case in Fig. 3.6b, we observe a similar behaviour. In the (light quark) chiral limit, we find a condensate indicating a 2^{nd} order phase transition, while already for a small mass of $m_l = 0.01$ MeV we find an indication for a crossover. From the figure we get an idea of the influence of the quark mass on the (chiral) quark condensate, where the absolute value of the slope decreases with increasing quark mass. For a light quark mass of $m_l = 0.01$ MeV we checked if two solutions are present indicating a first order regime, but only one solution was found.

The $N_f = 2+1$ flavour phase diagram and the critical surface

In this last section we want to explore the phase diagram of the $N_f = 2+1$ flavour calculation for finite light quark chemical potential μ_q. The result of our calculation is shown in Fig. 3.7, where we display different transition lines in the μ_q-T plane. In this phase diagram, the (pseudo-) critical temperature for the chiral transition was defined via the maximum of the chiral susceptibility Eq. (2.30), which ends in a 2^{nd} order critical endpoint at

$$(T^c, \mu_q^c) = (115, 168)\,\text{MeV}. \tag{3.26}$$

The deconfinement transition line was determined by Jan Lücker via the minimum of the Polyakov loop potential (see [68]), which shows a somewhat large difference to the chiral crossover at small μ_q. This is in part due to the two different ways of defining T^c: for the Polyakov loop potential the inflection point was used while here we applied the maximum of the susceptibility to find the pseudo-critical temperature in the chiral transition. In [68] the inflection point has been used for both order parameters giving closer transition lines also for small μ_q. However, at $\mu_q = 0$ there is only a crossover for both cases, therefore one can not find a unique value for T_c. At large chemical potential, the deconfinement and chiral transition lines meet in the critical endpoint. For convenience we also show lines with ratios of baryon chemical potential over temperature $\mu_B/T = 2$ and $\mu_B/T = 3$. In Fig. 3.7 our findings for the chiral transition line are also compared with predictions from lattice QCD by displaying extrapolations of the curvature of the chiral transition line from $N_f = 2+1$ lattice results of different groups at imaginary and zero chemical potential [146–151] into the real chemical potential region. We find good agreement of the predictions with our results. The curvature of our transition line is

$$\kappa_{\text{DSE}} = 0.248\,, \tag{3.27}$$

calculated by fitting Eq. (2.31) for $\mu < 100$ MeV to the chiral transition line. The result is a little bit smaller than the value reported in [66, 67] but still larger than the values $\kappa_{\text{LAT}} = 0.059 \ldots 0.180$ of the range found in lattice QCD [146–151].

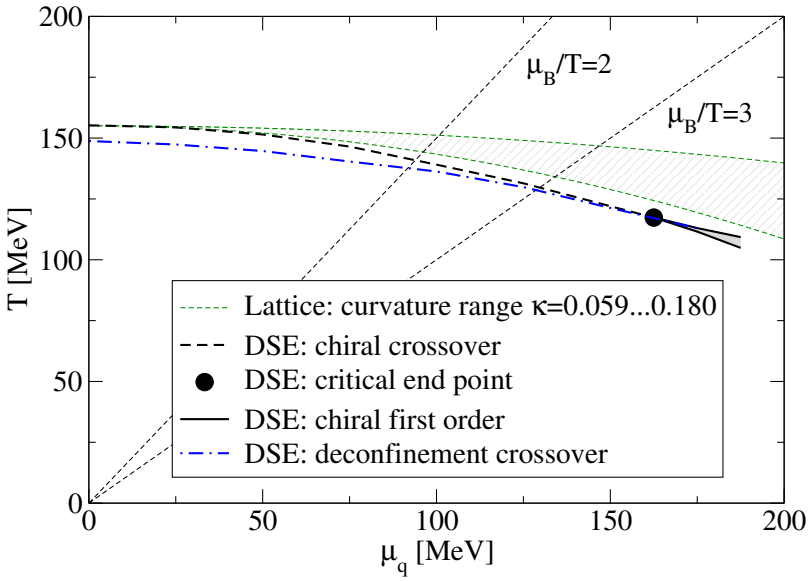

Figure 3.7. Resulting phase diagram for $N_f = 2 + 1$ quark flavours together with an extrapolation from values of the curvature for the chiral transition extracted at imaginary and small chemical potential from different lattice groups [146–151]. The figure is adapted from [80].

In order to gauge the effect of the infrared vertex strength d_1 on the phase diagram, we show results for its variation in Fig. 3.8. It is apparent that the mere shift at $\mu = 0$ of the transition (compare Fig. 3.5a) continues almost over the whole range of $\mu > 0$ and influences the position of the critical endpoint only by approximately five MeV in chemical potential. It is noteworthy that an increased infrared strength *lowers* the value for μ^c.

After investigating the influence of the vertex parameter we now explore the dependence on the quark masses for $\mu_q > 0$. In light of the Columbia plot it is very interesting to evaluate the resulting phase structure for various quark masses. In Fig. 3.9 we display the value for μ^c of the critical endpoint for each corresponding set of light and strange quark mass. We show results for three different strange quark masses: a strange quark mass of 21.6 MeV used in our calculations (solid black curve), for a value 50 percent smaller (red dash-dotted curve) and 50 percent bigger (blue dashed curve). All three curves show a decreasing behaviour with decreasing light quark mass, with slightly different slope, which tends to increase with decreasing strange quark mass. This fits the picture of the Columbia plot, where the 2$^{\text{nd}}$ order line appears for larger values of the light quark mass and a 1$^{\text{st}}$ order region potentially opens up. In addition we report the results of a fit to the curve for $m_s = 21.6$ MeV, where we used the function

$$\mu^c_{\text{fit}}(m_l) = a + b \cdot \sqrt{m_l} + c \cdot m_l \ , \tag{3.28}$$

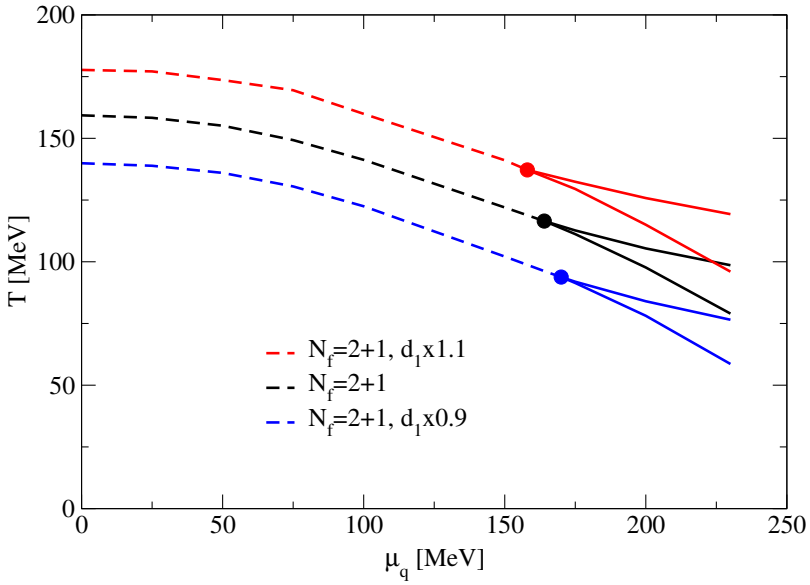

Figure 3.8. Resulting phase diagram for $N_f = 2 + 1$ flavours including a variation of the vertex strength d_1. Dashed lines represent a crossover, solid lines the spinodal lines of a 1st order transition and filled circles the corresponding critical endpoints.

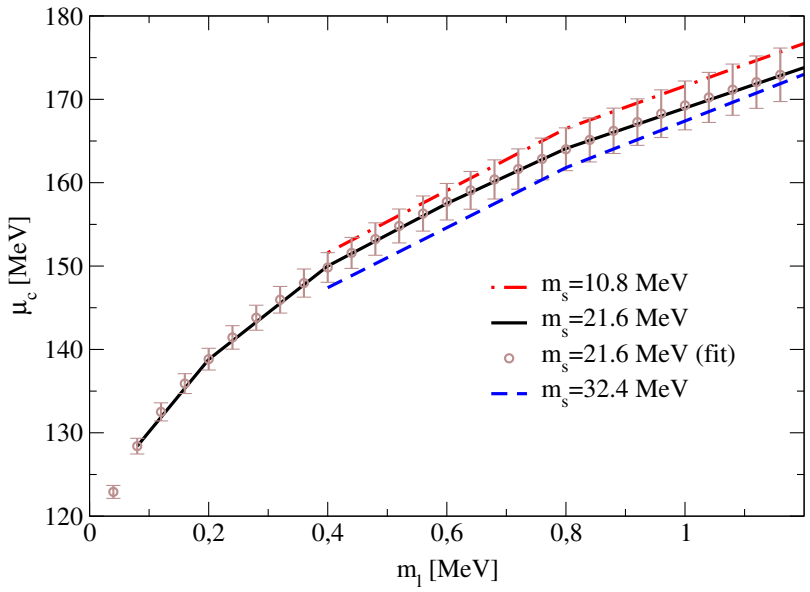

Figure 3.9. Cuts of the critical surface where we show the chemical potential of the corresponding CEP μ^c plotted against the light quark mass m_l for various strange quark masses m_s and a fit of $\mu^c(m_l)$ for $m_s = 21.6$ MeV.

and found resulting coefficients $a = 109.0 \pm 0.5$ MeV, $b = 2.277 \pm 0.046$ MeV$^{1/2}$ and $c = -11.70 \pm 1.04$. The error bars for the fit function in Fig. 3.9 are given by the maximum error due to the fitted parameters. If we compare our results to publications within the framework of lattice QCD [119, 120], we find a somewhat different behaviour. Our result for the critical surface is concave, i.e. it bends towards an orthogonal line (in μ direction) in the Columbia plot through the point with physical quark masses. This line eventually pinches through the critical surface at the critical endpoint reported in Eq. (3.26). On the contrary in an approach with imaginary chemical potential a convex behaviour was found in lattice QCD [119,120]. The calculations for the critical surface were done without using the asymptotic value for Z_m. However, comparison with Fig. 3.5b shows that for the here considered light quark masses the renormalisation constant Z_m is still in the same range as its asymptotic value. It is noteworthy, that comparing Fig. 3.6b and Fig. 3.9 leads to an apparent possible contradiction. Whereas in Fig. 3.6b we find a second order transition in the chiral limit for $\mu = 0$, the fit in Fig. 3.9 seems not to imply a 2$^{\text{nd}}$ order transition for any $\mu_q \lesssim 109$ MeV. However, we expect that the behaviour of the line in Fig. 3.9 might change more rapidly for small light quark masses which is possibly not captured by the masses we consider. This could resolve the discrepancy but needs higher numerical accuracy and left for future investigations.

Summary

In this chapter we presented a truncation to execute an $N_f = 2 + 1$ flavour QCD calculation featuring an unquenching procedure for the gluon in the non-perturbative Dyson-Schwinger approach, adjusted to the scale of $T_c(\mu = 0)$ from lattice QCD. We found the quark propagator to show appropriate vacuum limit behaviour for small temperatures and a growing influence of chirally restoring effects for larger temperatures reflected in the dressing functions. Some numerical problems in the imaginary part for $\mu > 0$ were highlighted, which are not affecting the results for the phase diagram. We discussed possible solutions together with another indicator of a CEP, visible in the difference of the A and C function. A proof for the isotropic extrapolation was shown as well as results for imaginary chemical potential. Results on the gluon propagator were presented, with emphasis on the influence of the quark-loop. We displayed the phase diagram resulting from our truncation featuring a CEP at $(T^c, \mu_q^c) = (115, 68)$ MeV and a curvature which agrees with some predictions from lattice QCD, along with results for the Columbia plot as well as some results on its finite μ version, where we find a concave critical surface bending towards the physical point.

4. The dynamical charm quark

> You know what charm is: a way of getting the answer yes without having asked any clear question.
>
> *(Albert Camus)*

Starting from the truncation scheme for $N_f = 2 + 1$ quark flavours presented in Ch. 3, it is an obvious yet crucial next step to investigate what is changing upon the inclusion of the other member of the second quark family. Therefore in this chapter we present results on a study about the impact of a fourth quark flavour, the charm quark, which is partly published in [80]. Due to the mass difference between the charm quark and the light sector, one might argue that a heavy quark, even dynamically treated, will not influence the system by much. However, there are corresponding results for $N_f = 2 + 1 + 1$ flavours from lattice QCD for transition temperatures and the equation of state using staggered [152, 152–155] and Wilson type quarks [156–158] available. A remarkable result of these studies is that the back reaction of the charm quarks onto the Yang-Mills sector of the theory may be quantitatively important. This motivated our study of the properties of finite temperature and finite density QCD including a dynamically treated fourth quark.

The chapter is organized as follows: in the first section we discus our ansatz to extend the system of quarks and gluons with a dynamical charm quark, including a discussion of choosing an appropriate scale in our quark-gluon vertex. In the second section we show various results for the case of finite temperature but zero chemical potential. This includes an $N_f = 2$ calculation performed to compare the unquenched gluon propagator with lattice results and eventually the results for the impact of the charm quark on the QCD phase diagram. In the end we highlight some results for $N_f = 2$, $N_f = 2+1$ and $N_f = 2+1+1$ with adjusted scales. In particular we discuss the effects of additional flavours on the quark-loop contribution of the Debye mass and the phase diagram.

4.1. Introducing the charm quark and choosing the scale

In Ch. 3 we have shown results for the standard truncation scheme which reproduces the regularised condensate for $N_f = 2 + 1$ from lattice QCD on a quantitative level. In particular the scale was set by adjusting d_1 to reproduce the correct crossover temperature at $\mu = 0$, whereas agreement in shape of the regularised condensate was an outcome and not fitted. To continue the same strategy in case of an $N_f = 2+1+1$ flavour calculation, the corresponding regularised condensate from lattice QCD is needed, which is not yet available. Merely adding an additional quark flavour to the system from Ch. 3 will change the scale and in particular observables in an unphysical manner.

For this reason we approach the problem from a different perspective and develop a scheme in which vacuum properties of pseudoscalar mesons are reproduced by our truncation, independent of the number of flavours taken into account. This was possible due to a recent development in [79], where the authors introduce a treatment of beyond rainbow-ladder kernels for the solution of the Bethe-Salpeter equation, a equation to determine properties of bound states with two underlying constituents, as introduced in Sec. 2.3. In particular, since we use the ansatz in Eq. (3.3) for the quark-gluon vertex the work published in [79] was necessary to make the calculation of mesonic properties in the vacuum possible. One of the authors of [79], Walter Heupel, supplied his program to do a study of pseudoscalar mesons aiming to reproduce their physical attributes within our truncation. The strategy to tackle the problem was the following:

1. Solve the coupled system of quark and gluon DSE with the desired number of flavours, quark properties and infrared vertex strength d_1 in the vacuum.

2. Calculate the complex quark using the unquenched gluon, renormalisation constants and given d_1 from 1. as input.

3. Solve the Bethe-Salpeter equation in order to find the corresponding mass(es) and decay constant(s) for the pseudoscalar meson(s) of interest.

4. Iterate 1.-3. until the properties of interest for the pseudoscalar mesons agree with the physical values.

At first glance, already the attempt to obtain the correct vacuum masses for the pion and kaon in an $N_f = 2+1$ calculation seems difficult, since finding the corresponding parameter d_1 and physical quark masses is a multidimensional fit. However, there are certain properties which are almost flat in one or more directions of the multi-parameter space. This is the case for the pion decay constant, which depends strongly on d_1 and only to a small extent on the light quark mass. The pion mass itself will

Set	$\mathbf{m_l}$	$\mathbf{m_s}$	$\mathbf{m_c}$	$\mathbf{d_1}$	$\mathbf{m_\pi}$	$\mathbf{m_k}$	$\mathbf{m_{\eta_c}}$	$\mathbf{f_\pi}$	$\mathbf{f_k}$
BSE_2	1.43	-	-	5.3	135	-	-	93	-
BSE_{2+1}	1.32	34.1	-	6.8	135	497	-	94	115
BSE_{2+1+1}	1.23	31.6	440	7.6	135	497	2,982	94	117
LAT_2	7.95	-	-	5.3	315	-	-	108	-
LAT_{2+1}	0.8	21.6	-	8.05	107	405	-	107	123
LAT_{2+1+1}	0.8	21.6	300	8.05	109	412	2,364	95	113
RPP (central val.)	3.4	93.5	1275	-	135	494	2,984	92.2	110

Table 4.1. Current quark masses, vertex parameter d_1 and resulting mesonic properties in the vacuum. The vertex strength d_1 is given in GeV^2, the other values in MeV. While BSE_{N_f} are fixed via the solution of BSEs to the corresponding vacuum properties of mesons, the sets LAT_{N_f} are related to results from lattice QCD. The light and strange quark masses from the Report of Particle Physics are given in the $\overline{MS}$ scheme at a renormalisation scale of 2 GeV, while the charm quark mass is given at m_c.

depend on both, the vertex strength d_1 and the light quark mass. The strange quark mass only influences the pion properties via its effect on the unquenched gluon and therefore, if within the right ballpark, can be varied separately to obtain the right kaon mass. In respect thereof it was useful to first adjust d_1 to approximately the right pion decay constant and then to vary the light quark mass until the physical pion mass was reproduced. If this was performed with a sensible value of the strange quark mass, the latter was then adjusted to obtain the correct kaon mass (given the fixed d_1 and m_l). In case of an $N_f = 2 + 1 + 1$ calculation the charm quark mass was then varied to obtain the physical value for the mass of the η_c meson. Note that in general the infrared strength of the vertex could be flavour dependent, as shown in [131], where an explicit calculation for the quark-gluon vertex was done in the vacuum. In particular the charm quark with its very high mass is supposed to have a considerably smaller vertex strength. Motivated by [131] we checked the influence of $d_1^{\text{charm}} = d_1^{\text{light}}/2$ and found only a very small effect in the vacuum, which was within our estimated precision. This gives us confidence to treat d_1 flavour independent in our calculations.

In Table 4.1 we summarize the results for the quark masses and the vertex infrared strength d_1 for different approaches, where we indicate parameter sets fixed via the above described approach with BSE_{N_f}. The other half of the given parameter sets, dubbed LAT_{N_f}, is related to comparisons with lattice QCD. Additionally we give the resulting properties of the pion, kaon and η_c. The sets LAT_{N_f} are designed in

the following way:

- LAT_2 is obtained by solving the BSE in our truncation analogously to the BSE_{N_f} sets, but aiming for $m_\pi = 315$ MeV to make a comparison for the unquenched gluon in [130] possible [1].

- LAT_{2+1} is our standard set reproducing the crossover temperature from lattice QCD [121] as described in Ch. 3, where the Gell-Mann-Oakes-Renner relation has been used to fix m_l and the ratio $m_s/m_l = 27$ subsequently determined the strange quark mass m_s, as described in [66].

- LAT_{2+1+1} is the same setup as for LAT_{2+1} with an additional charm quark added, having the same ratio of strange to charm quark mass as in BSE_{2+1+1}.

The pseudoscalar meson properties for the sets BSE_{N_f} are close to the results given in the Review of Particle Physics (*RPP*) [159]. While the pion decay constant was fitted, the kaon decay constant is a prediction and deviates from the RPP only by five (BSE_{2+1}) respectively seven (BSE_{2+1+1}) percent. The differences in the infrared strength of the vertex are mostly due to unquenching effects of the gluon. If one views the interaction as the combination of the quark-gluon vertex and the gluon propagator, one expects the same integrated strength to obtain the same pion mass. However, every additional quark flavour reduces the maximum in the gluon dressing function $\text{Z}(p^2)$ and modifies the thermal mass of the gluon, as we will show in the next section. We find the ratio of the strange to light quark mass for the sets BSE_{2+1} and BSE_{2+1+1} to be $m_s/m_l \approx 26$, which is very close to the value $m_s/m_l \approx 27$ used in [66] and the one given in the RPP of 27.5. The ratio of the charm to strange quark mass for set BSE_{2+1+1} is $m_c/m_s \approx 14$, which is within the same ballpark as results from lattice calculations, see e.g. [160, 161]. We emphasize that the quark masses themselves are renormalisation point and scheme dependent, therefore direct quantitative comparisons are not easily possible and need to be treated with care.

When inspecting the results for the pseudoscalar mesons for our standard set LAT_{2+1}, we observe that the pion mass is too small but particularly the pion decay constant too big, with the same being true for the kaon properties. Since we get the correct scale in the temperature dependent regularised condensate, our approach from Ch. 3 is designed for in-medium calculations with systematic uncertainties for the vacuum limit of about 20 percent (compare m_π and f_π for LAT_{2+1} and RPP). This is a result of the necessary truncation we made. A truncation describing both scenarios is desirable and has to be investigated in future work.

[1] d_1 was taken from BSE_2, to have the correct vacuum limit at the physical point.

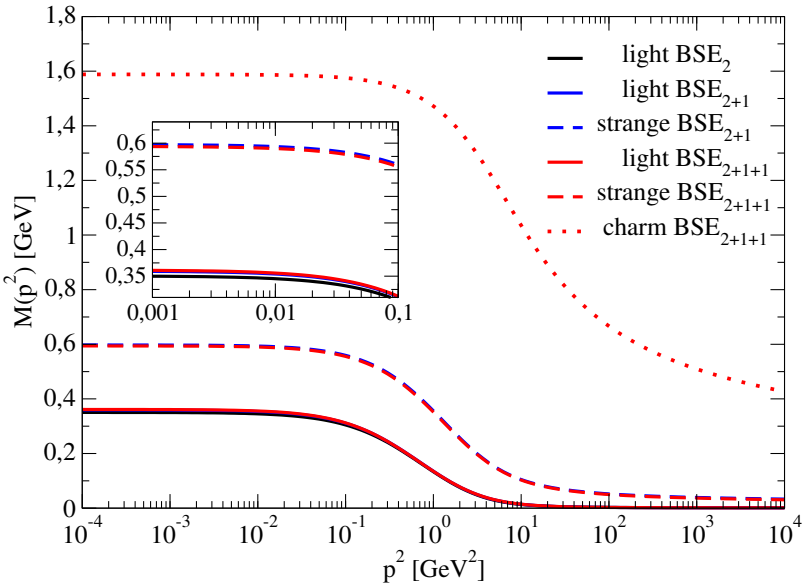

Figure 4.1. Results for the quark mass functions of the sets BSE_{N_f} in vacuum. Black represents the $N_f = 2$ calculation, while blue indicates $N_f = 2{+}1$ flavours and red $N_f = 2 + 1 + 1$ with the dynamical charm quark. Solid lines represent the light quarks, dashed lines the strange quarks and dotted lines the charm quark.

4.2. Results in the vacuum and the medium for different N_f

In this section we focus on results of the various parameter sets given in Table 4.1 in vacuum and in the medium, which will give an understanding of the impact of the dynamical charm quark. We start with the consideration of results in the vacuum.

Vacuum

The sets BSE_{N_f} are fixed to recover vacuum properties of mesons and it is interesting to compare results in the vacuum and investigate the implications of our procedure. In Fig. 4.1 the mass functions for the light, strange and charm quark are shown for the different sets BSE_{N_f}. When comparing the mass functions for the light quark for set BSE_2 (black solid curve), BSE_{2+1} (blue solid curve) and BSE_{2+1+1} (red solid curve) we observe that neither taking into account the strange quark nor the charm quark affects the light quark mass function considerably (see higher resolved panel in Fig. 4.1). Comparing the strange quark mass function for BSE_{2+1} (blue dashed curve) and BSE_{2+1+1} (red dashed curve) confirms that the charm quark has no influence on the mass function of the strange quark as well.

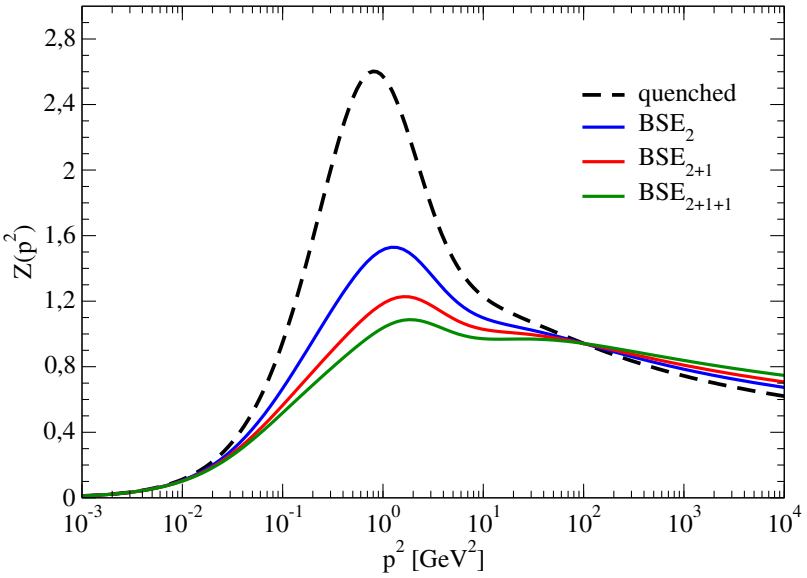

Figure 4.2. Results for the gluon dressing function of the sets BSE_{N_f} in vacuum. In the dashed black line is the result of the quenched gluon propagator from lattice QCD, the solid blue line for two degenerate light flavours, the red line represents an $N_f = 2 + 1$ calculation and green $N_f = 2 + 1 + 1$ flavours.

This is what we intuitively expected due to fixing each set to the same mesonic properties. However, it is not necessarily the case since the quark in the whole complex momentum-plane enters the BSE, whereas in Fig. 4.1 we solely consider it for real momenta. In Fig. 4.2 we display the (unquenched) gluon dressing function for the three sets BSE_{N_f} (blue, red and green solid lines) and the quenched lattice gluon (black dashed curve). The unquenching in our truncation including two light flavours reduces the maximum of the gluon by about 40 percent compared to the quenched calculation. It is reduced additionally by about 20 percent upon inclusion of the dynamical strange quark and the charm quark suppresses the bump from the $N_f = 2{+}1$ calculation further by about 10 percent. This is a surprisingly large impact if one bears in mind the bare mass of the charm quark, but can be explained by the dynamically generated mass differing only by approximately a factor of 2.5 between the strange and the charm quark (compare Fig. 4.1). The different behaviour for large momenta for the gluon in Fig. 4.2 is due to the anomalous dimension of the quark-gluon vertex, which depends on the number of flavours (see Eqs. (3.3) and (3.4)), having an impact on the quark-loop contribution to the UV part of the gluon.

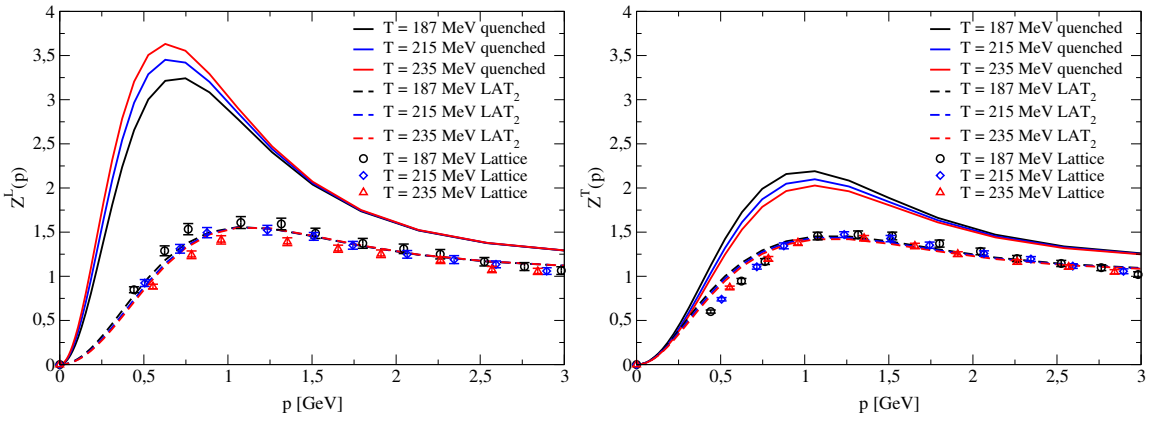

(a) (b)

Figure 4.3. Comparison of the unquenched gluon for $N_f = 2$ at $m_\pi = 315$ MeV. Shown are the quenched lattice gluon from (solid lines, see Sec. 3.1.2), results from set LAT_2 (dashed lines) and lattice results for the unquenched gluon propagator from [130] (symbols). In (a) we compare the longitudinal and in (b) the transverse part.

Finite temperature and zero chemical potential

We start this section with the results of LAT_2 at finite temperature. This set was designed to reproduce a pion mass of 315 MeV in order to make it comparable to lattice results, using the d_1 from set BSE_2. With the fixing procedure in the manner of the sets BSE_{N_f} we are in the position to update the calculations done in [66], where the quark mass was roughly fitted to the higher pion mass via the Gell-Mann-Oaks-Renner relation and compare to the results in [130]. For the sake of comparison, we used the same temperatures as given in [130] for the calculation of the unquenched gluon propagator. The results are presented in Fig. 4.3, where we compare the unquenched gluon dressing functions (dashed lines) with the quenched lattice data (solid lines) as well as the unquenched lattice calculation (symbols). We find good qualitative and quantitative agreement of the unquenching effects for the gluon. In particular we observe the established inversion of the temperature ordering compared to the quenched propagator, which was already predicted in [66]. One observes that the transverse part slightly disagrees for momenta below 1 GeV and that our calculation for the longitudinal part in Fig. 4.3a shows almost no temperature dependence for the given temperatures. One possible reason for the lack of spread could be, that while T^c in [130] is at approximately 200 MeV, the value for T^c in our approach is at about 170 MeV, both determined via the maximum of the chiral susceptibility. Indeed, if we compare the results for the dressing function at the same values of T/T^c rather than absolute temperatures, we find more influence of the temperature on the longitudinal part of the gluon dressing function. However, this does

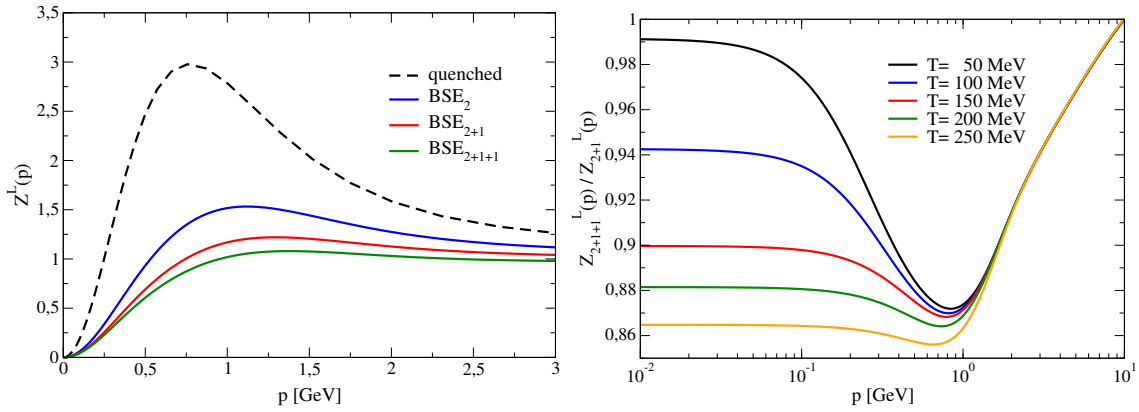

(a) (b)

Figure 4.4. Results for the longitudinal part of the gluon at $\mu = 0$. Left: $Z_L(p)$ for the sets BSE_{N_f} for a temperature of $T = 135$ MeV. Right: Ratio of $Z_L^{BSE_{2+1+1}}(p)$ to $Z_L^{BSE_{2+1}}(p)$ for different temperatures.

not resolve the general tendency of the spread being not as large as indicated by the lattice data.

Nevertheless, the good agreement for the unquenching effects gives confidence about the method we use for unquenching the gluon. Additionally our procedure to fit vacuum properties of mesons employed at finite temperature gives reasonable results also in the gluonic sector.

With this in mind we now investigate the results for the gluon propagator for the sets BSE_{N_f}. In particular we are interested if the impact of a dynamical charm quark of about 10 percent in the vacuum continues to be on the same level at finite temperature. To shed light on the behaviour of the gluon, we first draw our attention to Fig. 4.4a, where a comparison of the longitudinal parts of the gluon dressing functions at a temperature of $T = 135$ MeV is shown. We observe a similar behaviour as in the vacuum, with the largest effect introduced by taking into account the two degenerate light flavours and subsequently less impact of the strange quark and the charm quark. However, the contribution of the charm quark to the whole shift by the unquenching is not negligible and on the 10 to 15 percent level. In Fig. 4.4b we show to ratio of the longitudinal gluon dressing function for BSE_{2+1+1} to the one from BSE_{2+1}, which reveals the impact of the charm quark depending on temperature. Note that each additional quark flavour increases the thermal mass which reduces the electric dressing function in the infrared. The main impact of the charm quark, apart from the change of the thermal mass, is around the maximum in the dressing function at momenta close to 1 GeV, where the bump is reduced due to the additional charm quark by around 13 percent, almost independent of the temperature.

In order to have not only a relative but also a quantitative impression of the in-

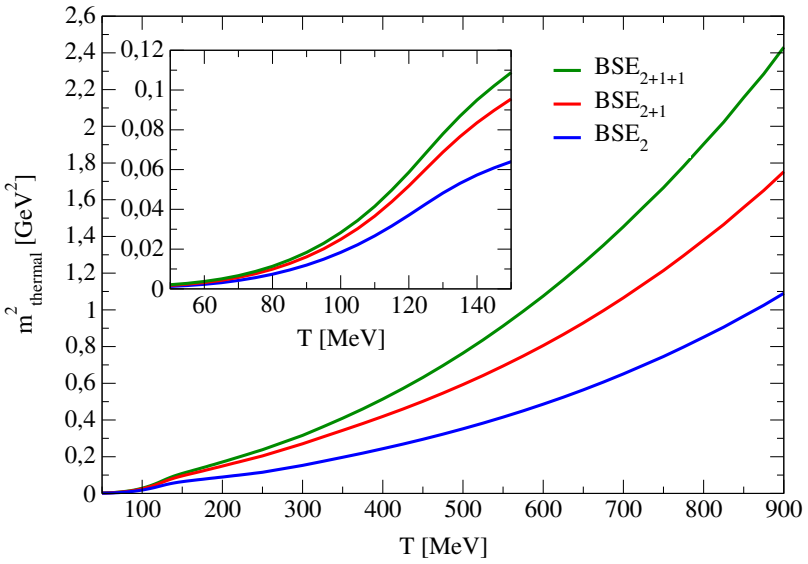

Figure 4.5. Quark-loop contribution to the Debye mass of the gluon for the sets BSE_{N_f} at $\mu = 0$.

frared properties of the gluon in the setup BSE_{N_f}, we show also the squared thermal mass of the chromo-electric gluon, as defined in Eq. (3.20), depending on the temperature in Fig. 4.5. The typical behaviour of the thermal mass showing an inflection point in the range where also the quark condensate displays a change in curvature is highlighted in the smaller panel. For much larger temperatures, one would expect behaviour predicted by HTL calculations, where the thermal mass of the gluon to one-loop order is calculated to be [101]

$$m^2_{\mathrm{thermal,HTL}} = 4\pi\alpha_\mu \left[\frac{N_c T^2}{3} + \frac{1}{6} \sum_f \left(T^2 + \frac{3}{\pi^2} \mu_f^2 \right) \right] , \tag{4.1}$$
$$\overset{\mu=0}{=} 4\pi\alpha_\mu \left(\frac{N_c}{3} + \frac{N_f}{6} \right) T^2 ,$$

which in particular is proportional to T^2 and depends linearly on the number of flavours taken into account. Note that we define the thermal mass solely via the quark-loop contribution. Therefore we expect our result to be exactly proportional to N_f, i.e. that there is no term proportional to N_c present. The latter term arises from the (pure) Yang-Mills part of the gluon DSE at finite temperature and is captured by the contribution to the Debye mass in the quenched gluon propagator [64]. Performing a fit on to the curves in Fig. 4.5, we find good agreement with a quadratic behaviour. In Table 4.2 the results for a fit-function given by

$$m^2_{\mathrm{fit}} = a \cdot T^2 , \tag{4.2}$$

Set	a	HTL
BSE_2	1.335	1.257
BSE_{2+1}	2.166	1.885
BSE_{2+1+1}	2.978	2.513

Table 4.2. High temperature ($0.6 \leq T \leq 0.9$ GeV) fit to the quark-loop contribution of the Debye mass for the sets BSE_{N_f} with $m^2_{\mathrm{fit}} = a \cdot T^2$ compared to predictions from HTL calculations.

are given together with predictions for the considered contribution from HTL calculations. We find satisfactory agreement with the prediction for the considered part of the thermal mass to be linear in N_f, This is verified by the ratio of the differences $\frac{a(BSE_{2+1})-a(BSE_2)}{a(BSE_{2+1+1})-a(BSE_{2+1})} \approx 1.025$. However, for the slope γ given by $a(N_f) = \gamma N_f$ we find $\gamma = 0.82 > \frac{4\pi\alpha_\mu}{6} = \gamma_{\mathrm{HTL}}$ and a linear extrapolation of the results for the here investigated number of flavours to $N_f = 0$ results in $a(N_f = 0) \approx -0.5$. In this quenched case however, there is no contribution to the Debye mass from the matter sector since there is no quark-loop. This discrepancy and the potentially non-trivial limit for $N_f = 0$ must be discussed elsewhere. Potential differences between HTL and our calculation are the use of degenerate bare quarks in HTL and the calculation to one-loop order, while we obtained fully dressed quark propagators in a resumed one-loop order scheme.

After investigating the impact of the charm quark on the finite temperature gluon, we now consider its impact on the chiral dynamics of the coupled system. One particularly interesting quantity to consider in this regard is the regularised condensate. In Fig. 4.6 we display this quantity for the various parameter sets with $N_f = 2 + 1$ and $N_f = 2 + 1 + 1$, where quadratic divergences due to the finite quark mass have been removed. One first and remarkable observation is, that the regularised condensates for BSE_{2+1} and BSE_{2+1+1} coincide. This immediately leads to the same chiral transition temperature if defined via the inflection point. It turns out that also T^c obtained via the maximum of the chiral susceptibility is the same for both sets within our numerical precision. By comparing the parameters in Table 4.1, this is by no means a trivial outcome. We draw the conclusion that if the pion mass and decay constant (as well as masses of other pseudoscalar mesons) in the vacuum are fixed, the quark condensate does not change upon inclusion of a dynamical charm quark at $\mu = 0$. The picture changes if we merely add a dynamical charm quark, as becomes obvious by comparing the result for LAT_{2+1} (red dashed line) and LAT_{2+1+1} (green dashed line). Here we find a shift of the critical temperature by about 20 MeV, whereas the slope of the regularised condensate around T^c remains approximately the same. From Table 4.1 we observe however, that the (important) scales in the vacuum have changed.

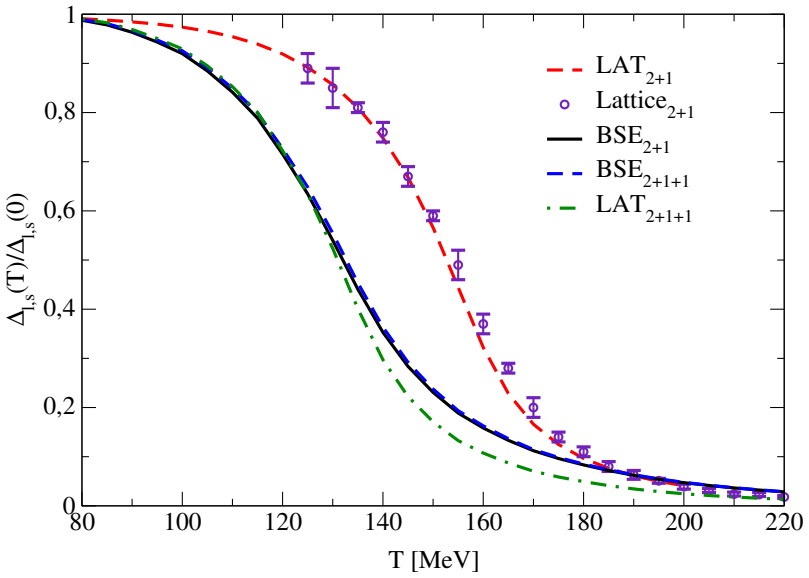

Figure 4.6. Regularised condensates for the parameter sets BSE_{2+1}, BSE_{2+1+1}, LAT_{2+1} and LAT_{2+1+1} compared to $N_f = 2+1$ results from lattice QCD ($\mathrm{Lattice}_{2+1}$) [121]. The scale of set LAT_{2+1} was chosen to agree with the transition temperature of the presented lattice results.

We are left at this point with a dilemma, as it seems: either we adjust d_1 to obtain the correct transition temperature from lattice QCD or we fix the scales in the vacuum correctly. To resolve this issue, improvement of our truncation scheme would be necessary and will be investigated in later chapters. For now we use information from both limits to extract knowledge about the finite temperature behaviour of our system. From Fig. 4.6 it is apparent, as already pointed out in Ch. 3, that LAT_{2+1} reproduces the results from lattice QCD (symbols) quite well. As noted, the charm quark has no influence on the regularised condensate if the scales are adjusted properly. We conclude, that also the results for LAT_{2+1} will not change upon the carefully adjusted inclusion of a charm quark at $\mu = 0$ and therefore resemble the situation for BSE_{2+1} and BSE_{2+1+1}, only at a different scale of T_c. We point out, that one can interpret the discrepancy in the vacuum properties for the set LAT_{2+1} and the reduction of T^c by about 20 MeV for the sets BSE_{N_f} compared to the lattice data, as the systematic errors due to the truncation scheme.

Phase diagram

Until now, at $\mu = 0$ we found that the charm quark, if taken into account properly with adjusted scales, has no impact on the chiral properties of the system. Naturally we are now interested if this continues to be the case at $\mu > 0$. For our considerations of the phase diagram we use the maximum of the chiral susceptibility to define the

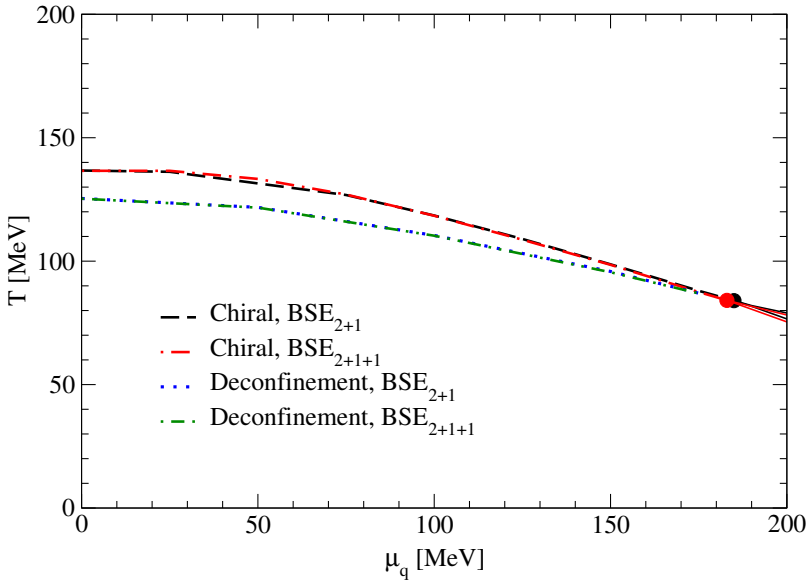

Figure 4.7. Phase diagram for the parameter sets BSE_{2+1} and BSE_{2+1+1} including chiral and deconfinement transitions.

chiral transition temperature. The deconfinement transition was calculated by Jan Lücker via the minimum of the background field potential where the inflection point method was used (see [68] for details). The different ways to fix T_c for the chiral and the deconfinement transition partly explain the somewhat large gap at $\mu = 0$. In [68] the authors used the inflection point for both order parameters, resulting in closer transition temperatures.

In Fig. 4.7 we present the phase diagram for the two sets BSE_{2+1} and BSE_{2+1+1}, showing some important results:

- At $\mu = 0$ also the deconfinement transitions coincide for both sets
- For $\mu > 0$ in the crossover regime the transition lines continue to be on top of each other
- Both sets produce a CEP which, within our numerical resolution, also coincides.

Additionally we observes that both crossover lines, for the chiral and the deconfinement transition, end in a CEP and we find spinodal lines indicating the region of a first order phase transition for $\mu > \mu_c$. With the results shown in Fig. 4.7 we conclude, that the dynamical charm quark, as we take it into account in the sets with fixed vacuum scales, has no influence on the phase structure. Therefore the prediction for the $N_f = 2 + 1 + 1$ version of the phase diagram in our truncation remains the same as for the $N_f = 2 + 1$ case from Ch. 3. In Table 4.3 we summarize the results for the critical endpoint found in our truncation with the parameter sets

Set	μ_c [MeV]	T_c [MeV]
BSE_2	195	80
BSE_{2+1}	185	84
BSE_{2+1+1}	183	84

Table 4.3. Results for the critical endpoint of the BSE fixed parameter sets.

BSE_{N_f}. The incorporation of the strange quark has a small yet non-negligible effect on the position of the CEP, while the inclusion of the charm quark almost has not impact at all. In any case the impact is well below the systematic error of 20 MeV as discussed in the last section. We find that the crossover transition line for the two-flavour case (not shown in Fig. 4.7) also lies on top of the results for $N_f = 2+1$ and $N_f = 2+1+1$. Only the position of the CEP is shifted along an (imagined) extension of the crossover transition line. These results show an important implication of our truncation: once the vacuum physics is fixed, the transition line is set and the exact position of the CEP only depends on the explicit number of quark flavours.

Finally we turn to the curvature of the chiral transition line for the parameter sets BSE_{N_f}. It has a value of

$$\kappa_{BSE} = 0.252 \,, \tag{4.3}$$

where we fitted Eq. (2.31) for $\mu_q \in \{25, 50, 75, 100\}$ MeV, which is the range for the given curve with $\mu_q/T < 1$. If we compare this result to the curvature given in Eq. (3.27) of set LAT_{2+1}, they do not differ by much. However, a comparison with results from lattice QCD in the range $\kappa_{\mathrm{LAT}} = 0.059 \ldots 0.180$ [146–151] proves that the curvature is still slightly larger.

Summary

In the current chapter an investigation about the impact of a dynamical charm quark on the properties of the coupled system of quarks and gluons in the vacuum as well as at finite temperature and chemical potential was presented. We use a bound state calculation of (pseudoscalar) meson observables to fix their properties in the vacuum by adjusting the infrared strength of the quark-gluon vertex. This enables us to have a common scale for calculations with and without the charm quark. We find that while the charm quark influences the gluon propagator on a 10 percent level, neither the regularised light quark condensate at $\mu = 0$ nor the phase diagram changes upon its inclusion. Therefore we continue to view the results of the $N_f = 2+1$ calculation from Ch. 3 as our prediction for the QCD phase diagram, also if a dynamical charm quark is added. Additionally we reported on the thermal mass of the gluon, finding

a behaviour partly in line with predictions from HTL. It appears proportional to the number of dynamical quark flavours, but does not reproduce the correct limit for the quenched case. Results for the quark mass functions for systems with two degenerate light quarks, an additional strange quark and also a dynamical charm quark show expected behaviour, where neither the strange nor the charm quark influences the lighter quarks on a relevant level.

5. Hadronic contributions and their effect on the phase structure of QCD

The secret of my influence has always been that it remained secret.

(Salvador Dali)

In the current chapter we extend the truncation from Ch. 3 to investigate the potential influence of hadronic degrees of freedom on the phase diagram of QCD. The investigation is to be understood as an exploratory study for $N_f = 2$, where we aim to quantify potential systematic errors due to the neglect of baryons, which have possibly an impact for large values of the quark chemical potential. There are only very few investigations of the back reaction from baryons onto the chiral properties of quark matter in the QCD phase diagram. In the FRG approach the case of two-colour QCD (QC_2D) was studied in a quark-meson diquark (QMD) model in [162] and in a Polyakov-loop extended QMD ($PQMD$) model in [41,42]. In QC_2D diquarks are colour neutral objects and constitute the $N_c = 2$ analogous to baryons. In [41,42] they find not only a difference in the position of a putative critical endpoint but also that its very existence vanishes upon the inclusion of diquarks.

To include baryons as degrees of freedom at finite temperature and finite chemical potential, it is necessary to have knowledge about their properties such as mass and wave functions. Those will be in interplay with changes of the quark sector (e.g. the quark condensate) across phase boundaries, for example the one of the liquid-gas transition [163]. There are a few investigations about those properties, e.g. in a lattice calculation [164], in a functional approach [165], in a Nambu-Jona-Lasinio model [166] and recently in a chiral soliton model [167] but to my knowledge no direct calculation back coupled to the fundamental degrees of freedom is available. There are investigations of the back coupling of (composite) pions, e.g. in the vacuum [168–172] and as external degrees of freedom in the medium [40,46,67,173,174]. The work presented in this chapter was partly published in [81].

The chapter is organized in the following way: in the first section we elaborate on the extension of our existing truncation scheme, where we introduce the ansatz

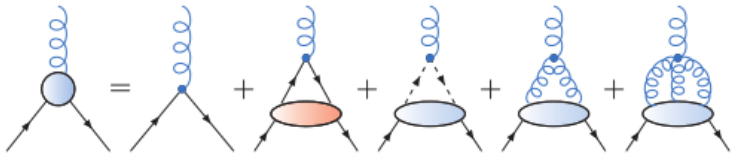

Figure 5.1. Diagrammatic representation of the full and untruncated DSE for the quark-gluon vertex [125]. All internal propagators are dressed, the top vertex is bare (figure taken from [81]).

to incorporate baryonic degrees of freedom. In the second section we present and discuss investigations and results in the vacuum and at finite temperature but zero chemical potential before we get to the details of the effects from baryons onto the phase diagram.

5.1. Extension of the standard truncation with baryons

In Ch. 3 we introduced a scheme to render the infinite tower of coupled integral equations finite. This standard truncation uses input for the quenched gluon propagator from lattice QCD, which is unquenched by solely adding the corresponding quark-loops. There is a second unknown ingredient to the truncated system: the quark-gluon vertex. This vertex is approximated by the first part of the so-called Ball-Chiu vertex [128], which was designed along the Ward–Takahashi identity, multiplied by an infrared enhanced function with appropriate UV behaviour, containing the infrared strength d_1 as a parameter. The parameter d_1 is fixed to reproduce the pseudo-critical temperature of the regularised condensate from lattice QCD and can be understood to absorb possible interactions in an effective way. In order to introduce baryonic effects we consider the DSE for the quark-gluon vertex itself, presented in one possible way in Fig. 5.1. The given diagrammatic representation corresponds to its full and untruncated version. Apart from the bare contribution, there are three one-loop and one two-loop diagram, for which all propagators, the quark (solid), gluon (curly) and ghost (dashed), are dressed with the vertices at the top being bare. The included four- and five-point functions are 1PI with respect to the external legs (in the t-channel). For our purpose it is useful to consider a resonance expansion of the included four- and five-point functions. Since we want to investigate the influence of baryons, we focus on the first non-trivial diagram (the so-called Abelian diagram). This diagram can be approximated in a resonance expansion in terms of Bethe-Salpeter or Faddeev-type vertices as well as propagators for mesons and baryons, which is given in Fig. 5.2. In detail the contributions in Fig. 5.2 are given as follows:

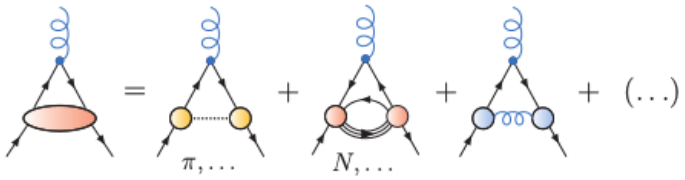

Figure 5.2. Resonance expansion of the first non-trivial diagram from Fig. 5.1 including a four-point function. The first contribution represents meson-exchanges, while the second includes a baryon-exchange diagram and the third a gluon exchange (figure taken from [81]).

- The first diagram collects possible off-shell meson exchange processes. The exchanged mesons are no degrees of freedom but composite particles of a quark-antiquark pair, interacting via the corresponding Bethe-Salpeter amplitudes (yellow vertices).
- In the second class of resonance diagrams we first encounter baryonic contributions. In this two-loop diagram, we have a composite baryon and a quark interacting via a Faddeev-type vertex.
- The third diagram represents a contribution due to a dressed one-gluon exchange where the quark-gluon vertex enters again.

The baryon-exchange diagram has been derived already in [168] on the level of the quark-gluon vertex DSE within the quark-diquark approximation for the baryon. We continue the investigation and introduce the baryonic contribution to the quark-gluon vertex into the quark DSE. As mentioned above, the effects of mesons (e.g. pions) have been studied in the vacuum [168–172], and require the solution of a coupled system of equations, DSE and BSE. We are interested in effects at finite temperature and chemical potential and focus on the baryonic contributions due to their potentially large impact at high quark chemical potential. Since little is known about the in-medium properties of baryons we apply an exploratory ansatz and use available vacuum properties. The baryon and meson off-shell propagators will be approximated by the corresponding free ones, where the masses and the normalisation have a potential dependence on temperature and chemical potential.

The strategy now is to make the baryonic contribution to the quark-gluon vertex DSE explicit in the quark DSE and understand all residual contributions to be absorbed in the vertex ansatz. In Fig. 5.3a we display the diagrammatic representation of the corresponding quark DSE, where we explicitly separated non-baryonic (NB) and baryonic parts. Note, the latter enter in form of a three-loop diagram. This is already a computationally demanding task to solve in the vacuum but would be even harder at finite temperature and chemical potential. In an exploratory study, solving a precise three-loop diagram but using other quantities only on an approximate level

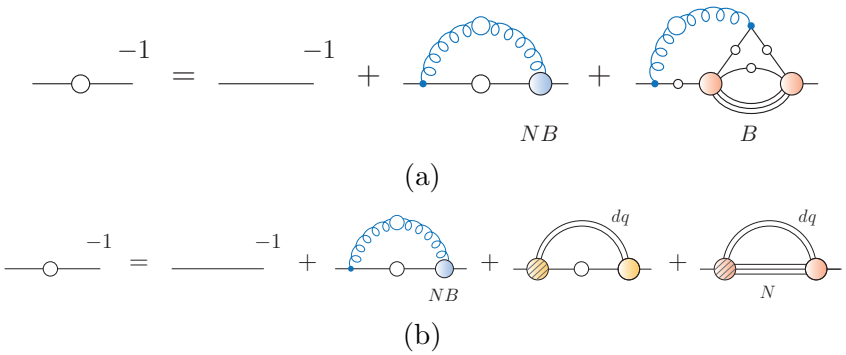

Figure 5.3. Diagrammatic representation of the quark DSE including baryonic contributions in (a) the full version and (b) within the quark-diquark approximation for the nucleon. Double lines represent diquarks, triple lines baryons, full circles corresponding BSAs and hatched circles effective BSAs (figures taken from [81]).

is unnecessary. Hence we introduce, as in [168], a separable quark-diquark ansatz for each three-body Faddeev amplitude converting the Faddeev vertices to quark-diquark Bethe-Salpeter amplitudes. This is a commonly used approximation for bound state calculations and in good agreement with results from a three-quark Faddeev calculation for the nucleon [175]. In Fig. 5.4 we present a diagrammatic derivation of possible contributions. While in the first line we account for the fact, that the gluon may couple to both quark lines, in the second the quark-diquark ansatz was used and the diagrams were already grouped by type, one where we find the incoming quark to couple to a diquark amplitude (left) and one where it couples to a quark-diquark amplitude. The open circles on the external legs have to be understood to be connected with a diquark (two lines) or a baryon (three lines) propagator. The hatched amplitudes are introduced to group the different types of diagrams and represent effective ones. The derivation was worked out by Gernot Eichmann and is taken from [81]. Introducing the resulting baryonic contribution within the quark-diquark approximation into the quark DSE leads to the form displayed in Fig. 5.3b, where two one-loop contributions replace the three-loop contribution. We find one quark-diquark and a diquark-baryon loop additional to the effective non-baryonic part. Note, a calculation of the three-loop diagram in Fig. 5.3a would involve a corresponding three-body Faddeev equation, which has been solved in the vacuum [172, 175–179].

To complete the ansatz for the baryonic contributions we yet have to specify the diquark and baryon propagators as well as the regular and effective (hatched) diquark and quark-diquark amplitudes. In Fig. 2.5 the diagrammatic representation of the Bethe-Salpeter equation for the baryon in the quark-diquark approximation was introduced. The interaction is interpreted as a quark exchange between the diquark and the third quark. The contained amplitude for the diquark has to be obtained

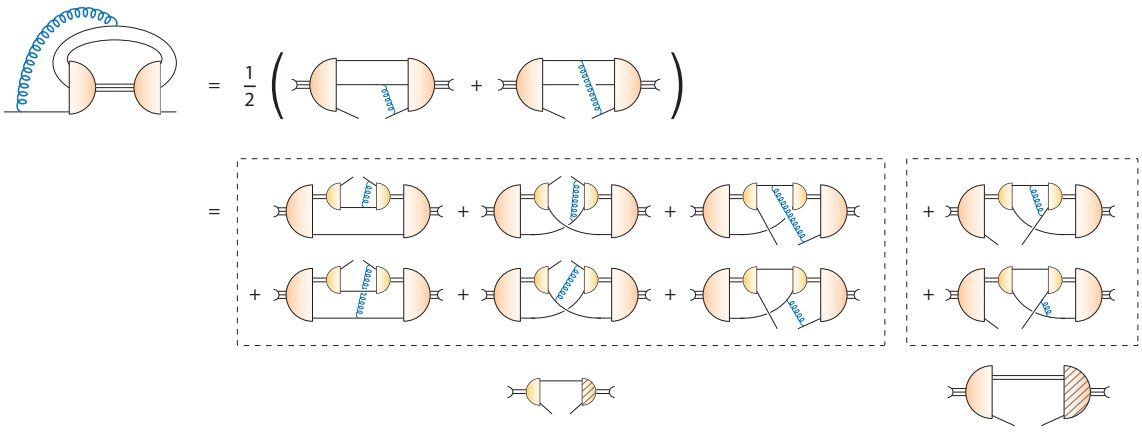

Figure 5.4. Diagrammatic derivation of changing from three-body Faddeev over to Bethe-Salpeter-type vertices for the baryonic contribution (figure taken from [81]).

from the solution of a separate BSE.

One possible approach to solve this BSE is to use simple models for the quark and diquark propagators and ansätze for the diquark amplitudes to obtain information about baryonic properties within the quark-diquark picture [180–183].

One can as well utilize the quark Dyson-Schwinger equation and an ansatz for the underlying quark-gluon vertex to obtain the quark propagator for complex momenta as well as the diquark amplitude and the diquark propagator from the corresponding BSE and scattering equation. The baryon is determined then without the introduction of any other parameters. Corresponding work has been published in [184–187] where a commonly used interaction kernel in the rainbow-ladder approximation was applied. The studies showed that a vacuum description of ground state properties of the nucleon as well as the Δ baryon can be achieved on a satisfying level by only using the scalar and axial-vector diquark states. If one is only interested in the main effects, even the scalar diquarks by themself give a satisfactory answer, since the axial-vector diquark contributions are below 20 percent of the impact from the scalar diquarks.

All the aforementioned investigations are done in the vacuum. Explicit finite temperature and chemical potential dependence of the amplitudes and propagators are not investigated. For our approach we assume the validity of the vacuum properties only modified by the splitting of the four momentum and consider only the scalar diquark correlations. Therefore the diquark as well as the nucleon can be represented by their leading tensor structure. In this case, the Bethe-Salpeter amplitudes of the

diquark (DQ) and the nucleon (N) are given by

$$\Gamma_{DQ}(q,P) = f_{DQ}(q^2)\,\gamma^5 C \otimes \frac{\epsilon_{ABE}}{\sqrt{2}} \otimes s^0_{ab}\,, \tag{5.1}$$

$$\Gamma_{N}(q,P) = f_{N}(q^2)\,\Lambda_+(P) \otimes \frac{\delta_{AB}}{\sqrt{3}} \otimes t^0_{ae}\,. \tag{5.2}$$

Here, q is the relative and P the total momentum of the bound states, $C = \gamma_4\gamma_2$ is the charge-conjugation matrix, Λ_+ a projector onto positive-energy states and we use normalised wave functions. The colour wave functions are defined with capital subscripts and the flavour wave functions with small subscripts; $s^0 = \frac{1}{\sqrt{2}}(ud^\dagger - du^\dagger) = \frac{1}{\sqrt{2}} i\sigma_2$ with Pauli matrices σ_i and $t^0 = (uu^\dagger + dd^\dagger) = \mathbb{1}$. The solutions for the diquark and nucleon amplitudes in the rainbow-ladder framework of [185–187] can be parametrized by

$$f_{DQ}(q^2) = \mathcal{N}_{DQ}\left(e^{-\alpha_{DQ}\cdot x} + \frac{\beta_{DQ}}{1+x}\right),$$
$$f_{N}(q^2) = \mathcal{N}_{N}\left(e^{-\alpha_{N}\cdot x} + \frac{\beta_{N}}{(1+x)^3}\right)$$

with $x = q^2/\Lambda^2$ and the scale $\Lambda = 0.7$ GeV. Normalising the corresponding full Bethe-Salpeter amplitudes gives the normalisation factors $\mathcal{N}_{DQ} = 15.6$ and $\mathcal{N}_N = 28.4$. These complete the parametrization together with the parameters $\alpha_{DQ} = 0.85$ and $\alpha_N = 1.0$ for the exponentials and $\beta_{DQ} = 0.02$ and $\beta_N = 0.03$ for the UV behaviour.

Thus far we only defined the regular amplitude but still need to quantify the effective one. Following [81], we argue that one can take the effective amplitude to be bare, meaning to use Eqs. (5.1) and (5.2) with $f_{DQ}(q^2) = f_N(q^2) = 1$. This approximation is similar to the one for pion-loop contributions in the quark DSE in [168,171,172]. Taking the effective amplitude to be bare can be motivated from its contribution to the quark condensate and therefore by estimating the overall strength of the baryonic diagrams. This can be achieved by connecting the quark lines with the scalar $q\bar{q}$ vertex (calculated from its inhomogeneous BSE). The obtained vacuum bubble $\mathcal{C}$ is proportional to the integrated (off-shell) scalar form factor of the nucleon given by

$$\mathcal{C} = \frac{2m_N}{3}\int\frac{d^4P}{(2\pi)^4}\,\frac{g_S(P^2, Q^2=0)}{P^2 + m_N^2}\,. \tag{5.3}$$

To calculate the on-shell value of the scalar form factor one uses the Feynman-Hellmann theorem [188, 189]

$$\sigma_N = m_q\, g_S(-m_N^2, 0) = m_q\,\frac{dm_N}{dm_q} \approx m_\pi^2\,\frac{dm_N}{dm_\pi^2}\,, \tag{5.4}$$

with the experimental value $\sigma_N = 45$ MeV. Together with an integral cutoff at $m_N = 0.94$ GeV, the order of magnitude of the calculated $\mathcal{C}$ is comparable to the

value obtained by numerically tracing the sum of the diquark and baryon diagrams in the quark DSE with a scalar vertex, but only with a bare amplitude in each case. The same approach with both vertices dressed overestimates the strength by far, due to the normalisation factors.

Before we get to the explicit baryonic contributions to the quark and gluon DSEs, we want to elaborate on the diquark and baryon propagators. Since we have no consistently calculated information on the behaviour of the masses of the scalar diquark or the baryon for finite temperature and chemical potential, we resort to the vacuum results and use the free propagators

$$D_{DQ}(q \pm p) = \frac{1}{(\boldsymbol{q} \pm \boldsymbol{p})^2 + (\omega_q \pm \omega_p + 2i\mu_q)^2 + m_{DQ}^2}\,,$$
$$D_N(q) = \frac{-i\boldsymbol{q}\boldsymbol{\gamma} - i(\omega_q + 3i\mu_q)\gamma_4 + m_N}{\boldsymbol{q}^2 + (\omega_q + 3i\mu_q)^2 + m_N^2}\,,$$

with $m_{DQ} = 0.81$ GeV and $m_N = 0.938$ GeV.

As we will see later, the hadronic effects on the quark propagator will be on a ten percent level. Since the hadronic diagrams are suppressed by a factor $1/N_c^2$, this is the order of magnitude we expect from the diagrammatic form of the quark-gluon vertex DSE. In the Yang-Mills sector of QCD the impact of quark corrections is suppressed by $1/N_c$. Therefore, hadronic contributions to the quark-loop diagram in the gluon DSE will be suppressed by $1/N_c^3$. This justifies to neglect the explicit hadronic contributions to the gluonic sector and we will use the same truncation for the gluon DSE as in Ch. 3 and previous studies [65, 66, 80].

At first sight the diquark-baryon loop appears to be independent of the quark and therefore independent of the chiral dynamics of the system. In our approach to the $N_f = 2$ coupled system we take into account only the lowest $\mathrm{J}^P = 1/2^+$ state in the baryon multiplet, namely the nucleon. Other baryons B would contribute as well, but would be suppressed by $\left(\frac{m_N}{m_B}\right)^2$. There is one exception we have to consider: the chiral partner of the nucleon. When chiral symmetry is (continuously) restored, the masses of chiral partners constantly align and become degenerate upon full restoration of chiral symmetry. We take this effect qualitatively into account by introducing the (complex) constant

$$M_\chi = \frac{M(T, \mu_q)|_{\boldsymbol{p}=0,\,\omega_0}}{M(0,0)|_{p=0}}\,, \tag{5.5}$$

which is the ratio of the renormalisation point independent quark mass function $M = B/A$ in the medium to the vacuum for zero spatial momentum and the 0^{th} Matsubara frequency. Without this effect, we would have problems concerning in the solution of the DSE towards the approximate chirally restored phase, since the diquark-baryon loop would enter as a momentum dependent shift which is independent of the quark propagator in the coupled system of integral equations. Indeed,

since the baryonic effects act chirally restoring, from a certain temperature on we find only a solution for the quark propagator with negative mass function B/A if the chiral partners are not considered. More details one this are given in App. B.2.

When performing the Dirac traces one finds, that the contribution from the chiral partner would cancel the contribution of the nucleon in the scalar dressing function B, while it adds to it in the vector and Matsubara dressing functions A and C. Appropriate prefactors have been added to the self-energy contribution of the diquark-baryon loop and are explicitly shown in the kernels Eq. (5.7). Note, that the diquark-loop has no such factor since it appears solely due to the introduction of the quark-diquark approximation of the baryon. In [165] the authors investigated the dependence of baryonic properties on the temperature (at $\mu = 0$) and found that amplitudes are almost independent of T, while the mass rapidly grows close to the phase transition. A similar effect is dynamically taken into account by the introduction of M_χ. However, a (close to) exponentially growing mass, as in [165], suppresses the A and C part of the self-energy equivalently to the B part, while the effect due to M_χ enhances the A and C contributions.

With all components specified, we can setup the equations for the quark DSE. We have to sum up all contributions shown in Fig. 5.3b for each dressing function, obtained by appropriately tracing with a projector. If we denote the dressing functions with $\mathcal{D}(p) \in \{A(p), B(p), C(p)\}$, we find the general form

$$\mathcal{D}(p) = Z_2\, \lambda_\mathcal{D} + \Sigma_\mathcal{D}^{NB} + \Sigma_\mathcal{D}^{DQ} + \Sigma_\mathcal{D}^{N}\,, \tag{5.6}$$

where we abbreviated the gluon and non-baryonic (NB), the diquark and the baryon-loop contributions to the quark self-energy by $\Sigma_\mathcal{D}^{NB}$, $\Sigma_\mathcal{D}^{DQ}$ and $\Sigma_\mathcal{D}^{N}$ respectively. $\lambda_B = m_0$ is the bare current-quark mass, $\lambda_A = \lambda_C = 1$, and Z_2 is the quark wave-function renormalisation constant. The gluon-dressing loop $\Sigma_\mathcal{D}^{NB}$ contains the unquenched, temperature- and chemical-potential dependent gluon propagator together with a model for the quark-gluon vertex containing all non-baryonic contributions, in the manner of Ch. 3. For the self-energy contributions from the diquark and baryon loop, one obtains after tracing over colour, flavour and the Dirac index with appropriate projections

$$\Sigma_\mathcal{D}^{DQ}(p) = \frac{1}{2}\sum\!\!\!\!\!\!\int_q \frac{f_{DQ}(\frac{q-p}{2})\, D_{DQ}(q+p)}{\boldsymbol{q}^2 A^2(q) + \tilde{\omega}_q^2 C^2(q) + B^2(q)}\, K_\mathcal{D}^{DQ},$$

$$\Sigma_\mathcal{D}^{N}(p) = \frac{1}{3}\sum\!\!\!\!\!\!\int_q \frac{f_{N}(\frac{q}{2}-p)\, D_{DQ}(q-p)}{\boldsymbol{q}^2 + (\omega_q + 3i\mu_q)^2 + m_N^2}\, K_\mathcal{D}^{N}$$

with

$$
\begin{aligned}
K_A^{DQ} &= \frac{\boldsymbol{p}\cdot\boldsymbol{q}}{\boldsymbol{p}^2}\,A(q)\,, \qquad & K_A^{N} &= \frac{\boldsymbol{p}\cdot\boldsymbol{q}}{\boldsymbol{p}^2}\times(2-M_\chi)\,, \\
K_C^{DQ} &= \frac{\tilde{\omega}_q}{\tilde{\omega}_p}\,C(q)\,, & K_C^{N} &= \frac{\omega_q+3i\mu_q}{\tilde{\omega}_p}\times(2-M_\chi)\,, \\
K_B^{DQ} &= -B(q)\,, & K_B^{N} &= -m_N\times M_\chi\,.
\end{aligned}
\tag{5.7}
$$

Again p, q serve as abbreviations for $p=(\omega_n,\boldsymbol{p})$, $q=(\omega_m,\boldsymbol{q})$ at finite temperature and chemical potential with the previously introduced fermionic and bosonic Matsubara frequencies. We represent the Matsubara sum as well as the integration over the loop three-momentum $\boldsymbol{q}$ by $\sum\!\!\!\!\!\!\int_q = T\sum_{n_q}\int\frac{d^3q}{(2\pi)^3}$. Note, the diquark carries two times and the baryon three times the quark chemical potential μ due to their number of contained quarks. The self-energy contributions $\Sigma_{\mathcal{D}}^{NB}$ are given in Eq. (B.1) in the appendix. The self-energy contributions in the vacuum are analogous to those given above and the constant M_χ is defined in Eq. (5.5).

Before we investigate the results of baryonic contributions we want to recapitulate the general idea to include them and the applied approximations:

- **Quark-gluon vertex DSE:** We introduce possible baryonic contribution in the quark-gluon vertex by investigating its DSE for $N_f=2$.
- **Abelian diagram and its resonance expansion:** Within the quark-gluon vertex DSE we identify the Abelian diagram including a four-point function with four quark legs to contain baryonic contributions. This becomes obvious after doing a resonance expansion.
- **Quark-diquark picture of the baryon:** For the quark-quark-baryon vertex we introduce the quark-diquark picture with scalar diquarks only and obtain a quark-diquark and a diquark-baryon loop contribution in the quark DSE.
- **Gluon DSE:** Due to a suppression by $1/N_c^2$ for the hadronic diagrams to the quark-loop we neglect explicit baryonic effects to the gluon.
- **Amplitudes and masses:** For the off-shell propagators we use the free counterparts with vacuum properties for the baryon and the diquark, extended only by the introduction of Matsubara frequencies and chemical potential. The amplitudes are taken from a calculation done in a rainbow-ladder approximation of the interaction, the Maris-Tandy model.
- **Chiral partner:** For the diquark-baryon loop we take into account the effect of the chiral partner of the nucleon by introducing the medium-to-vacuum ratio of the infrared value of the quark mass function at appropriate points. All other heavier baryons are neglected.

With this scheme we now investigate the influence of baryons in the vacuum and at finite temperature with $\mu = 0$, before we elaborate on the phase diagram. Some more details of the numerical implementation such as renormalisation and strategy to find different solutions are relegated to App. B.2

5.2. Results in the vacuum and at finite T with $\mu = 0$

Before considering results for baryonic contributions in the medium it is insightful to first study their influence in the vacuum. As discussed in [168] we expect chirally restoring effects, i.e reduction of the renormalisation point independent mass function in the infrared region and therefore less dynamical mass generation. In Fig. 5.5 we display the light quark mass function for a unquenched $N_f = 2$ calculation in the truncation described in the previous section. We used a light quark mass of $m(\zeta = 80 \text{ GeV}) = 0.8$ MeV and an infrared strength of the vertex $d_1 = 8.05$ GeV^2, adapted from LAT$_{2+1}$ (which corresponds to a two plus one flavour calculation reproducing the regularised condensate from lattice QCD). We observe a chirally restoring effect for each loop contribution separately, the quark-diquark loop and the diquark-baryon loop, and approximately find the sum of the effects upon inclusion of both loops at the same time[1]. The total impact on the infrared value of the mass function for both loops is approximately 15 percent while its negligible for larger momenta.

Later we will discuss the setup including baryonic degrees of freedom but with an enhanced infrared strength for the non-baryonic part of the vertex. The result for the mass function in the vacuum with the parameter d_1 increased by 11 percent would be on top of the black solid line (gluon dressing loop only) and is not show in Fig. 5.5. This can be interpreted as a possible absorption of the baryonic contributions into the effective vertex in the vacuum. In Fig. 5.6 we show the vacuum self energy contributions from the baryon and the diquark loop after convergence of a system where both structures have been taken into account. The displayed quantities confirm the observation for the mass function, that the diquark-baryon loop has a bigger influence than the quark-diquark loop. The scale for the baryonic contributions in our approach to both, A and B dressing functions, is of order 10^{-2}, while the contributions from the gluon dressing loop are of order 10^{-1}. Both loops decrease the B function and increase the A function, two effects decreasing the mass function. While for the diquark loop Σ_A^{DQ} is very small compared to Σ_B^{DQ}, for the baryon loop Σ_A^N is of the same order as Σ_B^N. Note, unquenching effect of this size, introduced only by the adaptation of baryonic degrees of freedom, seems rather dramatic. An estimate of an overall unquenching effect of approximately 20 percent was found on the lattice [190]. However, for an exploratory study an overestimation seems to serve the goal of gauging the maximal influence of the effect much better.

Now we focus on the case of finite temperature and remind of the definition of the

[1]Due the coupled nature of the system this would not necessarily have to be the case.

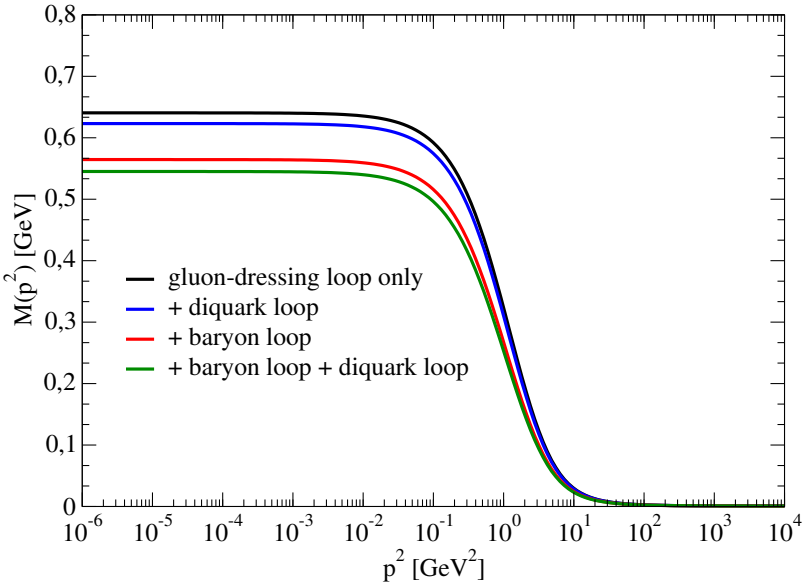

Figure 5.5. Impact of baryonic contributions on the quark mass function in vacuum for $N_f = 2$. Shown are the original setup, the contribution of each, the quark-diquark loop and the diquark-baryon loop separately and the combined effect.

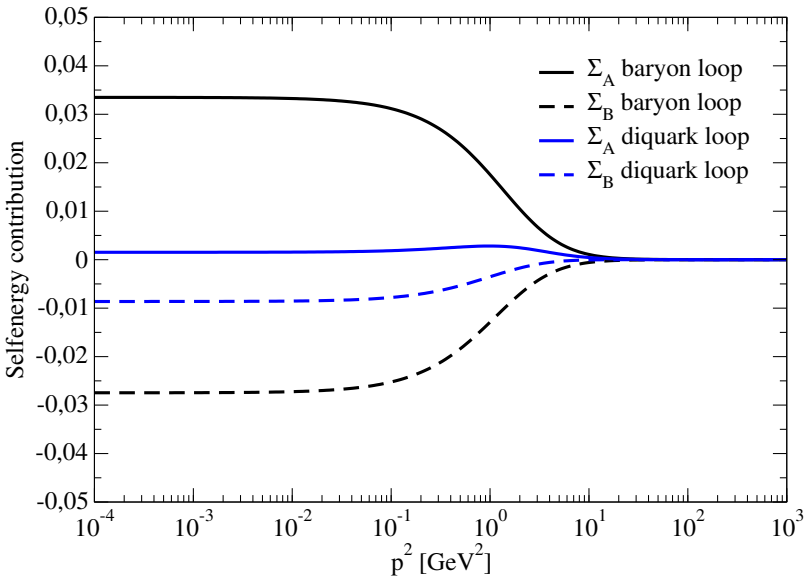

Figure 5.6. Different self-energy contributions due to explicit baryonic degrees of freedom in vacuum. Shown are the contributions from quark-diquark and diquark-baryon loop separately for the A and B dressing functions.

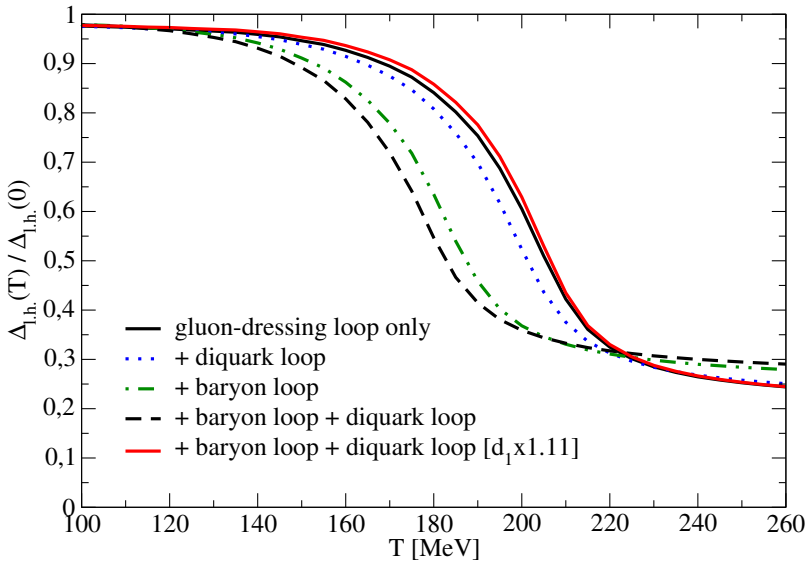

Figure 5.7. Comparison of the two flavour regularised condensate with and without baryonic contributions at $\mu = 0$. The original setup is compared to the effects of the quark-diquark loop and the diquark-baryon loop separately, their combined effect and a calculation with an enhanced infrared strength in the non-baryonic contribution.

regularised condensate given in Eq. (2.28). For the heavy test quark mass we choose $m_h(\zeta = 80\,\text{GeV}) = 100$ MeV and checked that changing this mass to 50 MeV and 200 MeV does not influence the outcome. To obtain the corresponding condensate $\langle\bar{\psi}\psi\rangle_h$ for the test quark in the $N_f = 2$ theory we would need to solve the complete coupled system of DSEs a second time for each temperature and chemical potential. However, the purpose of $\langle\bar{\psi}\psi\rangle_h$ is regularisation only and it turns out to be sufficient to evaluate the quark DSE with modified quark mass $m_l \to m_h$ in the bare quark propagator S_0^{-1}, but keeping the gluon and the quark-gluon vertex (including baryonic loops) from the light quark calculation. The condensate obtained through this procedure is given in Fig. 5.7. The $N_f = 2$ calculation in the manner of LAT_{2+1} (black solid line) gives a crossover temperature, defined via the maximum of the chiral susceptibility, of $T_c^\chi \approx 211$ MeV. The introduction of the baryon loops shows the same tendency as observed in vacuum (compare Fig. 5.5):

- Both loop contributions are chirally restoring and therefore decrease T_c^χ.
- The contribution from the baryon loop is bigger than the one from the diquark loop, the combined effect is the sum of the individual effects.
- The change in T_c^χ is about 15 percent upon inclusion of both loops.
- A rescaling of the infrared strength of the quark-gluon vertex by 11 percent

($d_1 = 8.05\ \mathrm{GeV}^2 \to d_1 = 8.94\ \mathrm{GeV}^2$) recovers to very good accuracy the original shape of the regularised condensate.

In particular the last point is important for our general strategy and the applicability of the results obtained for $N_f = 2$ to $N_f = 2 + 1$. In [80] the regularised condensate of the $N_f = 2 + 1$ theory, calculated on the lattice, has been reproduced point-wise in a setup using the gluon-dressing loop only and adjusting d_1, without making the baryonic degrees of freedom explicit. For $N_f = 2$ we observe that one can reproduce a similar functional dependence of $\Delta_{l,h}(T)$ using explicit baryonic degrees of freedom and a rescaled version of the quark-gluon interaction. This leads to the conclusion that the same behaviour may hold for the $N_f = 2 + 1$ theory.

Therefore we use the $N_f = 2$ theory with a rescaled infrared vertex strength d_1 as a template to study the baryonic effects at finite μ_q. While at zero chemical potential all effects can be absorbed into d_1, this is not *a priori* the case for finite chemical potential due to the potentially strong dependence of the diquark and baryon loops on μ_q. In the next section we will explore the consequences of these additional contributions for the location of the critical endpoint.

5.3. The phase diagram including baryonic degrees of freedom

As already seen in the previous Ch. 3 and Ch. 4, calculating the phase diagram and therefore introducing finite quark chemical potential is straightforward on a technical level. While the parameter μ only explicitly appears in the quark propagator, it also affects the gluon via the back coupling of the quark-loop and in particular the thermal mass. Baryonic degrees of freedom potentially modify the finite chemical potential dependence of the quark strongly. Hence an investigation of their effects onto the phase diagram is interesting.

Before we start considering the phase diagram itself it is insightful to first consider the self-energy contribution of the diquark-baryon loop, which is, as we have observed in the vacuum, the dominant contribution. In Fig. 5.8 we show the ratio of the infrared values from medium (0^{th} Matsubara frequency) to vacuum self-energy contributions for the three different dressing functions. Note that the corresponding vacuum value for the C function is as well the one of the A function. In Fig. 5.8a to Fig. 5.8c the behaviour of the unmodified contributions ($M_\chi = 1$) throughout the $T - \mu_q$ plane is shown and we observe a reduction with raising temperature independently of the value of the chemical potential. The C function reacts strongest to a change of the chemical potential which feeds back to the A contribution, while the contribution to the B part is almost constant for the relevant temperatures of $T > 100$ MeV. In Fig. 5.8d we compare the medium-to-vacuum ratio of the infrared values at $\mu_q = 0$ for the unmodified case ($M_\chi = 1$) and the case with M_χ as given

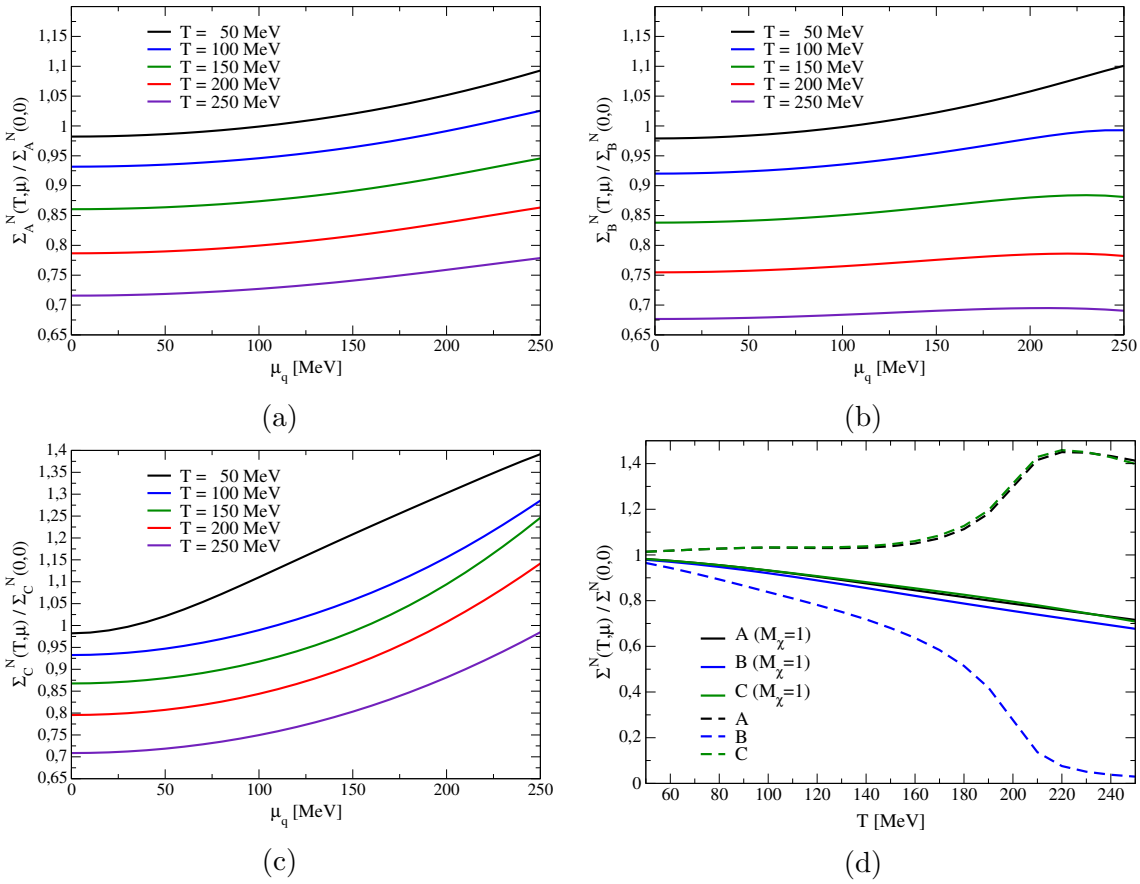

Figure 5.8. In (a) to (c) we show the medium-to-vacuum ratio of the self-energy contributions of the diquark-baryon loop to the A, B and C dressing functions depending on μ_q for various temperatures without the constant M_χ. In (d) we display a comparison at $\mu_q = 0$ for the medium-to-vacuum ratio of the infrared values for ($M_\chi = 1$, solid lines) and the case with M_χ as given in Eq. (5.5) (dashed lines) depending on temperature.

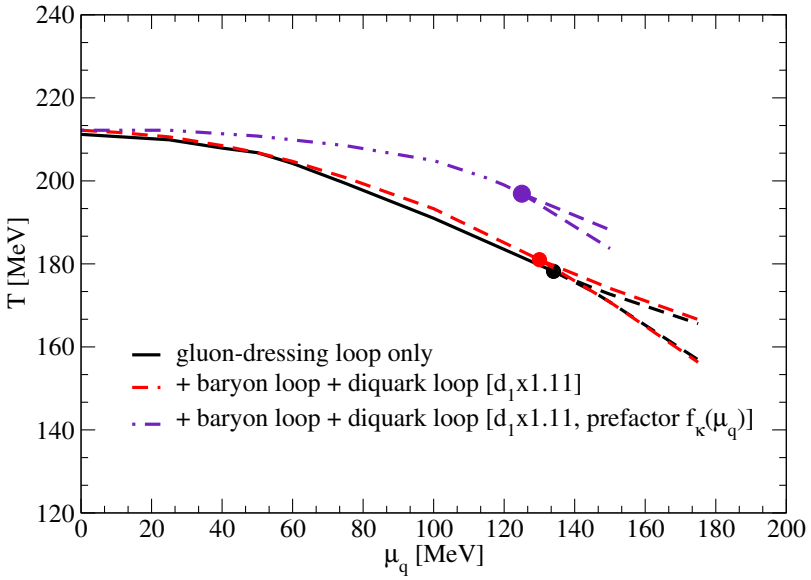

Figure 5.9. QCD phase diagram including baryonic contributions for $N_f = 2$ (red dashed line) compared to the phase diagram without explicit baryonic contributions (black lines) and a calculation adjusted to match a prediction for the curvature from lattice QCD [150](magenta dash-dotted line).

in Eq. (5.5) for an $N_f = 2$ calculation including baryonic loop contributions as well as the rescaled vertex strength. The effect of M_χ becomes apparent and is mirrored in the shape corresponding to the behaviour of the quark condensate, which is itself related to the infrared value of the mass function. With $M_\chi = 1$ we observe contributions from the diquark-baryon loop which are within ± 30 percent of the vacuum values.

Finally we turn to the consideration of the results for the phase diagram, which are displayed in Fig. 5.9, where we show the $T - \mu_q$ plane and three different setups. In the crossover regime we defined the pseudo-critical temperature via the maximum of the chiral susceptibility Eq. (2.30). The calculation without any explicit baryonic contributions, e.g. the gluon dressing loop only, is represented by the black solid curve and mirrors the results shown in Fig. 5.7 at $\mu = 0$. We observe, that in a region for small values of the chemical potential the transition is a crossover which ends in a 2^{nd} order critical endpoint, as indicated by the filled circle at the critical value $\mu_q = \mu_q^c$. The two dashed lines emerging from the CEP indicate the first order spinodal region for $\mu_q > \mu_q^c$. In case of the setup without explicit baryonic contributions we find a critical endpoint at

$$\text{CEP}_{\text{excl.B}} : \ (T^c, \mu_q^c) = (177, 134)\,\text{MeV} \ , \tag{5.8}$$

for the two-flavour theory $N_f = 2$. From a comparison with the red dashed curve, which includes explicit baryonic effects with the rescaled vertex strength d_1, we conclude:

- A critical endpoint still exists
- The chiral phase transition lines are almost on top of each other
- The critical endpoint is shifted by less than 5 MeV to smaller chemical potential along the transition line

The first point is particularly important in light of [41, 42], where the existence of a CEP in $\mathrm{QC_2D}$ vanished upon inclusion of effects equivalent to baryonic contributions. The second observation is not surprising for small chemical potential, since one expects little influence of baryonic degrees of freedom in this part. For the very same reason we compare the calculation including baryonic effects and a rescaled vertex strength against the setup with no explicit baryons. In this case, due to the adjustment process of the rescaled vertex, one has to find identical behaviour for $\mu = 0$. This continues to be the case to until the very end of the crossover transition line, resulting in a CEP which is only shifted by a few MeV and given by

$$\mathrm{CEP}_{\mathrm{incl.B}}: \ (T^c, \mu_q^c) = (181, 130)\,\mathrm{MeV}\ ,$$

which makes the little influence of the baryonic degrees of freedom obvious by comparing it to Eq. (5.8). It appears as the effects from baryonic degrees of freedom can be absorbed into the original vertex ansatz by a reparametrisation with a difference well within the systematic errors of the model.

This could be the case due to the approximations we have done, in particular the temperature and chemical potential independent mass as well as the modelled modification of their (vacuum) amplitudes as introduced with the factor M_χ. To gain some further insight in the dependence of the results we investigate three modifications of what was done so far:

- Modification of the wave function(s)
- Change of the baryon and diquark masses close to the CEP
- Application of different input for the system of quarks and gluons

These studies will be presented in the remaining part of the current chapter with particular emphasis on the effects close to the critical endpoint.

Modify the wave function of the baryonic contributions

Due to the lack of explicit knowledge we estimate changes of the wave functions with chemical potential by multiplying both hadronic loops with a function

$$f_\kappa(\mu_q) = 1 - \frac{\mu_q/\Lambda_\kappa}{1 + a_\kappa(\mu_q/\Lambda_\kappa) + b_\kappa(\mu_q/\Lambda_\kappa)^2}\,, \tag{5.9}$$

which solely depends on chemical potential and the three parameters a_κ, b_κ and Λ_κ. To fix these parameters we use recent evaluations of the curvature κ of the chiral transition line on the lattice [146–151]. An extrapolation of the transition line can be parametrized in terms the curvature (as discussed in Sec. 2.4.2)

$$\frac{T(\mu_q)}{T(0)} = 1 - \kappa_q \left(\frac{\mu_q}{T(\mu_q)}\right)^2,$$

which characterizes the lowest order coefficient in a Taylor expansion in the quark chemical potential μ_q. Recent results from lattice QCD for κ_q range between 0.059 and 0.180 [146–151], whereas we find a larger value in our calculations (see Ch. 3 and Ch. 4). For the purpose of our investigation we neglect $1/N_f$ corrections and adopt the $N_f = 2+1$ value $\kappa_q = 0.134$ from [150] for our $N_f = 2$ calculation. The parameters in Eq. (5.9) are determined to reproduce the lattice curvature in a region where the lattice extrapolation is still valid (assumed for $\mu_q \leq 75$ MeV). We proceeded in the following way: for six values of μ we added an additional factor to both, the quark-diquark and the diquark-baryon loop and modified this factor until the predicted transition temperature with the given κ_q was reproduced point-wise for each μ_q. The obtained factors and transition temperatures (as obtained from the maximum of the chiral susceptibility) are given in Table 5.1. Those values were then fitted with the function in Eq. (5.9) and we obtained $\Lambda_\kappa = 0.714$ GeV, $a_\kappa = -10.3$ and $b_\kappa = 36$, resulting in a function f_κ with a minimum at $\mu_q \approx 120$ MeV. For chemical potential exceeding this value we use $f_\kappa(\mu_q) = f_\kappa(\mu_q = 120\,\mathrm{MeV})$ to make the function monotonic. A calculation within this modified setup leads to a different crossover line in the phase diagram given as the dash-dotted indigo curve in Fig. 5.9, with a CEP at

$$\mathrm{CEP}_{f_\kappa}:\ (T^c, \mu_q^c) = (197, 125)\,\mathrm{MeV}\,.$$

As a result of the smaller curvature forced at low chemical potential we find the critical endpoint shifted by about 20 MeV towards larger temperature and 10 MeV towards smaller chemical potential in comparison to the $N_f = 2$ calculation without explicit baryons. The induced change in the ratio of μ_B^c/T^c from 2.3 to 1.9 is not a strong effect but would be quantitatively significant. This small effect is, however, introduced by a modification of the baryon wave function by about 50 percent, due to the function f_κ. If such a large variation is realistic or not requires direct calculation

μ_q [MeV]	$T_c^\kappa(\mu)$ [MeV]	$f_\kappa(\mu_q)$	$T_c^f(\mu)$ [MeV]
0	212.2	1.00	212.2
25	211.8	0.95	211.7
40	211.2	0.90	211.0
50	210.6	0.84	210.6
60	209.9	0.79	209.8
75	208.6	0.67	208.4

Table 5.1. Results for the pseudo-critical temperature $T_c^f(\mu)$ and the corresponding factor $f_\kappa(\mu_q)$ added to the hadronic contributions in our truncation to match a pseudo-critical temperature $T_c^\kappa(\mu)$ as given by the curvature κ_q from lattice QCD.

or at least more sophisticated estimates. In the approach to recover the curvature from lattice QCD we accounted the difference to be solely from baryonic contributions which is by no means clear but yet again gives an upper bound of their influence and shows a proof of principle that they could be (partly) responsible the differences in curvature. We always find the CEP shifting towards larger temperature and smaller chemical potential if $f_\kappa(\mu_q) < 1$ and therefore reducing the amplitude. Obviously the opposite effect is induced if $f_\kappa(\mu_q) > 1$, where the CEP shifts towards smaller temperatures and larger chemical potential. Thus far there is no reason why one or the other behaviour should be favoured, apart from the attempt to get closer to the extrapolated curvature from lattice QCD instead of away from it.

Modify the masses of the nucleon and diquark

We already highlighted the potential influence of the nucleon and diquark masses on the position of the critical endpoint. Investigations of the dependence of these masses are rare and also on an exploratory level [165, 166]. As in the modification above, where we included the function $f_\kappa(\mu_q)$, the truncation with both hadronic loops and a rescaled infrared strength of the quark-gluon vertex is the starting point, which we modify. We assume the masses of the diquark and nucleon to be at 50 percent of their physical value in the vicinity of the CEP. The resulting critical endpoint is found at

$$\mathrm{CEP}_{1/2\times\mathrm{m(DQ,N)}}: \ (T^c, \mu_q^c) = (168, 138)\,\mathrm{MeV}\,,$$

representing a shift of about 10 MeV in temperature and 5 MeV in chemical potential compared to the setup without explicit baryonic degrees of freedom Eq. (5.8).

Decreasing the masses of the diquark and the nucleon seems to shift the CEP in the opposite direction compared to the calculation with the rescaled vertex strength and the inclusion of chiral partners but physical hadron masses. The impact of the reduced masses is $(\Delta T^c, \Delta\mu_q^c) = (13, 8)$ MeV being a change on a $5-10\%$ level. This is a visible yet not significant change, keeping in mind the reduction of the mass by 50%. Note that increasing the masses of the nucleon and the diquark would lead to an even smaller change in the phase structure, since the self-energy contributions in our case are at least depending on their inverse masses.

Modify the setup for the quark sector

In all the investigations above we used a parameter set for the quarks and and the quark-gluon interaction, which stems from neglecting the strange quark in the $N_f = 2 + 1$ calculation with a regularised condensate matching predictions from lattice QCD. The corresponding crossover temperature found is at $T_c \approx 210$ MeV, being in an expected range. However, the corresponding values for the pion and diquark masses as well as for the pion decay constant in the vacuum are

$$M_\pi = 106 \text{ MeV} \ , \ f_\pi = 132 \text{ MeV} \ , \ M_{\text{DQ}} = 1079 \text{ MeV} \ ,$$

indicating we are not reproducing the vacuum limit for those quantities. In Ch. 4 we introduced the parameter set BSE_2, which is designed to reproduce the correct pion attributes for $T, \mu = 0$. For completeness we also used this parameter set, which has a crossover transition temperature at $\mu = 0$ of $T_\chi^c = 136$ MeV to investigate the effect of baryonic contributions. We proceeded as above and rescaled the quark-gluon vertex strength d_1 in such a way, that the value for $T^c(\mu = 0)$ without the inclusion of explicit baryons is reproduced, leading to an enhancement by 23%. With this setup the resulting phase structure with and without baryons can be compared. For the system without baryonic contributions, we already found in Ch. 4 the critical endpoint for BSE_2 at

$$\text{CEP}_{BSE_2} : \ (T^c, \mu_q^c) = (195, 80) \, \text{MeV} \, .$$

Here the position of the CEP changes upon the inclusion of baryonic degrees of freedom slightly and the crossover line ends in an endpoint at

$$\text{CEP}_{BSE_2, incl.B} : \ (T^c, \mu_q^c) = (175, 88) \, \text{MeV} \, ,$$

which is is a shift of about 20 MeV in μ^c and 8 MeV in T^c.

It is apparent that the quantitative influence of baryonic degrees of freedom depends on the parameter used. However, in our investigations we found, that the impact is on a level of 10% in all scenarios.

Summary

In this chapter we presented an exploratory study of effects on the phase structure of QCD by back coupling baryonic degrees of freedom to the fundamental quarks and gluons. We introduced a way of implementing explicit baryonic contributions into our truncation scheme, by considering the DSE for the quark-gluon vertex and identifying diagrams containing baryons in a resonance expansion of the Abelian part. The residual effects were assumed to be part of the already employed ansatz of the quark-gluon interaction with a rescaled infrared strength. For the appearing vertices we applied the well-known quark-diquark approximation for the baryons and obtain two additional diagrams in the quark DSE. In our investigation we find only little influence of baryonic degrees of freedom on the phase structure of $N_f = 2$ QCD and only a sizeable effect after decreasing the baryonic wave function or the masses of the baryon and the diquark by up to 50 percent. However, evidently the effect, be it on a level of 10 percent, needs to be investigated in an improved scheme, where as many properties of the baryons as possible are calculated self-consistently.

6. Investigation of the quark-gluon vertex at finite temperature

> The problems are solved, not by giving new information, but by arranging what we have known since long.
>
> *(Ludwig Wittgenstein)*

Thus far we used an (extended) truncation scheme which takes results from lattice QCD in Landau gauge as input for the quenched gluon propagator and features a procedure to account for back coupling from the matter to the gauge sector. The main part of the truncation is an ansatz for the quark-gluon interaction. This ansatz is designed along the Abelian counterpart of the Slavnov-Taylor identities, the Ward-Takahashi identity, by taking into account the first part of the Ball-Chiu construction [128] accompanied by a dressing function with an infrared enhancement and the appropriate perturbative behaviour for large momenta. Its infrared enhancement is adjusted to match phenomenology, where all contributions are subsumed into the dressing of the γ_μ component without considering other Dirac structures. While this is a valid ansatz for approaching finite temperature to obtain sensible results, the underlying structure of the quark-gluon vertex itself and in particular its temperature and flavour dependence is of major importance. The vertex ansatz from Ch. 3 has a mild flavour dependence via the first part of the Ball-Chiu vertex (proportional to the vector and Matsubara dressing functions) but is not connected to the chiral dynamics, e.g. via the scalar dressing function. However, there are dynamical chiral symmetry breaking ($DCSB$) as well as restoring effects in the vertex in different contributions for finite quark masses. Moreover one finds vanishing components of the quark-gluon vertex in the chiral limit observed in the vacuum [191], which is already dictated by perturbation theory. There are first approaches in the continuum to solve a back coupled quark-gluon vertex DSE by taking some of the diagrams in a two-particle irreducible ($2PI$) system into account [131, 192–194], which was also applied to bound state calculations in [179]. The approach for the continuum in [195] was performed in a 3PI to 3-loop order truncation to investigate bound state calculations. There is also work combining lattice predictions with DSE calculations to

obtain results for the quark-gluon vertex [127] as well as utilizing its counterpart in the background field method [196].

Up to now the investigations are not fully back coupled and in particular performed in the continuum. A full solution of the coupled system with a back coupled quark-gluon vertex is desired yet proves to be difficult even in the vacuum. However, the latter restriction is particularly interesting to lift and to perform an investigation of a truncated system at finite temperature and the resulting phase structure in the light of DCSB in the quark-gluon vertex itself. Up to now in the medium one mostly relies on model ansätze such as an extension to finite T of a simple effective interaction which reproduces bound state properties in the vacuum [74, 75] or the quark-gluon vertex we previously applied which is matched to phenomenology, developed in [63].

In this work we are following 2PI to 3-loop order inspired by [131, 179] and investigate the quark-gluon vertex DSE itself at finite temperature aiming to see a first hint of the flavour dependence and the impact of different contributions, as well as to go beyond implicitly subsuming contributions into the γ_μ part of the vertex. In the first section we therefore introduce our ansatz and the truncations made, before we show results for a calculation using an unquenched gluon propagator as input and end with a summary.

6.1. Truncation of the quark-gluon vertex DSE

In Ch. 5 we already showed a diagrammatic representation for the quark-gluon vertex DSE in Fig. 5.1, where the contributions were written in terms of the quark-quark, quark-ghost, quark-gluon and two-quark-three-gluon scattering kernels. We identified the appearance of baryonic contributions within the quark-gluon vertex DSE to be part of the non-trivial diagram featuring the quark-quark scattering kernel, after performing a resonance expansion. For the purpose in the present chapter we do not concern ourselves with the identification of hadronic poles. Instead we rewrite the quark-gluon vertex DSE in terms of one-particle irreducible Green's functions [191], shown in Fig. 6.1 where two representations are given. In the form of the DSE given in Fig. 6.1a we identify the first non-trivial diagram as the non-Abelian (NA) contribution, which we will mainly focus on here, and the second diagram as the Abelian (AB, for it having a corresponding contribution in the fermion-photon vertex). As mentioned in [191], the Abelian diagram is suppressed by a factor of $1/N_c^2$ compared to the contribution of the NA diagram after performing the colour trace. The ghost-loop, quark-loop and gluon-loop contribution including a two-quark-two-ghost vertex, a four-quark vertex and a two-quark-two-gluon vertex seem to be of one loop order. However, the aforementioned vertices have no tree-level contribution since they do not appear in the Lagrangian, therefore those diagrams are effectively at least of two-loop order. Fig. 6.1b, where the top vertex is dressed, seems simpler for it having only four contributions, one of them being of two-loop order containing a

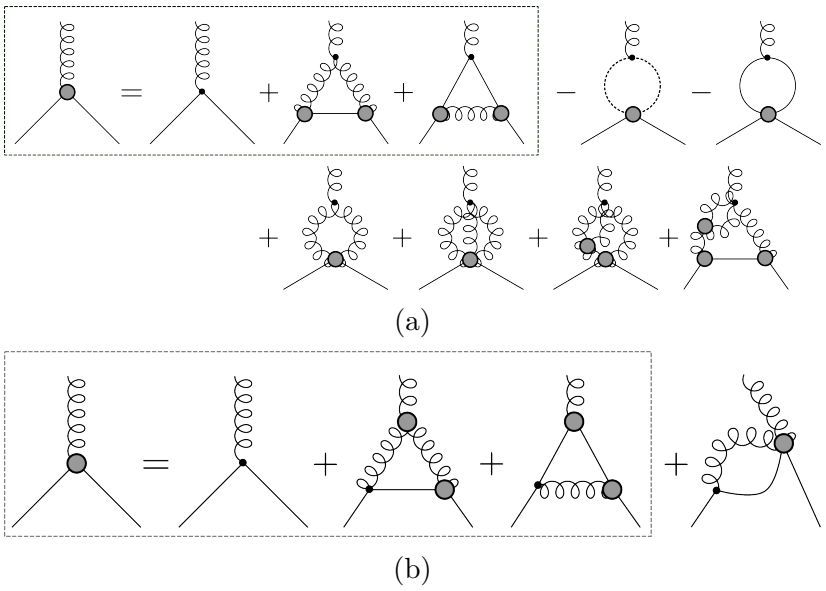

Figure 6.1. Sketch of two diagrammatic representation of the full and untruncated DSE for the quark-gluon vertex in terms of 1PI Green's functions, where all internal propagators are dressed and filled gray circles represent dressed vertices. While in (a) the top vertex is bare, in (b) the external gluon line attaches to a fully dressed vertex.

two-quark-two-gluon vertex.

In this work we perform a first step in a systematic investigation of the quark-gluon vertex by calculating two- and three-point functions using model input for internal three-point functions and neglect all contributions containing non-primitively diverging vertices/four-point functions. Applying this approximation to the representations of the quark-gluon vertex DSE in Fig. 6.1a and Fig. 6.1b (grey boxes), the latter equation looks better at first glance since only one contribution was neglected compared to six for Fig. 6.1a. However, applying an *a posteriori* determined counting scheme where we attribute mean-values to the different dressed vertices and neglect the momentum-dependence, indicates this conclusion can not be drawn easily. Guided by the corresponding infrared enhancement, we assign a value n to the fully dressed quark gluon vertex and a value of m to the fully dressed three-gluon vertex, with $m < n$ for the latter is known in the vacuum to be suppressed at scales relevant to QCD (see [197] for a three dimensional study on the lattice, [198, 199] for general arguments in perturbation theory and in the DSE approach as well as [200, 201] for calculations with Dyson-Schwinger equations). While the Abelian diagram in Fig. 6.1a and Fig. 6.1b as well as the non-Abelian contribution in Fig. 6.1a acquire a value of $2n$, the NA diagram in Fig. 6.1b is worth $n + m < 2n$ in this heuristic counting scheme. Thus in this configuration the one neglected diagram in Fig. 6.1b

might be more important compared to the six contributions we neglect in Fig. 6.1a. Hence we follow the vacuum literature [131] and start the systematic investigation by using a renormalisation-group improved 2PI action to three-loop order and therefore consider only the diagrams within the grey box in Fig. 6.1a.

In vacuum the quark-gluon vertex with incoming (outgoing) quark momentum q (p) can be decomposed as

$$\Gamma^\mu(q,p) = \sum_{i=1} f_i(q,p) F^\mu(q,p) \tag{6.1}$$

where the Dirac-Lorentz tensors $F^\mu(q,p)$ are linear combinations of

$$\begin{bmatrix} q^\mu \\ p^\mu \\ \gamma^\mu \end{bmatrix} \times \left[\mathbb{1},\ \not{q},\ \not{p},\ \not{q}\not{p}\right] \ , \tag{6.2}$$

with the coefficients $f_i(q,p)$, where the dependence on one momentum is lifted by momentum conservation. For our considerations it is of particular interest to consider the in-medium case, where we find a splitting of the four-momentum into a spatial part and a part in the direction of the heat bath, thus the Dirac-Lorentz tensors can be obtained by

$$\begin{bmatrix} \vec{q} \\ \vec{p} \\ \vec{\gamma} \\ \gamma_4 \end{bmatrix} \times \begin{bmatrix} \mathbb{1} \\ \gamma_4 \end{bmatrix} \times \left[\mathbb{1},\ (\vec{\gamma}\cdot\vec{q}),\ (\vec{\gamma}\cdot\vec{p}),\ (\vec{\gamma}\cdot\vec{q})\,(\vec{\gamma}\cdot\vec{p})\ \right] \ . \tag{6.3}$$

Since we work in Landau gauge, one may contract these tensor products with the transverse projector of the gluon propagator, consequently decreasing the number of components from 12 (32) to 8 (24) in vacuum (medium). The two diagrammatic corrections to the tree-level form of the quark-gluon vertex, which we want to investigate, are the non-Abelian and Abelian contribution, leading to the following form of the DSE for the quark-gluon vertex:

$$\Gamma^\mu(q,p) = Z_{1F}\gamma^\mu + \Lambda^\mu_{\mathrm{NA}} + \Lambda^\mu_{\mathrm{AB}} + \cdots \ . \tag{6.4}$$

Here the ellipsis denotes higher (loop) order corrections which we, as already pointed out, do not consider. $Z_{1F} = Z_2/\tilde{Z}_3$ is the renormalisation constant for the quark-gluon vertex in Landau gauge, which is related to the quark wave function renormalisation Z_2 and the ghost renormalisation $\tilde{Z}_3$. The used momentum routing for the two parts is displayed in Fig. 6.2 and for the explicit form we find

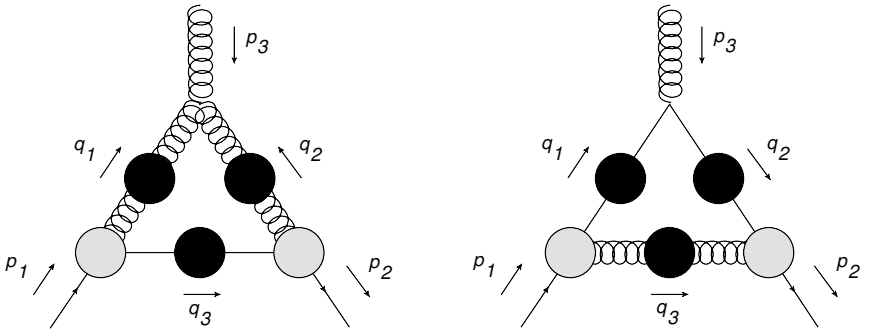

Figure 6.2. The investigated non-Abelian (left) and Abelian (right) contributions to the quark-gluon vertex including the momentum routing. Black filled circles indicate fully dressed objects while grey circles represent an input model for the quark-gluon vertex.

$$\Lambda^{\rho}_{\mathrm{NA}}(p_1,p_2) = \frac{g_s^2 N_c}{2}\int_l \hat{\Gamma}^{\mu}(p_1,q_3)S(q_3)\hat{\Gamma}^{\nu}(q_3,p_2) \times D_{\mu\alpha}(q_1)D_{\nu\beta}(q_2)\Gamma^{3g}_{\rho\alpha\beta}(p_3,q_1,q_2)\;, \tag{6.5}$$

$$\Lambda^{\rho}_{\mathrm{AB}}(p_1,p_2) = \frac{-g_s^2}{2N_c}\int_l \hat{\Gamma}^{\mu}(p_1,q_1)S(q_1)\hat{\Gamma}^{\rho}(q_1,q_2)S(q_2) \times \hat{\Gamma}^{\nu}(q_2,p_2)D_{\mu\nu}(q_3)\;, \tag{6.6}$$

with $q_1 = p_1 - l$, $q_2 = l - p_2$, $q_3 = l$. We labelled p_1 to be the incoming quark momentum, p_2 the outgoing quark momentum and p_3 the incoming gluon momentum with $p_3 = p_2 - p_1$. In Eqs. (6.5) and (6.6) we already traced out the colour indices making the suppression of the AB in comparison to the NA part by the factor $1/N_C^2$ apparent. Note that in the explicit equations the entering quark-gluon vertex should be the back coupled version obtained by simultaneously solving the coupled quark DSE, gluon DSE (including quark loops for unquenching) and the present quark-gluon vertex DSE. However, in this exploratory work we aim for a systematic study and in particular are constrained by computing time. Therefore we take the internal quark-gluon vertex to be a model, indicated by $\hat{\Gamma}$, instead of the fully back coupled version. This might introduce artificial behaviour and will lead to a model dependence, but has some technical advantages:

- The resulting quark-gluon vertex will depend on the fully dressed quark propagator and therefore implicitly on finite temperature, chemical potential and the quark flavour.
- We can adjust the scale of the internal vertex, similar to Ch. 3, Ch. 4 and Ch. 5 to obtain agreement with lattice QCD or phenomenology.
- Improvements of the truncation are possible in a systematic way.

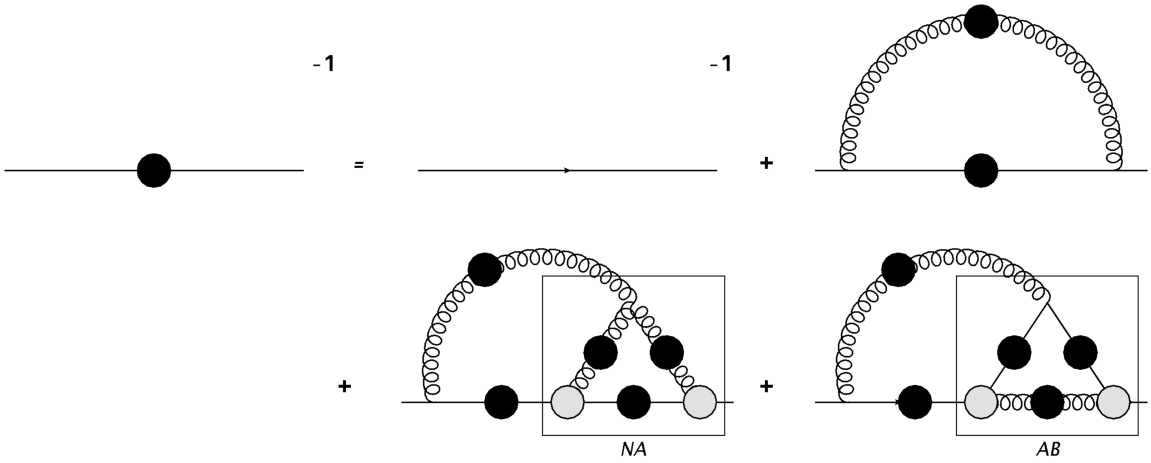

Figure 6.3. Resulting quark DSE including the investigated non-Abelian and Abelian vertex corrections and the bare part of the quark-gluon vertex (one gluon exchange). Black filled circles indicate fully dressed objects while grey circles represent an input model for the quark-gluon vertex.

The second ingredient for the solution of the quark-gluon vertex is the fully dressed gluon propagator. Throughout the investigation we apply the unquenched gluon for it features important temperature effects of the full gluon DSE. However, for the unquenched calculation we face another problem: as described in the discussion of Sec. 3.1.3, to solve the quark-loop we have to perform the full Matsubara sum, which would lead to a tremendous increase in computing time of the calculated quark-gluon vertex. Therefore we also take the unquenched gluon as (fixed) external input, where we used the system as solved in Ch. 3 and the fitted results for the quark-loop, as tabulated in App. C.

The investigation aims to obtain general conclusions and we view it as a first step towards a full calculation. Two main requirements on the internal model quark-gluon vertex are important for our investigation, where it should

1. feature the correct UV behaviour

2. depend on the quark propagator

While the first point is clear and introduced straightforward, the second demand renders the system a little bit more involved. By construction the quark-gluon vertex depends on the fully dressed quark propagator. Since we already have a vertex at hand, which fulfils the requirements, we use the vertex given in Sec. 3.1.1 as the internal model. This vertex features the first part of the Ball-Chiu vertex and therefore depends on the dressed quark propagator via the γ_μ component. Note that the full vertex would contain 24 tensor structures at finite temperature, making the back coupling not only tedious but also numerically very demanding. The general

strategy, however, would not change if all components are taken into account.

In Fig. 6.3 we display the quark DSE as it is effectively solved in our approach. The two diagrams in the bottom line feature a two-loop structure, which for numerical reasons we want to avoid solving in one step, particularly at finite temperature. Therefore the approach is, to solve the system in a micro-macro cycle in the following way:

1. Solve the quark DSE with the model vertex for initialisation
2. Calculate the two diagrams in Fig. 6.2 for the given quark (macro step)
3. Solve the quark DSE with the resulting quark-gluon vertex (boxes in Fig. 6.3) until it converges (micro cycle)
4. Iterate step 2. and step 3. until macro-convergence

Setting the infrared strength parameter for the internal vertex ansatz d_1^{int} also sets the scale for the results and has to be properly adjusted, similar to what is done in Ch. 3, Ch. 4 and Ch. 5. In all steps of the calculations we keep the gluon propagator fixed as external input.

6.2. Results for an $N_f = 2 + 1$ flavour gluon as input

In this section we present results for calculations using an unquenched $N_f = 2 + 1$ flavour gluon as input. We take the non-Abelian contribution as well as the Abelian diagram, where denoted, as part of the quark-gluon vertex DSE into account. The unquenched gluon was calculated in the setup of Ch. 3, which reproduces the corresponding regularised condensate from lattice QCD. To have a mass function which approaches the one for an unquenched quark given by lattice calculations [202], we used a renormalised mass of 13 MeV at a renormalisation scale of 80 GeV. The study of the temperature dependence of the mass function in Fig. 6.4a, where we used an internal d_1^{int} of 3.5 GeV^2, shows that we find good agreement with the vacuum limit of the unquenched lattice quark. This study was performed with only taking the NA contribution into account. In Fig. 6.4b we display the corresponding $Z(p) = 1/A(p)$ compared to lattice results. Since we only tuned the internal vertices and the renormalised mass to match the lattice mass function, the good agreement with the lattice results gives confidence about our approach.

Before we draw our attention to the temperature dependence of the results, we want to investigate the implications from the additional internal flavour dependence of the calculated vertex. In Fig. 6.5a we show the mass function $M = B/A$ for $T = 60$ MeV for three different quark masses, representing a light (black line), strange (blue line) and charm (red line) quark. For all flavours we observe DCSB in the infrared comparable to previous calculations. To shed some light on the difference in the flavour

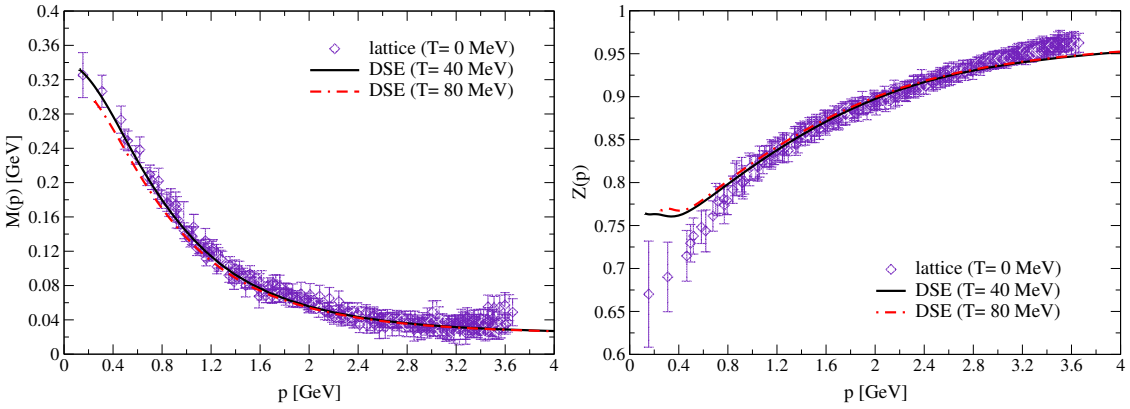

(a) (b)

Figure 6.4. Results for the solution of the quark DSE including a vertex calculation with the unquenched gluon as input. In the left figure we show the mass function compared to vacuum results from lattice QCD, in the right figure the Z-function also compared to lattice results. The Z-function is a renormalisation point dependent quantity and therefore can be rescaled.

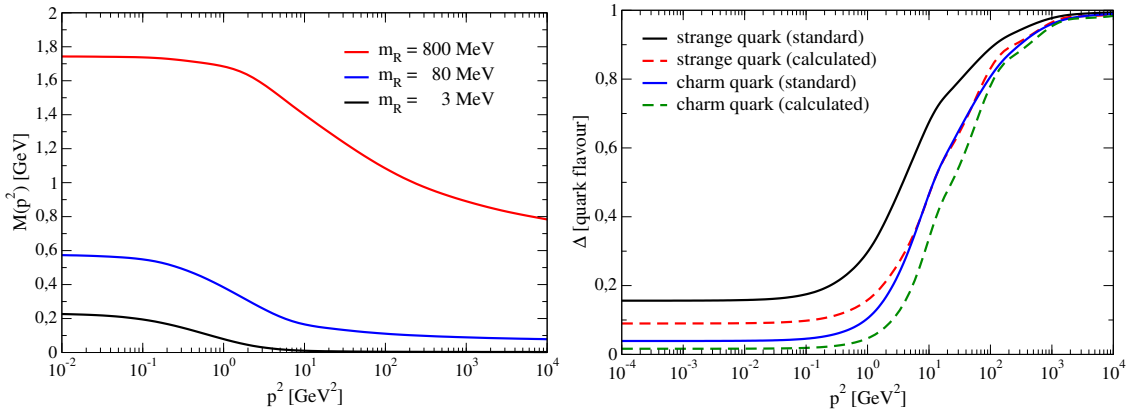

(a) (b)

Figure 6.5. Results implying the flavour dependence of the quark-gluon vertex. In (a) we show the resulting mass function for three different quark masses, corresponding to a light (3 MeV), a strange (80 MeV) and a charm quark (800 MeV). In (b) we show the ratio of the scalar self-energy divided by the quark mass for the strange/charm quark to the light quark for the standard and the calculated vertex.

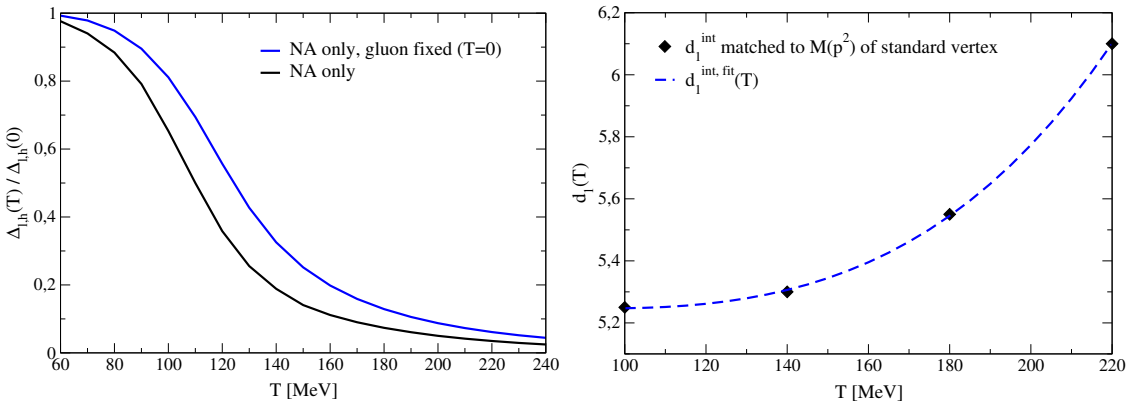

(a) (b)

Figure 6.6. Regularised condensate for the calculation with an unquenched gluon as input (left figure) and values of d_1^{int} necessary to reproduce the quark mass function obtained with the model vertex from Ch. 3 (right figure).

dependence for the calculated vertex and the standard one from Ch. 3 we plot the ratio

$$\Delta[\text{quark flavour f}] = \frac{\Sigma_B^{\text{f}}(\vec{p}, \omega_0)/m_R^{\text{f}}}{\Sigma_B^{\text{light}}(\vec{p}, \omega_0)/m_R^{\text{light}}}$$

at $T = 60$ MeV for the calculated and the standard vertex in Fig. 6.5b. We notice for the calculated vertex a stronger suppression of the strange and charm quark in the infrared, indicating a higher importance of the quark flavour. However, the relative suppression of the charm quark compared to the strange quark is roughly the same for both vertices and approximately one quarter. To ensure comparability we used the same gluon and the same quark masses ($m_R^{\text{light}} = 3$ MeV, $m_R^{\text{strange}} = 80$ MeV, $m_R^{\text{charm}} = 800$ MeV) in both calculations. Taking the internal model vertices to carry only a mild flavour dependence seems a good approximation in terms of our calculation. This is implied by continuum studies where the internal quark confers the majority of the flavour dependence in such kind of renormalisation group improved 2PI to 3-loop calculations [131].

Finally we are concerned with the behaviour of the condensate for the unquenched case, for it being a quantity predicted by lattice QCD. Note, the in Fig. 6.4a reproduced lattice quark mass function was for a unphysically heavy quark. To perform a calculation with an approximately physical quark we tuned the light quark mass to match the common result of $M(p = 19\ \text{GeV}) \approx 3.7$ MeV, which was achieved with a renormalised mass of $m_l = 3$ MeV at 80 GeV and $d_1^{\text{int}} = 3.5\ \text{GeV}^2$. With these parameters, the system of quark DSE and the quark-gluon vertex was solved in two step process with a variation of the number of internal Matsubara frequencies taken into account. We used $N_{\text{expl}} = 1$ for the number of explicit Matsubara frequencies

of the quark propagator and for the steps a and b the internal Matsubara grid was given by $\mathcal{N}^a = N^a_{pad} = 2$ and $\mathcal{N}^b = N^b_{pad} = 4$ (a definition of these quantities is given in App. B.1.3). Note that the massive condensate is polluted by quadratic divergences due to the finite bare quark mass, which cancel if one subtracts the rescaled massive condensate from a quark with heavier mass, where we used $m_h = 80$ MeV. The resulting regularised condensate is shown in Fig. 6.6a (black line). If one studies the massive quark condensate, artificial behaviour due to the rough Matsubara grid for small temperatures becomes apparent, which is however cancelled due to the regularisation. In Fig. 6.6a we additionally report on a calculation with a gluon propagator fixed at $T = 0$ (blue line), which shifts the scale of the pseudo-critical temperature by about 15 MeV and modifies the slope slightly. This result highlights the impact of the temperature behaviour of the (input) gluon itself. A calculation with both, the NA and AB part, but temperature dependent gluon shifts the scale of the NA calculation by only 2 MeV to smaller temperatures and is not shown. If we extract T_c, as defined via the inflection point of the condensate, from the black line we find it to be at about $T = 110$ MeV and therefore smaller than the state of the art prediction by lattice groups of $T_c^{\text{infl.}} \approx 155$ MeV. This is attributed to the unmatched scale of the internal vertex ansatz.

As we already have a truncation which reproduces the regularised condensate from lattice QCD, we performed an investigation where we roughly matched the light quark mass function as calculated in Ch. 3, by tuning the the internal vertex strength d_1^{int} for several temperatures. This gives an impression of how the fixed internal, temperature independent scale is modified by solving the quark-gluon vertex DSE. For the investigation we took also the AB part into account. The resulting parameter are shown in Fig. 6.6b, together with a fit showing the general tendency, which is given by the function

$$d_1^{\text{int,fit}} = aT^4 + bT^2 + c\,, \tag{6.7}$$

with $a = 559$ GeV^{-2}, $b = -10.4$, $c = 5.29$ GeV^2 and T given in GeV (fitted for $T = 0.10...0.22$ GeV). One remarkable feature, dictated by the data, of this function is, that it is even in T. This might be a result of the not exactly matching unquenched gluon and in particular the (squared) thermal mass $m^2_{thermal}$ in the longitudinal part of the gluon, which is proportional to T^2. If one considers the non-Abelian diagram in Fig. 6.2, it becomes apparent that there are contributions proportional to $Z^2_{L,T}$ but also combinations proportional to $Z_L Z_T$ possible, leading to contributions of $m^2_{thermal}$ and $m^4_{thermal}$ in the infrared. This possibly explains the dependence on T^4 of d_1^{int}. Therefore a full calculation featuring additionally the quark-loop in the manner of Ch. 3 with the calculated vertex would be certainly desirable. However, this leads to a tremendous increase in complexity and computation time and is left for future investigations.

Summary

In this chapter we presented an exploratory investigation of the quark-gluon vertex as given by a solution of its DSE at finite temperature. We aimed to lift the previous restriction of the vertex, where the necessary infrared enhancement of all vertex components was subsumed into the dressing of the γ_μ part only and where its infrared enhancement is fitted to reproduce phenomenology. Furthermore we were interested in the flavour and implicit temperature dependence of the quark-gluon vertex and the implications for the solution of the quark DSE. Similar investigations have been performed in the continuum, where we followed those given in [131,179]. In [179] the ansatz was applied for mesonic and baryonic spectra, but proved to be not effective due to a poor a-ρ splitting. One could argue about the applicability of this approach at finite temperature if matching hadronic spectra is not improved, despite effects of DCSB in the vertex. However, the tensor structures probed for hadronic spectra are potentially different from the relevant terms close the transition lines and the CEP. Hence we approached the quark-gluon vertex DSE in a renormalisation group improved 2PI to three-loop order system and chose a representation with a bare top vertex, considering mostly the non-Abelian diagram only. Since solving the system of equations fully back coupled proves already difficult in the vacuum, we used the previously applied vertex for the internal quark-gluon interaction and the unquenched gluon as input. We found a setup reproducing the quark mass function and the wave function given by lattice QCD. A flavour dependence of the quark mass function comparable to earlier investigations is observed. Quarks with masses of the order of a strange and a charm quark have a stronger relative suppression in the calculated vertex compared to the previous ansatz. The comparison of the regularised condensate for the calculated vertex with a temperature dependent gluon and input fixed at $T = 0$ shows a sizeable impact of the temperature behaviour of the gauge boson. Additionally we found that the internal scale of the quark-gluon vertex must rise in order to reproduce the mass function obtained with the standard vertex. This could be attributed to the impact of the unquenched gluon as input, in particular the thermal mass, as well as to the approximations made.

Possible next steps include to use the calculated vertex also in the unquenching process. Additionally the inclusion of quark chemical potential would be of interest, since the temperature dependence of the quark-gluon vertex can be adjusted to lattice results at $\mu = 0$ only and better understanding of the behaviour at $\mu > 0$ is desirable. Finally a full back coupling, also in a system with a reduced vertex DSE, is desirable yet a numerically challenging task. This is in particular important in the light of [195], where a setup going towards 3PI to 3-loop order was used showing that back coupled components of the vertex are possibly important. Therefore further investigations of the quark-gluon vertex in a systematic way are important to gain knowledge about QCD at finite temperature and chemical potential.

7. Analytic structure of the quark propagator

> He was determined to discover the underlying logic behind the universe. Which was going to be hard, because there wasn't one.
>
> *(Sir Terry Pratchett)*

In this chapter we are concerned with the analytic structure of correlation functions, which is interesting for various reasons. Knowledge about the analytic properties allows in particular a connection from calculations done in Euclidean space to results for the real world Minkowski space. At finite temperature the analytic structure enables the extraction of thermal properties and observables. Thermal properties of quarks and gluons give for example information about transport coefficients in the QGP phase. These are important input for hydrodynamical and transport approaches and in particular to be compared with experimental results. The spectral function, which entails the analytic structure of a correlator, and with this the shear viscosity over entropy ratio has been studied in the FRG approach in [69, 70] for gluons. In [43, 203, 204] the spectral function has been studied for mesons at finite temperature, which is relevant also for the hadronic phase. In this chapter we focus on analytic properties of the quark propagator in vacuum and medium. This is interesting for the connection to bound state calculations in the vacuum, but in particular important for the aforementioned transport coefficients as well as observables like dilepton spectra [139, 205–207] and the phenomenon of confinement/deconfinement at finite temperature and chemical potential. In the framework of DSEs the quark spectral function has been investigated in [71–75, 208], partly by using Bayesian methods and partly by assuming a certain shape of the function and applying a fitting algorithm. Investigations of quark spectral functions with the MEM applied to Matsubara propagators, which were calculated with a finite temperature extension of the Maris-Tandy model are available in [73–75]. The DSE approach was also used for quenched and unquenched QCD in [72, 94, 208] in a more advanced truncation scheme. A fitting algorithm was as well applied to extract information about the quark spectral function from the lattice, e.g. in [76–78].

In our work we are concerned with two related functions which carry information about the properties of an object in Minkowski space, deduced from knowledge about the Euclidean propagator, calculated either after a Wick rotation (vacuum) or in the imaginary time formalism (medium). These two, the Schwinger function and the spectral function, are powerful tools since they relate Minkowski space properties to Euclidean propagators. Additionally they are the key quantities for the definition of confinement via the violation of positivity. This definition states, if the propagator of any involved degree of freedom contains negative norm contributions it can not be part of the physical phase space, therefore does not necessarily have a Källén-Lehmann representation as a spectral function and is, in this sense, confined. In case one can find a spectral function corresponding to a positivity violating propagator, it will consequently contain negative parts and vice versa. The definition of (quark) confinement via the violation of positivity is one amongst a few, where another one to mention is the so-called linear rising potential between two (heavy) quarks. Such a potential implies an infinite amount of energy to be necessary in order to separate the two and they are, in this sense, confined. As discussed in Ch. 2, the linear rising potential is related to the Polyakov loop and the free energy of a (static) quark. Quark confinement has to be distinguished from colour confinement, which describes the absence of coloured objects from the physical phase space. Possible ways to understand colour confinement are the Kugo-Ojima scenario [96, 97] and the quartet mechanism in the Becchi-Rouet-Stora-Tyutin ($BRST$) symmetry [209], which are not investigated here but described in more detail in several publications, such as [89, 210].

For Euclidean quantum field theory, the term positivity is usually defined along the lines of the so called Osterwalder-Schrader axiom of reflection positivity [211]. For a general propagator $\Delta(x-y)$ the corresponding requirement for reflection positivity is given as

$$\int d^4x\, d^4y\, \bar{f}(\vec{x}, -x_0)\, \Delta(x-y)\, f(\vec{y}, y_0) \geq 0\ , \tag{7.1}$$

where $f(\vec{x}, x_0)$ is a complex valued function with $\mathrm{supp}(f) = \{(\vec{x}, x_0), x_0 > 0\}$ (support for positive times).

This chapter is organized in the following way: in the first section we investigate the Schwinger function, first in vacuum and then at finite temperature. We emphasize the implications of Eq. (7.1) and perform an analysis of the numerical precision for the in-medium case. In the second section we elaborate on a method to solve the inverse problem of obtaining the spectral function from the Schwinger function, introducing a Bayesian reconstruction. After this we move on to the quark spectral functions in the medium and their properties, before we turn to reconstruction of test data and comment on the solution of the inverse problem of data obtained from solving a DSE.

7.1. The Schwinger function

The Schwinger function is generally given as a Fourier transform of a (projected) Euclidean propagator $\sigma(p)$ with respect to the component of the Euclidean four-momentum related to (imaginary) time. It carries information about analytic properties of the quark propagator and therefore properties of the theory such as confinement.

7.1.1. Definition and results in vacuum

Despite we are mainly interested in analytic properties of the quark propagator at finite temperature, a study of the vacuum case is useful. On one hand it indicates how the analytic structure looks like in the low temperature limit. On the other hand it can give hints on aspects of the truncation and the impact of its extension. There have been many papers investigating the behaviour and attributes of the analytic properties in the vacuum, [170, 210, 212] and references therein, mainly concerned with the dependence on the truncation of the tower of Dyson-Schwinger equations. To make this investigation self-contained we repeat some results for the sake of comparison.

Due to the structure of the quark propagator in vacuum, there are two distinct projections $\sigma_{s,v}(p^2)$ and the corresponding Schwinger functions $\Delta_{s,v}(t)$. The Schwinger functions in vacuum are then given as

$$\Delta_{s,v}(t) = \int d^3x \int \frac{d^4p}{(2\pi)^4} \mathrm{e}^{ip\cdot x} \sigma_{s,v}(p^2) \;, \tag{7.2}$$

with the scalar and vector part respectively

$$\sigma_s(p^2) = \frac{B(p^2)}{p^2 A(p^2) + B(p^2)} \;, \quad \sigma_v(p^2) = \frac{A(p^2)}{p^2 A(p^2) + B(p^2)} \;.$$

For the special case of $\vec{p} = 0$ the Osterwalder-Schrader criterion can be linked to the Schwinger function

$$\begin{aligned} \Delta_{s,v}(t) &\overset{\vec{p}=0}{=} \frac{1}{2\pi} \int_{-\infty}^{\infty} dp_4 \; cos(p_4 \cdot t) \; \sigma_{s,v}(p_4^2) \;, \\ &\overset{Eq.\ (7.1)}{\geq} 0 \;. \end{aligned}$$

Before we investigate results from solutions of the quark DSE, it is useful to highlight the outcome of two cases of two-point correlation functions, following [210].

- **Real pole:** An example for a single pole on the real axis is a real scalar particle. The correlator $\sigma(p^2) = 1/(p^2 + m^2)$ produces a pole in the time-like ($p^2 < 0$)

momentum regime. This propagator does not *a priori* imply a deconfined particle, while its Schwinger function is exponentially damped

$$\Delta(t) \propto \mathrm{e}^{-mt} \ .$$

- **Pair of complex conjugated poles:** An excitation with a short lifetime could be described by a propagator with a pair of complex conjugate poles featuring a complex equivalent of masses $m = m_R \pm i m_I$. As discussed in [213] for this type of propagator, which is known as the Stingl propagator, causality is violated. Still the resulting S-matrix obeys causality and unitarity conditions. The Schwinger function for a pair of complex conjugated poles displays oscillatory behaviour

  $$\Delta(t) \propto \mathrm{e}^{-m_R t} \ \cos(m_I t + \delta) \ .$$

  This clearly leads to negative norm contributions in the Schwinger function. Nonetheless an effective mass can be defined by

  $$m_{eff}(t) = -\frac{d \ln \Delta(t)}{dt} \ .$$

In the vacuum we aim to describe Schwinger functions with either of these two possible underlying structures. However, we want to point out that in [210] the authors apply an ansatz to describe the quark propagator using a meromorphic form taking into account a number of (conjugated) poles and imprinting physical constraints on the system. As we will see, with only one pair of complex conjugate poles the behaviour of $\Delta(t)$ for small times is not well represented but the intermediate time region described correctly. Since we are more interested in the medium effects and only in the gross effects in the vacuum, we will not utilize the ansatz with multiple poles to calculate a more precise Schwinger function.

Results

We now want to focus on the results for different setups in the vacuum. First we investigate the well-known Maris-Tandy model used for bound state calculations [214–216] and other applications, e.g. in [115,175,217] (for reviews in the vacuum see [218,219] and references therein). This truncation was studied in previous work [210] and serves as a measure of our procedure and also as a reference to compare to. Then we focus on our standard truncation as presented in Ch. 3. A study of the analytic structure of the corresponding quark propagators in the vacuum is presented for the first time. The implications for the analytic properties of additional extensions, e.g. as in Ch. 4 and Ch. 5, are given. For the calculation of the renormalised quark propagators we used the standard iterative procedure with a high numerical

Set	A	m_R	m_I	δ	t_{fit}
light (M.-T. model)	0.492	0.546	0.312	-1.10	3,..,24
light (LAT_{2+1})	0.667	0.558	0.248	-1.20	3,..,24
strange (LAT_{2+1})	0.593	0.726	0.356	-1.16	3,..,16
light (BSE_{2+1})	0.913	0.472	0.150	-1.25	4,..,30
light (BSE_{2+1+1})	0.870	0.470	0.157	-1.24	4,..,30
strange (BSE_{2+1})	0.677	0.730	0.310	-1.15	2,..,17
strange (BSE_{2+1+1})	0.670	0.722	0.311	-1.15	2,..,17
charm (BSE_{2+1+1})	0.625	1.892	0.774	-1.17	2,..,6
light ($\text{LAT}_{(2+1)\to 2}$)	0.461	0.779	0.467	-1.15	3,..,17
light ($\text{LAT}_{(2+1)\to 2} + \text{B}$)	0.494	0.828	0.390	-1.17	3,..,17
light ($\text{LAT}_{(2+1)\to 2} + \pi$)	0.487	0.798	0.435	-1.20	3,..,17
light ($\text{LAT}_{(2+1)\to 2} + \text{B(resc.)}$)	0.438	0.761	0.470	-1.15	3,..,17

Table 7.1. Resulting parameter for a fit of the Schwinger function in the vacuum using an ansatz for the propagator with two complex poles. A, m_R and m_I are given in GeV while t_{fit} is given in GeV^{-1}.

accuracy for the numerical integration and the interpolation. The Schwinger function was then calculated from the quark propagator using the fftw-library [220], which applies a fast Fourier transformation. We present results for $\Delta_s(t)$ since this quantity is numerically more stable compared to its vector counterpart. By looking at results for the Schwinger function for both truncations in Fig. 7.1 we observe in each case an oscillatory behaviour and therefore use a fit function assuming two complex poles in the propagator

$$f(t) = A\, \mathrm{e}^{-m_R\, t}\, \cos(m_I\, t + \delta)\ ,$$

in a given interval for t_{fit}. This is in line with quarks being confined in the vacuum ($T = 0$, $\mu = 0$). The used intervals and resulting parameters are summarized in Table 7.1, where the fit was in each case performed on the Schwinger function calculated using a sampling size of $\delta p = 1.0e^{-7}$ and $N = 2^{30}$.

In Fig. 7.1a we show the calculated Schwinger function for a propagator corresponding to the Maris-Tandy interaction. In the main plot the result of the fit is compared against the Schwinger function for $\delta p = 1.0e^{-7}$. We observe a good agreement for the first two minima, which have been included in the fit, but the Schwinger function does not display a third minimum. The higher resolved panel indicates that the predicted 3^{rd} minimum arises for smaller sampling size close to the predicted

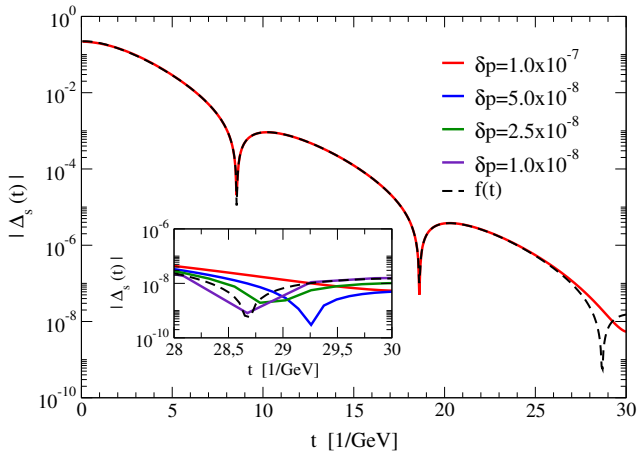

(a)

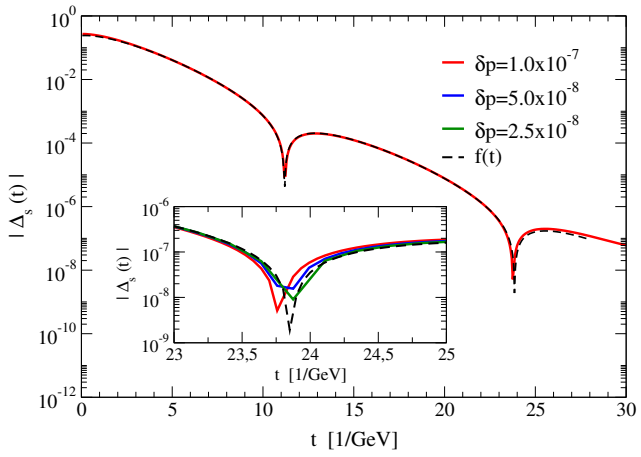

(b)

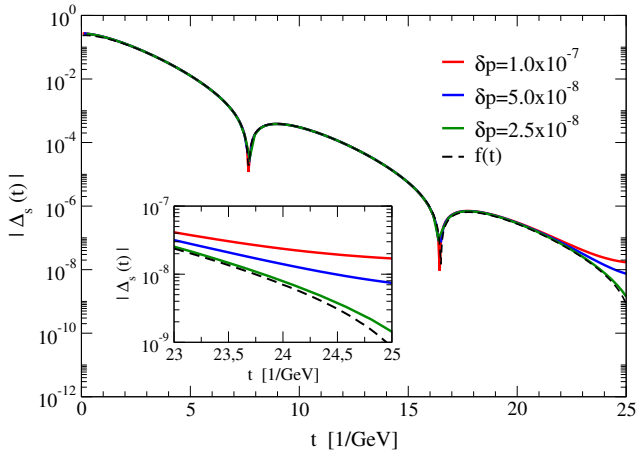

(c)

Figure 7.1. Results for the scalar Schwinger functions in vacuum where δp is given in GeV. In (a) the result for a light quark propagator calculated using the Maris-Tandy model is displayed, while in (b) and (c) we show the outcome for the light quark and the strange quark for set LAT_{2+1} respectively.

value for t. Therefore we find the result for the (most dominant) complex conjugate poles reliable. The complex poles are at $m = (0.546 \pm 0.312\ i)$ GeV, as also reported in Table 7.1. This result agrees very well with the results from [210], where they find a pole position at $m = (0.55 \pm 0.32\ i)$ GeV, giving us confidence about our procedure.

Next we want to focus on the vacuum results for our standard truncation, as described in Ch. 3. In Fig. 7.1b and Fig. 7.1c we show the results for the light quark and the strange quark respectively. In the case of the light quark, two stable roots of the Schwinger function were not found. Hence the fit region was chosen to not include the second zero crossing but to leave it as a check of the result. With decreasing sampling rate one finds the predicted minimum to be in the right ballpark compared to the outcome of the fit, but the resolution of δt to be coarser (compare zoomed-in box in Fig. 7.1b). We find that complex poles at $m = (0.558 \pm 0.248 i)$ GeV reproduce the light quark propagator for set LAT_{2+1} well. Due to the bigger mass of the strange quark we expect also the mass poles in the fit to be at larger $|m|$. This is indeed the case, the complex poles for the strange quark are found at $m = (0.726 \pm 0.356\ i)$ GeV and reproduce the strange quark correlator to very good accuracy. In this case we found a stable second zero crossing, but the slope of the Schwinger function for times just above the second root only approaches the prediction again with smaller sampling size.

Eventually we want to draw the attention to the results for the parameter sets BSE_{2+1} and BSE_{2+1+1} (see also Ch. 4) as reported in Table 7.1. In those sets the the pseudoscalar mesonic properties in vacuum are well reproduced. Hence we expect the pole structure to be very much similar for corresponding quark propagators, since the analytic structure of the quark is an important ingredient for the solution of the Bethe-Salpeter equation. Comparing the fit results for the light quarks and the strange quarks for sets BSE_{2+1} and BSE_{2+1+1}, we indeed find that the results for the fitted complex poles are almost identical within a few MeV.
In Table 7.1 we report as well on the properties of $N_f = 2$ calculations done with the light quark mass and infrared strength of the quark-gluon vertex from LAT_{2+1}, labelled $\mathrm{LAT}_{(2+1)\to 2}$. By comparing the two flavour calculation with the one for the light quark from LAT_{2+1}, one observes a huge influence of the additional strange quark also on the analytic structure of the quark propagator in the vacuum.

The baryonic degrees of freedom, applied as detailed in Ch. 5, have a bigger impact on the imaginary part of the complex conjugated poles assumed in our ansatz ($\mathrm{LAT}_{(2+1)\to 2}$ + B). For the light quark result with a rescaled infrared strength d_1 ($\mathrm{LAT}_{(2+1)\to 2}$ + B(resc.)), the analytic structure is similar. Comparing the findings in [170] with our results for the impact of the pion ($\mathrm{LAT}_{(2+1)\to 2} + \pi$), we observe a discrepancy: while our fits suggests that the real part of the poles grows while the imaginary part becomes smaller, in [170] the authors observe that both parts are decreasing. However, since the impact of the pion depends on the fully dressed quark propagator and might therefore be strongly dependent on the truncation, we do not regard this as a contradiction.

In general the phase δ is approximately the same for all calculations independently of the truncation used to obtain the quark propagator. However, the unquenched calculations seem to follow $\delta = 1.20 \pm 0.05$ while the Maris-Tandy interaction is at $\delta = 1.10$. The calculated Schwinger function is stable for a region with $t \leq 20$ GeV^{-1} and becomes sensitive to the sampling size for $20 \leq t \leq 25$ GeV^{-1}.

All the performed calculations have another feature in common: they are well reproduced by a propagator with two complex conjugated poles. Hence they all expose positivity violations and represent in this sense confined objects. This is exactly what one expects, since we observe only quarks and gluons confined in hadrons for vacuum conditions. With a quark-gluon vertex designed analogously to an electron-photon vertex in QED, this picture would change and a Schwinger function corresponding to a real scalar particle could be found, see [210].

7.1.2. Finite temperature and vanishing chemical potential

At finite temperature there have been a few investigations of the Schwinger function, e.g. [72] for the quenched system. Since we use the imaginary time and Matsubara formalism for the calculation of the in-medium propagators, the definition of the Schwinger function looks different to the one in the vacuum and is given for arbitrary spatial momenta by

$$\Delta_{\mathcal{D}}(\tau, \mathbf{p}) = -T \sum_n \mathrm{e}^{-i\tau\omega_n} S_{\mathcal{D}}(\omega_n, \mathbf{p}; \mu) \ , \tag{7.3}$$

where $S_{\mathcal{D}}(\omega_n, \mathbf{p}; \mu)$ could be any part or combination of the parts of the propagator. As dictated by the very nature of a quark being fermionic, a quark Schwinger function must obey anti-periodic boundary conditions,

$$\Delta(\tau - \beta, \mathbf{p}) = -\Delta(\tau, \mathbf{p}) \ \ , \tag{7.4}$$

which should hold, due to linearity of the propagator, for each part of the Schwinger function separately. Condition Eq. (7.4) includes, but is not only satisfied by $\Delta(0, \mathbf{p}) = -\Delta(\beta, \mathbf{p})$ and has no predictive power for the symmetry of a Schwinger function in the interval $\tau \in (0, \beta)$.

It is useful to define a set of Schwinger functions given by

$$\Delta_A(\tau, \mathbf{p}) = -T \sum_n \mathrm{e}^{-i\tau\omega_n} \frac{|\mathbf{p}| \, A(\omega_n, \mathbf{p})}{\tilde{\omega}_n^2 C^2(\omega_n, \mathbf{p}) + \mathbf{p}^2 A^2(\omega_n, \mathbf{p}) + B^2(\omega_n, \mathbf{p})} \tag{7.5}$$

$$\Delta_B(\tau, \mathbf{p}) = -T \sum_n \mathrm{e}^{-i\tau\omega_n} \frac{B(\omega_n, \mathbf{p})}{\tilde{\omega}_n^2 C^2(\omega_n, \mathbf{p}) + \mathbf{p}^2 A^2(\omega_n, \mathbf{p}) + B^2(\omega_n, \mathbf{p})} \tag{7.6}$$

$$\Delta_C(\tau, \mathbf{p}) = -T \sum_n \mathrm{e}^{-i\tau\omega_n} \frac{-i\tilde{\omega}_n C(\omega_n, \mathbf{p})}{\tilde{\omega}_n^2 C^2(\omega_n, \mathbf{p}) + \mathbf{p}^2 A^2(\omega_n, \mathbf{p}) + B^2(\omega_n, \mathbf{p})} \ , \tag{7.7}$$

which are real quantities also for finite chemical potential. We will make use of two specific limits, one where the spatial momentum is zero (*stat.*) and one in the chirally symmetric phase (χ), i.e. $B(\omega_n, \mathbf{p}) = 0$.

Since it will be of interest in later investigations we show an example for the Matsubara part of the propagator, which is proportional to ω_n and abbreviate this with

$$S_C(\mathbf{p}, \omega_n) = i\omega_n \cdot F(\mathbf{p}, \omega_n) \ ,$$

where we assume for simplicity the case $\mu = 0$, hence F is a real function with $F(\mathbf{p}, \omega_n) = F(\mathbf{p}, -\omega_n)$ and $F(\mathbf{p}, \omega_n) \propto \frac{1}{\omega_n^2 + const}$ for $\omega_n \to \infty$ with fixed $\mathbf{p}$. Inserting $S_C(\mathbf{p}, \omega_n)$ into Eq. (7.3), we find

$$\begin{aligned} \Delta_C(\tau, \mathbf{p}) &= -T \sum_n e^{-i\tau\omega_n} i\omega_n \cdot F(\mathbf{p}, \omega_n) \\ &= -T \sum_n \sin(\tau\omega_n) \cdot \omega_n \cdot F(\mathbf{p}, \omega_n) \\ &= -T \sum_n \sin\left[((2n+1)\pi \cdot T\tau\right] \omega_n F(\mathbf{p}, \omega_n) \ . \end{aligned} \tag{7.8}$$

An immediate observation is that for $\tau = 0$ and $\tau = \beta \left(= \frac{1}{T}\right)$ we have $S_C(\tau, \mathbf{p}) = 0$. However, the functional dependence on τ on the right hand side of Eq. (7.8) shows, that $S_C(\tau, \mathbf{p})$ is still antisymmetric in τ.

Results

We now discus results of the Schwinger functions for the Matsubara part and the scalar part of the propagator at zero spatial momentum $\Delta_{B,C}(\tau, \mathbf{0})$ at $\mu = 0$. The starting point is the Maris-Tandy interaction in the fashion of [73–75] in the chiral limit, e.g. $m_\mathrm{l} = 0$. In this case we verified a second order chiral phase transition with $T_c \approx 140$ MeV. The resulting Schwinger functions are shown in Fig. 7.2 for various temperatures. Note that while we display $\Delta_B(\tau)$ on one side, we show $\ln \Delta_C(\tau)$ on the other side. It is immediately apparent that the two Schwinger functions $\Delta_{B,C}(\tau)$ obey different symmetries with respect to $\tau T = 0.5$. For the Matsubara part we observe symmetric behaviour while the scalar part displays an antisymmetric dependence with respect to $\tau T = 0.5$. This does not contradict the inherent anti-periodic boundary condition Eq. (7.4).

For the Matsubara part in Fig. 7.2b one observes a change of the curvature of $\ln(\Delta_C(\tau))$ for $T = 80$ MeV. This is also verified numerically to be the case, while already for $T = 100$ MeV the curvature is convex for all τ. Once the temperature exceeds the phase transition temperature, there is only little change in $\Delta_B(\tau)$ as well as in $\ln(\Delta_C(\tau))$. In the case of $\Delta_B(\tau)$ in Fig. 7.2a the change in the curvature is inherent from the symmetry with respect to $\tau T = 0.5$ and the anti-periodic boundary

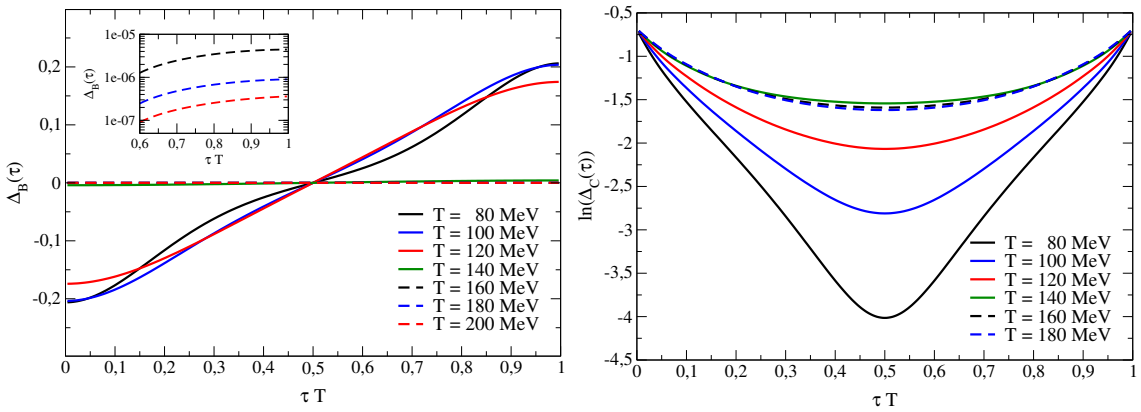

(a) (b)

Figure 7.2. Schwinger functions for the Maris-Tandy model in the chiral limit. In the left figure we display $\Delta_B(\tau)$ and in the right figure $\ln(\Delta_C(\tau))$.

condition. The non-vanishing $\Delta_B(\tau)$ for temperatures above T^c stems from a B dressing function not identical to zero due to numerics. Since $\Delta_C(\tau = 0, \beta) = 0$, we do not show the points for $\tau = 0, \beta$ in our plots.

In Fig. 7.3 we display the corresponding results for the Maris-Tandy interaction with a finite (light) quark mass. In this case the nature of the phase transition changes from a second order phase transition to a crossover, leading to a smooth change in the scalar dressing function of the quark. This translates into one of the key difference between Fig. 7.2 and Fig. 7.3: while $\Delta_B(\tau)$ becomes (almost) zero above T^c in the chiral limit we have a smooth change of $\Delta_B(\tau)$ due to a non-vanishing but decreasing scalar dressing function in the crossover scenario. A second difference is the temperature ordering of $\Delta_C(\tau)$. While in the chiral limit only temperature effects change the C function, for finite mass also the change of the B function feeds back in the solution of the coupled set of equations. These two competing effects can be observed by comparing Fig. 7.2b and Fig. 7.3b. One can see that temperature effects slightly decrease $\Delta_C(\tau)$ if the scalar dressing function is negligible (Fig. 7.2b), while the reduction of B with temperature in the crossover case leads to a net increases of $\Delta_C(\tau)$ in (Fig. 7.3b).

After investigating the Schwinger function of the Maris-Tandy model, we want to draw our attention to a more sophisticated calculation of the quark propagator using the previously defined unquenching procedure and the setup which reproduces the regularised condensate from lattice QCD. In this case we find a chiral crossover with a crossover temperature, defined via the inflection point, of $T_c \approx 0.155$ GeV. In Fig. 7.4 the corresponding Schwinger functions are displayed. They show a qualitatively similar behaviour as the results for the Maris-Tandy interaction with finite quark mass. For $\Delta_B(\tau)$ we observe a bigger incline in the region around $\tau T = 0.5$ as well as slightly slower convergence for the boundary value related to a different shape in

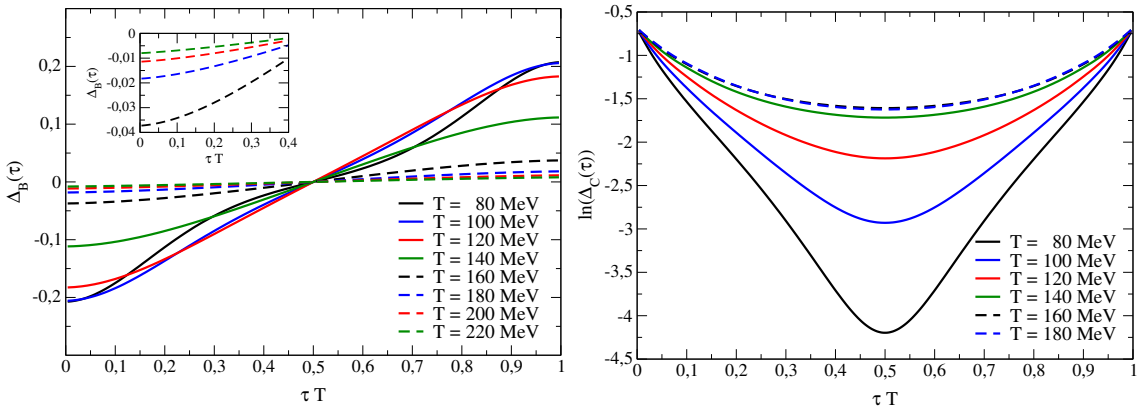

(a) (b)

Figure 7.3. Schwinger functions for the Maris-Tandy model with $m_l = 3.4$ MeV. In the left figure we display $\Delta_B(\tau)$ and in the right figure $\ln(\Delta_C(\tau))$.

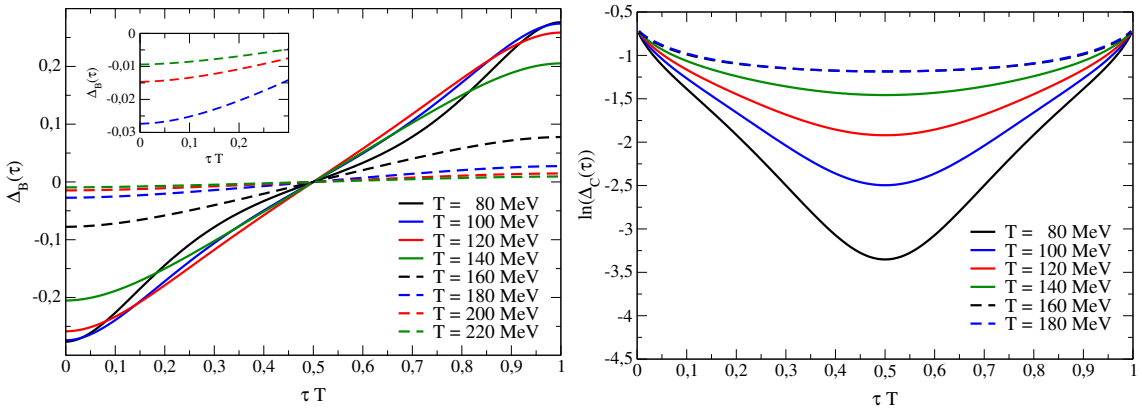

(a) (b)

Figure 7.4. Schwinger functions for the unquenched calculation fixed to lattice data (LAT_{2+1}). In the left figure we display $\Delta_B(\tau)$ and in the right figure $\ln(\Delta_C(\tau))$.

the quark condensate. For $\ln(\Delta_C(\tau))$ we find in general a smaller Schwinger function compared to the case with the Maris-Tandy interaction but a similar temperature ordering. However, above the (pseudo-) critical temperature T_c we observe a more flat shape for $\ln(\Delta_C(\tau))$ compared to the case in Fig. 7.2b and Fig. 7.3b.

Error analysis

Before we move on to the Bayesian reconstruction, which will be our tool to obtain a spectral function from a given Schwinger function, we want to investigate the numerical accuracy of Schwinger functions calculated in a DSE approach. For the evaluation of the change in $\Delta(\tau)$ due to a variation of the numerical parameter, we consider

$$\delta\Delta(\tau) = 2\left|\frac{\Delta_1(\tau) - \Delta_2(\tau)}{\Delta_1(\tau) + \Delta_2(\tau)}\right| \tag{7.9}$$

as the relative change, which has to be smaller than a desired precision for a reasonable step-size of the variation. By solving a quark DSE at finite temperature and potentially finite chemical potential one has the possibility to adjust various numerical parameters as well as techniques to treat the finite grid on which the functions are defined. Details are given in App. B and we summarize here for convenience:

- **External grid:** number of interpolation points N_{Spline} and explicitly used Matsubara frequencies N_{expl}.
- **Internal integration:** number of points for radial $N_{\text{r,int}}$ and angular integration $N_{\theta,\text{int}}$ points as well as cutoff for radial integral Λ.
- **Internal Matsubara sum:** number of explicitly summed $\mathcal{N}$ and implicit N_{pad} Matsubara frequencies.
- **Cutoff for Matsubara sum in the Fourier transformation:** Number of Matsubara frequencies $N_{\omega,\text{FT}}$ used in Eq. (7.3).

The numerics of the calculation with the Maris-Tandy interaction is, compared to the solution of the unquenched system, easier to handle. Therefore we start with this case for the chiral limit but checked that achieved precision also applies for the case with finite quark mass. The level of convergence was checked for two temperatures ($T = 0.16$ and $T = 0.26$ GeV) and $|\mathbf{p}| = 0$.

A variation of one of the aforementioned parameters has possibly either or both of two effects: introducing oscillations or a shift of the Schwinger function. While we account oscillations as numerical inaccuracy important for our precision, a (τ-dependent) shift is counted towards systematic errors and will be much smaller compared to systematic uncertainties due to the truncation. We use the setup summarized in Table 7.2. As indicated we sum up all Matsubara frequencies in the DSE explicitly to the cutoff, which is numerically less demanding for the Maris-Tandy model.

Setup	N_{Spline}	N_{expl}	$N_{\text{r,int}}$	$N_{\theta,\text{int}}$	$\mathcal{N}$	N_{pad}
MT	89	40	89 x 7	192 x 2	max	0
LAT_{2+1}	89	9	89 x 5	160 x 2	20	32

Table 7.2. Parameter for the high precision Schwinger functions in the medium. Additionally we used $\Lambda = 100$ GeV and $N_{\omega,\text{FT}} = 10^8$ in both cases.

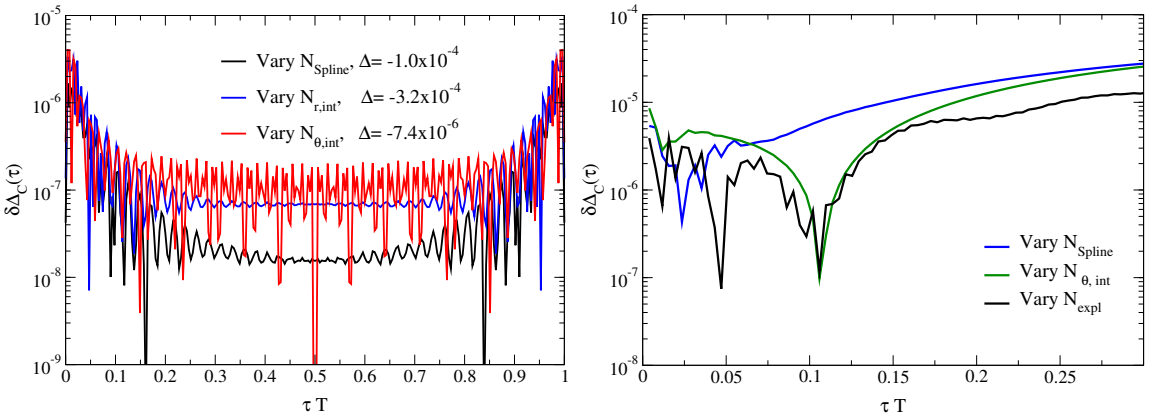

(a) (b)

Figure 7.5. Relative difference for the in-medium Schwinger function for the variation of certain numerical parameter for the Maris-Tandy model in the chiral limit (a) and the unquenched $N_f = 2 + 1$ system (b)

In Fig. 7.5a we show the influence of $N_{\text{Spline}} = 89 \to 99$ (involving a larger integration grid $N_{\text{r,int}} = 99\times7$), $N_{\text{r,int}} = 7\times89 \to 8\times89$ and $N_{\theta,\text{int}} = 192\times2 \to 224\times2$ on $\Delta_C(\tau)$.. For all variations we shifted the results by the indicated Δ. One observes oscillations smaller than 10^{-5} for all displayed variations. We also checked $N_{\text{expl}} = 40 \to 45$ which leads to oscillations smaller than 10^{-5}. If one varies $N_{\omega,\text{FT}} = 10^7 \to 10^8$ the resulting oscillations are below 10^{-6} and feature an even smaller shift. The influence of the cutoff was tested with an otherwise fixed setup going from $\Lambda = 100$ GeV $\to 500$ GeV, which seems a huge step-size but is small on a logarithmic grid as we use it. For this variation we find relevant oscillations of approximately 2.0×10^{-5} and a τ-dependent shift which is maximal at $\tau T = 0.5$ and of order 10^{-3}. The behaviour apparent in Fig. 7.5a, where the oscillations increase towards the boundary, is observed for most of the tested variations.

Next we want to draw our attention to the unquenched system for our calculations with the set LAT_{2+1}. The numerical treatment in this situation is more sensitive since the quark-loop also couples to the system. We found that particularly the thermal mass of the gluon depends on N_{expl} in a non-trivial way. Since the quark-loop and the thermal mass are independent quantities for the numerical analysis, we fixed

$N_{\text{expl}}^{\text{thermal mass}} = 5$ in the calculation of the thermal mass (but increase it to N_{expl} in the DSE) and accounted this as part of the truncation to make the analysis easier to track. Nevertheless we left the number of interpolation points in the quark-loop $N_{\text{Spline}}^{\text{QL}}$ to investigate in the numerical analysis. For the other quantities the situation is the same, we observe oscillations smaller than 10^{-5} close to the boundaries and a τ-dependent shift increasing towards $\tau T = 0.5$. Particularly a change in $\mathcal{N}$ and N_{pad} has little influence while a change in $N_{\text{Spline}}^{\text{QL}}$ only gives a τ-dependent shift. We checked that this shift does not hide oscillations on smaller scales.

The study of the Schwinger function for finite temperature can also be connected to details about confinement and positivity violations. As we will see after introducing the Bayesian reconstruction, in particular the curvature of $\ln(\Delta_C)$ is connected to those properties via the Spectral function.

7.2. Solving an inverse problem - method of the Bayesian reconstruction

We now come back to our main goal and aim to describe the quark spectral function at finite temperature. Therefore we need to introduce an approach to solve the inverse problem at hand,

$$\Delta_E(\tau, \mathbf{p}) = \int \mathcal{K}_E(\omega, \tau)\rho(\omega, \mathbf{p})\, d\omega \,, \tag{7.10}$$

$$\Delta_{KL}(\Omega, \mathbf{p}) = \int \mathcal{K}_{KL}(\omega, \Omega)\rho(\omega, \mathbf{p})\, d\omega \,, \tag{7.11}$$

where the kernels $\mathcal{K}$ are in Euclidean (E) and Källén-Lehmann (KL) representation respectively and given by

$$\mathcal{K}_E(\omega, \tau) = \cosh(\tau\omega) - \sinh(\tau\omega)\tanh(\frac{\omega}{2}\beta) \,, \tag{7.12}$$

$$\mathcal{K}_{KL}(\omega, \Omega) = \frac{1}{\Omega^2 + \omega^2} \,, \tag{7.13}$$

with Ω being an imaginary frequency, not necessarily a Matsubara frequency. Bayesian methods, like the one we introduce in this section, are widely applied, see e.g. [221–226]. Here we review the general ideas in form of a summary of [82]. We contrast the used Bayesian approach, which was developed by the participating authors Yannis Burnier and Alexander Rothkopf, with the MEM used in earlier works [71–75, 227].

In [227] the authors sketch the general idea of a Bayesian reconstructions and introduce the Maximum-Entropy method, which is one particular Bayesian reconstruction. All reconstructions of this form rely on the Bayesian interpretation of probabilities, particularly Bayes' theorem

$$P\left[A|B\right] = \frac{P\left[B|A\right] P\left[A\right]}{P\left[B\right]} \,,$$

where $P[A|B]$ is the conditional probability of an event A given B. This is in our case translated to

$$P[\rho|\Delta\mathcal{P}] = \frac{P[\Delta|\rho\mathcal{P}]\,P[\rho|\mathcal{P}]}{P[\Delta|\mathcal{P}]}\,, \tag{7.14}$$

where the abbreviations are assigned as Δ being the data, in our case the quark propagator, $\mathcal{P}$ representing the prior knowledge about the function to be reconstructed and ρ being the spectral function we aim to reconstruct. If one now investigates the single parts closely, it becomes apparent that $P[\Delta|\rho\mathcal{P}]$ describes the probability of a propagator given the prior and the reconstructed spectral function, which is the definition of the so-called likelihood L. The term $P[\rho|\mathcal{P}]$ describes how plausible a given ρ is, assuming the given prior knowledge. This leads to the core of the Bayesian reconstruction, where this prior probability is described using a functional called entropy or prior functional S and a given prior function m. In the case of the MEM the considered entropy is used to be the so-called Shannon-Jaynes entropy S_{SJ}. In the process of the Bayesian reconstruction the likelihood part fits the function of interest to the data, while the prior probability imprints the prior function on the reconstruction, which is by default the correct spectral function if there is no data present. The part $P[\Delta|\mathcal{P}]$ can be viewed as a normalisation factor. The Bayesian reconstruction uses this interplay between the likelihood L and the entropy S to find the most plausible reconstructed function of interest in a Bayesian sense. For the Bayesian method we apply, the construction of the entropy S is dictated by a number of axioms, which also show the differences between the novel Burnier-Rothkopf algorithm and MEM, where we follow the list in [82].

- **Axiom I: Subset independence:** This axiom translates to S being linear in ω, namely $S[\Omega_1, m(\Omega_1)] + S[\Omega_2, m(\Omega_2)] = S[\Omega_1 \cup \Omega_2, m(\Omega_1 \cup \Omega_2)]$, and is valid for any Bayesian reconstruction. This is satisfied if S is written as an integral over ω.

- **Axiom II: Scale invariance:** While the Shannon-Jaynes entropy S_{SJ} depends on the prior m(ω) by itself and therefore on the scale it carries, we use an entropy which only depends on the ratio ρ/m and is therefore scale independent. The hyperparamter $\tilde{\alpha}$ is introduced which carries dimensions.

- **Axiom III: Smoothness of the reconstruction:** The prior functional S should incorporate that the reconstruction results in a smooth function. This is imposed by making it more unlikely that two adjacent frequencies have different values even if it was possible within the error bars, leading to a specific form of the entropy $S = \tilde{\alpha}\int d\omega \left(a - b\frac{\rho}{m} + c\ln\left(\frac{\rho}{m}\right)\right)$. $S_{S,J}$ is not constructed according to this assumption.

- **Axiom IV: Maximum at the prior:** If there is no available data, S should be maximal at $\rho = m$, where one usually choose S to vanish. This constraint

imposes values for a,b and c up to an overall prefactor, which is absorbed into $\alpha \propto \tilde{\alpha}$.

By taking these axioms into account one arrives at the used entropy

$$S_\alpha = \alpha \int d\omega \left(1 - \frac{\rho}{m} + \ln\left(\frac{\rho}{m}\right)\right) . \tag{7.15}$$

According to the authors in [82] the prior distribution in Eq. (7.15) has, just as S_{SJ}, a quadratic shape around the minimum $\rho = m$ and therefore the uniqueness criteria is fulfilled analogously to MEM. As the authors point out, for any discretised point in frequency ω_l

$$\rho(\omega_l), m(\omega_l) \ll \frac{1}{\alpha} , \quad \rho(\omega_l) \ll m(\omega_l) ,$$

the functional S_α in Eq. (7.15) does not show asymptotic flatness which is inherent in S_{SJ}. This difference makes S_α superior to S_{SJ} and is one of the two pillars to distinguish the two approaches. The other pillar is the treatment of the (positive) parameter α. The reconstruction algorithm uses Eq. (7.14) in form of

$$P\left[\rho_\alpha | \Delta\mathcal{P}\alpha\right] \propto e^{Q_\alpha[S_\alpha, L]} ,$$

where $Q_\alpha[S_\alpha, L] = S_\alpha - L \leq 0$ and the most probable reconstruction for a given α is at

$$\left.\frac{\partial Q}{\partial \rho(\omega)}\right|_{\rho=\rho_\alpha} = 0 .$$

In MEM one reconstructs for several values of α and uses an average weighted by the evidence, which depends on a Gaussian approximation, to obtain the final reconstruction. The approach of Burnier and Rothkopf does not rely on a Gaussian approximation and α is integrated out to obtain $P\left[\rho|\Delta\mathcal{P}\right]$. For more details we refer to [82, 227] and references therein. For the reconstruction we can use information from either or both representations in Eqs. (7.10) and (7.11), i.e. using the Schwinger function, an Euclidean propagator for imaginary frequencies or a combination of both.

7.3. Quark spectral functions at finite temperature

In this paragraph we introduce the quark spectral function, which is not only interesting for its connection from calculations done in Euclidean space to Minkowski space but also for its contained information about thermal properties such as transport coefficients or observables like dilepton spectra [205]. Before we start investigating

results for the spectral function, we want to elaborate on the technical details.

Due to analyticity and causality, the quark propagator in imaginary time formalism has a spectral representation. This can be written for the Matsubara propagator as

$$\begin{aligned} S_{ab}(i\omega_n, \mathbf{p}) &= \int_{-\infty}^{\infty} \frac{\mathrm{d}\omega}{2\pi} \frac{\rho_{ab}(\omega, \mathbf{p})}{i\omega_n - \omega} \\ &= \int_{-\infty}^{\infty} \frac{\mathrm{d}\omega}{2\pi} \frac{\rho_{ab}(\omega, \mathbf{p}) \cdot (-i\omega_n - \omega)}{\omega_n^2 + \omega^2} \\ &= \int_{0}^{\infty} \frac{\mathrm{d}\omega}{2\pi} \left[(-i\omega_n) \frac{\rho_{ab}(\omega, \mathbf{p}) + \rho_{ab}(-\omega, \mathbf{p})}{\omega_n^2 + \omega^2} - \omega \frac{\rho_{ab}(\omega, \mathbf{p}) - \rho_{ab}(-\omega, \mathbf{p})]}{\omega_n^2 + \omega^2} \right] . \end{aligned} \tag{7.16}$$

The Källén-Lehmann kernel Eq. (7.13) is related to a special case of Eq. (7.16), where an even (with respect to ω) spectral function is considered and prefactors are divided out. The relation for the imaginary time propagator follows directly after the Fourier transformation to be

$$\begin{aligned} \Delta_{ab}(\tau, \mathbf{p}) &= \int_{-\infty}^{\infty} \frac{\mathrm{d}\omega}{2\pi} \frac{e^{\,(1/2-\tau T)\omega/T}}{e^{\,\omega/2T} + e^{\,-\omega/2T}} \rho_{ab}(\omega, \mathbf{p}) \, , \\ &= \int_{-\infty}^{\infty} \frac{\mathrm{d}\omega}{2\pi} \mathcal{K}_E(\tau, \omega) \, \rho_{ab}(\omega, \mathbf{p}) \, , \end{aligned} \tag{7.17}$$

where the kernel $\mathcal{K}_E(\tau, \omega)$ is equivalent to Eq. (7.12) and a positive function. Therefore, if the considered spectral function $\rho(\omega, \mathbf{p})$ is positive definite, the Schwinger function $\Delta(\tau, \mathbf{p})$ is positive definite as well.

The spectral function $\rho_{ab}(\omega, \mathbf{p})$, at zero chemical potential μ in a phase of even parity, which is T-symmetric and isotropic, can be split according to the Dirac structure of the quark propagator into separate matrix parts

$$\rho_{ab}(\omega, \mathbf{p}) = 2\pi \left(\rho_4(\omega, |\mathbf{p}|) \cdot [\gamma_4]_{ab} + \rho_v(\omega, |\mathbf{p}|) \cdot \left[\frac{i\boldsymbol{\gamma} \cdot \mathbf{p}}{|\mathbf{p}|} \right]_{ab} - \rho_s(\omega, |\mathbf{p}|) \cdot \mathbb{1}_{ab} \right) , \tag{7.18}$$

with the Matsubara and vector dressing ρ_4, ρ_v and ρ_s being the (scalar) dressing functions of the spectral representation. By comparing Eq. (7.18) with the definition of the quark propagator, the connection between the two sets of dressing functions is apparent. If the Fock space of the interacting theory under investigation is positive definite, the dressing functions in Eq. (7.18) obey an inequality [94], given by

$$\rho_4(\omega, |\mathbf{p}|) \geq \sqrt{\rho_v^2(\omega, |\mathbf{p}|) + \rho_s^2(\omega, |\mathbf{p}|)} \geq 0 \, . \tag{7.19}$$

This inequality gives information about the sign of $\rho_4(\omega, |\mathbf{p}|)$ and the relative size of the three dressing functions of the spectral function in case of a positive Fock

space. It implies by no means that a positive Fock space induces $\rho_{v,s}(\omega, |\mathbf{p}|) > 0$. A fundamental sum rule, fulfilled by a fermionic spectral function is

$$[\gamma_4]_{ab} = \frac{Z_2}{2\pi} \int_{-\infty}^{\infty} \mathrm{d}\omega \ \rho_{ab}(\omega, \mathbf{p}) \ ,$$

which can be derived from the canonical commutation relations and leads to

$$\begin{aligned} 1 &= Z_2 \int_{-\infty}^{\infty} \mathrm{d}\omega \ \rho_4(\omega, |\mathbf{p}|) \\ 0 &= \int_{-\infty}^{\infty} \mathrm{d}\omega \ \rho_v(\omega, |\mathbf{p}|) \\ 0 &= \int_{-\infty}^{\infty} \mathrm{d}\omega \ \rho_s(\omega, |\mathbf{p}|) \ , \end{aligned}$$

giving constraints for the symmetries of the three dressing function in Eq. (7.18) and again shows that $\rho_{v,s}(\omega, |\mathbf{p}|)$ alone can not be positive definite. Due to possible positivity violations a spectral function $\rho_4(\omega, |\mathbf{p}|)$ may contain negative contributions and therefore Eq. (7.19) could be violated, being a possible indication for confinement of the states in the Fock space. Eq. (7.19) implies that there are different sensible combinations of the dressing functions leading to a positive semi-definite spectral function:

- **Chirally symmetric case:** In the chirally symmetric phase it is $B(\omega_n, |\mathbf{p}|) = 0$ and therefore $\rho_s(\omega, |\mathbf{p}|) = 0$. If Eq. (7.19) is valid, one finds two positive semi-definite combinations

$$\rho_\chi^\pm(\omega, |\mathbf{p}|) = \rho_4(\omega, |\mathbf{p}|) \pm \rho_v(\omega, |\mathbf{p}|) \, .$$

- **Static case $|\mathbf{p}| = 0$:** In this case $\rho_v(\omega, 0) = 0$ and therefore Eq. (7.19) implies two positive semi-definite combinations

$$\rho_{stat}^\pm(\omega) = \rho_4(\omega, 0) \pm \rho_s(\omega, 0) \, .$$

- **General case:** As already pointed out, one can investigate $\rho_4(\omega, |\mathbf{p}|)$ by itself for positivity violations. There is the possibility of introducing an angle and define the spectral function depending on it [71]. This makes it possible to investigate the behaviour of a massive fermionic field at non-vanishing momentum.

With the scalar combinations in the chirally symmetric and the static case one can write the full spectral function as

$$\rho_{ab}(\omega, \mathbf{p}) = \rho^+(\omega, |\mathbf{p}|) \left[\mathbb{P}^+(\mathbf{p})\right]_{ac} [\gamma_4]_{cb} + \rho^-(\omega, |\mathbf{p}|) \left[\mathbb{P}^-(\mathbf{p})\right]_{ac} [\gamma_4]_{cb} \ ,$$

where $\rho^{\pm}$ are defined according to the specific case and with the projectors for the two cases being

$$\mathbb{P}^{\pm}_{\chi}(\mathbf{p}) = \frac{1}{2}\left[1 \mp \frac{i\boldsymbol{\gamma}\cdot\mathbf{p}}{|\mathbf{p}|}\right] \;, \quad \mathbb{P}^{\pm}_{stat} = \frac{1}{2}\left[1 \mp \gamma_4\right] \;.$$

It is noteworthy that $\mathbb{P}^{\pm}_{\chi}$ can be viewed as the energy projectors for massless modes and the spectral functions in the static case contains information about the (effective) thermal mass of the quark. The corresponding projections of the Matsubara propagator are

$$S^{\pm}_{\chi}(\omega_n, |\mathbf{p}|) = -\frac{i\omega_n C(\omega_n, |\mathbf{p}|) \pm |\mathbf{p}| A(\omega_n, |\mathbf{p}|)}{\omega_n^2 C^2(\omega_n, |\mathbf{p}|) + |\mathbf{p}|^2 A^2(\omega_n, |\mathbf{p}|)}$$
$$S^{\pm}_{stat}(\omega_n) = -\frac{i\omega_n C(\omega_n 0) \pm B(\omega_n, 0)}{\omega_n^2 C^2(\omega_n, 0) + B^2(\omega_n, 0)} \,,$$

where the imaginary time correlators follow with Eqs. (7.6) and (7.7) to be

$$\Delta^{\pm}_{\chi}(\tau, |\mathbf{p}|) = \Delta^{\chi}_{C}(\tau, |\mathbf{p}|) \mp \Delta^{\chi}_{A}(\tau, |\mathbf{p}|) \tag{7.20}$$
$$\Delta^{\pm}_{stat}(\tau) = \Delta_{C}(\tau, 0) \mp \Delta_{B}(\tau, 0) \,, \tag{7.21}$$

and the suffix χ indicating $B(\omega_n, |\mathbf{p}|) = 0$ in Eqs. (7.5) and (7.7).

A positive definite spectral function always leads to a positive definite Schwinger function. Additionally, there is a connection between positivity violations and the curvature of a corresponding Schwinger function at finite temperature, detailed in [94]. To make this thesis self-contained we repeat the key points of the derivation from [94], which could be applied to $\Delta_C(\tau, \mathbf{p})$ or one of the quantities defined in Eqs. (7.20) and (7.21) (or any combination obeying Eq. (7.19)). We start with considering the second derivative of the logarithm of Eq. (7.17),

$$\begin{aligned}\frac{\partial^2}{\partial\tau^2}\ln\Delta(\tau|\mathbf{p}|) &= -\left(\frac{\int \rho(\omega|\mathbf{p}|)\ \left(\frac{\partial}{\partial\tau}k(\tau,\omega)\right)}{\int \rho(\omega,|\mathbf{p}|)\ k(\tau,\omega)}\right)^2 + \frac{\int \rho(\omega,|\mathbf{p}|)\ \left(\frac{\partial^2}{\partial\tau^2}k(\tau,\omega)\right)}{\int \rho(\omega,|\mathbf{p}|)\ k(\tau,\omega)} \\ &= \frac{1}{\int \rho(\omega,|\mathbf{p}|)\ k(\tau,\omega)}\left[-\frac{\left(\int \rho(\omega,|\mathbf{p}|)\ k(\tau,\omega)\ \omega\right)^2}{\int \rho(\omega,|\mathbf{p}|)\ k(\tau,\omega)} + \int \rho(\omega,|\mathbf{p}|)\ \omega^2\ k(\tau,\omega)\right] \,.\end{aligned} \tag{7.22}$$

Using the Cauchy-Schwarz inequality the expression in square brackets in the second line of Eq. (7.22) is positive semi-definite [94]. One can deduce that

$$\rho(\omega, |\mathbf{p}|) \geq 0 \implies \frac{\partial^2}{\partial\tau^2}\ln\Delta(\tau, |\mathbf{p}|) \geq 0 \,,$$

and therefore a concave curvature of the Schwinger function implies that positivity is violated in the spectral function. However, this does not imply a positive definite spectral function given a convex Schwinger function.

Using this as a bound for the existence of a positive definite spectral representation, we are in position to define a lower bound on the deconfinement transition. Later, this can also be compared to the outcome of a spectral reconstruction.

7.4. Bayesian reconstruction of test data

Before we confront the Bayesian reconstruction with data obtained from solving a (coupled) system of Dyson-Schwinger equations, we want to evaluate the reconstruction procedure with realistic mock data using Eq. (7.17). In [74, 75] the authors obtain, using the MEM, two different kinds of positive definite spectral functions for ρ_4, both with regular peaks at finite ω and one featuring additionally a zero mode. We approximate this shape with a Breit-Wigner function for the regular peaks and a Gaussian for the zero mode

$$\rho_{\text{gaus.}}(\omega) = Ae^{-\omega^2/\sigma^2}$$
$$\rho_{\text{B.-W.}}(\omega) = \frac{k\Gamma M^2}{(\omega^2 - M^2)^2 + M^2\Gamma^2}\ , \quad k = \frac{2^{3/2}\gamma}{\pi\sqrt{1+\gamma}}, \quad \gamma = \sqrt{1 + \frac{\Gamma^2}{M^2}}\ .$$

Precision analysis

Using Eq. (7.17) immediately gives the corresponding Schwinger function after solving an integral. However, at this point we need to investigate the impact of our numerical approach. Exploiting the symmetries of the integrand, leaves us with

$$\Delta(\tau) = 2\int_\epsilon^\Lambda \frac{\mathrm{d}\omega}{2\pi}\mathcal{K}(\tau,\omega)\,\rho(\omega)\ ,$$

where we suppress the argument for the spatial momentum and already took into account that we need to evaluate this integral numerically with the introduction of an IR and an UV cutoff. An investigation of the precision of the result in a controlled manner, depending on the order N of the used Gauss-Legendre integration as well as ϵ and Λ is needed. As we will see later, we assume a certain relative precision on the imaginary time correlator for the reconstruction algorithm, which we can investigate in case of a given spectral function by varying N, ϵ and Λ.

For $\rho(\omega) = \rho_{\text{gaus.}}(\omega) + \rho_{\text{B.-W.}}(\omega)$ with $A = 1\ \text{GeV}^{-1}$, $\sigma = 0.5$ GeV, $M = 2$ GeV and $\Gamma = 0.75$ GeV (shown in Fig. 7.6a, together with the influence of a variation of M) we investigated the influence of N, ϵ and Λ for a temperature of $T = 0.2$ GeV and the number of data points in imaginary time $N_\tau = 128$. In Fig. 7.7a and Fig. 7.7b we display the dependence of $\delta\Delta(\tau)$ on ϵ and Λ, aiming for a precision in the sense of Eq. (7.9) of $\delta\Delta(\tau) = 10^{-6}$ for all τ. For the infrared cutoff ϵ we find a value of about 10^{-7} GeV satisfactory while an ultraviolet cutoff of 100 GeV seems to be large enough. Its remarkable that while the infrared cutoff has a relative impact almost independent of τ, the UV cutoff is important mainly at the corners of the interval $[0, \tau]$. However, we find an interval for ω spanning over many orders of magnitude, making a logarithmic grid necessary. The variation of N was done in advance and checked for convergence for each set of (ϵ, Λ). In Fig. 7.6b we show the influence of a variation of the model parameter for $\rho(\omega)$ on the Schwinger function.

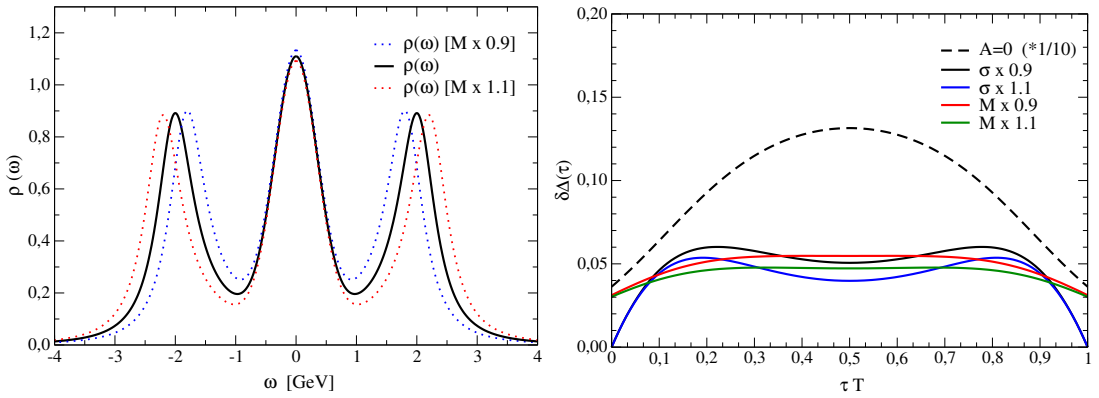

(a) (b)

Figure 7.6. Mock spectral function including two Breit-Wigner peaks and a Gaussian zero mode and the dependence of the Schwinger function on the parameter. Left: $\rho(\omega)$ for the standard setup and a variation of M. Right: Influence of a variation of A,σ and M on the $\delta\Delta(\tau)$.

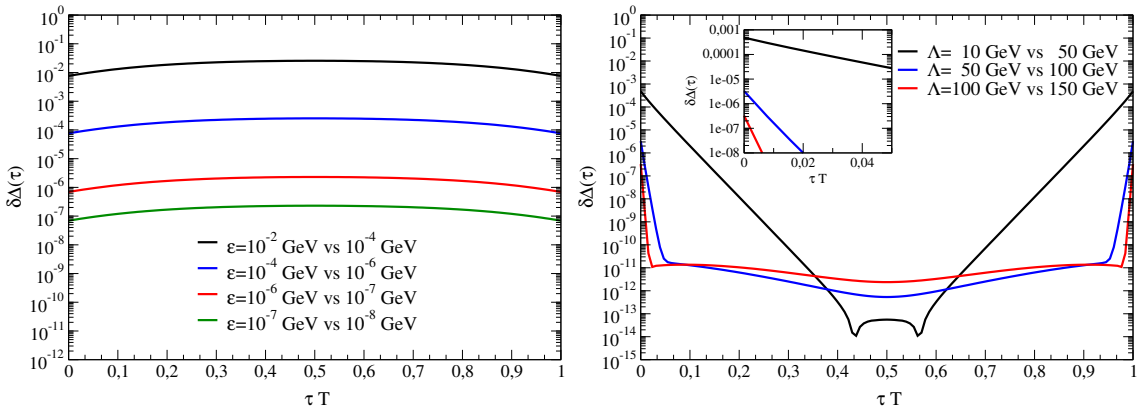

(a) (b)

Figure 7.7. Relative difference for the in-medium Schwinger function calculated from a Mock spectral function for the variation of the cutoff parameter. In the left figure we show a variation of the IR cutoff ϵ and in the right figure a variation of the UV cutoff Λ.

For this variation we also checked that convergence is still on the same level and the differences for Δ are not due to improperly adjusted numerics. Fig. 7.6b puts us into position to gauge how precise the reconstruction of a given Schwinger function could be, if one had the perfect method to solve the inverse problem and find the exact solution. Particularly the difference in the Schwinger function with and without the zero mode is large.

Finally we also checked, that the numerical precision for the Mock data is also high enough if one uses the representation Eq. (7.11), which involves the numerically less demanding kernel Eq. (7.13).

Now that we have a Schwinger function as well as data on the Matsubara modes (and in between) with a well controlled precision, we are in good shape to test the reconstruction algorithm. From the above analysis we learn that a logarithmic grid is a potentially important ingredient.

Reconstructing the test spectral function

The investigation presented in this chapter was performed in collaboration with Alexander Rothkopf, who supplied his program for the Bayesian reconstruction and supported the calculations. Before we start exploiting the power of the Bayesian reconstruction, we want to define some terminology and methodology. In the process of the Bayesian reconstruction we need to calculate the likelihood function where an error σ enters. We assume a constant relative error, which one can decrease and therefore take the (ideal) data to be more and more precise. For an error of $\frac{\Delta X}{X} = 10^{-N}$ we simply write dDN and investigate the change for $dDN \to dD(N+1)$, where our actual data should be of higher precision than dD(N+1). Another limit to be considered is the change with the number of data points N_τ and N_Ω taken into account.

For the following investigation we used a linear grid in ω for the reconstruction and therefore for the involved integrals for the likelihood L and entropy S. This is potentially possible, if the assumed error dDN is bigger than the error introduced via the numerical solution of the integral. Note, that the kernel $\mathcal{K}_{KL}$ is in this case independent of the temperature and we use a temperature-independent grid for the values of Ω, where we divide the interval $[0,\Lambda_\Omega]$ with N_Ω points, including imaginary frequencies on the Matsubara poles and beyond. For the reconstruction grid in ω we have $N_\omega = 2500$ points in total, of which we locate 1250 in the interval [0,4] and the rest in $[4, \Lambda_\omega]$. While the interval of the Schwinger function is fixed with the temperature, $\Lambda_\tau = \beta$, the cutoffs Λ_ω and Λ_Ω need to be subject to investigations of their temperature dependence and the influence on the outcome of the reconstruction.

A collection of results from the Bayesian reconstruction is shown in Fig. 7.8. In (a) we compare the results for imaginary frequency input data (e.g. solving the inverse problem of Eq. (7.11)), for two different values for N_Ω and the assumed precision dDN for $N \in \{3, 4, 5\}$, with the correct result (indigo double-dash-dotted line). We find little influence of the additional data points for $N_\Omega = 128$ at larger frequen-

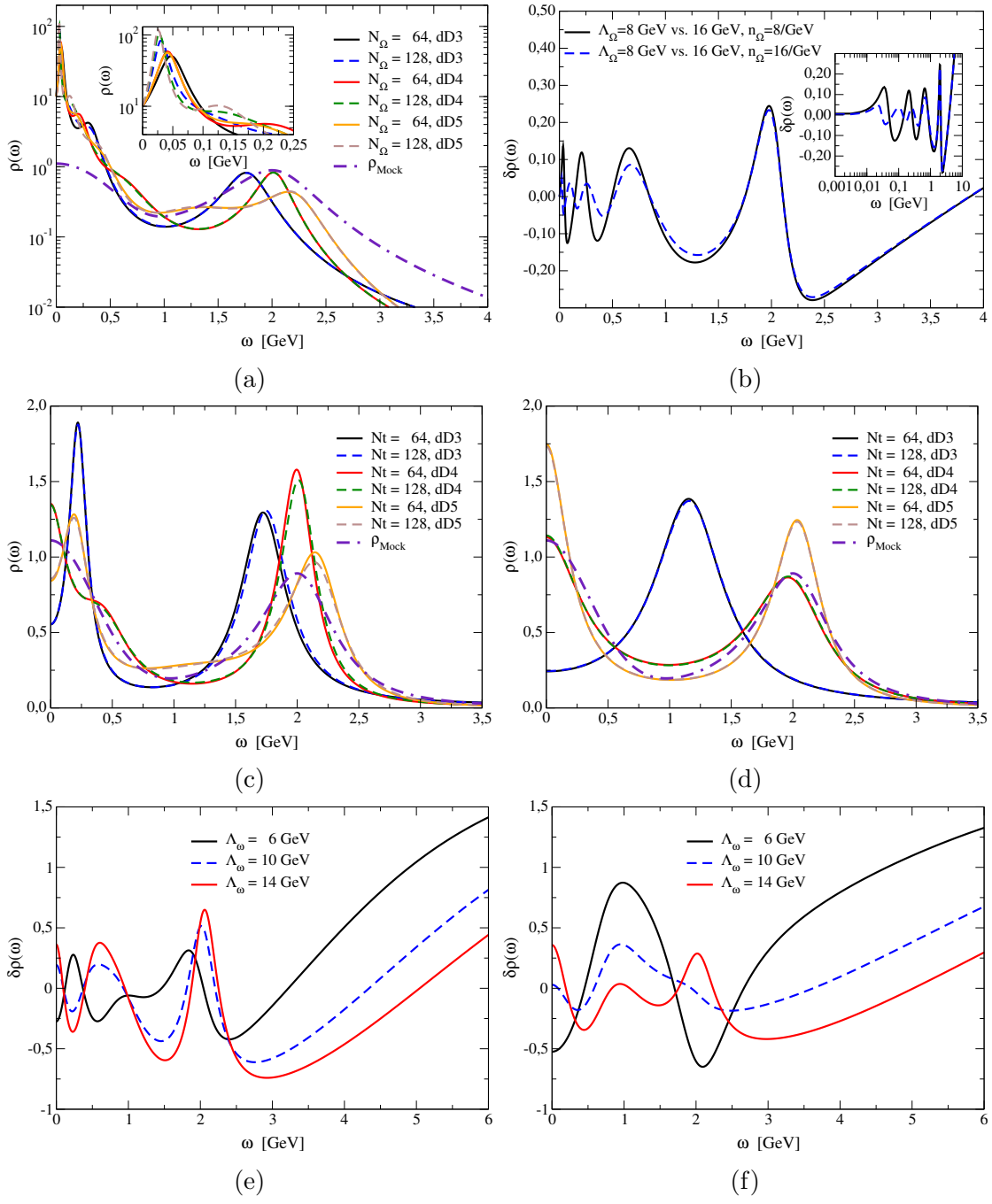

Figure 7.8. Collection of results for the Bayesian reconstruction of test data. In (a) we plot the results from solely imaginary frequencies and compare the influence of the number of data points N_Ω and the assumed precision dDN. (b) highlights the influence of Λ_Ω, where we show the relative differences for $\Lambda_\Omega = 8$ and 16 GeV with the same spacing for Ω. (c) and (d) show the reconstruction for imaginary time data from the Schwinger function, compared for different N_τ and dDN for $T = 0.1$ GeV and $T = 0.5$ GeV. In (e) and (d) the relative difference for a smaller ($\Lambda_\omega = 6$ GeV) and a bigger ($\Lambda_\omega = 14$ GeV) reconstruction grid is displayed.

cies, while there is some deviation for $\omega < 1$ GeV (compare solid and dashed lines). While the results for $dD4$ seem to predict the peak position to a very good accuracy, the reconstruction with $dD5$ deviates more, which presumably is where the precision of the integration starts to matter. However, observing the change induced from $dD3 \to dD4$ we conclude it would be necessary to have a stable result for $dD5$ (and even beyond), in order to prove convergence. In (b) we compare the relative difference (analogously defined to Eq. (7.9)) of the reconstruction results, where we vary Λ_Ω, the cutoff for the imaginary frequencies. For the comparison, we leave the point-density constant, e.g. $n_\Omega = N_\Omega/\Lambda_\Omega = \text{const}$. It is apparent, that for smaller frequencies $\omega < 3$ GeV, the influence of Λ_Ω depends on n_Ω, while it seems to be independent of n_Ω beyond this point and rises. However, (a) implies that beyond $\omega = 3$ GeV the result should be already one order of magnitude smaller, therefore the net-influence will be little. Figures (c)-(d) show results for the reconstruction of imaginary time input, e.g. solving the inverse problem in Eq. (7.10). In (c) and (d) we display a comparison of $N_\tau = 64$ and $N_\tau = 128$ as well as dDN for $N \in \{3, 4, 5\}$ to the exact solution for $T = 0.1$ GeV and $T = 0.5$ GeV. For $T = 0.1$ GeV in (c), we find little but still observable difference for a higher number of data points, which seems not to be the case in (d) for $T = 0.5$. This can be explained by reminding of the definition $\Lambda_\tau = \beta$, where with given N_τ the data point density increases with increasing temperature. For our purpose the precision due to a change in N_τ is satisfactory, while we find again that the results for $dD4$ seem to reproduce some features of the test function ρ_{Mock} quite well, but $dD5$ then is further away from the spectral function used as input. However, in (d) we observe a general tendency towards better reconstruction, which lead us to the investigation of the temperature dependence of Λ_ω in (e) and (f), performed again for $T = 0.1$ GeV and $T = 0.5$ GeV. For this purpose we varied Λ_ω by $\pm 40\%$, resulting in an interval still on the same scale. For the smaller temperature we observe, that decreasing the cutoff of the reconstruction interval gives a result a little bit closer to the exact result. For $T = 0.5$ GeV in Fig. 7.8f however, this is not in general true, where a bigger interval seems to be better for $\omega > 0.5$ GeV, but not for smaller frequencies. Note, the wiggles at small frequencies ω, as apparent in some of the curves shown Fig. 7.8, have already been observed in the context of the Bayesian reconstruction, see e.g. [224].

An investigation of combined input from imaginary time and imaginary frequencies was performed by Alexander Rothkopf for slightly different mock data. He observed a tendency towards better reconstruction performance with this input, which is one way to constrain the spectral function in separate ranges of ω with different sources for the input.

Realistic spectral functions and perspectives

From the above analysis we learn, that implementing a logarithmic grid for the Bayesian reconstruction of fermionic spectral functions will be necessary in order

to check the convergence in some well defined limits. It is of course tempting, to confront the analysis and reconstruction with realistic data, obtained by solving the Dyson-Schwinger equations at finite temperature, e.g. as done in Ch. 3, Ch. 4 and Ch. 5. However, before doing so, the numerical details for the reconstruction have to be understood in more detail and features such as the logarithmic grid, which makes it possible to extend the interval to higher Λ_ω without increasing the calculation time tremendously by keeping the same density for ω points, must be implemented. We already performed first calculations with a logarithmic grid, which need to be investigated further in order to give stable and well understood results. Once this numerical details are set, one could take the Schwinger function and the data for imaginary frequencies as input and give first results on a Dyson-Schwinger prediction of the quark spectral function.

Summary

In this chapter we investigated details on the analytic structure of the quark propagator in the vacuum and at finite temperature. The calculation of the so-called Schwinger function, as the Fourier transform with respect to (imaginary) time, gave results in agreement with earlier works for a rainbow-ladder model for the interaction for a fit of two complex poles. Results for the truncation developed in Ch. 3, Ch. 4 and Ch. 5 are presented and in good agreement with expectations, such as relative magnitude of the complex mass from a fit and agreement in the analytical structure for $N_f = 2 + 1$ and $N_f = 2 + 1 + 1$ calculations with fixed properties of pseudoscalar mesons. Results for the finite temperature Schwinger functions are in agreement with fundamental requirements such as antiperiodic boundary conditions. A study of the numerical precision for the Schwinger function obtained from the Maris-Tandy interaction and calculations in our standard truncation are presented and show that a precision of 10^{-5} is possible. We also introduced one way to tackle the inverse problem of finding a spectral function with given correlator data, which is the Rothkopf-Burnier version of a Bayesian reconstruction. Finally we present investigations of this reconstruction method with mock data, performed in collaboration with Alexander Rothkopf, which show that some numerical problems have to be solved for the reconstruction of fermionic spectral functions, before the method can be confronted with (non-ideal) input data obtained from the solution of a coupled set of Dyson-Schwinger equations.

8. Conclusion and outlook

Coming back to where you started is
not the same as never leaving.

(Sir Terry Pratchett)

In the work presented here we executed investigations of the phase diagram of strongly interacting matter, by approaching the theory of quantum chromodynamics in the non-perturbative functional approach of Dyson-Schwinger equations. Those are the quantum (field) equations of motions for correlators, giving informations about the fundamental degrees of freedom in the phase of the quark-gluon plasma, quarks and gluons. The studied phase transitions are mostly connected to chiral symmetry, which changes its manifestation in form of dynamical chiral symmetry with temperature, from a chirally broken to a restored phase. Confinement/deconfinement transitions are as well studied in some selected scenarios.

In Ch. 3 we gauged our ansatz by comparing results in the state of the art unquenched calculation for $2+1$ quark flavours to previous work. In this setup, which one calls a truncation for its truncating the system of Dyson-Schwinger equations (represented by an infinite tower of coupled integral equations), self-consistent back coupling from the matter (quarks) to the gauge (gluons) sector is achieved by taking the quark-loop in the gluon DSE into account, while at the same time all other contributions to the gluon are assumed to be given by a quenched lattice correlator. To close the system another component, the quark-gluon vertex, was needed. For this vertex we used a well established ansatz, consisting of the first term of the so-called Ball-Chiu vertex obeying the Abelian counterpart of the Slavnov-Taylor identities, multiplied by an infrared enhanced dressing function assumed to mimic the non-Abelian contributions and provided with the correct perturbative behaviour. The truncation was designed in earlier works to reproduce the crossover scale from lattice QCD at zero light quark chemical potential and as a result, also matching its shape. The presented results for the propagators are in line with previous works and consequently we find agreement for the phase diagram for $N_f = 2+1$. Features of this phase diagram are a critical endpoint with $\mu_B/T > 2$ and a curvature of the chiral transition line which is in the range of some lattice predictions, with the tendency of being to large. The ability to obtain results at finite quark chemical potential in a sensible calculation, where gluonic as well as thermal properties of the quarks agree with lattice results puts us into position to extend the given system in

order to obtain improved results.

We were in particular interested in the influence of additional degrees of freedom on the phase structure. In earlier works, the inclusion of a dynamical strange quark proved to be important to the manifestation of the phase diagram. Therefore, as a first step towards a systematically improved setup, we added the charm quark as a dynamical degree of freedom in Ch. 4. From perturbation theory one assumes the charm quark effects to be suppressed due to its mass. However, this is not *a priori* true in non-perturbative approaches. The performed calculation was the first of its kind, where we found the most important aspect to be properly adjusted scales. In a system, where the vacuum properties of the relevant pseudoscalar mesons were fixed separately for $N_f = 2 + 1$ and $N_f = 2 + 1 + 1$, by solving the Bethe-Salpeter equation within our truncation, we found the charm quark to have no influence on the phase diagram. On the other hand an investigation of the thermal mass of the gluon for high temperatures showed appropriate scaling with the number of dynamically treated quark flavours, also proving the charm quark to be non-negligible for the unquenching of the gluon. However, the net-influence on the phase structure induced by the dynamical charm quark is negligible and therefore the $N_f = 2 + 1$ prediction for the phase diagram in the standard setup from Ch. 3 is found to be valid also for four dynamical quark flavours. Apart from the charm quark there is another species of degrees of freedom potentially having a sizeable influence on the QCD phase diagram, in particular in the region of large chemical potential. These are the hadronic degrees of freedom as the bound states formed by quarks and gluons. In Ch. 5 an investigation about the impact of the nucleon in an $N_f = 2$ flavour calculation was presented. Throughout this exploratory work parts of the quark-gluon vertex, which contain baryonic contributions, where identified. By expressing the baryon as a bound state of mostly quark-diquark correlations an extension of the standard truncation was introduced, where baryons and diquarks played a crucial role. Due to the lack of explicit knowledge about their finite temperature and chemical potential dependence, we referred to vacuum results were possible and investigated variations of possible temperature-dependent quantities such as the mass of the hadrons and their wave functions. Nonetheless we found an impact only on a 10% level, which is surprisingly small, since the nucleon depends on the quark chemical potential as $\mu_B = 3\mu_q$. A systematic investigation of baryonic properties at finite temperature and chemical potential is certainly one way to improve the exploratory work presented here and left for future investigations.

While these extensions of the system were concerned with additional degrees of freedom, we also followed an approach for a systematic investigation in terms of the DSE for the quark-gluon vertex. This DSE proves to be a difficult system yet encodes information about flavour, temperature and chemical potential dependence of the vertex via the internal quark and gluon propagators and various three-point functions. The work presented in Ch. 6 applies an internal model for the quark-gluon vertex, where a full calculation would feature the fully back coupled quark-gluon vertex it-

self. The model-vertex, which we chose as the one we widely employed throughout this work, depends on the attached quark lines making the ansatz comparable to the actual full version in terms of numerical logistics. First results in this simple setup show a dependence on the internal infrared strength of the quark-gluon vertex and also make the necessity of self-consistently calculating the quark-loop apparent. Nonetheless it already sets the stage for systematic improvement and possible extensions, be it more consistent flavour, temperature and chemical potential dependence or the inclusion of mesons or baryons on a level different to the study in Ch. 5.

An investigation concerned with the analytical properties of the quark supplemented the other investigations from a different point of view. Knowledge about the so-called spectral function, which encodes all information about the analytic structure, grants access to informations about Minkowski space properties, deduced from calculations in Euclidean space. For the quark propagator these properties feature informations about bound states. In Ch. 4 and Ch. 5 bound states in vacuum were used as input, while for the solution of the bound state equation an important ingredient is the complex quark propagator. However, we were mainly concerned with effects at finite temperature, where the spectral function gives access to important observables such as dilepton production rates and transport coefficients. In Ch. 7 the Schwinger function, as the Fourier transform with respect to (imaginary) time, encodes information about the possible pole-structure of the quark and is closely related to the spectral function. Results for the vacuum as well as the medium were presented, agreeing with previous work were comparison was possible. The Matsubara propagator and the Schwinger function are related to the spectral function by an ill-defined inverse problem. Our strategy to solve for the spectral function was introduced with the Rothkopf-Burnier algorithm, which is a Bayesian reconstruction able to return the Bayesian answer to the inverse problem. The status of the reconstruction for test data was presented, showing that yet some numerical details for the reconstruction with fermionic kernels have to be investigated, in order to obtain reliable results after confronting it with data from the Dyson-Schwinger equation. At finite chemical potential the imaginary part of the dressing functions is non-vanishing. To address spectral properties in this case, we first need to resolve artificial behaviour for the ultraviolet in the imaginary part of the quark propagator. The resolution of this numerical artefact is not only necessary for the spectral function, but also for connected quantities, such as the quark number density. The impact of this behaviour on the position of transition lines and the CEP is little, due to its appearance in the UV and the scale of the imaginary part of the dressing functions being at least one order of magnitude smaller compared to the real part. An answer to the inverse problem and therefore the spectral function in the whole $T - \mu$ plane is certainly important, since it directly connects calculations in our functional approach to the real world and therefore to the experiment, independent of the applied truncation. Therefore further studies, building upon the here presented investigations are necessary to obtain a reliable answer and are left for future investigations.

What became apparent throughout all chapters is, that the state of the art truncation, as presented in Ch. 3, remains to give still valid predictions, even if the charm quark or baryons in the manner of Ch. 4 and Ch. 5 are included.

Future work should be concerned with two main subjects: first, the numerical artefacts in the imaginary part of the quark propagator should be resolved and the calculation of the quark spectral function has to be put forward, in order to make a connection to experiments possible to eventually gauge the applied truncation. This truncation is the content of the second direction, where one has to try to systematically develop a setup in view of Ch. 4, Ch. 5 and particularly Ch. 6, covering all necessary aspects for an appropriate description of the QCD phase diagram in a functional approach.

9. Acknowledgement

> The presence of those seeking the truth is infinitely to be preferred to the presence of those who think they've found it.
>
> *(Sir Terry Pratchett)*

Throughout the time of working on my dissertation, a lot of people supported and helped me to finish it. At this point I want to take the opportunity to thank all of them.
First I want to thank my thesis advisor Prof. Christian S. Fischer for giving me the opportunity to work in his group on this difficult yet fascinating topic, for his guidance and support as well as his ever-open door.
Next I would like to thank Prof. Lorenz von Smekal, not only for being the second examiner of this thesis and his interest in its content but also for interesting and helpful discussions during my HGS-HIRE PhD committee meetings.
In the early stage of my work the help by Jan Lücker was very important, since he shared his knowledge about finite temperature QCD and Dyson-Schwinger equations with me and helped to solve some problems of the 'find the needle in the haystack'-kind. I also want to thank Jan Haas for ensuring that my caffeine level was always high enough and sharing the work on the computer administration with me. Thorsten Steinert was very helpful during discussions in the second half of my work giving me some insights and ideas as well as distraction when needed. Both, Helios Sanchis-Alepuz and particularly Richard Williams helped me in many different ways: very insightful discussions and joyful conversations about physics as well as non-physics topics in addition to them making sure I do my weekly workload concerning our computing-cluster made them an essential part of my daily work. I am grateful to Richard Williams for introducing me to the bittersweet world of the quark-gluon vertex and for our cooperation on its representation at finite temperature. Many thanks go to Gernot Eichmann for our collaboration on the baryonic contributions to the phase diagram. For the collaboration on the spectral properties of quarks I want to thank Prof. Jan M. Pawlowski and in particular Alexander Rothkopf for sharing his expertise, his program and his time for the Bayesian reconstruction of spectral functions with me. I am truly grateful for the help of Richard Williams and

Jan Lücker who proof-read the main body of my thesis as well as Alessia Palmese, Eduard Seifert and Thorsten Steinert for their comments on the introduction.

It is with particular pleasure that I thank my friends and family. I am grateful to my friends Magdalena Untenecker, Alessia Palmese, Richard Williams and all those others who kept my spirits up. I also want to thank my girlfriend Christine for all the joyful hours and not giving up on me and my time schedule. In the end I would especially like to mention my mother Petra and my sister Katharina, whose support and care ensured that I find enough time for my studies and as well as for the endless hours of me spending on my PhD.

Appendices

A. Conventions

In our work we follow the conventions from [67,72]. All calculations are preformed in Euclidean space-time, with the flat metric $g_{\mu\nu} = \delta_{\mu\nu}$. The connection to Minkowski space is apparent from the imaginary time formalism with

$$\tau = -it \,, \tag{A.1}$$

$$k_4 = \omega_k = i\omega \,, \tag{A.2}$$

with t being the (Minkowski) time and ω the 0^{th} component of the momentum in Minkowski space while k_4 represents the momentum after the Wick rotation to imaginary time in Euclidean space. Note that the standard procedure for going from Minkowski to Euclidean space is done in momentum space and features a relative sign compared to the imaginary time formalism ($p_0 = -i\omega$), which does not influence the resulting metric. The situation for the rotation is visualised in Fig. A.1. This needs

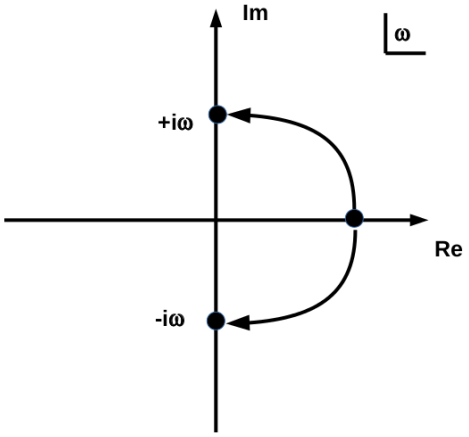

Figure A.1. Comparison of the Wick rotation to common Euclidean space and in the imaginary time formalism

to be kept in mind for analytic continuation but has no influence on observables, since summations are over positive and negative (imaginary) frequencies.

For the Dirac γ-matrices we use

$$\begin{aligned} \gamma_4 &= -\gamma_0^M \\ \gamma_j &= -i\gamma_j^M, \end{aligned} \tag{A.3}$$

with

$$\{\gamma_\mu, \gamma_\nu\} = 2\delta_{\mu,\nu} \ , \tag{A.4}$$

$$\gamma_1^2 = \gamma_2^2 = \gamma_3^2 = \gamma_4^2 = 1 \ , \tag{A.5}$$

with the anti-commutator $\{.,.\}$.

B. Numerical details

B.1. Propagators and quark DSE

B.1.1. Explicit equations for the resulting quark DSE

The quark DSE for the truncation in Ch. 3 in its explicit form is given by

$$\begin{aligned} A(\mathbf{p},\omega_p) &= Z_2 + Z_2\, C_F\, g^2 \sum\!\!\!\!\!\!\int_l \frac{\Gamma(q^2)}{D(l)}\, \frac{A(l)K_{AA} + C(l)K_{AC}}{\mathbf{p}^2}\,, \\ B(\mathbf{p},\omega_p) &= Z_2 Z_m m_R + Z_2\, C_F\, g^2 \sum\!\!\!\!\!\!\int_l \frac{\Gamma(q^2)}{D(l)}\, B(l)\, K_{BB}\,, \\ C(\mathbf{p},\omega_p) &= Z_2 + Z_2\, C_F\, g^2 \sum\!\!\!\!\!\!\int_l \frac{\Gamma(q^2)}{D(l)}\, \frac{A(l)K_{CA} + C(l)K_{CC}}{\tilde{\omega}_p}\,, \end{aligned} \tag{B.1}$$

where $q = p - l$, $C_F = \frac{4}{3}$ is the Casimir, Z_2 is the wave-function and Z_m the mass renormalisation constant The Matsubara sum as well as the integration over the loop three-momentum $\mathbf{l}$ is represented by

$$\sum\!\!\!\!\!\!\int_l \cdots = T \sum_{\omega_{n(l)}} \int_\epsilon^\Lambda \frac{d^3 l}{(2\pi)^3} \cdots \tag{B.2}$$

with the infrared cutoff ϵ, the UV cutoff Λ and the Matsubara index $n(l)$ for fermionic Matsubara frequencies $\omega_{n(l)} = [2n(l)+1]\,\pi T$.

The denominator-part of the quark propagator is given by

$$D(\mathbf{l},\omega_l;\mu) = \mathbf{l}^2 A^2(\mathbf{l},\omega_l;\mu) + \tilde{\omega}_l^2\, C^2(\mathbf{l},\omega_l;\mu) + B^2(\mathbf{l},\omega_l;\mu)\,,$$

where μ enters as an external parameter, also visible in the definition $\tilde{\omega}_l = \omega_l + i\mu$ and the kernels of the integral read

$$K_{AA} = \Gamma_S \left[\frac{Z_L}{q^2} \frac{\omega_q^2}{q^2} \left(\mathbf{p}\cdot\mathbf{l} - 2\,\frac{\mathbf{p}\cdot\mathbf{q}\,\mathbf{l}\cdot\mathbf{q}}{\mathbf{q}^2} \right) \right. \tag{B.3}$$

$$\left. + 2\,\frac{Z_T}{q^2}\frac{\mathbf{p}\cdot\mathbf{q}\,\mathbf{l}\cdot\mathbf{q}}{\mathbf{q}^2} \right] + \Gamma_4\,\frac{Z_L}{q^2}\frac{\mathbf{q}^2}{q^2}\,\mathbf{p}\cdot\mathbf{l}\,, \tag{B.4}$$

$$K_{AC} = (\Gamma_S + \Gamma_4)\,\frac{Z_L}{q^2}\,\frac{\mathbf{p}\cdot\mathbf{q}}{q^2}\,\tilde{\omega}_l\,\omega_q\,, \tag{B.5}$$

$$K_{BB} = \Gamma_S \left(2\frac{Z_T}{q^2} + \frac{Z_L}{q^2}\frac{\omega_q^2}{q^2} \right) + \Gamma_4\,\frac{Z_L}{q^2}\frac{\mathbf{q}^2}{q^2}, \tag{B.6}$$

$$K_{CA} = (\Gamma_S + \Gamma_4)\,\frac{Z_L}{q^2}\,\frac{\mathbf{l}\cdot\mathbf{q}}{q^2}\,\omega_q\,, \tag{B.7}$$

$$K_{CC} = \Gamma_S \left(2\,\frac{Z_T}{q^2} + \frac{Z_L}{q^2}\frac{\omega_q^2}{q^2} \right) \tilde{\omega}_l - \Gamma_4\,\frac{Z_L}{q^2}\frac{\mathbf{q}^2}{q^2}\,\tilde{\omega}_l\,. \tag{B.8}$$

Note, that for $\mu \neq 0$, the imaginary part has no homogeneous term in the quark DSE. This has potential influence on the solution space.

B.1.2. Representation of the quark and gluon propagator

Quark

For the representation of numerical objects we used two different approaches with some features in common. For the quark propagator it is obvious, that one can only calculate it for a finite number of Matsubara frequencies. This is justified by the restoration of O(4)-invariance at some scale (see also main body Ch. 3). Therefore it is useful to define a set of interpolation objects, one for each Matsubara frequency, where the number of (positive) frequencies taken into account is N_{expl} leading to $2N_{\text{expl}}$ interpolators in $|\mathbf{p}|$. Each interpolator is defined on N_{Spline} points in an interval of $[\epsilon, \Lambda]$, where we use the O(4) cutoff (Λ) to keep the grid independent of the Matsubara mode. This technically leads to a different interval in p^2 for each Matsubara frequency, which is however a negligibly small difference. If the quark propagator is evaluated for a spatial momentum beyond the defined interval, it is constantly extrapolated from the last point, if not otherwise indicated. Due to O(4) invariance we can extrapolate the dressing functions in Matsubara direction in the following way

$$\mathcal{D}(|p|,\omega_n) = \begin{cases} \mathcal{D}(\sqrt{|p| + \omega_n^2 - \omega_{N_{\text{expl}}-1}^2}\,, \omega_{N_{\text{expl}}-1}) & \text{if } \omega_n > 0 \\ \mathcal{D}(\sqrt{|p| + \omega_n^2 - \omega_{-N_{\text{expl}}}^2}\,, \omega_{-N_{\text{expl}}}) & \text{if } \omega_n < 0 \end{cases}, \tag{B.9}$$

for $\mathcal{D} \in \{A, B, C\}$. In the beginning of the work on the thesis we used a representation by Chebychev-polynomials but switch to natural splines later.

Gluon and quark-loop

For the quenched part of the gluon we have a functional representation, as given in Eq. (3.6). It is important to mention, that in Eq. (3.6) the dressing function seems to depend on the square of the four momentum. This is in general not true for finite temperature due to the introduction of a heat bath, where one would have different dressings for each Matsubara mode. However, it has been shown that the quenched gluon correlator fulfils to very good precision the O(4) invariance already for the 0^{th} Matsubara frequency [64, 109], namely

$$Z_{T,L}(\mathbf{q}^2, \omega_q) \approx Z_{T,L}(\mathbf{q}^2 + \omega_q^2, 0) \; . \tag{B.10}$$

With this approximation and Eqs. (3.6) and (3.7) we are able to calculate the quenched gluon propagator for any given temperature and momentum. For the quark-loop we need a numerical representation for the 0^{th} Matsubara frequency, which we treated equivalently to the quark propagator. However, for its evaluation some technical details are necessary. The Matsubara sums are evaluated explicitly for all Matsubara frequencies up to the the closest Matsubara above the cutoff. $\Pi_{L,T}^{regular}(\mathbf{q}^2, 0)$, which looks similar to the vacuum quark-loop, is obtained by subtracting $\lim_{\mathbf{q}\to 0} \Pi_{L,T}(\mathbf{q}^2, \omega_q = 0)$ within the same numerical precision, while the thermal mass itself must be evaluated for a cutoff of $\Lambda_{\text{thermal mass}} = 2000$ GeV, including a full Matsubara sum, in order to achieve stability of this quantity. In the evaluation of the thermal mass it is necessary to recover the vacuum limit $A(l) = C(l)$ at high four momentum squared. This condition is implemented by the substitution

$$C(l) \to \left(1 - e^{-\frac{l^2}{\Lambda_{AC}}}\right) \cdot A(l) + e^{-\frac{l^2}{\Lambda_{AC}}} \cdot C(l) \; , \tag{B.11}$$

where we take $\Lambda_{AC} = 40$ GeV^2. The introduction of this behaviour is solely necessary due to the numerical evaluation of the the system, where it should be fulfilled automatically if solved exactly.

As a last remark we want to highlight, that the initial quark-loop is calculated with $A = C = 1$ and B either 10 MeV or 1 GeV, to achieve convergence in a first order phase transition region towards either of the two possible stable solutions. Since the quenched vacuum gluon fulfils $Z^{vac}(q^2 = 100 \text{ GeV}^2) \approx 1$, we normalise the quark-loop to be 0 at $q^2 = 100$ GeV^2 and transfer this information from the vacuum to the medium in form of a shift.

B.1.3. Matsubara sum and solution of the integrals

The sum of the Matsubara frequencies in the quark DSE is divided into two parts in order to minimize the numerical effort. In one part, the Matsubara sum is carried out explicitly for $\mathcal{N}$ (positive) Matsubara frequencies, while for the other part it is

approximated by an integral

$$\begin{aligned} \mathrm{T}\sum_{n:\,\omega_n^2<\Lambda^2} \mathrm{f}(\omega_n) &\to \frac{1}{2\pi}\int_{-\Lambda}^{\omega_{-\mathcal{N}}-\pi T} \mathrm{f}(\omega)\mathrm{d}\omega + \mathrm{T}\sum_{-\mathcal{N}\leq n\leq \mathcal{N}-1} \mathrm{f}(\omega_n) + \frac{1}{2\pi}\int_{\omega_{\mathcal{N}-1}+\pi T}^{\Lambda} \mathrm{f}(\omega)\mathrm{d}\omega \,, \\ &\to \sum_m c_m\ \mathrm{f}(\omega_m)\ . \end{aligned} \tag{B.12}$$

Note, that each Matsubara frequency covers a range of $2\pi T$, therefore the integral limits are always half a Matsubara frequency away from the last explicitly calculated Matsubara mode. The integrals are numerically solved with a Gauss-Legendre routine, where it turns out to be of advantage to apply a log-grid in ω, where log represents the natural logarithm. In the second step of Eq. (B.12) we imply the numerical integration. Therefore the normal Matsubara modes with coefficients T are a subset of the ω_m. Eq. (B.12) needs to modified in case of a calculation of frequencies not on the Matsubara poles. If we calculate the system shifted by δ, e.g $\hat{\omega}_n = \omega_n + \delta$, we need to take the different limits in the integrals into account as well, otherwise the resulting dressing functions display wrong behaviour in the UV, which in particular manifests in the C function. Therefore Eq. (B.12) is modified to

$$\mathrm{T}\sum_{n:\,\omega_n^2<\Lambda^2} \mathrm{f}(\omega_n) \to \frac{1}{2\pi}\int_{-\Lambda}^{\omega_{-\mathcal{N}}-\pi T+\delta} \mathrm{f}(\omega)\mathrm{d}\omega + \mathrm{T}\sum_{-\mathcal{N}\leq n\leq \mathcal{N}-1} \mathrm{f}(\omega_n) + \frac{1}{2\pi}\int_{\omega_{\mathcal{N}-1}+\pi T+\delta}^{\Lambda} \mathrm{f}(\omega)\mathrm{d}\omega \,, \tag{B.13}$$

which leads to a asymmetry in the integration intervals. Note that the shift is always smaller than the difference of two Matsubara frequencies, therefore $\delta < 2\pi\mathrm{T}$, which is a negligible shift compared to the size of Λ.

For the radial and angular parts of the integral we refer as well to the Gauss-Legendre integral routine. For the radial part we work on a log-grid in $\mathbf{p}^2$ and substitute cos(θ)=z. One angle can be integrated out easily giving a factor of 2π, resulting in

$$\int^{\mathbf{\Lambda_n}} \mathrm{d}^3\mathrm{p}\ \mathrm{f}(\mathbf{p}) \to 2\pi \int_{\log(\epsilon^2)}^{\log(\mathbf{\Lambda_n}^2)} |\mathbf{p}|^3 \mathrm{d}|\mathbf{p}| \int_{-1}^{1} \mathrm{f}(|\mathbf{p}|, z)\ \mathrm{dz}\ . \tag{B.14}$$

For the numerical implementation it is useful to divide the angular-interval in exactly two subintervals $[-1, 0]$ and $[0, 1]$. Additionally we want to highlight the character of $\mathbf{\Lambda}$, which depends on the current value of the Matsubara frequency:

$$\mathrm{T}\sum_n \int^{\mathbf{\Lambda_n}} \mathrm{d}^3\mathrm{p} = \sum_m c_m \int^{\mathbf{\Lambda}_m=\sqrt{\Lambda^2-\omega_m^2}} \mathrm{d}^3\mathrm{p}\ , \tag{B.15}$$

where Λ is the O(4) cutoff, as well used for the vacuum calculation, where the integration is done analogously.

In order to generate an appropriate integration grid, we separate the interval (ϵ^2, Λ_m^2) in subintervals according to the grid spanned by the external momenta. Within those subintervals we apply a Gauss-Legendre integration, where an appropriate order is 6. Therefore in total we have a maximum of $N_{\mathrm{r,int}} = N_{\mathrm{Spline}} \times 6$ integrations points per Matsubara mode, depending on the number of external momenta in (ϵ^2, Λ_m^2). The number of explicitly summed Matsubara frequencies $\mathcal{N}$ (counted only for positive direction) is usually defined to be the number of explicit Matsubara frequencies we defined the quark propagator for (N_{expl}), but sometimes it is useful to increase this number to stabilize the system, as in Ch. 6. The number of grid points for the integral approximation of the higher Matsubara modes is dubbed N_{pad}. A value of $N_{\mathrm{pad}} = 32$ is sufficient for high precision calculations.

B.2. Details on the baryonic contributions

B.2.1. Renormalisation

The quark-quark-diquark and quark-diquark-baryon vertices are calculated within the Maris-Tandy interaction model, which uses a renormalisation point of $\zeta_{MT} = 19$ GeV. Since in the calculations of Ch. 5 are done for a renormalisation point of $\zeta = 80$ GeV we have to take corresponding changes in the renormalisation scale into account.

From the baryonic contributions in Fig. 5.3b we deduce which factors are needed, to ensure multiplicative renormalisability and to adjust for a common renormalisation scale:

- **Baryon-diquark loop:** Since the (bare) diquark and nucleon propagators contain no renormalisation constants, but the whole diagram is proportional to Z_2, each quark-diquark-baryon vertex must contribute a factor of $\sqrt{Z_2}$. Therefore the complete expression for the renormalisation factors for this part is

$$\frac{Z_2(\zeta)}{Z_2^{n_d/2}(\zeta_{MT})} ,$$

  with n_d being the number of dressed quark-diquark-baryon vertices.

- **Quark-diquark loop:** A similar reasoning is applicable for the quark-diquark loop. The diagram must be proportional to Z_2, taking into account the renormalisation constants of the internal propagator, we find for the expression of the renormalisation factors

$$\frac{Z_2^2(\zeta)}{Z_2^{m_d}(\zeta_{MT})} ,$$

with m_d being the number of dressed quark-diquark vertices.

The two constants $Z_2(\zeta)$ and $Z_2(\zeta_{MT})$ can be obtained from the (original system) to keep consistency. Note that the effect of the mentioned factors is small, since Z_2 is usually very close to 1.

B.2.2. Finding (non-negative) solutions

During the investigations discussed in Ch. 5, some numerical details became apparent:

- It is essential for the space of solutions of the quark DSE including the baryonic loops, that scales are matched. When solely adding the diquark-baryon loop without any adjustment, it is possible that this shift-function pushes the system to a (dominant) negative solution (see Fig. B.1), which is the case e.g. for the calculation with BSE_2 and no rescaling of the vertex strength. This will always be the case, if the negative solution is dominant and one uses an iterative procedure. The contribution from the chiral partner of the nucleon, as introduced via M_χ, works as a regulator of the diquark-baryon loop and avoids the collapse of the positive solution.

- It is recommended that for the solution of the DSE including baryonic degrees of freedom all contributions are taken into account from the beginning. In particular it is not ideal to start with only the Yang-Mills part of the self-energies and switch on the baryonic diagrams later. This makes it impossible to find the spinodal region beyond the critical endpoint.

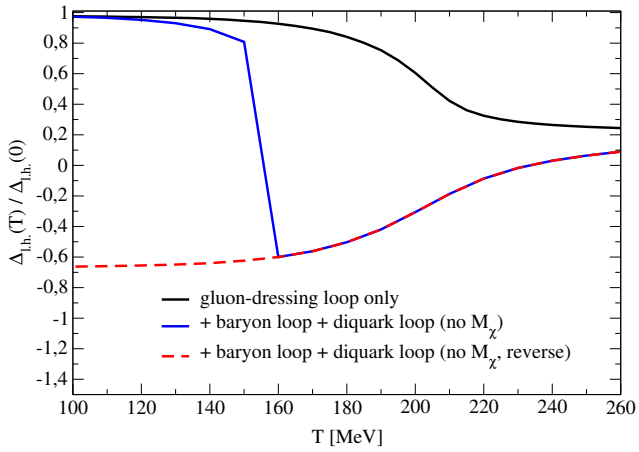

Figure B.1. Regularised condensate including baryonic contributions as in Ch. 5 without M_χ.

C. Quark-loop: Fit for $N_f = 2 + 1$

In the following we summarize the results for a fit to the longitudinal and the transverse parts of the quark-loop with the fit functions

$$\Pi^T_{\text{fit}} = \frac{a_T + b_T p^2}{1 + c_T p^2 + d_T p^4} - \mathcal{N}_\Pi \,, \tag{C.1}$$
$$\Pi^L_{\text{fit}} = \frac{a_L + b_L p^2}{1 + c_L p^2 + d_L p^4} - \mathcal{N}_\Pi + \frac{2m^2_{thermal}}{p^2} \,,$$

with the normalisation $\mathcal{N}_\Pi = 0.2282$ obtained from the vacuum calculation. The fit was done on an interval of $0.01 \cdots 10$ GeV^2 in p^2 for the given temperatures including the vacuum.

The quark-loop, as given in Eq. (C.1), can be directly used to obtain the unquenched gluon dressing functions in the manner of Eq. (3.17), which is repeated here for convenience:

$$\left[Z^{unq.}_{L,T}(q^2)\right]^{-1} = \left[Z^{que.}_{L,T}(q^2)\right]^{-1} + \Pi_{L,T}(q^2) \,.$$

It is noteworthy, that we found a fit function including also odd powers of p seemed to reproduce our results much better. However, due to the desired O(4) invariance, we used the ansatz given in Eq. (C.1).

T [GeV]	a_T	b_T [GeV^{-2}]	c_T [GeV^{-2}]	d_T [GeV^{-4}]
0.0	0.96847	0.30261	0.81065	0.01136
0.03	0.96967	0.30253	0.80929	0.01129
0.04	0.97207	0.30458	0.81385	0.01141
0.05	0.97612	0.30789	0.82090	0.01160
0.06	0.98036	0.31056	0.82714	0.01172
0.07	0.98385	0.31128	0.82976	0.01168
0.08	0.98505	0.30854	0.82574	0.01140
0.09	0.98449	0.30322	0.81575	0.01096
0.1	0.98220	0.29522	0.79964	0.01033
0.11	0.97552	0.28560	0.77927	0.00975
0.12	0.96750	0.27512	0.75609	0.00914
0.13	0.95781	0.26428	0.73124	0.00856
0.14	0.94486	0.25416	0.70610	0.00819
0.15	0.92881	0.24124	0.67410	0.00760
0.16	0.90186	0.22324	0.62858	0.00696
0.17	0.86782	0.19649	0.56504	0.00566
0.18	0.83548	0.17409	0.50934	0.00470
0.19	0.80539	0.15481	0.46097	0.00394
0.2	0.77834	0.13893	0.41951	0.00336
0.21	0.75425	0.12688	0.38750	0.00291
0.22	0.73093	0.11550	0.35491	0.00270
0.23	0.71034	0.10561	0.32769	0.00240
0.24	0.69117	0.09667	0.30314	0.00214
0.25	0.67328	0.08747	0.27902	0.00182

Table C.1. Fit results for the transverse part of the quark-loop corresponding to the set LAT_{2+1}.

T [GeV]	a_L	b_L [GeV^{-2}]	c_L [GeV^{-2}]	$d_L T$ [GeV^{-4}]	$m^2_{thermal}[GeV^2]$
0	0.96847	0.30261	0.81065	0.01136	0.00000
0.03	0.9665	0.30184	0.80753	0.01127	0.00077
0.04	0.96689	0.30337	0.81068	0.01138	0.00110
0.05	0.96779	0.30587	0.8155	0.01154	0.00164
0.06	0.96707	0.30707	0.81782	0.01162	0.00256
0.07	0.96291	0.30577	0.81476	0.01156	0.00415
0.08	0.95329	0.30102	0.80424	0.0113	0.00673
0.09	0.93852	0.2945	0.78841	0.011	0.01069
0.1	0.91848	0.28604	0.76719	0.01062	0.01645
0.11	0.89079	0.27665	0.743	0.01033	0.02436
0.12	0.8569	0.26574	0.71433	0.00998	0.03517
0.13	0.81477	0.2521	0.67874	0.00949	0.04988
0.14	0.76165	0.2353	0.63421	0.00899	0.06935
0.15	0.69919	0.20514	0.56009	0.00755	0.09355
0.16	0.64548	0.1748	0.48509	0.00622	0.11453
0.17	0.61041	0.1471	0.41871	0.00482	0.12849
0.18	0.58382	0.12888	0.37282	0.00401	0.14045
0.19	0.56038	0.11252	0.33178	0.00331	0.15205
0.2	0.54008	0.09993	0.29872	0.00282	0.16363
0.21	0.52217	0.0935	0.27976	0.00271	0.17506
0.22	0.50566	0.08236	0.25005	0.00229	0.18637
0.23	0.49136	0.07193	0.22284	0.00187	0.19763
0.24	0.47853	0.06327	0.19982	0.00155	0.20873
0.25	0.46691	0.05278	0.17284	0.00112	0.21966

Table C.2. Fit results for the longitudinal part of the quark-loop corresponding to the set LAT_{2+1}.

Bibliography

[1] "The Frontiers of Nuclear Science, A Long Range Plan," 2008.

[2] J. Letessier and J. Rafelski, *Hadrons and Quark Gluon Plasma; new ed.* Cambridge monographs on particle physics, nuclear physics, and cosmology, Cambridge: Cambridge Univ., 2005.

[3] B. Müller, "A New Phase of Matter: Quark-Gluon Plasma Beyond the Hagedorn Critical Temperature," in *Melting Hadrons, Boiling Quarks - From Hagedorn Temperature to Ultra-Relativistic Heavy-Ion Collisions at CERN: With a Tribute to Rolf Hagedorn* (J. Rafelski, ed.), pp. 107–116, 2016.

[4] B. Friman, C. Hohne, J. Knoll, S. Leupold, J. Randrup, R. Rapp, and P. Senger, "The CBM physics book: Compressed baryonic matter in laboratory experiments," *Lect. Notes Phys.*, vol. 814, pp. pp.1–980, 2011.

[5] K. Adcox *et al.*, "Suppression of hadrons with large transverse momentum in central Au+Au collisions at $\sqrt{s_{NN}}$ = 130-GeV," *Phys. Rev. Lett.*, vol. 88, p. 022301, 2002.

[6] B. B. Back *et al.*, "The PHOBOS perspective on discoveries at RHIC," *Nucl. Phys.*, vol. A757, pp. 28–101, 2005.

[7] I. Arsene *et al.*, "Quark gluon plasma and color glass condensate at RHIC? The Perspective from the BRAHMS experiment," *Nucl. Phys.*, vol. A757, pp. 1–27, 2005.

[8] K. Adcox *et al.*, "Formation of dense partonic matter in relativistic nucleus-nucleus collisions at RHIC: Experimental evaluation by the PHENIX collaboration," *Nucl. Phys.*, vol. A757, pp. 184–283, 2005.

[9] J. Adams *et al.*, "Experimental and theoretical challenges in the search for the quark gluon plasma: The STAR Collaboration's critical assessment of the evidence from RHIC collisions," *Nucl. Phys.*, vol. A757, pp. 102–183, 2005.

[10] L. Kumar, "Review of Recent Results from the RHIC Beam Energy Scan," *Mod. Phys. Lett.*, vol. A28, p. 1330033, 2013.

[11] R. Hagedorn, "Statistical thermodynamics of strong interactions at high-energies," *Nuovo Cim. Suppl.*, vol. 3, pp. 147–186, 1965.

[12] K. Huang and S. Weinberg, "Ultimate temperature and the early universe," *Phys. Rev. Lett.*, vol. 25, pp. 895–897, 1970.

[13] J. C. Collins and M. J. Perry, "Superdense Matter: Neutrons Or Asymptotically Free Quarks?," *Phys. Rev. Lett.*, vol. 34, p. 1353, 1975.

[14] N. Cabibbo and G. Parisi, "Exponential Hadronic Spectrum and Quark Liberation," *Phys. Lett.*, vol. B59, pp. 67–69, 1975.

[15] S. A. Bass *et al.*, "Microscopic models for ultrarelativistic heavy ion collisions," *Prog. Part. Nucl. Phys.*, vol. 41, pp. 255–369, 1998. [Prog. Part. Nucl. Phys.41,225(1998)].

[16] W. Cassing, A. Palmese, P. Moreau, and E. L. Bratkovskaya, "Chiral symmetry restoration versus deconfinement in heavy-ion collisions at high baryon density," *Phys. Rev.*, vol. C93, p. 014902, 2016.

[17] O. Linnyk, E. L. Bratkovskaya, and W. Cassing, "Effective QCD and transport description of dilepton and photon production in heavy-ion collisions and elementary processes," *Prog. Part. Nucl. Phys.*, vol. 87, pp. 50–115, 2016.

[18] P. Moreau, W. Cassing, A. Palmese, and E. Bratkovskaya, "Hadron Production within PHSD," in *11th Workshop on Particle Correlations and Femtoscopy (WPCF 2015) Warsaw, Poland, November 3-7, 2015*, 2016.

[19] R. D. de Souza, T. Koide, and T. Kodama, "Hydrodynamic approaches in relativistic heavy ion reactions," *Progress in Particle and Nuclear Physics*, vol. 86, pp. 35 – 85, 2016.

[20] H. Song, S. A. Bass, and U. Heinz, "Viscous QCD matter in a hybrid hydrodynamic+Boltzmann approach," *Phys. Rev.*, vol. C83, p. 024912, 2011.

[21] B. Schenke, S. Jeon, and C. Gale, "(3+1)D hydrodynamic simulation of relativistic heavy-ion collisions," *Phys. Rev.*, vol. C82, p. 014903, 2010.

[22] H. Petersen, J. Steinheimer, G. Burau, M. Bleicher, and H. Stöcker, "Fully integrated transport approach to heavy ion reactions with an intermediate hydrodynamic stage," *Phys. Rev. C*, vol. 78, p. 044901, Oct 2008.

[23] P. Petreczky, "Lattice QCD at non-zero temperature," *J. Phys.*, vol. G39, p. 093002, 2012.

[24] A. Bazavov, "Lattice QCD at Non-Zero Temperature," in *Proceedings, 32nd International Symposium on Lattice Field Theory (Lattice 2014)*, 2015.

[25] H. B. Meyer, "QCD at non-zero temperature from the lattice," in *Proceedings, 33rd International Symposium on Lattice Field Theory (Lattice 2015)*, 2015.

[26] D. Sexty, "Simulating full {QCD} at nonzero density using the complex langevin equation," *Physics Letters B*, vol. 729, pp. 108 – 111, 2014.

[27] G. Aarts, F. Attanasio, B. Jäger, E. Seiler, D. Sexty, and I.-O. Stamatescu, "QCD at nonzero chemical potential: recent progress on the lattice," *AIP Conf. Proc.*, vol. 1701, p. 020001, 2016.

[28] G. Aarts, E. Seiler, D. Sexty, and I.-O. Stamatescu, "Simulating qcd at nonzero baryon density to all orders in the hopping parameter expansion," *Phys. Rev. D*, vol. 90, p. 114505, Dec 2014.

[29] G. Aarts, "Introductory lectures on lattice QCD at nonzero baryon number," *J. Phys. Conf. Ser.*, vol. 706, no. 2, p. 022004, 2016.

[30] S. P. Klevansky, "The Nambu-Jona-Lasinio model of quantum chromodynamics," *Rev. Mod. Phys.*, vol. 64, pp. 649–708, 1992.

[31] J. Morais, J. Moreira, B. Hiller, A. H. Blin, and A. A. Osipov, "The T–μ Phase Diagram of the Nambu–Jona-Lasinio Model in the Presence of Explicit Symmetry-breaking Interactions," *Acta Phys. Polon. Supp.*, vol. 8, no. 1, p. 199, 2015.

[32] B.-J. Schaefer and J. Wambach, "The Phase diagram of the quark meson model," *Nucl. Phys.*, vol. A757, pp. 479–492, 2005.

[33] K. Fukushima, "Chiral effective model with the Polyakov loop," *Phys. Lett.*, vol. B591, pp. 277–284, 2004.

[34] E. Megias, E. Ruiz Arriola, and L. L. Salcedo, "Polyakov loop in chiral quark models at finite temperature," *Phys. Rev.*, vol. D74, p. 065005, 2006.

[35] C. Ratti, M. A. Thaler, and W. Weise, "Phases of QCD: Lattice thermodynamics and a field theoretical model," *Phys. Rev.*, vol. D73, p. 014019, 2006.

[36] M. Dutra, O. Lourenço, A. Delfino, T. Frederico, and M. Malheiro, "Polyakov-Nambu-Jona-Lasinio phase diagrams and quarkyonic phase from order parameters," *Phys.Rev.*, vol. D88, p. 114013, 2013.

[37] Z.-f. Cui, C. Shi, W.-m. Sun, Y.-l. Wang, and H.-s. Zong, "The Wigner Solution and QCD Phase Transitions in a Modified PNJL Model," *Eur. Phys. J.*, vol. C74, p. 2782, 2014.

[38] B.-J. Schaefer, J. M. Pawlowski, and J. Wambach, "The Phase Structure of the Polyakov–Quark-Meson Model," *Phys. Rev.*, vol. D76, p. 074023, 2007.

[39] V. Skokov, B. Stokic, B. Friman, and K. Redlich, "Meson fluctuations and thermodynamics of the Polyakov loop extended quark-meson model," *Phys. Rev.*, vol. C82, p. 015206, 2010.

[40] T. K. Herbst, J. M. Pawlowski, and B.-J. Schaefer, "The phase structure of the Polyakov–quark–meson model beyond mean field," *Phys. Lett.*, vol. B696, pp. 58–67, 2011.

[41] N. Strodthoff, B.-J. Schaefer, and L. von Smekal, "Quark-meson-diquark model for two-color QCD," *Phys. Rev.*, vol. D85, p. 074007, 2012.

[42] N. Strodthoff and L. von Smekal, "Polyakov-Quark-Meson-Diquark Model for two-color QCD," *Phys. Lett.*, vol. B731, pp. 350–357, 2014.

[43] R.-A. Tripolt, N. Strodthoff, L. von Smekal, and J. Wambach, "Spectral Functions for the Quark-Meson Model Phase Diagram from the Functional Renormalization Group," *Phys. Rev.*, vol. D89, no. 3, p. 034010, 2014.

[44] J. Braun, L. M. Haas, F. Marhauser, and J. M. Pawlowski, "Phase Structure of Two-Flavor QCD at Finite Chemical Potential," *Phys.Rev.Lett.*, vol. 106, p. 022002, 2011.

[45] L. M. Haas, *QCD at finite density with Dyson-Schwinger equations*. PhD thesis, 2012.

[46] T. K. Herbst, J. M. Pawlowski, and B.-J. Schaefer, "Phase structure and thermodynamics of QCD," *Phys. Rev.*, vol. D88, no. 1, p. 014007, 2013.

[47] T. K. Herbst, M. Mitter, J. M. Pawlowski, B.-J. Schaefer, and R. Stiele, "Thermodynamics of QCD at vanishing density," *Phys. Lett.*, vol. B731, pp. 248–256, 2014.

[48] T. K. Herbst, J. Luecker, and J. M. Pawlowski, "Confinement order parameters and fluctuations," 2015.

[49] L. Fister and J. M. Pawlowski, "Yang-Mills correlation functions at finite temperature," 2011.

[50] J. M. Pawlowski and N. Strodthoff, "Real time correlation functions and the functional renormalization group," *Phys. Rev.*, vol. D92, no. 9, p. 094009, 2015.

[51] C. D. Roberts and S. M. Schmidt, "Dyson-Schwinger equations: Density, temperature and continuum strong QCD," *Prog.Part.Nucl.Phys.*, vol. 45, pp. S1–S103, 2000.

[52] M. D. J. Nickel, *Color-superconductivity from a Dyson-Schwinger perspective*. PhD thesis, TU Darmstadt, June 2007.

[53] D. Mueller, *QCD at finite density with Dyson-Schwinger equations*. PhD thesis, TU Darmstadt, 2013.

[54] D. K. Hong, V. A. Miransky, I. A. Shovkovy, and L. C. R. Wijewardhana, "Schwinger-Dyson approach to color superconductivity in dense QCD," *Phys. Rev.*, vol. D61, p. 056001, 2000.

[55] D. Nickel, J. Wambach, and R. Alkofer, "Color-superconductivity in the strong-coupling regime of Landau gauge QCD," *Phys. Rev.*, vol. D73, p. 114028, 2006.

[56] D. Nickel, R. Alkofer, and J. Wambach, "On the unlocking of color and flavor in color-superconducting quark matter," *Phys. Rev.*, vol. D74, p. 114015, 2006.

[57] D. Müller, M. Buballa, and J. Wambach, "Dyson-Schwinger approach to color superconductivity at finite temperature and density," *Eur. Phys. J.*, vol. A49, p. 96, 2013.

[58] D. Müller, M. Buballa, and J. Wambach, "Dyson-Schwinger Approach to Color-Superconductivity: Effects of Selfconsistent Gluon Dressing," 2016.

[59] M. G. Alford, A. Schmitt, K. Rajagopal, and T. Schäfer, "Color superconductivity in dense quark matter," *Rev. Mod. Phys.*, vol. 80, pp. 1455–1515, 2008.

[60] A. Maas, J. Wambach, B. Gruter, and R. Alkofer, "High-temperature limit of Landau-gauge Yang-Mills theory," *Eur. Phys. J.*, vol. C37, pp. 335–357, 2004.

[61] B. Gruter, R. Alkofer, A. Maas, and J. Wambach, "Temperature dependence of gluon and ghost propagators in Landau-gauge Yang-Mills theory below the phase transition," *Eur. Phys. J.*, vol. C42, pp. 109–118, 2005.

[62] C. S. Fischer, "Deconfinement phase transition and the quark condensate," *Phys.Rev.Lett.*, vol. 103, p. 052003, 2009.

[63] C. S. Fischer and J. A. Mueller, "Chiral and deconfinement transition from Dyson-Schwinger equations," *Phys.Rev.*, vol. D80, p. 074029, 2009.

[64] C. S. Fischer, A. Maas, and J. A. Muller, "Chiral and deconfinement transition from correlation functions: SU(2) vs. SU(3)," *Eur.Phys.J.*, vol. C68, pp. 165–181, 2010.

[65] C. S. Fischer, J. Luecker, and J. A. Mueller, "Chiral and deconfinement phase transitions of two-flavour QCD at finite temperature and chemical potential," *Phys.Lett.*, vol. B702, pp. 438–441, 2011.

[66] C. S. Fischer and J. Luecker, "Propagators and phase structure of Nf=2 and Nf=2+1 QCD," *Phys.Lett.*, vol. B718, pp. 1036–1043, 2013.

[67] J. Luecker, *Chiral and deconfinement phase transitions in Nf=2 and Nf=2+1 quantum chromodynamics*. PhD thesis, Justus-Liebig-Universitaet, Otto-Behaghel-Str. 8, 35394 Giessen, 2013.

[68] C. S. Fischer, L. Fister, J. Luecker, and J. M. Pawlowski, "Polyakov loop potential at finite density," *Phys.Lett.*, vol. B732, pp. 273–277, 2014.

[69] M. Haas, L. Fister, and J. M. Pawlowski, "Gluon spectral functions and transport coefficients in Yang–Mills theory," *Phys. Rev.*, vol. D90, p. 091501, 2014.

[70] N. Christiansen, M. Haas, J. M. Pawlowski, and N. Strodthoff, "Transport Coefficients in Yang–Mills Theory and QCD," *Phys. Rev. Lett.*, vol. 115, no. 11, p. 112002, 2015.

[71] D. Nickel, "Extraction of Spectral Functions from Dyson-Schwinger Studies via the Maximum Entropy Method," *Annals Phys.*, vol. 322, pp. 1949–1960, 2007.

[72] J. A. Mueller, C. S. Fischer, and D. Nickel, "Quark spectral properties above Tc from Dyson-Schwinger equations," *Eur. Phys. J.*, vol. C70, pp. 1037–1049, 2010.

[73] S.-x. Qin, L. Chang, Y.-x. Liu, and C. D. Roberts, "Quark spectral density and a strongly-coupled QGP," *Phys.Rev.*, vol. D84, p. 014017, 2011.

[74] S.-x. Qin and D. H. Rischke, "Quark Spectral Function and Deconfinement at Nonzero Temperature," *Phys. Rev.*, vol. D88, p. 056007, 2013.

[75] F. Gao, S.-X. Qin, Y.-X. Liu, C. D. Roberts, and S. M. Schmidt, "Zero mode in a strongly coupled quark gluon plasma," *Phys. Rev.*, vol. D89, no. 7, p. 076009, 2014.

[76] F. Karsch and M. Kitazawa, "Spectral properties of quarks above in quenched lattice QCD," *Physics Letters B*, vol. 658, pp. 45 – 49, 2007.

[77] F. Karsch and M. Kitazawa, "Quark propagator at finite temperature and finite momentum in quenched lattice QCD," *Phys.Rev.*, vol. D80, p. 056001, 2009.

[78] O. Kaczmarek, F. Karsch, M. Kitazawa, and W. Soldner, "Thermal mass and dispersion relations of quarks in the deconfined phase of quenched QCD," *Phys.Rev.*, vol. D86, p. 036006, 2012.

[79] W. Heupel, T. Goecke, and C. S. Fischer, "Beyond Rainbow-Ladder in bound state equations," *Eur.Phys.J.*, vol. A50, p. 85, 2014.

[80] C. S. Fischer, J. Luecker, and C. A. Welzbacher, "Phase structure of three and four flavor QCD," *Phys. Rev.*, vol. D90, no. 3, p. 034022, 2014.

[81] G. Eichmann, C. S. Fischer, and C. A. Welzbacher, "Baryon effects on the location of QCD's critical end point," *Phys. Rev.*, vol. D93, no. 3, p. 034013, 2016.

[82] Y. Burnier and A. Rothkopf, "Bayesian Approach to Spectral Function Reconstruction for Euclidean Quantum Field Theories," *Phys.Rev.Lett.*, vol. 111, 2013.

[83] L. Faddeev and V. Popov, "Feynman diagrams for the Yang-Mills field," *Physics Letters B*, vol. 25, no. 1, pp. 29 – 30, 1967.

[84] V. Gribov, "Quantization of non-Abelian gauge theories," *Nuclear Physics B*, vol. 139, pp. 1 – 19, 1978.

[85] A. G. Williams, "QCD, gauge fixing, and the Gribov problem," *Nucl.Phys.Proc.Suppl.*, vol. 109A, pp. 141–145, 2002.

[86] A. G. Williams, "Nonperturbative QCD, gauge fixing, Gribov copies, and the lattice," *Prog.Theor.Phys.Suppl.*, vol. 151, pp. 154–160, 2003.

[87] P. J. Silva and O. Oliveira, "Gribov copies, lattice QCD and the gluon propagator," *Nucl. Phys.*, vol. B690, pp. 177–198, 2004.

[88] C. S. Fischer, "Infrared properties of QCD from Dyson-Schwinger equations," *J.Phys.*, vol. G32, pp. R253–R291, 2006.

[89] C. S. Fischer, A. Maas, and J. M. Pawlowski, "On the infrared behavior of Landau gauge Yang-Mills theory," *Annals Phys.*, vol. 324, pp. 2408–2437, 2009.

[90] A. Sternbeck, *The Infrared behavior of lattice QCD Green's functions.* PhD thesis, Humboldt U., Berlin, 2006.

[91] B. Holdom, "Gribov copies and anomalous scaling," *Phys. Rev.*, vol. D78, p. 125030, 2008.

[92] A. Sternbeck and M. Müller-Preussker, "Lattice evidence for the family of decoupling solutions of Landau gauge Yang-Mills theory," *Phys. Lett.*, vol. B726, pp. 396–403, 2013.

[93] C. S. Fischer, *Nonperturbative propagators, running coupling and dynamical mass generation in ghost - anti-ghost symmetric gauges in QCD.* PhD thesis, 2003.

[94] J. A. Mueller, *A Dyson-Schwinger Approach to Finite Temperature QCD*. PhD thesis, TU Darmstadt, January 2011.

[95] M. Peskin and D. Schroeder, *An Introduction to Quantum Field Theory*. Advanced book classics, Addison-Wesley Publishing Company, 1995.

[96] T. Kugo and I. Ojima, "Local Covariant Operator Formalism of Nonabelian Gauge Theories and Quark Confinement Problem," *Prog. Theor. Phys. Suppl.*, vol. 66, pp. 1–130, 1979.

[97] T. Kugo, "The Universal renormalization factors Z(1) / Z(3) and color confinement condition in nonAbelian gauge theory," in *BRS symmetry. Proceedings, International Symposium on the Occasion of its 20th Anniversary, Kyoto, Japan, September 18-22, 1995*, pp. 107–119, 1995.

[98] R. Alkofer, C. S. Fischer, and L. von Smekal, "Kugo-Ojima confinement criterion, Zwanziger-Gribov horizon condition, and infrared critical exponents in Landau gauge QCD," in *Quark confinement and the hadron spectrum. Proceedings, 5th International Conference, Gargnano, Italy, September 10-14, 2002*, pp. 148–157, 2003.

[99] J. Greensite, "The Confinement problem in lattice gauge theory," *Prog. Part. Nucl. Phys.*, vol. 51, p. 1, 2003.

[100] J. Greensite, K. Langfeld, S. Olejnik, H. Reinhardt, and T. Tok, "Color Screening, Casimir Scaling, and Domain Structure in G(2) and SU(N) Gauge Theories," *Phys. Rev.*, vol. D75, p. 034501, 2007.

[101] J. I. Kapusta and C. Gale, *Finite-temperature field theory : principles and applications*. Cambridge University Press, 2 ed., Aug. 2006.

[102] T. M. Doi, H. Suganuma, and T. Iritani, "Relation between Confinement and Chiral Symmetry Breaking in Temporally Odd-number Lattice QCD," *Phys. Rev.*, vol. D90, no. 9, p. 094505, 2014.

[103] M. Le Bellac, *Thermal field theory*. Cambridge monographs on mathematical physics, Cambridge: Cambridge Univ. Press, 1996.

[104] F. J. Dyson, "The s matrix in quantum electrodynamics," *Phys. Rev.*, vol. 75, pp. 1736–1755, Jun 1949.

[105] J. S. Schwinger, "On the Green's functions of quantized fields. 1.," *Proc. Nat. Acad. Sci.*, vol. 37, pp. 452–455, 1951.

[106] R. Alkofer, M. Huber, and K. Schwenzer, "Algorithmic derivation of Dyson–Schwinger equations," *Computer Physics Communications*, vol. 180, no. 6, pp. 965 – 976, 2009.

[107] L. von Smekal, K. Maltman, and A. Sternbeck, "The Strong coupling and its running to four loops in a minimal MOM scheme," *Phys. Lett.*, vol. B681, pp. 336–342, 2009.

[108] A. Maas, *The high-temperature phase of Yang-Mills theory in Landau gauge*. PhD thesis, Darmstadt, Tech. Hochsch., 2005.

[109] A. Maas, J. Wambach, and R. Alkofer, "The High-temperature phase of Landau-gauge Yang-Mills theory," *Eur. Phys. J.*, vol. C42, pp. 93–107, 2005.

[110] A. Cucchieri, A. Maas, and T. Mendes, "Infrared properties of propagators in Landau-gauge pure Yang-Mills theory at finite temperature," *Phys. Rev.*, vol. D75, p. 076003, 2007.

[111] H. Munczek, "Dynamical chiral symmetry breaking, Goldstone's theorem and the consistency of the Schwinger-Dyson and Bethe-Salpeter Equations," *Phys.Rev.*, vol. D52, pp. 4736–4740, 1995.

[112] C. L. Smith, "A relativistic formulation of the quark model for mesons," *Annals of Physics*, vol. 53, no. 3, pp. 521 – 558, 1969.

[113] R. E. Cutkosky and M. Leon, "Normalization of Bethe-Salpeter Wave Functions and Bootstrap Equations," *Phys. Rev.*, vol. 135, pp. B1445–B1446, Sep 1964.

[114] N. Nakanishi, "Normalization Condition and Normal and Abnormal Solutions of the Bethe-Salpeter Equation," *Phys. Rev.*, vol. 138, pp. B1182–B1192, Jun 1965.

[115] G. Eichmann, *Hadron Properties from QCD Bound-State Equations*. PhD thesis, Karl-Franzens-Universität Graz, 2009.

[116] J. Braun, H. Gies, and J. M. Pawlowski, "Quark Confinement from Color Confinement," *Phys.Lett.*, vol. B684, pp. 262–267, 2010.

[117] L. Fister and J. M. Pawlowski, "Confinement from Correlation Functions," *Phys. Rev.*, vol. D88, p. 045010, 2013.

[118] C. DeTar and U. Heller, "QCD Thermodynamics from the Lattice," *Eur.Phys.J.*, vol. A41, pp. 405–437, 2009.

[119] C. Bonati, M. D'Elia, P. de Forcrand, O. Philipsen, and F. Sanfilippo, "The chiral phase transition for two-flavour QCD at imaginary and zero chemical potential," *PoS*, vol. LATTICE2013, p. 219, 2014.

[120] C. Bonati, P. de Forcrand, M. D'Elia, O. Philipsen, and F. Sanfilippo, "Chiral phase transition in two-flavor QCD from an imaginary chemical potential," *Phys. Rev.*, vol. D90, no. 7, p. 074030, 2014.

[121] S. Borsanyi *et al.*, "Is there still any T_c mystery in lattice QCD? Results with physical masses in the continuum limit III," *JHEP*, vol. 1009, p. 073, 2010.

[122] G. Endrődi, "QCD phase diagram: overview of recent lattice results," *J. Phys. Conf. Ser.*, vol. 503, p. 012009, 2014.

[123] C. Bonati, M. D'Elia, P. de Forcrand, O. Philipsen, and F. Sanfillippo, "The chiral phase transition for two-flavour QCD at imaginary and zero chemical potential," *PoS*, vol. LATTICE2013, p. 219, 2014.

[124] N. Su, "A brief overview of hard-thermal-loop perturbation theory," *Commun. Theor. Phys.*, vol. 57, p. 409, 2012.

[125] W. J. Marciano and H. Pagels, "Quantum Chromodynamics: A Review," *Phys. Rept.*, vol. 36, p. 137, 1978.

[126] A. C. Aguilar, D. Binosi, J. C. Cardona, and J. Papavassiliou, "Nonperturbative results on the quark-gluon vertex," 2013. [PoSConfinementX,103(2012)].

[127] E. Rojas, J. P. B. C. de Melo, B. El-Bennich, O. Oliveira, and T. Frederico, "On the Quark-Gluon Vertex and Quark-Ghost Kernel: combining Lattice Simulations with Dyson-Schwinger equations," *JHEP*, vol. 10, p. 193, 2013.

[128] J. S. Ball and T.-W. Chiu, "Analytic Properties of the Vertex Function in Gauge Theories. 1.," *Phys. Rev.*, vol. D22, p. 2542, 1980.

[129] C. S. Fischer and R. Alkofer, "Nonperturbative propagators, running coupling and dynamical quark mass of Landau gauge QCD," *Phys.Rev.*, vol. D67, p. 094020, 2003.

[130] R. Aouane, F. Burger, E. M. Ilgenfritz, M. Müller-Preussker, and A. Sternbeck, "Landau gauge gluon and ghost propagators from lattice QCD with N_f=2 twisted mass fermions at finite temperature," *Phys. Rev.*, vol. D87, no. 11, p. 114502, 2013.

[131] R. Williams, "The quark-gluon vertex in Landau gauge bound-state studies," *Eur. Phys. J.*, vol. A51, no. 5, p. 57, 2015.

[132] N. Brown and M. R. Pennington, "Studies of confinement: How quarks and gluons propagate," *Phys. Rev. D*, vol. 38, pp. 2266–2276, Oct 1988.

[133] P. J. Silva, O. Oliveira, P. Bicudo, and N. Cardoso, "Gluon screening mass at finite temperature from the Landau gauge gluon propagator in lattice QCD," *Phys. Rev.*, vol. D89, no. 7, p. 074503, 2014.

[134] P. Buescher, *Phase diagram of two-color QCD in a Dyson-Schwinger approach.* PhD thesis, TU Darmstadt, 2014.

[135] Y. Jiang, L.-J. Luo, and H.-S. Zong, "A Model study of quark number susceptibility at finite temperature beyond rainbow-ladder approximation," *JHEP*, vol. 1102, p. 066, 2011.

[136] A. Bazavov, H. T. Ding, P. Hegde, F. Karsch, C. Miao, S. Mukherjee, P. Petreczky, C. Schmidt, and A. Velytsky, "Quark number susceptibilities at high temperatures," *Phys. Rev.*, vol. D88, no. 9, p. 094021, 2013.

[137] X.-y. Xin, S.-x. Qin, and Y.-x. Liu, "Quark number fluctuations at finite temperature and finite chemical potential via the Dyson-Schwinger equation approach," *Phys. Rev. D*, vol. 90, p. 076006, Oct 2014.

[138] H. T. Ding, S. Mukherjee, H. Ohno, P. Petreczky, and H. P. Schadler, "Diagonal and off-diagonal quark number susceptibilities at high temperatures," *Phys. Rev.*, vol. D92, no. 7, p. 074043, 2015.

[139] A. Bandyopadhyay, N. Haque, M. G. Mustafa, and M. Strickland, "Dilepton rate and quark number susceptibility with the Gribov action," *Phys. Rev.*, vol. D93, no. 6, p. 065004, 2016.

[140] J. Takahashi, H. Kouno, and M. Yahiro, "Quark number densities at imaginary chemical potential in $N_f = 2$ lattice QCD with Wilson fermions and its model analyses," *Phys.Rev.*, vol. D91, no. 1, p. 014501, 2015.

[141] O. Philipsen and C. Pinke, "Nature of the Roberge-Weiss transition in $N_f = 2$ QCD with Wilson fermions," *Phys. Rev.*, vol. D89, no. 9, p. 094504, 2014.

[142] C. Bonati, P. de Forcrand, M. D'Elia, O. Philipsen, and F. Sanfilippo, "Chiral phase transition in two-flavor QCD from an imaginary chemical potential," *Phys.Rev.*, vol. D90, no. 7, p. 074030, 2014.

[143] A. Roberge and N. Weiss, "Gauge Theories With Imaginary Chemical Potential and the Phases of QCD," *Nucl. Phys.*, vol. B275, p. 734, 1986.

[144] C. S. Fischer, J. Luecker, and J. M. Pawlowski, "Phase structure of QCD for heavy quarks," *Phys. Rev.*, vol. D91, no. 1, p. 014024, 2015.

[145] S. Borsányi, Z. Fodor, S. D. Katz, S. Krieg, C. Ratti, and K. Szabo, "Freeze-out parameters: lattice QCD meets heavy-ion experiments," *PoS*, vol. QCD-TNT-III, p. 033, 2013.

[146] G. Endrodi, Z. Fodor, S. Katz, and K. Szabo, "The QCD phase diagram at nonzero quark density," *JHEP*, vol. 1104, p. 001, 2011.

[147] O. Kaczmarek, F. Karsch, E. Laermann, C. Miao, S. Mukherjee, P. Petreczky, C. Schmidt, W. Soeldner, and W. Unger, "Phase boundary for the chiral transition in (2+1) -flavor QCD at small values of the chemical potential," *Phys. Rev.*, vol. D83, p. 014504, 2011.

[148] P. Cea, L. Cosmai, and A. Papa, "On the critical line of 2+1 flavor QCD," *Phys.Rev.*, vol. D89, p. 074512, 2014.

[149] C. Bonati, M. D'Elia, M. Mariti, M. Mesiti, F. Negro, and F. Sanfilippo, "Curvature of the chiral pseudocritical line in QCD: Continuum extrapolated results," *Phys. Rev.*, vol. D92, no. 5, p. 054503, 2015.

[150] R. Bellwied, S. Borsanyi, Z. Fodor, J. Günther, S. D. Katz, C. Ratti, and K. K. Szabo, "The QCD phase diagram from analytic continuation," *Phys. Lett.*, vol. B751, pp. 559–564, 2015.

[151] P. Cea, L. Cosmai, and A. Papa, "Critical line of 2+1 flavor QCD: Toward the continuum limit," *Phys. Rev.*, vol. D93, no. 1, p. 014507, 2016.

[152] S. Borsanyi, G. Endrodi, Z. Fodor, S. D. Katz, S. Krieg, C. Ratti, C. Schroeder, and K. K. Szabo, "The QCD equation of state and the effects of the charm," *PoS*, vol. LATTICE2011, p. 201, 2011.

[153] A. Bazavov *et al.*, "Update on the 2+1+1 flavor QCD equation of state with HISQ," *PoS*, vol. LATTICE2013, p. 154, 2014.

[154] A. Bazavov *et al.*, "The melting and abundance of open charm hadrons," *Phys. Lett.*, vol. B737, pp. 210–215, 2014.

[155] C. Ratti, S. Borsanyi, G. Endrodi, Z. Fodor, S. D. Katz, S. Krieg, C. Schroeder, and K. K. Szabo, "Lattice QCD thermodynamics in the presence of the charm quark," *Nucl. Phys.*, vol. A904-905, pp. 869c–872c, 2013.

[156] F. Burger, G. Hotzel, M. Müller-Preussker, E.-M. Ilgenfritz, and M. P. Lombardo, "Towards thermodynamics with $N_f = 2 + 1 + 1$ twisted mass quarks," *PoS*, vol. Lattice2013, p. 153, 2013.

[157] A. Trunin, F. Burger, E.-M. Ilgenfritz, M. P. Lombardo, and M. Muller-Preussker, "Topological susceptibility from $N_f = 2 + 1 + 1$ lattice QCD at nonzero temperature," *J. Phys. Conf. Ser.*, vol. 668, no. 1, p. 012123, 2016.

[158] F. Burger, E.-M. Ilgenfritz, M. P. Lombardo, M. Muller-Preussker, and A. Trunin, "Towards the quark–gluon plasma Equation of State with dynamical strange and charm quarks," *J. Phys. Conf. Ser.*, vol. 668, no. 1, p. 012092, 2016.

[159] K. A. Olive *et al.*, "Review of Particle Physics," *Chin. Phys.*, vol. C38, p. 090001, 2014.

[160] N. Carrasco *et al.*, "A determination of the average up-down, strange and charm quark masses from $N_f = 2 + 1 + 1$," *PoS*, vol. LATTICE2013, p. 312, 2014.

[161] A. Bazavov *et al.*, "Charmed and strange pseudoscalar meson decay constants from HISQ simulations," *PoS*, vol. LATTICE2013, p. 405, 2014.

[162] N. Khan, J. M. Pawlowski, F. Rennecke, and M. M. Scherer, "The Phase Diagram of QC2D from Functional Methods," 2015.

[163] W. Weise, "Nuclear chiral dynamics and phases of QCD," *Prog.Part.Nucl.Phys.*, vol. 67, pp. 299–311, 2012.

[164] I. Pushkina, P. de Forcrand, M. Garcia Perez, S. Kim, H. Matsufuru, A. Nakamura, I.-O. Stamatescu, T. Takaishi, and T. Umeda, "Properties of hadron screening masses at finite baryonic density," *Phys. Lett.*, vol. B609, pp. 265–270, 2005.

[165] K.-l. Wang, Y.-x. Liu, L. Chang, C. D. Roberts, and S. M. Schmidt, "Baryon and meson screening masses," *Phys.Rev.*, vol. D87, no. 7, p. 074038, 2013.

[166] D. Blaschke, A. Dubinin, and D. Zablocki, "NJL model approach to diquarks and baryons in quark matter," in *Proceedings, 22nd International Baldin Seminar on High Energy Physics Problems, Relativistic Nuclear Physics and Quantum Chromodynamics, (ISHEPP 2014)*, 2015.

[167] H. Zhang, R. Dong, and S. Shu, "The baryon mass calculation in the chiral soliton model at finite temperature and density," *Int. J. Mod. Phys.*, vol. E24, no. 04, p. 1550025, 2015.

[168] C. S. Fischer, D. Nickel, and J. Wambach, "Hadronic unquenching effects in the quark propagator," *Phys. Rev.*, vol. D76, p. 094009, 2007.

[169] C. S. Fischer and R. Williams, "Beyond the rainbow: Effects from pion back-coupling," *Phys.Rev.*, vol. D78, p. 074006, 2008.

[170] C. S. Fischer, D. Nickel, and R. Williams, "On Gribov's supercriticality picture of quark confinement," *Eur.Phys.J.*, vol. C60, pp. 47–61, 2009.

[171] C. S. Fischer and R. Williams, "Probing the gluon self-interaction in light mesons," *Phys.Rev.Lett.*, vol. 103, p. 122001, 2009.

[172] H. Sanchis-Alepuz, C. S. Fischer, and S. Kubrak, "Pion cloud effects on baryon masses," *Phys. Lett.*, vol. B733, pp. 151–157, 2014.

[173] C. S. Fischer and J. A. Mueller, "On critical scaling at the QCD Nf=2 chiral phase transition," *Phys. Rev.*, vol. D84, p. 054013, 2011.

[174] S. Ghosh, A. Lahiri, S. Majumder, R. Ray, and S. K. Ghosh, "Shear viscosity due to Landau damping from the quark-pion interaction," *Phys. Rev.*, vol. C88, no. 6, p. 068201, 2013.

[175] G. Eichmann, R. Alkofer, A. Krassnigg, and D. Nicmorus, "Nucleon mass from a covariant three-quark Faddeev equation," *Phys. Rev. Lett.*, vol. 104, p. 201601, 2010.

[176] H. Sanchis-Alepuz, G. Eichmann, S. Villalba-Chavez, and R. Alkofer, "Delta and Omega masses in a three-quark covariant Faddeev approach," *Phys. Rev.*, vol. D84, p. 096003, 2011.

[177] G. Eichmann, "Nucleon electromagnetic form factors from the covariant Faddeev equation," *Phys. Rev.*, vol. D84, p. 014014, 2011.

[178] H. Sanchis-Alepuz and C. S. Fischer, "Octet and Decuplet masses: a covariant three-body Faddeev calculation," *Phys. Rev.*, vol. D90, no. 9, p. 096001, 2014.

[179] H. Sanchis-Alepuz and R. Williams, "Probing the quark–gluon interaction with hadrons," *Phys. Lett.*, vol. B749, pp. 592–596, 2015.

[180] M. Oettel, G. Hellstern, R. Alkofer, and H. Reinhardt, "Octet and decuplet baryons in a covariant and confining diquark-quark model," *Phys. Rev.*, vol. C58, pp. 2459–2477, 1998.

[181] M. Oettel, R. Alkofer, and L. von Smekal, "Nucleon properties in the covariant quark diquark model," *Eur. Phys. J.*, vol. A8, pp. 553–566, 2000.

[182] I. C. Cloet, G. Eichmann, B. El-Bennich, T. Klahn, and C. D. Roberts, "Survey of nucleon electromagnetic form factors," *Few Body Syst.*, vol. 46, pp. 1–36, 2009.

[183] J. Segovia, I. C. Cloet, C. D. Roberts, and S. M. Schmidt, "Nucleon and Δ elastic and transition form factors," *Few Body Syst.*, vol. 55, pp. 1185–1222, 2014.

[184] G. Eichmann, A. Krassnigg, M. Schwinzerl, and R. Alkofer, "A Covariant view on the nucleons' quark core," *Annals Phys.*, vol. 323, pp. 2505–2553, 2008.

[185] G. Eichmann, I. C. Cloet, R. Alkofer, A. Krassnigg, and C. D. Roberts, "Toward unifying the description of meson and baryon properties," *Phys. Rev.*, vol. C79, p. 012202, 2009.

[186] D. Nicmorus, G. Eichmann, and R. Alkofer, "Delta and Omega electromagnetic form factors in a Dyson-Schwinger/Bethe-Salpeter approach," *Phys. Rev.*, vol. D82, p. 114017, 2010.

[187] G. Eichmann and D. Nicmorus, "Nucleon to Delta electromagnetic transition in the Dyson-Schwinger approach," *Phys. Rev.*, vol. D85, p. 093004, 2012.

[188] H. Hellmann, "Zur Rolle der kinetischen Elektronenenergie für die zwischenatomaren Kräfte," *Zeitschrift für Physik*, vol. 85, no. 3, pp. 180–190.

[189] R. P. Feynman, "Forces in Molecules," *Phys. Rev.*, vol. 56, pp. 340–343, 1939.

[190] W. Kamleh, P. O. Bowman, D. B. Leinweber, A. G. Williams, and J. Zhang, "Unquenching effects in the quark and gluon propagator," *Phys. Rev.*, vol. D76, p. 094501, 2007.

[191] R. Alkofer, C. S. Fischer, F. J. Llanes-Estrada, and K. Schwenzer, "The Quark-gluon vertex in Landau gauge QCD: Its role in dynamical chiral symmetry breaking and quark confinement," *Annals Phys.*, vol. 324, pp. 106–172, 2009.

[192] A. Windisch, M. Hopfer, and R. Alkofer, "Towards a self-consistent solution of the Landau gauge quark-gluon vertex Dyson-Schwinger equation," 2012. [Acta Phys. Polon. Supp.6,347(2013)].

[193] M. Hopfer, *Gauge Theories: QCD and Beyond*. PhD thesis, Karl-Franzens-Universität Graz, 2014.

[194] A. Windisch, *Features of strong quark correlations at vanishing and non-vanishing density*. PhD thesis, Karl-Franzens-Universität Graz, 2014.

[195] R. Williams, C. S. Fischer, and W. Heupel, "Light mesons in QCD and unquenching effects from the 3PI effective action," *Phys. Rev.*, vol. D93, no. 3, p. 034026, 2016.

[196] A. C. Aguilar, "A new method for computing the quark-gluon vertex," *J. Phys. Conf. Ser.*, vol. 631, no. 1, p. 012058, 2015.

[197] A. Cucchieri, A. Maas, and T. Mendes, "Exploratory study of three-point Green's functions in Landau-gauge Yang-Mills theory," *Phys. Rev.*, vol. D74, p. 014503, 2006.

[198] A. C. Aguilar, D. Binosi, D. Ibañez, and J. Papavassiliou, "Effects of divergent ghost loops on the Green's functions of QCD," *Phys. Rev.*, vol. D89, no. 8, p. 085008, 2014.

[199] M. Pelaez, M. Tissier, and N. Wschebor, "Three-point correlation functions in Yang-Mills theory," *Phys. Rev.*, vol. D88, p. 125003, 2013.

[200] A. Blum, M. Q. Huber, M. Mitter, and L. von Smekal, "Gluonic three-point correlations in pure Landau gauge QCD," *Phys. Rev.*, vol. D89, p. 061703, 2014.

[201] G. Eichmann, R. Williams, R. Alkofer, and M. Vujinovic, "The three-gluon vertex in Landau gauge," *Phys.Rev.*, vol. D89, no. 10, p. 105014, 2014.

[202] P. O. Bowman, U. M. Heller, D. B. Leinweber, M. B. Parappilly, A. G. Williams, and J.-b. Zhang, "Unquenched quark propagator in Landau gauge," *Phys. Rev.*, vol. D71, p. 054507, 2005.

[203] R.-A. Tripolt, L. von Smekal, and J. Wambach, "Flow equations for spectral functions at finite external momenta," *Phys. Rev.*, vol. D90, no. 7, p. 074031, 2014.

[204] R.-A. Tripolt, *Spectral Functions and Transport Coefficients from the Functional Renormalization Group*. PhD thesis, Darmstadt, Tech. U., 2015.

[205] E. Braaten, R. D. Pisarski, and T. C. Yuan, "Production of soft dileptons in the quark-gluon plasma," *Phys. Rev. Lett.*, vol. 64, pp. 2242–2245, May 1990.

[206] A. Peshier and M. H. Thoma, "Quark dispersion relation and dilepton production in the quark gluon plasma," *Phys.Rev.Lett.*, vol. 84, pp. 841–844, 2000.

[207] T. Kim, M. Asakawa, and M. Kitazawa, "Dilepton production spectrum above Tc with a lattice quark propagator," *Phys. Rev.*, vol. D92, no. 11, p. 114014, 2015.

[208] C. Welzbacher, "Quark spectral functions at finite temperature in a Dyson-Schwinger approach," Master's thesis, 2012.

[209] N. Nakanishi and I. Ojima, "Covariant operator formalism of gauge theories and quantum gravity," *World Sci. Lect. Notes Phys.*, vol. 27, pp. 1–434, 1990.

[210] R. Alkofer, W. Detmold, C. Fischer, and P. Maris, "Analytic properties of the Landau gauge gluon and quark propagators," *Phys.Rev.*, vol. D70, p. 014014, 2004.

[211] K. Osterwalder and R. Schrader, "Axioms for Euclidean Green's functions," *Comm. Math. Phys.*, vol. 31, no. 2, pp. 83–112, 1973.

[212] S. M. Dorkin, L. P. Kaptari, T. Hilger, and B. Kampfer, "Analytical properties of the quark propagator from a truncated Dyson-Schwinger equation in complex Euclidean space," *Phys. Rev.*, vol. C89, p. 034005, 2014.

[213] M. Stingl, "A Systematic extended iterative solution for quantum chromodynamics," *Z. Phys.*, vol. A353, pp. 423–445, 1996.

[214] P. Maris, C. D. Roberts, and P. C. Tandy, "Pion mass and decay constant," *Phys.Lett.*, vol. B420, pp. 267–273, 1998.

[215] P. Maris and P. C. Tandy, "The pi, K+, and K0 electromagnetic form-factors," *Phys.Rev.*, vol. C62, p. 055204, 2000.

[216] P. Maris and C. D. Roberts, "Dyson-Schwinger equations: A Tool for hadron physics," *Int.J.Mod.Phys.*, vol. E12, pp. 297–365, 2003.

[217] W. Heupel, G. Eichmann, and C. S. Fischer, "Tetraquark Bound States in a Bethe-Salpeter Approach," *Phys.Lett.*, vol. B718, pp. 545–549, 2012.

[218] C. D. Roberts, "Strong QCD and Dyson-Schwinger Equations," 2012.

[219] H. Sanchis-Alepuz and R. Williams, "Hadronic Observables from Dyson-Schwinger and Bethe-Salpeter equations," *J. Phys. Conf. Ser.*, vol. 631, no. 1, p. 012064, 2015.

[220] M. Frigo and S. G. Johnson, "The design and implementation of FFTW3," *Proceedings of the IEEE*, vol. 93, no. 2, pp. 216–231, 2005. Special issue on "Program Generation, Optimization, and Platform Adaptation".

[221] A. Rothkopf, "A first look at Bottomonium melting via a stochastic potential," *JHEP*, vol. 04, p. 085, 2014.

[222] S. Kim, P. Petreczky, and A. Rothkopf, "Lattice NRQCD study of S- and P-wave bottomonium states in a thermal medium with $N_f = 2 + 1$ light flavors," *Phys. Rev.*, vol. D91, p. 054511, 2015.

[223] Y. Burnier, O. Kaczmarek, and A. Rothkopf, "Static quark-antiquark potential in the quark-gluon plasma from lattice QCD," *Phys. Rev. Lett.*, vol. 114, no. 8, p. 082001, 2015.

[224] S. Kim, P. Petreczky, and A. Rothkopf, "Lattice NRQCD study on in-medium bottomonium spectra using a novel Bayesian reconstruction approach," *AIP Conf. Proc.*, vol. 1701, p. 060017, 2016.

[225] Y. Burnier and A. Rothkopf, "A gauge invariant Debye mass and the complex heavy-quark potential," *Phys. Lett.*, vol. B753, pp. 232–236, 2016.

[226] Y. Burnier, O. Kaczmarek, and A. Rothkopf, "Quarkonium at finite temperature: Towards realistic phenomenology from first principles," *JHEP*, vol. 12, p. 101, 2015.

[227] M. Asakawa, T. Hatsuda, and Y. Nakahara, "Maximum entropy analysis of the spectral functions in lattice QCD," *Prog.Part.Nucl.Phys.*, vol. 46, pp. 459–508, 2001.

Erklärung

Ich erkläre: Ich habe die vorgelegte Dissertation selbständig und ohne unerlaubte fremde Hilfe und nur mit den Hilfen angefertigt, die ich in der Dissertation angegeben habe. Alle Textstellen, die wörtlich oder sinngemäß aus veröffentlichten Schriften entnommen sind, und alle Angaben, die auf mündlichen Auskünften beruhen, sind als solche kenntlich gemacht. Bei den von mir durchgeführten und in der Dissertation erwähnten Untersuchungen habe ich die Grundsätze guter wissenschaftlicher Praxis, wie sie in der *Satzung der Justus-Liebig-Universität Gießen zur Sicherung guter wissenschaftlicher Praxis* niedergelegt sind, eingehalten.

Gießen, den 25.08.2016

Christian Andreas Welzbacher